FACULDADE DE ENGENHARIA DA
UNIVERSIDADE DO PORTO

Segmentation and classification of structures of the carotid and coronary arteries for image-based evaluation of atherosclerotic lesions

Danilo Samuel Jodas

U. PORTO

FEUP **FACULDADE DE ENGENHARIA**
UNIVERSIDADE DO PORTO

Segmentation and classification of structures of the carotid and coronary arteries for image-based evaluation of atherosclerotic lesions

Thesis submitted in partial fulfillment of the requirements for the degree of Doctor in Informatics Engineering by the Faculty of Engineering of the University of Porto

Danilo Samuel Jodas

Master of Computer Science from the Universidade Estadual Paulista "Júlio de Mesquita Filho" (2012)

Bachelor of Computer Science from the Centro Universitário do Norte Paulista (2008)

Supervisor

João Manuel Ribeiro da Silva Tavares

Associate Professor of the Mechanical Engineering Department

Faculdade de Engenharia da Universidade do Porto

Co-Supervisor

Aledir Silveira Pereira

Assistant Professor of the Computer Science and Statistics Department

Universidade Estadual Paulista "Júlio de Mesquita Filho"

November, 2017

Acknowledgments

I would like to thank Professor João Tavares for his valuable contributions that have indeed improved my PhD project at each stage of the developed work. The advice provided by Professor João Tavares contributed to my training as a good researcher. Moreover, his effort for my coming to Portugal made me have wonderful experiences and knowledge about the Portuguese and European cultures.

I would like to thank my co-supervisor Professor Aledir Silveira Pereira for all the support provided during the development of this PhD project and his dedicated effort that made possible my coming to Portugal. This PhD thesis was possible thanks to the opportunity that Professor Aledir Silveira Pereira gave me some years ago to start my MSc project.

I want to show all my gratitude to my parents who gave me an excellent education and raised me with all the effort and affection that made me a better person every single day. Even with all the difficulties, my parents always offered me all the support for a good education, which contributed to my personal and professional development. I thank them so much for everything they have done for me.

I want to show my sincere gratitude to all my friends that have worked with me and with whom I have had happy and memorable moments. Thank you for sharing experiences and knowledge that have helped me a lot during my studies. It was a pleasure to have met them.

"The memory is the result of the interest. The greater the interest for something, the easier the way it will be kept in the memory. It is a mistake try to keep in the mind information that are not interesting for you. The memory is a selective element that represents the principle of the knowledge structuring."

Olavo de Carvalho

Abstract

Evaluation of the arterial system represents an important step towards the identification of disorders related to the reduction or even the blockage of the blood flow to vital structures of the body. The presence of atherosclerosis represents a risk to the life of the patients and needs to be treated as early on as possible to avoid the occurrence of heart attacks and strokes. The advent of novel imaging systems contributed to the envisage of the anatomy of the arterial system and the accurate identification of abnormalities that may impair the blood flow through the arteries under analysis. However, the manual delineation of arterial structures in medical images is a time consuming and subjective task. Therefore, the development of automatic algorithms for image segmentation is necessary to expedite the diagnosis and treatment planning before the onset or even the recurrence of symptoms.

This project focused on the assessment of image processing and analysis algorithms to address the automatic segmentation of structures of the arterial system, particularly those present in the carotid and coronary arteries. A study of classification models for identifying calcifications in atherosclerosis of the carotid artery in computed tomography angiography images was also carried out. Computational algorithms for the segmentation of the arterial system and analysis of the atherosclerotic plaque components were reviewed and classified according to the computational technique and imaging modality used. The complexity of the structures and intensity variations of the images were seen to be a challenge to the development of new fully automatic segmentation methods. Clustering algorithms and deformable models were found to be promising for the segmentation of structures belonging to carotid and coronary arteries. Therefore, the first step in the development of segmentation methods was the identification of the lumen in carotid and coronary arteries. The low intensity and circular shape of the lumen in axial magnetic resonance images of the carotid artery were taken as premise to propose a new automatic method without any type of user interaction. The combination of the K-means clustering algorithm and the circularity index was used to separate the low intensity regions of the magnetic resonance images and to select the one which represents the potential lumen region of the carotid artery. Additionally, an active contour model was employed to refine the contour of the identified lumen region.

The ability of the proposed automatic segmentation method to identify the lumen region in intravascular ultrasound images of the coronary artery with the same parameters previously defined for magnetic resonance images of the carotid artery was also assessed in this project. This was relevant since the intensity and shape of the lumen in intravascular ultrasound images of the coronary artery are similar to the ones in axial black-blood magnetic resonance images of the carotid artery. Modifications were made to improve the shape of the segmented lumen contour and eliminate one parameter previously included

to identify regions segmented by the K-means clustering algorithm that represent noise. Moreover, a new approach was proposed to identify and eliminate side branches present in bifurcations of the coronary artery.

The combination of a distance map and a new external energy for the Snake model was adopted to segment the outer boundary of the carotid artery in magnetic resonance images. To prevent gradient vectors close to the boundary of the lumen region, the segmented lumen contour was used as a baseline for the first outwards expansion based on the distance map of the grayscale intensities of the magnetic resonance image under study. Thereafter, an external energy based on the intensity of the input image was then integrated in the active contour model to complete the expansion of the contour towards the carotid artery boundary. The proposed approach was also conceived to effectively handle with carotid arteries having large wall thickness.

Concerning the identification of calcium regions in computed tomography angiography images of the carotid artery, a two-stage classification approach was adopted to first identify the regions where calcified components may be present based on features extracted from each pixel inside the carotid artery wall. Then, features extracted from each identified region were submitted to the second stage to determine the regions that represent the true calcifications of the atherosclerosis. The geometrical and intensity features adopted in the second classification stage revealed to be promising in identifying and eliminating regions with intensities similar to the ones of the calcifications present in atherosclerotic lesions of the carotid artery.

The results obtained by the proposed methods were compared against the corresponding manual delineations, as well as with methods reported in literature. The effectiveness of the developed methods was confirmed and the aspects that might be improved were identified.

Keywords: Medical images, Image analysis, Segmentation, Deformable models, Atherosclerosis, Classification.

Resumo

A avaliação do sistema arterial representa um passo importante para a identificação de distúrbios relacionados à redução ou mesmo ao bloqueio do fluxo sanguíneo para estruturas vitais do corpo. A presença de aterosclerose nas artérias representa um risco para a vida dos doentes e precisa ser tratada o mais cedo possível para evitar a ocorrência de ataques cardíacos e acidentes vasculares cerebrais. O advento de novos sistemas de diagnóstico por imagem tem contribuído para a visualização da anatomia do sistema arterial e a identificação precisa de anormalidades que podem prejudicar o fluxo sanguíneo através das artérias em análise. No entanto, a marcação manual das estruturas das artérias em imagens médicas é uma tarefa bastante demorada e subjectiva. Portanto, o desenvolvimento de algoritmos de segmentação automática é necessário para acelerar o diagnóstico e o planeamento do tratamento antes do início ou até mesmo da recorrência de sintomas.

Este projeto focalizou a avaliação de algoritmos de processamento e análise de imagem para abordar a segmentação automática de estruturas do sistema arterial, particularmente aquelas presentes nas artérias carótida e coronária. Também foi realizado um estudo de modelos de classificação para a identificação de calcificações em ateroscleroses presentes na artéria carótida em imagens de angiografia por tomografia computadorizada. Algoritmos computacionais para a segmentação do sistema arterial e análise da composição de ateroscleroses foram identificados e classificados de acordo com a técnica computacional e modalidade de imagem em causa. A complexidade das estruturas e variações de intensidade das imagens foram vistas como um desafio para o desenvolvimento de novos métodos de segmentação totalmente automáticos. Algoritmos de *clustering* e modelos deformáveis foram identificados como promissores para a segmentação de estruturas pertencentes às artérias carótida e coronária. Portanto, o primeiro passo no desenvolvimento de métodos de segmentação foi a identificação do lúmen nas artérias carótida e coronária. A baixa intensidade e forma circular do lúmen em imagens de ressonância magnética axial da artéria carótida foram tomadas como premissa para o desenvolvimento de um novo método automático sem qualquer tipo de intervenção manual. A combinação do algoritmo *K-means* com o índice de circularidade foi adotada para separar as regiões de baixa intensidade das imagens de ressonância magnética e selecionar a que representa a possível região do lúmen da artéria carótida. Além disso, foi utilizado um modelo de contorno ativo para refinar o contorno da região do lúmen.

A capacidade do método de segmentação automática para a identificação da região do lúmen em imagens de ultrassom intravascular da artéria coronária com os mesmos parâmetros previamente definidos para imagens de ressonância magnética da artéria carótida também foi avaliada neste projeto. Esta adequação foi testada devido ao facto de que a intensidade e a forma do lúmen nas imagens de ultrassom intravascular da artéria

coronária são semelhantes às encontradas em imagens de ressonância magnética axial *black-blood* da artéria carótida. Foram feitas modificações para melhorar o formato do contorno do lúmen e eliminar um parâmetro previamente adotado para identificar regiões segmentadas pelo algoritmo *K-means* que representam possíveis ruídos. Além disso, uma nova abordagem foi proposta para identificar e eliminar ramos laterais presentes nas bifurcações da artéria coronária.

A combinação de um mapa de distâncias e uma nova energia externa proposta para o modelo de contorno ativo conhecido por "Snake" foi adotada para segmentar a borda externa da artéria carótida em imagens de ressonância magnética. A fim de evitar os vetores de gradiente próximos da borda da região do lúmen, o contorno do lúmen foi usado como contorno inicial para a primeira expansão com base no mapa de distâncias das intensidades da imagem de ressoância magnética. Em seguida, uma energia externa baseada na intensidade da imagem em estudo foi integrada ao modelo de contorno ativo para completar a expansão do contorno em direção à borda da artéria carótida. A abordagem proposta foi concebida para lidar de maneira eficiente com artérias carótidas de grande espessura.

Relativamente à identificação de calcificações em imagens de angiografia por tomografia computadorizada da artéria carótida, uma abordagem de classificação em duas etapas foi adotada para primeiramente identificar as regiões que representam possíveis componentes calcificados com base em características extraídas de cada pixel contido na parede da artéria carótida. Em seguida, as características extraídas de cada região foram submetidas à segunda etapa para determinar as regiões que representam as verdadeiras calcificações da aterosclerose. As características geométricas e de intensidade adotadas na segunda fase de classificação revelaram-se promissoras para identificar e eliminar regiões com intensidades similares às das calcificações presentes nas lesões ateroscleróticas da artéria carótida.

Os resultados obtidos dos métodos propostos foram comparados com as respectivas marcações manuais, bem como com os métodos relatados na literatura. A eficácia dos métodos desenvolvidos foi confirmada e os aspectos que podem ser melhorados foram identificados.

Palavras-chave: Imagem médica, Análise de imagem, Segmentação, Modelos deformáveis, Aterosclerose, Classificação.

Contents

Contents

Part A:

Thesis report

1 Introduction

Cardiovascular diseases still remain one of the most leading causes of death in the world. According to the World Health Organization, in 2011, cardiovascular diseases represented 31% of deaths of people around the world [1]. In 2008, cardiovascular diseases were responsible for the death of more than 17 million people under 60-year old [1]. Smoking, lack of physical exercise, inadequate food and excessive alcohol consumption are the primary causes of this type of disease [1]. Pathologies associated to cardiovascular diseases might lead to serious complications such as amaurosis fugax, heart attacks and strokes. Hence, the early diagnosis is important to minimize the risks of appearance or recurrence of those symptoms.

One of the main underlying process of cardiovascular diseases is the atherosclerosis, which results from the formation of fatty material and cholesterol inside the walls of the arterial system. In the advanced stage, an atherosclerosis is composed by lipid core, fibrous tissue, intraplaque hemorrhage and calcifications. Atherosclerosis reduces or occludes the blood flow through the artery, leading to serious complications such as angina, heart attack and vascular cerebral accident. An aneurysm is another type of cardiovascular disease that can arise as a result of a weakened artery wall. The formation and rupture of blood clots originated from an aneurysm might induce hemorrhages, thrombosis and hypovolemia shocks.

The interruption of the blood flow to a portion of the brain is the underlying condition for the appearance of cerebrovascular diseases [2]. Small blood clots produced by abnormal beating of the heart are one of the causes of cerebral events [2]. Shedding of such clots into the bloodstream through the carotid arteries might block small vessels of the brain, causing lack of oxygen and, consequently, a stroke. The formation of cholesterol deposits in the wall of the carotid artery is also responsible for impairing the normal blood flow to regions of the brain. Cholesterol debris detached from such deposits might enter the bloodstream and travel to small vessels of the brain, resulting in the blockage of such vessels and, consequently, in cerebral events. Transient ischemic attack and stroke are the most common types of cerebrovascular diseases [2].

The assessment of atherosclerosis in the arterial system plays an important role in the care of patients subjected to the above-mentioned cardiovascular and cerebrovascular diseases. The early diagnosis allows timely planning of an adequate treatment for limiting the disease progression. The degree of stenosis is commonly used to assess the percentage of artery narrowing at the location of the atherosclerotic plaque. The degree of stenosis is usually classified as mild (0-29%), moderate (30-69%) and high (70-99%) [3]. In general, patients with high degree of stenosis have a higher chance of developing a cerebral event

and therefore are selected for a surgical or endovascular procedure [3, 4]. However, the quantification of atherosclerosis proved to be a more accurate and reliable diagnosis to select the most appropriate treatment for each patient and identify those with higher risk for future symptomatic events.

Technological advances made in computational systems of imaging diagnosis allow the assessment and detection of cardiovascular and cerebrovascular diseases in a less invasive manner. Computed Tomography (CT) and Magnetic Resonance Imaging (MRI) are examples of less invasive techniques that have been widely used for identification of diseases and dysfunctions of the internal organs. CT is a technique for image reconstruction which relies on the radiologic attenuation of the anatomical regions under evaluation [5]. In CT exams, a device composed by x-ray emission sources rotates around the region of interest to generate 2D images of the related anatomical structures. The quality of CT images is better than those generated by traditional x-ray systems.

In spite of its advantages over the traditional catheter diagnosis, CT might be harmful to the health of patients due to the x-rays emission. It is sometimes possible to overcome this problem by using other imaging systems such as ultrasound and magnetic resonance, which are widely used and accepted by physicians. The diagnosis performed by the MRI exam represents a lower risk to human health as a result of the non-exposure to the ionizing radiation. Magnetic Resonance Angiography (MRA) is an MRI diagnosis of blood vessels commonly adopted to evaluate diseases of the cardiovascular system. MRA is a noninvasive technique and safer than traditional angiography exams, since there is no exposure to the x-rays emission. Other MRI exams such as Time-of-Flight (TOF) angiography are also used for generating images without injection of contrast dye [6], which is important to avoid allergic reactions in the patient.

Intravascular Ultrasound (IVUS) is another imaging technique which allows the visualization of the morphology of blood vessels by means of ultrasound waves acquired from a small ultrasound transducer attached to the top of a catheter that is inserted into the artery to be diagnosed. Although it is an invasive imaging technique, IVUS allows experts to detect and quantify atherosclerosis, as well as to assess the shape and size of the vessel under analysis.

Techniques of image processing and analysis are commonly necessary to identify structures in images in order to obtain statistic data or apply intelligent algorithms for pattern recognition tasks. Regarding the usage in medical applications, techniques of image processing and analysis are important to improve the quality of medical images and consequently, the detection of structures associated to the pathologies to be evaluated. Techniques such as smoothing filtering, contrast enhancement and segmentation algorithms are commonly adopted to minimize noise effects, perform contrast correction and

divide an original image in order to separate its main regions. Hence, image segmentation is an important process for generating information to be processed in many applications found in medicine.

Image segmentation can be carried out in the following manners:

- Manual: the pixels belonging to the regions of interest are explicitly defined by the user. However, it is an unfeasible task in images with a large amount of pixels or from complex scenarios;

- Automatic: a computational algorithm automatically identifies the image pixels based on pre-established rules. However, these algorithms may not always provide the most efficient results due to the complexity of the images or/and of the structures involved;

- Semiautomatic: the approaches discussed above are combined in order to enable the user to provide critical information about the structures of interest. Moreover, semiautomatic algorithms can be used to manually correct errors or inaccurate results obtained by automatic methods.

Automatic and semiautomatic methods of image segmentation have been developed in order to accurately detect arteries and blood vessels in images acquired from different imaging techniques [7–9]. These methods provide fast identification of the structures for evaluating pathologies in an efficient way. Moreover, the common acquisition of large volumes of images of the arterial system stimulates the development of algorithms to automatically identify the lumen and outer boundary of the arteries, as well as the detection of diseases such as aneurysm, stenosis and atherosclerosis [10–13].

2   Main objectives of the project

The objectives defined for this PhD project were the following ones:

- To prepare a literature review of the atherosclerotic plaque components and the association between atherosclerosis and cerebrovascular diseases, as well as the imaging modalities used to identify plaque components; to identify the computational algorithms based on image processing, clustering and supervised classification adopted for identification and quantification of atherosclerotic plaque components in images;

- To evaluate the relevance of magnetic resonance (MR) images in the identification and analysis of the structures of the carotid artery; to address the automatic segmentation of the lumen and outer boundaries in MR images of the carotid artery and explore the main difficulties associated with the intensity variation inside the artery under analysis;

- To study the applicability of the segmentation method proposed for identifying the lumen region in MR images of the carotid artery to detect the lumen in IVUS images of the coronary artery; to evaluate the similarities of the grayscale intensity of both imaging modalities in order to employ the same lumen segmentation method in IVUS images of the coronary artery without modification of the parameter values defined for MR images of the carotid artery;

- To evaluate the use of deformable models for the segmentation of the outer boundary of the carotid artery in magnetic resonance images. Variations of the grayscale intensity are a challenge to the expansion of the segmented lumen contour towards the boundary of the carotid artery in the image under analysis. Additionally, carotid arteries with large wall thickness may still affect the convergence of the contours to the boundaries of interest. Hence, the development of new approaches based on deformable models is important to improve the accuracy of the segmentation of carotid artery boundaries in magnetic resonance images;

- To develop a new classification model which identifies calcifications in atherosclerotic plaques present in carotid arteries; to handle the incorrect detection of regions with intensities similar to calcified components resulting from the inaccurate registration of the ground truths obtained from histological images with the corresponding *in vivo* Computed Tomography Angiography (CTA) images.

In summary, the development of algorithms to segment, characterize and classify structures of the carotid and coronary arteries in MR and IVUS images was the main focus of this project. More particularly, the segmentation of the lumen and outer boundaries in MR images of the carotid artery and classification of calcified regions in atherosclerotic lesions of the carotid artery in CTA images were the main purposes of this project. An algorithm for the fully automatic segmentation of the lumen in IVUS images of the coronary artery was also developed.

3   Organization of the Thesis

This Thesis is organized in two main parts: Part A and Part B. This part (Part A) presents the context in which the work was developed, the main objectives defined for this PhD project, a summarized description of the tasks developed, the main contributions achieved, the final conclusions and a discussion of the future works. Part B is composed of five articles written during the development of the PhD project. The articles provide a detailed description of the state-of-the-art related to the project, the new fully automatic segmentation algorithms developed and the classification model proposed to identify calcifications in atherosclerotic lesions of the carotid artery in CTA images. The following articles are included in Part B:

Article 1

> *A review of computational methods applied for identification and quantification of atherosclerotic plaques in images*
>
> Danilo Samuel Jodas, Aledir Silveira Pereira, João Manuel R. S. Tavares
>
> Expert Systems with Applications, 46:1-14, 2016

Article 2

> *Lumen segmentation in magnetic resonance images of the carotid artery*
>
> Danilo Samuel Jodas, Aledir Silveira Pereira, João Manuel R. S. Tavares
>
> Computers in Biology and Medicine, 79(1):233-242, 2016

Article 3

> *Automatic segmentation of the lumen region in intravascular images of the coronary artery*
>
> Danilo Samuel Jodas, Aledir Silveira Pereira, João Manuel R. S. Tavares
>
> Medical Imaging Analysis, 40:60-79, 2017

Article 4

> *Using a distance map and an active contour model to segment in proton density weighted magnetic resonance images the carotid artery boundary from the lumen contour*
>
> Danilo Samuel Jodas, Maria Francisca Monteiro da Costa, Tiago A. A. Parreira, Aledir Silveira Pereira, João Manuel R. S. Tavares

Submitted to an international journal, 2017

Article 5

Classification of calcified regions in atherosclerotic lesions of the carotid artery in computed tomography angiography images

Danilo Samuel Jodas, Aledir Silveira Pereira, João Manuel R. S. Tavares

Submitted to an international journal, 2017

4 Brief description of the developed work

The segmentation of structures of the carotid artery is a challenge due to the usual intensity variation of the images and weak boundaries of the regions of interest. This PhD project concerned the development of fully automatic methods for the segmentation of the lumen and carotid artery boundaries in magnetic resonance images. The applicability of the proposed automatic segmentation method used in axial magnetic resonance images to detect the lumen in intravascular ultrasound images of the coronary artery was also assessed. Additionally, a two-stage classification process to be applied in CTA images was developed to detect calcium regions present in atherosclerotic lesions of the carotid artery. The following works were accomplished to fulfill the objectives established in this project:

- The state-of-the-art of the methods already used in the identification and quantification of atherosclerotic plaque components in images was reviewed. The most important studies related to the segmentation of atherosclerotic plaques and the associated components in images acquired from the carotid and coronary arteries by ultrasound, CTA and MRI techniques were categorized in terms of image processing and analysis, clustering algorithms and supervised classification. The advantages and limitations of each study were also discussed. This comprehensive review summarizes the most important computational methods employed to identify structures of the carotid and coronary arteries in medical images, particularly the atherosclerotic plaques and their main components. Additionally, the most used image modalities in diagnosis, visualization and characterization of the atherosclerotic plaque components are identified. The review is presented in Article 1 included in Part B;

- The segmentation of the lumen region in MR images of the carotid artery plays an important role in evaluating the pathologies associated to cardiovascular diseases.

Intensity variation and the presence of noisy artifacts represent a challenge to the development of fully automatic segmentation methods which identify the correct location of the lumen region of the carotid artery. A method for the fully automatic segmentation of the lumen region in axial MR images of the carotid artery was proposed. This new method is based on the fact that the lumen occupies a circular-shaped region with low grayscale intensity in axial MR images. The new approach is based on the following stages: i) separation of the regions in the input MR image by means of the K-means clustering algorithm with subtractive clustering; ii) evaluation of the regions belonging to the cluster with low intensities by the modified mean roundness to calculate their circularity index; the one with the maximum value represents the potential lumen region of the carotid artery; and iii) refinement of the boundary of this region by an active contour algorithm. The proposed method proved to be effective in identifying the correct location of the lumen region in 181 Proton Density Weighted (PDW) and 181 3D-T1-Weighted MR images of the carotid artery. The new method is presented in Article 2 included in Part B;

- The segmentation of the lumen and media-adventitia regions in IVUS images of the coronary artery is an intensive focus of research since it plays an important role towards the identification and quantification of atherosclerosis. A fully automatic method for the segmentation of the lumen in IVUS images of the coronary artery was developed. The new method is based on the following steps: i) the down-sampling of the input image resolution by means of the Gaussian pyramid; ii) the identification of the regions present in the IVUS image using the K-means clustering algorithm with subtractive clustering; iii) the identification of noisy artifacts in the regions with low grayscale intensity using a morphological opening operation with an adaptive structuring element; iv) the identification and removal of parts of bifurcation regions; v) the employment of a circularity index to identify the potential lumen region; vi) the refinement of the boundary of this region by means of an active contour algorithm; and vii) the post-processing of the lumen contour based on the morphological opening and dilation operations with adaptive structuring elements. The proposed method was evaluated on 326 IVUS images of the coronary artery acquired at a frequency of 20 MHz. The method is described and discussed in Article 3 included in Part B;

- The segmentation of the boundary of the carotid artery represents the first step towards the identification of the atherosclerotic plaques and analysis of the morphology of the associated components. Deformable models have been successfully

employed to segment the outer boundary of the carotid artery in MR images. However, carotid arteries having large wall thickness and gradient vectors close to the lumen regions represent a challenge to expand the segmented lumen contours towards the outer boundaries of interest. Hence, a method to automatically identify the boundary of carotid arteries in PDW MR images was developed. The gray-weighted distance is firstly used to generate a distance map of the intensities of the input MR image of the carotid artery. The Snake model is then applied on the distance map to expand the segmented lumen contour beyond the boundary of the lumen region. An ellipse constraint is also included in the Snake model to avoid local convergence and maintain the contour with elliptical shape. Thereafter, a new external energy for the Snake model called Weighted External Energy is employed to complete the convergence of the expanded contour towards the true boundary of the carotid artery. The method was effective in segmenting the outer boundaries of the carotid artery in 185 PDW MR images, showing better results than the ones obtained by using a Gradient Vector Flow-based force commonly used as external energy in active contour models. The new approach is presented in Article 4 included in Part B;

- The diagnosis of the progression of atherosclerotic plaques is often made by identifying and evaluating the morphology of their main components. A new classification model was proposed to identify calcified regions in atherosclerotic plaques of the carotid artery in CTA images. Since parts of the lumen and other structures of the carotid artery may affect the classification results due to the similarity of their grayscale intensities with the calcium regions, the proposed classification model is composed of two stages. The first stage is the classification per pixel, which is based on the features extracted from each pixel inside the carotid wall. The resulting regions are then submitted to the second stage, the classification per region, to identify those representing the correct calcified components of the atherosclerotic lesion. Additionally, outlier removal is performed to improve the accuracy of the classification model, which is presented in Article 5 included in Part B.

The steps of the work developed in this PhD project along with examples of corresponding results are illustrated in Figure 1.

5   Main contributions achieved

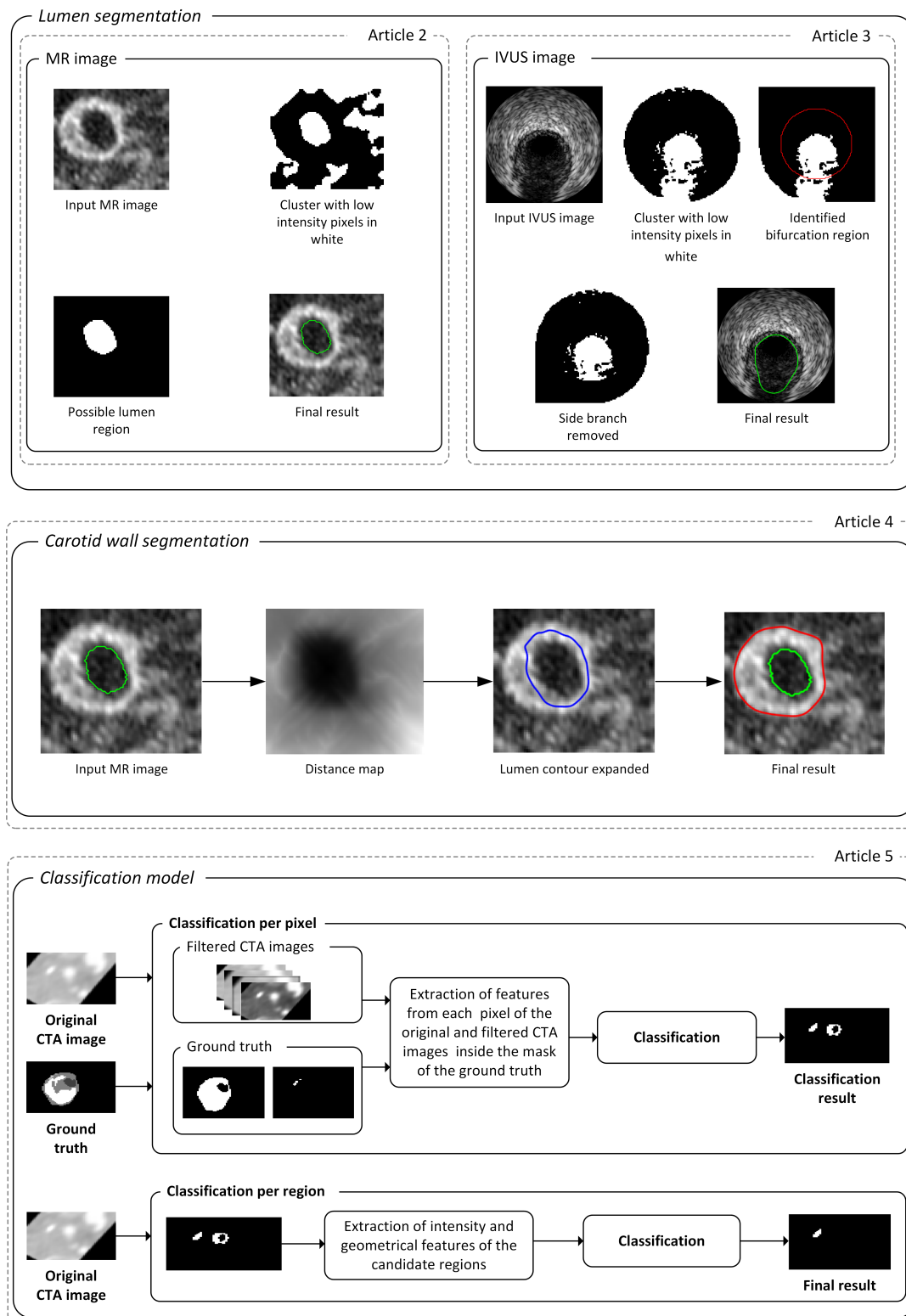The main contributions of this PhD project were the following ones:

Figure 1: Steps of the work developed during this PhD project along with examples of corresponding results. The articles indicated in each step and included in Part B of this report provide a detailed description of the developed methods. Article 1 is a comprehensive review of the related work and therefore does not appear in this diagram.

- A comprehensive review of the computational methods for the segmentation of atherosclerosis and assessment of the associated components was successfully produced. The context comprised in this review is important to provide a comprehension of the theories related to: cardiovascular diseases, imaging systems for visualization of the carotid and coronary arteries, clinical methods usually adopted in the diagnosis of symptomatic and asymptomatic patients, and the identification of the main approaches applied to segment and assess the structures of the carotid and coronary arteries, particularly the atherosclerotic plaque components. The methods described in this review are classified per computational technique used to segment the main components of the atherosclerosis. This can help other researchers to investigate the appropriate algorithms and image modalities used to identify structures of the carotid and coronary arteries for future research works;

- A novel automatic method was developed to identify the location of the lumen region in axial MR images of the carotid artery. Segmentation based on the subtractive clustering algorithm was adopted to improve the stability concerning the establishment of the values of the cluster centroids used in the K-means clustering algorithm. A circularity index is used to identify the lumen of the carotid artery, which normally has a circular shape in axial MR images. The following circularity index was proposed to evaluate each region with low grayscale intensity segmented by the K-means clustering algorithm:

$$E = MR + \frac{1}{Ir} + \frac{1}{d},\tag{1}$$

where MR is the mean roundness that assesses the circularity of the region under analysis, Ir is an irregularity index used to avoid regions with irregular contours and d is the centre index that represents the distance of the centre of the region under analysis to the centre of the input image. The region that provides the maximum value for E is assumed to be the lumen of the carotid artery under study.

Based on comparisons against manual delineations, the proposed method was shown to be effective in identifying the correct lumen region without any manual intervention. Comparison with results obtained from studies found in the literature also suggested the superiority of the proposed method;

- The applicability of the proposed fully automatic method for segmenting the lumen in IVUS images of the coronary artery with the same parameters defined for the MR images of the carotid artery was assessed. This novel approach was able to

identify the lumen in IVUS images without any changes in the values of the parameters previously established for the MR images. Improvements in the method were also accomplished in order to increase the automaticity and performance whilst improving the shape of the lumen contour. Moreover, the method is able to identify and remove side branches in IVUS images with a bifurcation in the coronary artery. In IVUS images of the coronary artery, bifurcations represent the extension of the low grayscale intensity from the lumen region to the border of the input image. Regions representing this extension are generated when the cluster corresponding to the low-intensity values is built by the K-means clustering algorithm. Bifurcation regions are not assessed in the subsequent processing steps of the method proposed for the segmentation of the lumen region in MR images of the carotid artery, since the regions at the border of the input image are discarded before the identification of the lumen. Hence, a new approach to identify and remove bifurcations in IVUS images of the coronary artery was developed. Bifurcation regions are removed from the binary images generated by the K-means clustering algorithm according to:

$$r = min(dist(Cp, Bp)) - min(dist(Cp, Rp)), \qquad (2)$$

where C_p is the pixel at the centre of the input image, B_p is the set of pixels of the bifurcation region that are at the border of the input image and R_p is the set of all pixels of the contour of the bifurcation. Based on the analysis of the regions of the input binary image generated by the K-means clustering algorithm, the bifurcation is assumed to be the region that is in the centre and with pixels at the border of the image under analysis. Once a bifurcation is found, the proposed formulation defined in Equation 2 is used to generate a circle with radius r centred at the center of the image in order to delimit the regions with the possible lumen. The region outside this circle that represents the side branch of the bifurcation is removed from the binary image corresponding to the low grayscale intensity. This approach is shown to be effective in decreasing the segmentation errors and, consequently, improving the segmentation accuracy;

- A new approach to segment the boundaries of carotid arteries in PDW MR images based on the expansion of the segmented lumen contours was proposed and developed in this project. The combination of a gray-weighted distance map of the intensities of the input MR images with a novel external energy for the Snake model proved to be effective in segmenting carotid arteries with weak boundaries or large wall thickness. The distance map of the input MR image is calculated according to:

$$t_f(P) = \sum_{i=1}^{l} \frac{f(p_i - 1) + f(p_i)}{2}, \tag{3}$$

where $f(p_i - 1)$ and $f(p_i)$ are the intensities of the adjacent pixels $p_i - 1$ and p_i along the minimum cost path $t_f(P)$, and l is the length of the path P. The resulting distance map image is then used as input to the Snake model with an ellipse shape constraint to expand the segmented lumen contour beyond the boundary of the lumen region. Then, the following weighted external energy was proposed to complete the evolution of the expanded contour towards the boundary of the carotid artery:

$$E_{ext} = A * ((F_{balloon} * (1 - \Omega)) + (F_{NNGVF} * \Omega)), \tag{4}$$

where $F_{balloon}$ is the balloon force of the contour to be deformed, F_{NNGVF} is a Gradient Vector Flow based force called Neighbourhood-Extending and Noise-Smoothing Gradient Vector Flow (NNGVF), Ω is a term which controls the application of the balloon and NNGVF based forces and A is a penalty term proposed to decrease the evolution of the contour when regions with low intensity are found.

To the best of our knowledge, no other study presented the combination of the gray-weighted distance map and the active contour model for the segmentation of structures in medical images. Therefore, the proposed approach is an important contribution to improve the accuracy of the segmentation results;

- A novel classification model was developed to identify calcified regions present in atherosclerotic lesions of the carotid artery in CTA images. The proposed approach combines two stages, being the first one the classification per pixel and the second one the classification of the resulting regions in order to handle the incorrect identification of parts of the lumen as calcium regions. The geometrical and intensity features adopted in the second stage provide more accurate information to determine which regions are the true calcifications of the atherosclerosis. The outlier removal was also important to improve the detection of the calcium regions and consequently approximate them to the corresponding ground truths. The stages of the proposed classification model with examples of resultant images are illustrated in Figure 2. The features used as input to each stage of the proposed classification approach are indicated in Table 1.
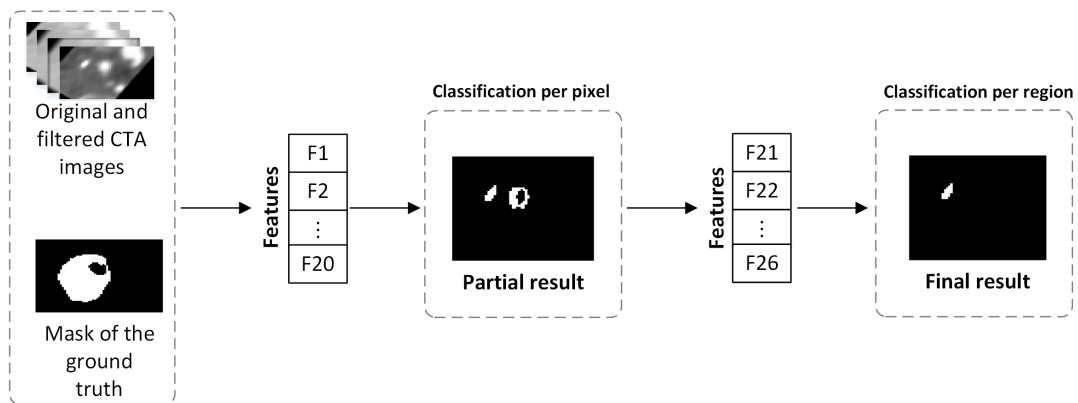
Figure 2: Two-stage classification model proposed to detect the calcified regions in atherosclerotic lesions of the carotid artery in CTA images. The features used in the pixel classification stage are extracted from each pixel of the CTA images inside the mask of the ground truth. The features used in the classification per region stage are extracted from each region resultant from the previous stage. (The features used in each stage of the classification model are indicated in Table 1.)

Table 1: Features used in the proposed classification model.

Id.	Classification per pixel	Id.	Classification per region
F1	Intensity of the original image	F21	Percentage of the area relatively to the carotid wall
F2	Intensity of the image (Gaussian filter)	F22	Area of the region
F3	Intensity of the image (Mean filter)	F23	Average intensity of the lumen †
F4	Intensity of the image (Sigmoid filter)	F24	Average intensity of the carotid wall †
F5	Average intensity (Original image)*	F25	Distance of the centroid of the region to the lumen
F6	Average intensity (Gaussian filter)*	F26	Distance of the centroid of the region to the carotid wall
F7	Average intensity (Mean filter)*		
F8	Average intensity (Sigmoid filter)*		
F9	Minimum intensity (Original image)*		
F10	Minimum intensity (Gaussian filter)*		
F11	Minimum intensity (Mean filter)*		
F12	Minimum intensity (Sigmoid filter)*		
F13	Maximum intensity (Original image)*		
F14	Maximum intensity (Gaussian filter)*		
F15	Maximum intensity (Mean filter)*		
F16	Maximum intensity (Sigmoid filter)*		
F17	Average intensity of the lumen †		
F18	Average intensity of the carotid wall †		
F19	Distance of the pixel to the lumen contour		
F20	Distance of the pixel to the carotid wall contour		

*Features extracted from a 3x3 neighbourhood centred at each pixel of the original and filtered CTA images.
†Features extracted from the original CTA image.

Based on the main contributions of this project, five articles were written and submitted to international journals; in addition, several articles were presented in international conferences.

6   Conclusions and Future works

Segmentation of the lumen and vessel wall boundaries of the arterial system, as well as the identification of atherosclerotic plaque components, is still an intensive focus of research. The main contributions of this PhD project concern the development of fully automatic segmentation methods of the lumen and carotid artery boundaries in MR images and the classification of calcium regions present in atherosclerotic lesions of carotid arteries in CTA images. The intensity of the lumen region in IVUS images of the coronary artery is similar to the one of the carotid artery in black-blood MR images. Improvements on the segmentation method previously adopted to identify the lumen regions in MR images of the carotid artery were also accomplished for effectively identifying the lumen in IVUS images of the coronary artery. The classification of calcium regions is carried out in a two-stage approach to avoid parts of the lumen region being incorrectly classified as calcifications in atherosclerotic lesions of the carotid artery.

Variations in the grayscale intensities inside the regions of interest represent a challenge to the development of fully automatic algorithms used to identify structures of the arterial system in medical images. Moreover, reducing the number of empirical parameters is necessary to increase the automaticity and reliability of the segmentation methods. Concerning the classification of calcified regions, manual delineations made directly in the *in vivo* CTA images can lead to more accurate classification results. Although the proposed methods were shown to be effective in segmenting and classifying the structures present in carotid and coronary arteries, it is recognized that there are limitations which can be tackled by the following future works:

- The evaluation of the proposed segmentation algorithms in other datasets with the same parameters established for the image dataset used in this project. The proposed algorithms rely on a set of parameters that have been empirically defined. The possibility of reducing the number of parameters and using a learning-based approach to determine their appropriate values should be investigated. Additionally, the study of other features (such as those obtained from texture-based methods) in the subtractive clustering algorithm adopted in the lumen segmentation process should be carried out;

- The enhancement of the algorithm described in Article 3 of Part B in order to allow the segmentation of the lumen region in IVUS images acquired at a frequency of 40 MHz, which involves other image artifacts that make the segmentation more difficult and subject to errors. The transducer reflection is represented by a bright ring located at the center of the IVUS images, which is commonly found in IVUS

images acquired at a frequency of 40 MHz. The elimination of the transducer reflection should be considered in a pre-processing step before the identification process of the lumen. Future works should also address the segmentation of the media-adventitia boundary in IVUS images of the coronary artery;

- Besides the identification of calcified regions in CTA images of the carotid artery, the classification of other components of the atherosclerotic plaques based on other image modalities should be considered to provide more details of the disease progression. Additionally, the extraction of the pixels inside the carotid wall was done through manual delineations provided with the dataset used in this project. Automatic segmentation of the lumen and carotid wall boundaries in CTA images should also be addressed in future works;

- The study concerning the 3D reconstruction of the segmented structures to provide a better overview of the morphology of the arterial system and the measurement of the volume of the atherosclerosis should be addressed in the near future. Additionally, 3D image-based models should be used in subject-specific hemodynamic simulations to evaluate, for example, the stress on the reconstructed vessel wall.

References

[1] S. Mendis, P. Puska, and B. Norrving. *Global atlas on cardiovascular disease prevention and control*. World Health Organization, 2011. ISBN 978-92-4-156437-3.

[2] P. Sobieszczyk and J. Beckman. Carotid artery disease. *Circulation*, 114(7):e244–e247, 2006. ISSN 00097322. doi: 10.1161/CIRCULATIONAHA.105.542860.

[3] C. Warlow. MRC european carotid surgery trial: interim results for symptomatic patients with severe (70-99%) or with mild (0-29%) carotid stenosis. *The Lancet*, 337 (8752):1235–1243, 1991. ISSN 00034819. doi: 10.1016/0140-6736(91)92916-P.

[4] N. Collaborators. Beneficial Effect of Carotid Endarterectomy in Symptomatic Patients with High-Grade Carotid Stenosis. *New England Journal of Medicine*, 325 (7):445–453, 1991. ISSN 00034819. doi: 10.1056/NEJM199108153250701.

[5] A. S. Clemente Filho. Hierarquização dos métodos de exame pela imagem. *Jornal Brasileiro de Pneumologia*, 10(4):259–261, 1984.

[6] S.-E. Kim and D. L. Parker. *Time-of-Flight Angiography*, pages 39–50. Springer New York, New York, NY, 2012. ISBN 978-1-4419-1686-0. doi: 10.1007/978-1-4419-1686-0_2.

[7] A. M. Mendonça and A. Campilho. Segmentation of retinal blood vessels by combining the detection of centerlines and morphological reconstruction. *IEEE Transactions on Medical Imaging*, 25(9):1200–1213, 2006. ISSN 0278-0062. doi: 10.1109/TMI.2006.879955.

[8] K.-P. Tung, W.-Z. Shi, R. de Silva, E. Edwards, and D. Rueckert. Automatical vessel wall detection in intravascular coronary OCT. In *IEEE International Symposium on Biomedical Imaging: From Nano to Macro*, pages 610–613. IEEE, March 2011. ISBN 978-1-4244-4127-3. doi: 10.1109/ISBI.2011.5872481.

[9] M. M. G. de Macedo, C. K. Takimura, P. A. Lemos, and M. A. Gutierrez. A robust fully automatic lumen segmentation method for in vivo intracoronary optical coherence tomography. *Research on Biomedical Engineering*, 32(1):35–43, March 2016. ISSN 2446-4740. doi: 10.1590/2446-4740.0759.

[10] S. Abdelazeem. Micro-aneurysm detection using vessels removal and circular Hough transform. In *Proceedings of the Nineteenth National Radio Science Conference*, pages 421–426. IEEE, 2002. ISBN 977-5031-72-9. doi: 10.1109/NRSC.2002.1022650.

[11] H. Prasetya, T. L. R. Mengko, O. S. Santoso, and H. Zakaria. Detection method of cerebral aneurysm based on curvature analysis from 3D medical images. In *2nd International Conference on Instrumentation, Communications, Information Technology and Biomedical Engineering*, pages 141–144. IEEE, 2011. ISBN 978-1-4577-1167-1. doi: 10.1109/ICICI-BME.2011.6108612.

[12] S. Cetin, G. Unal, and M. Degertekin. An automatic branch and stenoses detection in computed tomography angiography. In *9th IEEE International Symposium on Biomedical Imaging*, pages 582–585. IEEE, 2012. ISBN 978-1-4577-1857-1. doi: 10.1109/ISBI.2012.6235615.

[13] D. S. Jodas, A. S. Pereira, and J. M. R. S. Tavares. A review of computational methods applied for identification and quantification of atherosclerotic plaques in images. *Expert Systems with Applications*, 46:1–14, 2016. ISSN 0957-4174. doi: 10.1016/j.eswa.2015.10.016.

Part B - Article 1:

A review of computational methods applied for identification and quantification of atherosclerotic plaques in images

Danilo Samuel Jodas, Aledir Silveira Pereira, João Manuel R. S. Tavares

Abstract

Evaluation of the composition of atherosclerotic plaques in images is an important task to determine their pathophysiology. Visual analysis is still as the most basic and often approach to determine the morphology of the atherosclerotic plaques. In addition, computer-aided methods have also been developed for identification of features such as echogenicity, texture and surface in such plaques. In this article, a review of the most important methodologies that have been developed to identify the main components of atherosclerotic plaques in images is presented. Hence, computational algorithms that take into consideration the analysis of the plaques echogenicity, image processing techniques, clustering algorithms and supervised classification used for segmentation, i.e. identification, of the atherosclerotic plaque components in ultrasound, computerized tomography and magnetic resonance images are introduced. The main contribution of this paper is to provide a categorization of the most important studies related to the segmentation of atherosclerotic plaques and its components in images acquired by the most used imaging modalities. In addition, the effectiveness and drawbacks of each methodology as well as future researches concerning the segmentation and classification of the atherosclerotic lesions are also discussed.
Keywords: Stroke, Medical imaging, Image analysis, Image segmentation

1 Introduction

Cardiovascular diseases represent the main causes of an increasing number of deaths around the world since they impair the heart and vascular system functions. Hence, the early diagnosis of these pathologies is important to minimize clinical cases such as thrombosis, heart attacks, transient ischemic attacks and even the occurrence of strokes. In a broader research study, Mendis et al. [1] revealed alarming numbers regarding cardiovascular disease prevention and control: according to the World Health Organization, in 2011 the cardiovascular diseases represented 31% of the death of people around the world; in 2008, the cardiovascular diseases caused the death of more than 17 millions of people around the world with less than 60-year old. Smoking, lack of physical exercises, inadequate food and excessive consume of alcoholic drinks are the major causes of this disease [1].

One of the main cardiovascular diseases is the atherosclerosis, which occurs as a result of the formation of lipid plaques in the artery wall. The atherosclerosis reduces or

occludes the blood flow through the artery, which can cause amaurosis fugax, transient ischemic attack and strokes [2–4].

Technological advances in computerized systems for imaging diagnosis have allowed less invasive ways of analysis and detection of cardiovascular pathologies. Computerized Tomography (CT), Magnetic Resonance Imaging (MRI) and ultrasound are examples of less invasive procedures that have been widely used for evaluating the presence and characteristics of atherosclerotic plaques [5–7]. Although CT provides better image quality for visualization of the diseases and less invasive procedures compared to the traditional catheter diagnosis, it can be harmful to the health of patients due to the x-rays emission [8, 9]. Unlike computerized tomography, ultrasound imaging is a safer procedure since it not exposes the patients to the ionizing radiation. However, the poor image contrast and the speckle noises are the main drawbacks of ultrasound imaging when compared to CT and MRI modalities [10–12].

Expedite the carotid endarterectomy is important after onset of symptoms in order to avoid recurrent strokes. In addition, a recurrent stroke can arise within the first two weeks after onset of symptoms and beyond this time a surgical procedure can be inefficient [13]. Degree of stenosis has been covered as an indicator for evaluating the risks associated with neurological events. In general, patients with degree of stenosis greater or equal than 70% are selected for carotid endarterectomy in order to prevent the risk of stroke [14, 15]. Although it is a broadly measure related in various studies for selecting patients for carotid endarterectomy, the majority of the patients with significant degree of stenosis remained stroke-free even after years [16]. In addition, patients with moderate degree of stenosis can also develop symptoms over time [17]. Therefore, the analysis of the plaques composition provides the ability of evaluating the progression of atherosclerotic plaques.

Characteristics of echogenicity, texture and surface of atherosclerotic plaques are also addressed in various studies [5, 16, 18–20] as indicators of neurological symptoms. Echolucent lesions, heterogeneous plaques and ulcerations are described in many studies as the main characteristics associated with high risk for neurological symptoms [21]. One of the most used measure to quantitatively evaluate the plaques echogenicity is the GrayScale Median (GSM). In various studies [21–26] the GSM was found to be low in plaques with high risk of neurological symptoms.

Previous studies [26–28] have addressed the importance of the atherosclerotic plaque burden in evaluating the risks of neurological events. Such components allow the assessment of risks of plaque rupture and embolization, as well as the evaluation of future risks for transient ischemic attacks, amaurosis fugax and strokes. Although visual analysis is a well established method for quantifying the plaque burden, the intra and intervariability between experts may impair the diagnosis. Therefore, development of computational

algorithms plays an important role to expedite the assessment of atherosclerotic plaques and avoid the intervariability between experts.

As to expert systems, the identification of atherosclerotic plaques and its main components plays an important role in the evaluation of the disease progression. The classification of such plaques in symptomatic or asymptomatic, for example, is crucial to avoid future cerebral events. In addition, features extracted from the atherosclerotic plaque components allow the development of expert systems to provide medical doctors with an auxiliary tool to automatically classify the occurrence of such events or even the atherosclerotic lesion type. The identification of the lesion type according to the American Heart Association (AHA) classification standard [29] is also a valuable contribution for evaluating the progression of the disease. The composition of the plaque is the basis for classifying the lesion type according to the AHA classification standard. It provides the assessment of the atherosclerotic plaque progression in order to determine the mechanisms that cause its rupture. Hence, the segmentation task represents an essential key in the development of medical decision-making systems that could provide a complementary diagnosis for the atherosclerotic plaques.

A considered number of studies addressing the segmentation of atherosclerotic plaques and its components, as well as the assessment of the occurrence of future cerebral events based on the plaque characteristics, have been proposed. However, the categorization of the main studies is important not only to present an overview of such methodologies, but also to provide the researchers with the employed techniques, the imaging modalities and the effectiveness and drawbacks of each one, as well as future researches to overcome the limitations and improve the accuracy of the current results.

This article presents a review of existing methodologies applied for characterization and quantification of atherosclerotic plaques in ultrasound, CT and magnetic resonance (MR) images. An overview of visual assessment and quantitative analysis applied for characterization of atherosclerotic plaques is presented in section 2. In addition, a definition about the atherosclerotic plaque components is also presented. Computational algorithms based on image processing techniques, clustering and supervised classification applied for identification and quantification of atherosclerotic plaque components are presented in section 3. Section 4 is dedicated to discuss advantages and limitations of each methodology. Finally, conclusions and future works are presented in the last section.

2 Atherosclerotic plaque characterization

In order to identify the most important characteristics of atherosclerotic plaques associated with neurological events, as well as to quantify the amount of histological components, studies using images acquired from well-known imaging modalities have been presented. Furthermore, the study of the atherosclerotic plaques morphology provides specialists an understanding of its behavior at the moment of treatment and allows to determine whether the plaque will resist the deployment of stents or not [30]. Biasi et al. [21] reported that dangerous plaques are more predisposed to shed embolic material into the bloodstream when they are manipulated with stent devices. Thus, the identification of safe or dangerous plaques is important to avoid risks prior an angioplasty procedure.

Analysis either using visual classification or computational algorithms have been presented for identification and quantification of atherosclerotic plaques. Computational methods such as image processing techniques and clustering algorithms have been presented in order to automatically outline the atherosclerotic plaque boundaries and classify their main components. In addition, computational algorithms may avoid the intra/inter-variability and the expensive work to manually outline atherosclerotic plaques in images. A review of the most important studies addressing the assessment of the atherosclerotic plaques morphology and histological components identification is presented in this article according to the classification illustrated in Figure 1.

2.1 Analysis of atherosclerotic plaques morphology

Visual analysis of the atherosclerotic plaques echogenicity in ultrasound images has been addressed in several studies for evaluating the presence or absence of neurological symptoms. Echogenicity represents the distribution of the grayscale values within a plaque. Echogenicity is represented by echolucent/anechogenic pattern (dark regions) or echogenic/hyperechogenic pattern (bright regions) [17]. In this type of study, an observer performs the visual classification of the plaques based on their echolucent or echogenic pattern. A study performed by Steffen et al. [18] presented the evaluation of carotid plaques in ultrasound images in order to determine the echogenicity patterns associated with the presence or absence of symptoms. In the study, four types of echogenic and echolucent patterns were used to classify the carotid plaques in symptomatic or asymptomatic groups: type 1 - uniformly echolucent; type 2 - predominantly echolucent with small areas of echogenic pattern; type 3 - predominantly echogenic with small echolucent regions; and type 4 - uniformly echogenic. The results shown that types 1 and 2 were more predominant in symptomatic plaques (67%) and types 3 and 4 were predominant

Computational algorithms
- Image processing
  - Molinari et al. (2007, 2010)
  - Kerwin et al. (2001, 2007)
  - Liu et al. (2006)
  - de Weert et al. (2006)
  - de Graaf et al. (2013)
  - Vukadinovic et al. (2012)
  - Wintermark et al. (2008)
- Supervised classification
  - Anderson et al. (2006)
  - Clarke et al. (2003, 2006)
  - Hofman et al. (2006)
  - van Engelen et al. (2012a, b)
  - van 't Klooster et al. (2012)
- Clustering
  - Adame et al. (2004a, b)
  - Itskovich et al. (2004)
  - Karmonik et al. (2006, 2009)
  - Sun et al. (2006, 2008)
  - Xu et al. (2001)

Visual analysis and computer aided
- Visual Analysis
  - Widder et al. (1990)
  - Lal et al. (2006)
  - Steffen et al. (1989)
  - Geroulakos et al. (1993)
  - Lovett et al. (2004)
- Computer aided
  - Biasi et al. (1998)
  - El-Barghouty et al. (1995)
  - Elatrozy et al. (1998)
  - Pedro et al. (2000)
  - Grogan et al. (2005)
  - Salem et al. (2014)

Figure 1: Classification of the methods reviewed in this article.

in asymptomatic ones (87%). Thus, it shows that symptomatic plaques are more echolucent than asymptomatic ones. Similar results were achieved by Geroulakos et al. [19], where the same types were used for classifying the carotid plaques. However, a fifth type was included in order to classify plaques with higher amount of calcification and acoustic shadows. In the study, types 1 and 2 were predominant in symptomatic plaques (81%), whereas types 3 and 4 were found in asymptomatic ones (59%). No results concerning the fifth type were presented either for symptomatic or asymptomatic plaques.

Characterization of symptomatic and asymptomatic plaques has been addressed in studies such as the one presented by Lal et al. [16]. Furthermore, morphological charac-

teristics are also evaluated in order to correlate them with the plaque components [5, 20]. In a study proposed by Lal et al. [16], the identification of intraplaque hemorrhage, large lipid cores and their proximity to the lumen was performed in ultrasound images of carotid plaques in order to correlate them with symptomatic and asymptomatic groups. The authors found that hemorrhage and lipid components were higher in symptomatic plaques, whereas calcium percentage was higher in asymptomatic ones. In addition, lipid core presented higher area and lower distance to the lumen in symptomatic plaques when compared to asymptomatic ones.

Widder et al. [5] performed an evaluation of the morphological features of carotid plaques in ultrasound images in order to correlate them with the presence of ulcerations and intraplaque hemorrhage. Ultrasound images of the carotid artery have been used to evaluate the border, density and echo structure of plaques. According to the results, regular borders, an echogenic pattern and heterogeneous plaques are indicators for discarding the probability of ulcerations and intraplaque hemorrhage.

Lovett et al. [20] performed a comparison between the surface of carotid plaques provided by angiography imaging with histological features. The analysis shown that the increase of the carotid plaque and lipid core components, as well as the decrease of fibrous tissue, are higher in irregular and ulcerated plaques. In addition, irregular and ulcerated plaques were considered 44% and 50% as definitely unstable, respectively, whereas smooth plaques was considered 53% as definitely stable.

2.2 GrayScale Median of atherosclerotic plaques: A quantitative analysis

Although visual classification showed good results for characterization of atherosclerotic plaques morphology, the subjective analysis among experts may impair the diagnosis. To overcome this problem, computer-aided methods have been proposed for the efficient quantitative analysis of atherosclerotic plaques.

In order to evaluate the relationship between echogenicity pattern and atherosclerotic plaques with evidence of cerebral infarction, a measure called GSM was introduced by El-Barghouty et al. [22]. The GSM value is used to determine the global plaque echogenicity. A plaque with a GSM value below a certain threshold is considered echolucent and of high risk for neurological symptoms.

In a study conducted by El-Barghouty et al. [22], the GSM values of 184 carotid plaques in duplex ultrasound images were calculated by using Adobe Photoshop™ software. The results shown that of the 64 plaques with $GSM > 32$, only 11% were associated to brain infarction, whereas of the 84 plaques with $GSM \leq 32$, 55% were associated to

brain infarction. In addition, of the 53 plaques associated to brain infarction, 13% has *GSM* > 32 and 87% has *GSM* ≤ 32. Of the 95 plaques not associated to brain infarction, 60% has *GSM* > 32 and 40% has *GSM* ≤ 32. In short, the study concludes that echolucent pattern could be considered as high-risk for unstable plaques, whereas echogenic characteristic is associated to stable plaques.

Several studies evaluating the plaques echogenicity with the GSM analysis have been conducted using different threshold values. In addition, other characteristics have been included in order to improve the accuracy of the evaluation. Elatrozy et al. [23] presented the evaluation of carotid plaques in ultrasound images in order to obtain the most important features associated with ipsilateral hemispheric symptoms. The analysis has been performed in order to measure the GSM and the Percent of Echolucent Pixels (PEP) of carotid plaques, as well as to measure the homogeneity, entropy and contrast. To determine how homogeneous is a plaque, the homogeneity has been used. Entropy indicates the dissimilarity of the gray level values into the carotid plaques so that heterogeneous plaques have higher entropies. Contrast is a measure that determines the variability of gray scale differences so that large values indicate high variation in the gray scale of the pixels. The results shown that the GSM and the PEP were not statiscally significant for asymptomatic plaques, but significant differences were found for symptomatic plaques. According to the results, more symptomatic plaques were found with GSM < 40 (84%) and PEP > 50 (80%) and multiple regression analysis demonstrated that these feature are the most important predictors for the presence or absence of ipsilateral hemispheric symptoms. In addition, the entropy was the measure that presented statistical significance in differentiating symptomatic from asymptomatic plaques. According to this measure, symptomatic plaques tend to be less heterogeneous due to the lower entropy (lower than 2.9).

The relationship between echogenicity and atherosclerotic plaques with evidence of cerebral infarction was addressed in the study of Biasi et al. [21]. In this study, the GSM was calculated as the global echogenicity measure of the plaques in order to find an association with symptoms, evidence of cerebral infarction and degree of stenosis. The results shown that symptomatic plaques have more evidence of cerebral infarction (32%) when compared to asymptomatic ones (16%). In addition, plaques with more evidence of cerebral infarction are more echolucent than those with no evidence (40% vs 9%, respectively). Symptomatic plaques have lower GSM values (38 ± 13) when compared to asymptomatic ones (56 ± 14). No statistical significance was found for GSM and degree of stenosis.

In the study of Pedro et al. [24] the GSM, percentage of pixels below the value 40 (echolucent pixels), presence of echogenic cap, plaque disruption, echogenic cap thick-

ness, the percentage of echolucent juxtaluminal region and the percentage of echolucent region were considered in the analysis of carotid plaques in ultrasound images. The results shown that symptomatic plaques associated with Brain Infarction (BI) have low GSM and more echolucent pixels when compared to asymptomatic plaques not associated with BI. For the homogeneous characteristic, symptomatic plaques associated with BI shown lower GSM, higher percentage of echolucent pixels and higher surface disruption, whereas the presence of echogenic cap was higher in asymptomatic plaques not associated with BI. For the heterogeneous group, symptomatic plaques associated with BI shown lower GSM value and higher echolucent juxtaluminal region. It is important to note that the GSM value was lower in all cases.

Grogan et al. [25] presented a study which aimed to find the most relevant features associated with symptomatic plaques. GSM was obtained from B-mode ultrasound images (ex-vivo carotid plaques) and preoperative color Doppler ultrasound. Calcified and necrotic area, as well as the distance of the necrotic core to the lumen, was calculated from histopathological analysis. The authors found more echolucency, less calcified components and lower GSM value in symptomatic plaques. In addition, the percentage of necrotic area was higher in symptomatic plaques and its distance to the lumen is lower compared to asymptomatic ones. The mean GSM calculated from B-mode ultrasound images shown a value of 41 for symptomatic plaques and 60 for asymptomatic ones. These results are statiscally close to those presented by color Doppler, in which the mean GSM with 33.8 is echolucent, whereas the mean GSM with 53.6 is echogenic.

Salem et al. [26] evaluated patients with low risks for unstable plaques by comparing the ultrasound images and histological analysis. In addition to the GSM value, juxtaluminal black area and plaque area were also considered in the study. A correlation between the characteristics acquired from the ultrasound images and the histological classification (stable/unstable) of the plaques was performed in order to select the most significant association. The results shown that a GSM < 25, a plaque area > 95 mm^2 and a juxtaluminal black area > 6 mm^2 are the features associated with unstable plaques.

2.3   Atherosclerotic plaque components

An atherosclerotic plaque is formed by components such as lipid core, fibrous tissue, smooth muscle cells, intraplaque hemorrhage and calcifications. The American Heart Association (AHA) lesion type classification is a histological examination that divides the atherosclerotic plaques in categories based on the components within the plaques [29]. Thus, a matching of imaging features and the histological examinations provided by this standard aid the physicians in accurately determining the atherosclerotic lesion type. The

AHA classification of atherosclerotic plaques based on their components is shown in Table 1.

Table 1: AHA Lesion Type Classification [29].

Type	Description
Type I	Initial lesion
Type II	Fatty streak with multiple foam cells layers
Type III	Intermediate lesion (preatheroma)
Type IV	Atheroma
Type Va	Fibroatheroma
Type Vb	Calcified (lesion type VII)
Type Vc	Fibrotic lesion (lesion type VIII)
Type VI	Lesion with surface defect, and/or hematoma-hemorrhage, and/or thrombotic deposit

A foam cell is a macrophage cell that engulfs fatty components. The accumulation of this type of cells in regions with a large amount of fatty components represents the first stage to the development of atherosclerosis [29]. Types I, II and III are considered intermediate lesions, whereas the other types belong to the advanced lesions group. In addition, narrowing of the lumen or obstruction of the blood flow does not occur in these lesion types [29]. Lesion types I and II can occur in the childhood, but adults are also likely to these lesions, type III appears after the puberty, whereas type IV appears in the third decade. Subjects after third decade are likely to lesion types V and VI [29]. In Figure 2 is shown an illustration of the progression of an atherosclerotic disease.
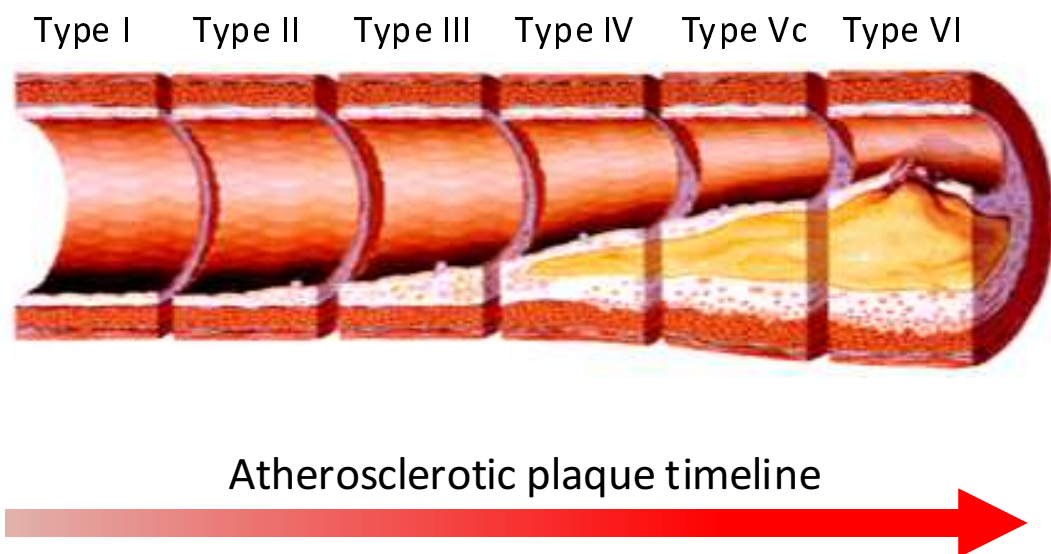

Figure 2: An example of atherosclerotic plaque progression over time (adapted from Koenig and Khuseyinova [31]).

Since the components identified in atherosclerotic plaques are addressed in the AHA lesion type classification, the method can be used in the classification of atherosclerotic lesion types. In fact, several researches addressing the classification of atherosclerotic plaques based on the AHA classification can be found in studies such as those of Cai [32], Kampschulte et al. [33] and Saam et al. [34].

The composition of atherosclerotic plaques has been addressed as an important factor for evaluating the risks of plaque rupture, as well as risks for embolization and neurological events. Histological analysis of the carotid specimens has proved a higher amount of lipid and cholesterol components in symptomatic plaques when compared to asymptomatic ones [27]. Unstable plaques associated with majority of strokes contain features such as hemorrhage, large lipid cores, thrombus and plaque inflammation [26]. Takaya et al. [28] showed that the presence of thin or ruptured fibrous cap, intraplaque hemorrhage, lipid-rich necrotic core, as well as a larger mean area of intraplaque hemorrhage, larger maximum percentage of lipid-rich necrotic core and maximum wall thickness, were the factors associated with the risk of neurological events.

Identification of atherosclerotic plaque components can be performed in images provided by ultrasound, CT and MRI examinations. The identification of plaque components in ultrasound images is difficult due to their low resolution and artifacts such as noises and acoustic shadows caused by high calcification. Furthermore, the analysis of morphological characteristic of atherosclerotic plaques associated with the presence of components still presents a lack of consensus. As an example, in the study of Bluth et al. [35] the incidence of intraplaque hemorrhage was higher in heterogeneous plaques (81%), whereas 96% of the homogeneous plaques did not present intraplaque hemorrhages. In contrast, the study of Schulte-Altedorneburg et al. [36] showed that hemorrhage was associated with echolucent and homogeneous plaques.

Intravascular Ultrasound (IVUS) is an invasive imaging procedure which allows the evaluation of arterial morphology from within the vessel lumen. Although it is a broadly procedure used for evaluating the arterial diseases, the poor quality of the IVUS images difficult the identification of the plaque components, particularly by automatic algorithms [30]. Intravascular Ultrasound Virtual Histology (IVUS-VH) provides color-mapped images that represent the plaque constitution. The plaque components are identified during the IVUS procedure based on the returned frequency of the transducer. That frequency varies depending on the tissue type. These variations allow the real time identification of the components. Several studies [30, 37, 38] dealing with IVUS-VH examination provide the characterization of the following plaque components: fibrous, fibrofatty, necrotic lipid core and calcifications. Although the IVUS-VH provides an accurate real-time evaluation of the plaques constitution, the procedure is invasive for the patient. Furthermore,

IVUS-VH is limited after a stenting procedure because the metal stent is classified as calcification [30].

Lal et al. [39] discussed the importance in analyzing the internal structure of carotid plaques in order to characterize their components and select patients at high risk for strokes and atheroembolization. The possibility of identifying carotid plaque components in B-mode ultrasound images is addressed in the study. The methodology called Pixel Distribution Analysis (PDA) was based on the mean grayscale value of subcutaneous fat, muscle, fibrous tissue and calcified structure calculated from control images in order to find these components in carotid plaques. The following mean grayscale values were found for each component: Hemorrhage was 2 (0 up to 4), lipid was 12 (8 up to 26), muscular tissue was 53 (41 up to 76), fibrous tissue was 172 (112 up to 196) and calcium was 221 (211 up to 255). Based on the PDA, the authors found higher levels of blood and lipid components in symptomatic patients (11.22% $\pm$ 3.16 and 29.38% $\pm$ 5.96, respectively), whereas in asymptomatic patients the calcium and fibromuscular were the components with higher concentration (11.13% $\pm$ 1.29 and 42.77% $\pm$ 5.93, respectively). The analysis takes into consideration the components with statistical significance. According to the Spearman correlation coefficient, the correlation between PDA and histological analysis for blood, lipid, calcium and fibromuscular components was 0.61, 0.77, 0.85 and 0.53, respectively.

Identification of plaque components on magnetic resonance images has been addressed in some studies. Toussaint et al. [40] presented the ability of T2W images in identifying in vivo and in vitro carotid atherosclerotic plaque components based on the T2 signal. Identification of lipid-rich necrotic cores and intraplaque hemorrhages in MR images performed by Yuan et al. [41] shown high accuracy when correlated to histological assessment. The study presented by Saam et al. [42] aimed the evaluation of the ability of MRI exams in quantifying the main components of carotid atherosclerotic plaques. Time-of-Flight (TOF), T1-, T2- and Proton Density Weighted (PDW) images were used to classify the lipid-rich necrotic core, calcification, loose matrix and fibrous tissue in carotid plaques. The components were identified by two radiologists based on the signal intensity (SI) of each MR image. Table 2 indicates the SI values of the plaque components in each MR image.

The results shown a sensitivity of 92%, 76%, 82% and 64% for lipid-rich necrotic core, calcification, hemorrhage and loose matrix, respectively. Kappa values were 0.73, 0.75, 0.71 and 0.53, respectively. The correlation was higher for lipid-rich necrotic core and calcification (0.75 and 0.74, respectively) when compared to hemorrhage, loose matrix and fibrous tissue (0.66, 0.70 and 0.55, respectively). The intra and inter-reader reproducibility were also higher for lipid-rich necrotic core and calcification.

Table 2: Tissue classification criteria proposed by Saam et al. [42].

	TOF	T1W	PDW	T2W
LR/NC with				
No or little hemorrhage	o	o/+	o/+	-/o
Fresh hemorrhage	+	+	-/o	-/o
Recent hemorrhage	+	+	+	+
Calcification	-	-	-	-
Loose matrix	o	-/o	+	+
Dense (fibrous) tissue	-	o	o	o

*The classification into the subgroups is based on the following SIs relative to the adjacent muscle: +, hyperintense; o, isointense; -, hypointense.

According to Chu et al. [43] the identification of hemorrhage component stages provides the ability of analyzing the progression of the atherosclerotic plaques. Thus, in their study the ability of T1W, T2W, PDW and TOF images in detecting the hemorrhage components stages in atherosclerotic carotid plaques was addressed. The classification of hemorrhages into fresh, recent and old was based on the signal intensity from each MR weighted image and the results were correlated with histological analysis. The sensitivity and specificity found for the hemorrhage areas were 90% and 74%, respectively; while the hemorrhage stages classification shown moderate kappa value which did not reached 0.80. The kappa value for one expert was 0.66, whereas for the other expert was 0.44. The worst result presented by the second expert can be explained by the difference in the calcium and old hemorrhage determination. These components presented low signal intensity, although the calcification has well-defined borders.

Because thin fibrous cap are likely the most cause of cerebral ischemic diseases in patients with carotid plaques, its evaluation is important to detect possible embolus and hemorrhages. In the study of Yuan [44] the identification of fibrous cap tissues and its classification into intact and thick, intact and thin and ruptured was performed by evaluating the signal intensity and lumen surface in TOF, T1W, T2W and PDW images. The author found that intact and thick fibrous cap has continuous dark band adjacent to the lumen on TOF images and smooth lumen surface on PDW, T1W and T2W images; intact and thin fibrous cap not presented visible dark band adjacent to the lumen on TOF images, whereas smooth lumen surface is also presented in this fibrous cap type in all other images; finally, the ruptured fibrous cap not present visible dark band adjacent to the lumen on TOF images. Unlike the intact and thin fibrous cap, it was found that ruptured fibrous cap present irregular boundaries on PDW, T1W and T2W images.

In a study presented by Watanabe et al. [45] the evaluation of the ability of Time-of-Flight Magnetic Resonance Angiography (TOF-MRA) images in detecting fibrous cap

rupture of atherosclerotic carotid plaques was performed. Fibrous cap status was determined by using the SI of the TOF-MRA. A hypointense band signal with various thickness indicates the presence of fibrous cap, whereas the absence of this signal represents a ruptured fibrous cap. The TOF-MRA images were examined by two radiologists who evaluate the fibrous cap status and reached a consensus about their opinion. In order to evaluate the results, histological specimens obtained from carotid endarterectomy were evaluated by pathologists who identified the fibrous cap rupture and the major components of the plaques. The analysis of histological and MR images shown high sensitivity and moderate specificity (90% and 69%, respectively). In addition, the concordance level provided by k-value was moderate (0.59).

3 Atherosclerotic plaque characterization with computational algorithms

The aforementioned studies have been proposed to demonstrate the viability of using imaging diagnosis to identify the atherosclerotic plaque components. However, the manual outline of atherosclerotic plaques is a very time consuming task. The development of computational algorithms have been addressed in various studies in order to automatically detect the plaque components and expedite the diagnosis of possible risks for neurological events. In addition, the inter-variability among diagnosis performed by several experts may be avoid by using computational algorithms.

This section presents a review of computational algorithms used for the identification of atherosclerotic plaque components in images acquired from the most common imaging examinations. The computational algorithms reviewed in this section are grouped into image processing techniques, clustering algorithms and supervised classification. A summary of each study containing the author names, the publication year, the used imaging modality and the applied algorithm is presented in the final of each subsection.

3.1 Image processing

The segmentation is recognized as one of the major tasks in image processing. Usually, segmentation is an essential process to identify structures within an image that can be made in a manual, semiautomatic or automatic way. It constitutes the first step to solve many complex tasks of image processing and analysis, particularly in medical applications. In addition, features extracted, i.e. segmented, from image processing techniques contain important information for the identification and evaluation of risk of diseases

either by statistical analysis or by intelligent algorithms. The segmentation of atherosclerotic plaques has been addressed in several studies such as those presented by Loizou et al. [46, 47].

In two studies presented by Molinari et al. [48, 49] a method for extraction and characterization of carotid plaques was presented in order to classify them as stable or unstable. In these works, a contrast agent was used to enhance the tissues of the plaques since each component absorbs the contrast agent differently. In the first study, the intima-media thickness and plaques profiles were extracted by using the Completely User-Independent Extraction (CULEX2) algorithm, which was proposed by the same authors [50]. Afterward, the identification of each component of the plaques was performed based on the PDA values [39]. The results proved that the injection of a contrast agent can improve the areas with echolucent characteristic so that accurate segmentation can be reached. Before the contrast injection, the authors reached a segmentation error of 5% for stable plaques and 35% for unstable plaques. However, after the contrast injection the segmentation error for stable plaques was 2%, whereas for those unstable was 8%. In addition, the carotid plaques segmentation error between the manual and automatic segmentation was 1.2%. Regarding the identification of the carotid plaques, the authors found that the presence of 42% or more of fibrous components represents a stable plaque, whereas an unstable plaque is composed by 25-30% of hemorrhage and lipid core components.

The same approach applied to the first study to extract the carotid plaque and its components was used in the second study of Molinari et al. [49]. However, the composition of the soft unstable plaques presented by both histological analysis and automatic methods was:

- Hemorrhage: 12% for the histological analysis and 8% for the automatic method;

- Lipids: 35% for the histological analysis and 36% for the automatic method;

- Fibrous and muscular: 53% for the histological analysis and 50% for the automatic method;

- Calcium: no presence for both strategies.

Kerwin et al. [51] provided a method for the segmentation of atherosclerotic lesions in MR images using grouping of similar pixels and active contours, as well as the classification of the tissue types. In addition, the 3D reconstruction of the artery is performed in order to provide the visualization of the stenosis and the tissues volume. The algorithms used in the study were compiled in a package called Quantitative Vascular Analysis System (QVAS). The 5 steps performed by the proposed framework are:

- Grouping pixels with similar intensities into clusters;

- Place nodes along the boundaries of the regions and connect them with paths in order to determine the initial boundaries. Manual corrections can be necessary;

- Refine the initial contours by using active contours;

- Tissue classification based on the comparison of the mean brightness values from regions of the images and from a compiled library with standard regional mean values of each component;

- Generation of the 3D model.

The method is feed forward, i.e., the results from the previous image are used in the next image in order to reduce the processing time. In addition, this procedure allows the measurement of the lesions volume. The lumen and wall boundaries are used and refined in the next image. Then, the regions from the previous images are used to seek the regions with similar intensities in the next image. In addition, the classification of the tissues in lipid core, fibrous cap or calcification is performed based on the mean brightness value, which change among patients. Regional brightness values and the associated tissue types were defined in a library. Mean brightness value is calculated from the segmented regions and the labeling is performed based on the mean value defined in the library that is closer to that calculated for the regions. In order to minimize the errors caused by the variation of the mean value between patients, the mean values are adapted according to the current tissue.

In a study of Liu et al. [52] a method called Morphology-Enhanced Probabilistic Plaque Segmentation (MEPPS) for segmentation of carotid plaques based on probability density functions and active contours method was presented. The carotid plaques acquired from T1W, T2W, PDW, TOF and Contrast-Enhanced (CE) imaging were segmented into four tissues: necrotic core, calcification, loose matrix and fibrous tissue. Correction of intensities, normalization, generation of a probability map of each pixel belonging to each tissue type and the application of an active contour in order to delineate the boundaries based on the probabilities maps were the steps performed by the proposed method. The probability map was generated based on the intensity of each contrast weighted image and on two morphological features: distance of the pixel to lumen and wall thickness. Afterward, the active contour method was applied in order to maximize the probabilities and refine the boundaries, as well as avoid noisy artifacts. The image dataset was divided into training set and validation set, being the first one used to generate probabilities maps that represent the probability of each pixel to belong to a tissue type. The results shown

a correlation coefficient of 0.78, 0.83, 0.41 and 0.82 for necrotic core, calcification, loose matrix and fibrous tissue, respectively. The sensitivity and specificity were higher for MEPPS when compared to manual segmentation, except for calcification. The sensitivity for necrotic core, calcification, loose matrix and fibrous was 0.75, 0.65, 0.51 and 0.88 and the specificity was 0.92, 0.98, 0.97 and 0.84, respectively.

In another study performed by Kerwin et al. [53] the MEPPS algorithm was used to segment the atherosclerotic plaque components. The method begins with the identification of the lumen and outer wall boundaries by using the B-spline snake algorithm [54]. Then, the identification of plaque components, particularly the necrotic core and calcification components, was performed by the MEPPS framework. The normalized wall thickness (area of the wall divided by the total vessel area) and the maximal wall thickness, as well as the average of the necrotic core and calcification from all slices, were calculated for comparison against the manual segmentation. The results shown a high correlation between the manual and automated methods: Normalized wall thickness: 0.90; Maximum wall thickness: 0.84; Necrotic core: 0.86; Calcification: 0.96. The intraclass correlation coefficient showed good reproducibility of the automatic and manual measurements: Normalized wall thickness: 0.97 and 0.90; Maximum wall thickness: 0.95 and 0.89; Necrotic core: 0.87 and 0.95; and calcification: 0.94 and 0.98, respectively. Reproducibility was higher for normalized wall thickness, maximum wall thickness and calcification in automatic method, but lower for necrotic core.

Studies performed on Computerized Tomography Angiography (CTA) images have also been proposed for characterization of atherosclerotic plaques. The identification of plaques components using Hounsfield Unit (HU) Attenuation values was described in various studies [6, 55–58]. HU represents the X-Ray attenuation unit used in CT scan examinations [59]. It characterizes the relative density of a substance, i.e. the amount of X-Ray radiation absorbed by each element in the tissue [60]. A value between -1000 (air, black) and +3000 (dense bone, white) is assigned to each image element [60].

A study conducted by de Weert et al. [6] presented the Hounsfield Unit ranges of fibrous, calcium and lipid-core components in carotid plaques in order to determine the ability of CTA images in identifying such components. The tracing of two regions of interest (ROI) in Multidetector Computer Tomography (MDCT) images was performed by two operators. First, the vessel wall boundary was outlined and the HU ranges of each component were determined. Second, the lumen boundary was outlined and its HU range was determined, as well as the HU of the fibrous tissue near to the lumen. The results shown larger total plaque and calcified areas in MDCT images, whereas fibrous and lipid core areas were smaller when compared to the histological images. According to the authors, the plaque area was larger in MDCT images due to the shrinkage caused

by the preparation step of the histological specimens. The lipid-core areas presented the worst results due to the blooming of calcifications area that overshadows area of soft tissue. Thus, it may affect the accuracy and segmentation of lipid-core areas. However, lipid-cores with mildly calcified area shown better results compared to those obtained with hard calcium. It was due to lower blooming effect of the calcium areas. Linear regression showed the following correlations between the proposed method and the analysis of histological specimens: 0.73, 0.74, 0.76 and 0.24 for total plaque area, calcified area, fibrous area and lipid-core area with hard calcium, respectively. Also, the lipid-core area was measured with different levels of calcification. The best correlation was provided by 0-10% level of calcification (R=0.77).

An automatic method for quantification of atherosclerotic plaques in CTA images of coronary arteries was proposed in de Graaf et al. [55]. Four components were identified: fibrous, fibro-fatty, necrotic core and dense calcium. The extraction of each component was performed by using two approaches: fixed threshold and dynamic threshold. The first approach used fixed HU ranges for extraction of each component, whereas the second one define the cut-off values based on the luminal intensity. The dynamic threshold is based on the fact that the lower luminal intensity, the lower will be the HU value of the plaque. Thus, the HU of the tissue are defined based on the luminal attenuation. A study performed by Dalager et al. [61] confirmed the correlation between the attenuation of plaque HU values and the decreasing of the luminal density. Registration of the CTA images with corresponding IVUS images was also performed in order to correlate the results. The results shown that vessel, lumen and plaque volume calculated from CTA images shown high correlation with IVUS results. Regarding the identification of plaque components, a good correlation between CTA and IVUS images was also found as for fixed threshold as for dynamic threshold. However, the correlation coefficient for necrotic core was lower when compared to the other components.

An automatic method for segmentation of the lumen and artery wall boundaries in CTA images was presented in the study of Vukadinovic et al. [62]. Furthermore, the identification of atherosclerotic plaque components based on HU values was also performed by the proposed method. A set of 40 dataset was used to perform a correlation between the automatic and manual tracing, as well as a interobserver analysis. Another set of 90 dataset was used for evaluating the accuracy of the automatic method. The method starts with the segmentation of the lumen boundary using a level set approach. Afterward, the calcium components and the pixels belonging to the vessel region were detected using a GentleBoost framework. Then, calcium and pixels classified in the vessel wall were used to fit an ellipsoid in the vessel wall. From the 40 dataset, the correlation between the manual tracing performed by two observers and the automatic methods showed the worst

results for the lipid component: 0.68 (observer 1) and 0.79 (observer 2) in lipid volume; 0.52 (observer 1) and 0.57 (observer 2) in lipid percentage. However, the calcium and fibrous components showed moderate and high correlation: 0.97 for both observer in calcium volume, 0.94 for both observer in calcium percentage, 0.94 (observer 1) and 0.87 (observer 2) in fibrous volume, and 0.79 (observer 1) and 0.73 (observer 2) in fibrous percentage. In addition, the fibrous and lipid percentages obtained from 90 databases also presented the worst correlation coefficients: 0.77 and 0.55, respectively. This was possibly caused by overlapping between the HU ranges of lipid and fibrous tissues.

Wintermark et al. [58] proposed the identification of carotid plaque components in CTA images based on HU values. Connective tissue, lipid-rich necrotic core, hemorrhage and calcifications were segmented in each 2x2 mm^2 region created from a grid delineation in the histological images in combination with micro CT images. Also, the mean Hounsfield attenuation calculated from each corresponding 2x2 mm^2 region in the CTA images were used in a linear mixed model in order to obtain the mean Hounsfield attenuation for each plaque component. The results shown an overall agreement of 72.6% between CTA and histological analysis. The CTA classification of the calcium component is in perfect concordance with the histological analysis. However, the small lipid-core did not present good concordance and it can be assigned to the overlapping of the Hounsfield threshold of the lipid-core and connective tissues. When the large lipid-core is evaluated (equal to or higher than 5 pixels) the results showed good agreement (k=0.796). Hemorrhage also presented good agreement when large amount (equal to or higher than 5 pixels) were considered (k=0.712). The identification of the ulceration also showed good results (k=0.855). The thickness of the fibrous cap showed good correlation between CTA and histological classification (R^2=0.77).

The proposed studies for identification of atherosclerotic plaque components based on image processing techniques are summarized in Table 3.

Table 3: Proposed methodologies for segmentation of atherosclerotic plaque components based on image processing techniques.

Author	Year	Imaging modality	Segmentation method
Molinari et al. [48]	2007	Ultrasound	PDA
Molinari et al. [49]	2010	Ultrasound	PDA
Kerwin et al. [51]	2001	MRI	Active Contour and clustering
Liu et al. [52]	2006	MRI	Active Contour
Kerwin et al. [53]	2007	MRI	Active Contour
de Weert et al. [6]	2006	CTA	Ranges of Hounsfield Unit values
de Graaf et al. [55]	2013	CTA	Ranges of Hounsfield Unit values
Vukadinovic et al. [62]	2012	CTA	Level set and GentleBoost
Wintermark et al. [58]	2008	CTA	Ranges of Hounsfield Unit values

3.2   Clustering algorithms

Clustering represents the partitioning of a dataset in subsets that have similar characteristics. Hence, the similar pixels of an image are partitioned in regions with similar characteristics by using measures such as mean, intensity and standard deviation calculated from the image pixels. Clustering algorithms have also been proposed for segmentation of atherosclerotic plaque components [63–68]. Since each component is composed by similar intensities, clustering algorithms can be applied to separate the regions of atherosclerotic plaques according to determined criteria.

Adame et al. [63] presented a study which the aim was the automatic detection of the boundaries of the lumen and vessel wall based on ellipse fitting and fuzzy clustering. Ellipse fitting was used to detect the outer vessel wall boundary, while fuzzy clustering was applied to identify the lumen boundary and the carotid plaque boundary. Lumen area, outer wall area and fibrous cap thickness were also measured. The definition of an ellipse centered in the lumen center point defined by the user is made to refine the lumen boundary. In addition, fuzzy clustering was used to first segment the lumen region and then the plaque region (represented by the lipid core). In order to perform the experiments, the authors used 50 images acquired from PDW (23) and T1W (27) examinations. The luminal area (mm^2), outer wall area (mm^2) and fibrous cap thickness were taken into account in the manual tracing and in the automatic method. The fibrous cap thickness was determined by measuring the mean minimal distance of the lumen and lipid core points. The thickness of the fibrous cap had an acceptable correlation (0.72), whereas the correlations of the lumen and outer wall boundaries were high (0.92 and 0.91, respectively).

In a similar study, Adame et al. [64] performed the segmentation of the outer vessel wall, lumen and lipid component in carotid arteries based on fuzzy clustering and ellipse fitting. The first step consists in detecting the outer wall by fitting an ellipse to its boundaries. The regions inside the outer wall was classified into three classes by the fuzzy C-means algorithm: lumen, plaque and wall tissue. The clustering was based on the intensity of T1W or PDW images or even on the combination of the two types of images. The last step comprises the segmentation of the lipid component by using the same clustering algorithm but, this time, two classes were established: wall tissue and lipid component.The automatic method was compared to manual outlines performed by experts and good correlation was found for the three components: 0.94 for lumen, 0.92 for outer wall and 0.76 for fibrous cap thickness.

Itskovich et al. [65] proposed an approach to segment the coronary plaque components in ex-vivo MR images based on a clustering algorithm. The Spatially Enhance Cluster Analysis (SECA) was used to identify loose fibrous, fibrocellular, lipid-rich necrotic

core, thrombus and dense fibrous components. Combined intensities from the T1W, T2W and PWD images were used to initialize the clusters. In order to refine the clusters, the SECA performed the minimization of the chromatic variance and the discontiguity. The first aspect represents the compactness of the cluster and the second one is the rate of the pixels that are not in the same cluster as their neighboring pixels. After the clustering step, the AHA classification of the plaques was performed by experts and compared with those performed by histopathologists in the histological specimens. Regarding the results, the classification based on cluster-analyzed MR images shown good overall agreement with AHA lesion type classification (k=0.89) and it was better when compared to the color composite (k=0.78), T1W (k=0.29), T2W (k=0.42) and PDW images (k=0.31). In addition, the quantification of the components was performed by calculating its area as the percentage of the total plaque area. When compared to color-spacing, the clustering-analyzed images shown the best correlation with histological analysis. The Pearson correlation for loose fibrous, fibrocellular, lipid-rich necrotic core, thrombus and dense fibrous components were 0.82, 0.89, 0.79, 0.98 and 0.83, respectively.

In the study of Karmonik et al. [66, 67] the identification and quantification of carotid plaques in MR images was performed by the k-means clustering algorithm. The first study was performed on images of ex-vivo carotid plaques, whereas the second one was performed on in-vivo images. The k-means algorithm considered points composed by the combination of the intensity values of the PDW, T1W and T2W MR images. The k-means algorithm classified each point into six classes: fibrous, calcium, thrombus, lipid, normal and background. Comparison between histological section analysis and the corresponding k-means classification was performed in order to evaluate the accuracy of the proposed method. A convergence threshold was used in order to determine the assignment of the points in each cluster. This assignment continues until the sum of the distances of the cluster centers between two iterations is smaller than the convergence threshold. The second study was similar to the first one, but the different approach is the inclusion of in vivo images. The mean differences between histological analysis and the clustering algorithm were 5.8 ± 4.1, 1.5 ± 1.4, 4.0 ± 2.8, 8.2 ± 10 and 2.4 ± 2.2 for thrombus, calcification, fibrous, normal and lipid components, respectively.

The identification of coronary plaque components based on a spatial penalized fuzzy C-means algorithm and the signal intensities of the components was proposed in the study of Sun et al. [69]. T1W, T2W, PDW and DW (Diffusion Weighted) images acquired from ex-vivo coronary arteries were used to identify and classify the lipid/necrotic core, fibro-cellular/fibrous cap, fibrous tissue, thrombus and calcification components. These components were also identified in histological sections of the coronary arteries in order to provide a ground truth for evaluating the proposed method. A spatial penalized fuzzy

C-means algorithm was performed to partition the groups corresponding to the plaque components. The pixel intensity of each MR weighted image was used by the algorithm. Then, the components were labeled based on their signal intensity pattern. However, the thrombus component was manually outlined on DW images due to its heterogeneous intensity in T1W, T2W and PDW images. Regarding the results, the Pearson correlation coefficient was 0.98 and 0.97 for histology and fresh condition and histology and preserved condition, respectively.

In a similar study, Sun et al. [70] proposed a method called Prior Information Enhanced Clustering (PIEC) for classification and labeling of the coronary plaque components based on a spatial fuzzy C-means algorithm and T2 values of the components. As in the previous study, the same spatial fuzzy C-means algorithm was used to segment the regions based on the pixel intensities of T1W, T2W and PDW images. However, only the T2 values were used to labeling the clusters as calcification, adipose fat, loose matrix, necrotic tissue or fibrocellular component. According to the authors, T2 values are not dependent on the imaging parameters, but only on the temperature and magnetic field strength. This justifies the use of these values for labeling the plaque components. Regarding the results, the true positive rate for calcification, adipose fat, loose matrix, necrotic tissue and fibrocellular was 88.9, 70.6, 69.2, 94.7 and 75.0, respectively.

Xu et al. [68] presented the segmentation of carotid plaque components based on a modified mean-shift algorithm [71]. MRI diagnosis was performed in carotid specimens in order to obtain four ex-vivo MR contrast weighted images: T1W, T2W, PDW and TOF. However, T2W images were removed from the data set due to the similarity with PDW images. A modified mean-shift algorithm was proposed in order to correctly estimate the initial center of the clusters. In addition, a sphere with dynamic size was considered to minimize the problems of fixed radius used in the original mean-shift algorithm. Calcium, necrotic core, foam cells and fibrous tissues were the components under consideration and the segmentation results were compared to the histological analysis. The misclassification rate values of the calcium, necrotic core, foam cell and fibrous tissue were 2.8, 11.1, 10.0 and 4.6, respectively. In addition, loose fibrous tissue showed the worst results (misclassification rate of 13.5).

The proposed studies for identification of atherosclerotic plaque components based on clustering algorithms are summarized in Table 4.

3.3 Supervised classification of plaque components

Supervised classification is an important step for solving many pattern recognition problems. In contrast to unsupervised classification, which the classified samples are unla-

Table 4: Proposed methodologies for segmentation of atherosclerotic plaque components based on clustering algorithms.

Author	Year	Imaging modality	Clustering technique
Adame et al. [63]	2004	MRI	Fuzzy clustering
Adame et al. [64]	2004	MRI	Fuzzy clustering
Itskovich et al. [65]	2004	MRI	SECA
Karmonik et al. [66]	2006	MRI	K-Means
Karmonik et al. [67]	2009	MRI	K-Means
Sun et al. [69]	2006	MRI	Spatial fuzzy C-Means
Sun et al. [70]	2008	MRI	Spatial fuzzy C-Means
Xu et al. [68]	2001	MRI	Modified Mean-Shift

beled, the supervised classification allows the building of statistic models based on desired outputs provided by experts for each sample. Thus, the classification model may be combined with experience of experts about a certain pattern recognition problem. Supervised classification have been proposed in order to classify the components of atherosclerotic plaques. In addition, the classification of atherosclerotic plaques in symptomatic or asymptomatic was also addressed in several studies [72–76].

Anderson et al. [77] presented the segmentation of atherosclerotic plaque components based on predictive models. T1W, T2W and PDW images were acquired from coronary artery specimens. The k-means clustering algorithm was applied in order to extract the cluster membership of each pixel. In addition, Discrete Cosine Transform and measures extracted from a neighborhood of pixels were also used as input variables by the predictive models. Three predictive models based on an artificial neural network known as Relevant Input Processor Network (RIPNet) were created for a pixel-by-pixel classification of fibrous tissues and lipid components. Each model receives a set of values calculated from the above-mentioned methods. The results showed that the predictive models presented better results when compared to k-means and logistic regression. The results of the predictive models were between 25% and 30% better than k-means algorithm and approximately 8% better than the logistic regression.

In a study of Clarke et al. [78] the identification of fibrous tissue, loose connective tissue, necrotic core and calcification was performed by a minimum distance classifier in eight MR contrast weighted images. Tracing of fibrous, loose connective tissue and necrotic core on histological images were performed by a pathologist in order to provide a ground truth for validating the classifier results. In addition, calcifications were identified on micro CT images. Four ROIs corresponding to each component were outlined in each MR contrast weighted image. The mean value of each ROI was calculated in each MR image. Then, a pixel-by-pixel classification was performed by calculating the euclidean

distance of the pixel to be classified from each mean value belonging to a tissue type so that it is assigned to the tissue associated to the minimum distance. The training of the classifier was performed by using four percent of the total number of pixels. The results shown an overall accuracy of 73.5%. The sensitivity for necrotic core, fibrous tissue, loose connective tissue and calcification were 83.9%, 60.4%, 65.2% and 97.6%, respectively. In addition, the reproducibility of the tracing performed by the pathologist was also higher: 96.9%, 85.1%, 93.8% and 100% for necrotic core, fibrous tissue, loose connective tissue and calcification, respectively.

In another study of Clarke et al. [79] the identification of carotid plaque components on MR images was performed by using a maximum likelihood classifier. A pixel-based classification was performed in order to assign each one of them into the following five components: fibrous, loose connective tissue, necrotic core, hemorrhage and calcium. The results were compared to histological analysis and micro CT images which served as a gold standard to validate the ability of the MR images in detecting these components. Only 2.5% of the total plaque area was selected to train the maximum likelihood classifier and these small areas containing the plaque components were obtained from all images. For every pixel of the image, the assignment of its corresponding class was performed by using the maximum likelihood classifier and the comparison of the results was performed by overlapping the MR and histological images. The best overall accuracy was provided by the PDW, T1W and Diffusion-Weighted (DW) images and by the combination of all 8 contrast images used in the study ($78\% \pm 15\%$ for both set of images).

In a study of Hofman et al. [80] the segmentation of carotid plaque components was performed by using Bayes classifier, k-NN, neural network and Bayes2 classifier. Images acquired from MRI diagnosis were submitted to pre-processing algorithms in order to extract the Ratio Signal Intensity (rSI) of the carotid artery pixels. Also, the carotid artery boundaries were manually outlined by using an in-house software developed in Mathematica. ROIs defined in all MR weighted images were used in order to obtain the pixels of the homogeneous regions that represent the tissue to be classified. A total of 1811 pixels were extracted from the ROIs and used to train the classifiers. Bayes classifier, k-NN, neural network and Bayes2 classifier were used to classify the pixels into the following four tissue types: fibrous, calcium, hemorrhage and lipid core. Bayes, k-NN and neural network classification were based on the individual rSI of the pixels, whereas the Bayes2 was based on the spatial context of the neighborhood of the pixels. The classification was performed in each MR image slice. The final area of each component was obtained from the sum of each area from each slice divided by the number of slices. The results provided by Bayes, k-NN and Bayes2 classifiers presented reasonably results. The neural network presented the worst results. Calcium component presented the worst results in all

classifiers. Although the results were moderated and reasonably, no classifier has reached a correlation coefficient of 0.80.

A method for segmentation of atherosclerotic plaques in ex-vivo MR images using a linear discriminant classifier was proposed in van Engelen et al. [81]. Thirty-two features extracted from intensities, gradient, laplacian and euclidean distances of the voxels to the lumen and vessel wall were used as input for the classifier. The study describes the use of histological images as a ground truth for fibrous and necrotic core, whereas micro CT images were used as ground truth for calcification. The lumen, outer vessel wall and lipid-rich necrotic core were manually drawn on the digitized histological slices, while the calcification was determined by using a Hounsfield threshold value in the micro CT images. The remain component was classified as fibrous tissue. Registration of the ex-vivo MRI and micro CT with histology images were performed in order to obtain a ground truth image with the three components. The results shown an improvement of the accuracy when all 32 features were included. The sensitivity and specificity were 81% and 97% for calcification; 85% and 60% for fibrous; and 52% and 89% for necrotic core, respectively. Percentage of plaque volume of each component was measured and correlated with the ground truth segmentation. The Spearman coefficient for calcification, fibrous and lipid rich necrotic core was 0.86, 0.71 and 0.72, respectively.

In another study, van Engelen et al. [82] described that histological sections are not well aligned with corresponding images due to the deformation caused by the histology processing. In addition, inter and intra-variability, as well as the overlapping between classes, are the most problems of the use of manual segmentation as ground truth. Based on these problems, the authors provided the classification of plaque components (fibrous tissue, lipid-rich necrotic core and calcium) based on the probability of each voxel belongs to a component. The probability was calculated by using the Gaussian blur and the dice overlapping. The main objective of the study was deal with inaccuracies registrations between in vivo and histological data by measuring the probability and dice overlap of each voxel. Thus, samples near to borders or with low dice overlap have lower contribution in the classifier. The ground-truth segmentation was obtained from the manual outline of the components in histological and micro CT images, being the last one used as ground-truth for calcium. After registration of the in-vivo with histologic and micro CT images, each component of the ground-truth segmentation was binarized and blurred with Gaussian filter in order to create soft labels that indicate the probability of each voxel belonging to a component. The soft labels were multiplied with the Dice overlap coefficient calculated from the overlapping between the segmentation of the vessel wall in histology and MR images. It was performed in order to determine the weight of each voxel so that samples close to the boundaries or with low dice overlap coefficient contribute less with

the classifier. Twenty three features were extracted from each voxel and together with the soft labels the training was performed by using a linear discriminant classifier. Regarding the results, the Spearman correlation between soft and hard labels per subject was 0.88, 0.71 and 0.75 for calcification, fibrous and necrotic core, respectively. In addition, the soft labels presented lower volume difference when compared with the hard label (manual segmentation of histology and micro CT images) for fibrous and lipid-rich necrotic core components. Per slice, the difference between the classifier results and ground truth using hard labels were -0.3 $\pm$ 3.6% for calcification, 9.5 $\pm$ 19.5% for fibrous tissue and -9.2 $\pm$ 19.3% for necrotic tissue. In contrast, the use of soft labels yielded a difference of -0.6 $\pm$ 3.7% for calcification, 6.0 $\pm$ 20.8% for fibrous tissue and -5.4 $\pm$ 20.4% for necrotic tissue.

van 't Klooster et al. [83] proposed the classification of carotid plaque components using a linear discriminant classifier. A group of 60 patients were selected for diagnosis and 3D-TOF, T1W, T2W and PDW images were acquired from MRI examinations. Signal intensities of each MR image were used to manually identify the calcification, hemorrhages, lipid core and fibrous components. The manual segmentation was used as a ground truth to evaluate the performance of the automatic method. The automatic classification was performed by a linear discriminant classifier, which receives features such as normalized signal intensity, zero-, first- and second-order derivatives, distance to the inner and outer vessel wall and local vessel wall thickness calculated from each pixel in each MR image. The training of the classifier was performed by using images of 20 patients, whereas the validation was performed in images of 40 patients. Regarding the results, the proposed method showed good agreement for presence or absence of each component when compared to the manual classification. An agreement of 80%, 82.5% and 97.5% was presented for calcification, hemorrhage and lipid core, respectively. In addition, the Pearson correlation coefficient obtained from the volumes calculated by the manual and automatic classifications was 0.80, 0.88, 0.80 and 0.10 for hemorrhage, lipid core, fibrous and calcium, respectively. According to the authors, the small number of calcifications compared to other components have in part contributed for the poor results. Also, similar signal intensities of calcifications close to the lumen and other components may explain the poor results.

The reviewed studies for identification of atherosclerotic plaque components based on supervised classification are indicated in Table 5.

Table 5: Reviewed methodologies for segmentation of atherosclerotic plaque components based on supervised classification.

Author	Year	Imaging modality	Classifier
Anderson et al. [77]	2006	MRI	RIPNet (Based on ANN)
Clarke et al. [78]	2003	MRI	Minimum Distance
Clarke et al. [79]	2006	MRI	Maximum Likelihood
Hofman et al. [80]	2006	MRI	ANN, Bayes and K-NN
van Engelen et al. [81]	2012	MRI	Linear Discriminant
van Engelen et al. [82]	2012	MRI	Linear Discriminant
van 't Klooster et al. [83]	2012	MRI	Linear Discriminant

4 Discussion

The correct quantification of atherosclerotic plaques is an important key to perform the assessment of risks of neurological events. Studies addressing specifically the segmentation of atherosclerotic plaque components using image processing, clustering algorithms and supervised classification were presented in this review.

Active contours and level sets algorithms have been used in many problems dealing with correct delineation of structural boundaries. Chan-Vese active contours [84] have been covered in many researches dealing with boundaries segmentation [85–88]. An advantage of using Chan-Vese segmentation method concerns the identification of the boundaries without the need of gradient information. Studies such as those presented by Kerwin et al. [51] and Liu et al. [52] used active contours algorithms to improve the boundaries of the plaque components.

Clustering have also been proposed for image segmentation. Based on similar characteristics shared by the pixels of the images, clustering algorithms such as k-means and fuzzy C-means have been used in order to partition the images in different regions of interest [89–91]. Although k-means is a well established clustering algorithm that has been proposed in various studies dealing with unsupervised classification, a certain data may belongs to more than one cluster with a certain membership degree [92]. In many image segmentation problems one intensity value can belongs to more than one cluster due to the overlapping of the gray-scale of different regions. Thus, based on the fuzzy concepts the intensity value could have a membership degree in each cluster. In fuzzy clustering each data element can belongs to more than one cluster with a certain membership level, whereas in hard cluster the data can belongs to one cluster only. Fuzzy C-Means was proposed in the study of Adame et al. [63, 64] for the segmentation of the lipid core in carotid plaques. In the study of Sun et al. [69, 70] spatial fuzzy C-Means was proposed as the method for segmentation of the main components in coronary arteries. In addition, results

provided by a clustering algorithm can be used to refine the boundaries of the detected regions as shown in the study of Kerwin et al. [51].

Artificial neural networks, Bayes classifier, k-nearest neighbor and decision tree are examples of algorithms used in supervised classification. Supervised classification also provides the ability of identifying patterns on images based on features extracted from the pixels. Such features are submitted to a classifier which provides an output that represents the class of the presented pattern. However, the classifier model must be constructed by a training set composed by examples along with the corresponding desired outputs. After training, the built model can be used to classify new patterns not belong to the training set. With respect to identification of atherosclerotic plaque components, supervised classification has been proposed in various studies [77–82] to classify each pixel into a tissue type.

Although the aforementioned studies have proved to be effective on identifying atherosclerotic plaque components, some drawbacks must be highlighted. PDA provides constant values for the segmentation of atherosclerotic plaque components in ultrasound images [39]. However, redefinition of the gray levels of the components could be necessary due to different gray levels among images acquired with different equipments. In addition, calcified plaques could harm the segmentation due to projected shadow that can precludes regions of interest [49]. The use of HU values in CTA images also presents drawbacks. Similarly to the problems of PDA, the values of HU may change with different datasets. In the study of de Weert et al. [6] lipid-core comprised lipid, hemorrhage and thrombus components due to the difficulty of detecting thrombus and hemorrhage in MDCT images. Also, lipid-core with mildly calcified area shown better results compared to those obtained with hard calcium. According to the authors, it was due to lower blooming effect of the calcium areas [6].

Similarity of intensity values hampers the discrimination of plaque components. In the study of Vukadinovic et al. [62] the overlapping of the HU values corresponding to the lipid and fibrous tissues hampers the distinction of these components. Similar difficulties can be found in the study of Adame et al. [63] and van Engelen et al. [81]. Difficulties in detecting lipid core close to lumen is also covered in another study of Adame et al. [64].

The main drawback of supervised classification is still the need for a training step to build a predictive model. In addition, complex models with a high number of input elements achieved similar results to those presented with simpler algorithms. Clustering has been proposed for image segmentation as a simple methodology based on less complex mathematical models and no need for a training step. In combination with image processing techniques, methodologies to partition similar regions of an image and refine the boundaries of these regions with active contour algorithms can improve the results of ex-

isting methods of characterization of atherosclerotic plaque components. Since clustering algorithms provide unsupervised classification, the identification of the categories belonging to the partitioned regions becomes a problem due to the lack of labels corresponding to each region.

The main limitations of the works and proposals surveyed in this article are summarized in Table 6.

Studies addressing the combination of spatial fuzzy C-Means algorithms with active contours for identifying the components on atherosclerotic plaques is expected to be considered in the future. Spatial fuzzy C-means proved to be effective to overcome the presence of noises in images and improve the cluster partitioning [93–96]. Use of spatial fuzzy C-means algorithms could also overcome the problems with transitions of intensities values belonging to a same component. In addition, the use of Adaptive Resonance Theory (ART) models [97, 98] such as Fuzzy-ART and Fuzzy-ARTMAP can also be considered as alternative methods to classify the regions corresponding to the atherosclerotic plaque components.

5 Conclusion and future research

Quantification of atherosclerotic plaque components has been addressed in studies assessing the risks associated with neurological events. The morphology of such plaques is a well established indicator to predict events such as transient ischemic attacks, amaurosis fugax and strokes. Several methodologies has been proposed to quantify atherosclerotic plaques in the most popular imaging diagnosis. Automatic identification of plaque components performed by computational algorithms provides an expedited diagnosis of possible neurological events. Thin fibrous cap, lipid rich-necrotic core and intraplaque hemorrhages were covered as the components associated with high risk for such event.

The automatic classification of the atherosclerotic plaques is a demanding challenge to the expert systems usage. An auxiliary diagnosis of the disease progression performed by these systems allows the medical doctors to identify the characteristics of the diseases as soon as possible and, consequently, to expedite the treatment planning. As previously mentioned, the features extracted from the atherosclerotic plaques represent a key point for developing machine learning based expert systems to recognize the atherosclerotic lesion type or determine whether it is symptomatic or asymptomatic.

Future studies addressing the improvement of the proposed computational algorithms could provide more accuracy in identifying the components and correctly delineating their boundaries. The overlapping of the main components associated with high risk

Table 6: Limitations of computational algorithms applied for identification and quantification of atherosclerotic plaques

Author(s) (year(s))	Technique(s)	Limitations
Image processing		
Molinari et al. [48, 49]	PDA	Redefinition of the gray levels of the components may be necessary
Kerwin et al. [51]	AC	Manual interaction for correcting the edges; No comparisons with radiologists were presented
Liu et al. [52]	AC	Need for a training step for generating the probability maps
Kerwin et al. [53]	AC	The use of the MEPPS algorithm presented the same limitations of the study of Liu et al. [52]
de Weert et al. [6]	HU	Difficulty in detecting thrombus and hemorrhage
de Graaf et al. [55]	HU	It depends on the correct segmentation of the lumen region for calculating the threshold values
Vukadinovic et al. [62]	LS and GB	Overlapping of the HU values hampers the identification of lipids and fibrous tissues
Wintermark et al. [58]	HU	Variations on the HU values within the 2x2 grid may impair the correct determination of the mean value
Clustering		
Adame et al. [64]	FC	Difficulty in detecting lipid core close to lumen due to its similarity
Adame et al. [63]	FC	Difficulty in detecting the lipid and fibrous cap due to the similarity of these components in PDW and T1W images
Itskovich et al. [65]	SECA	Calcification was not addressed in the study
Karmonik et al. [66, 67]	K-Means	Choose a converge threshold is computational expensive; K-means algorithm is sensitive to noisy data; Furthermore, difficulties in treating similar data belonging to different clusters are also a problem for k-means algorithm
Sun et al. [69]	SFC	The use of the signal intensity is not adequate since it changes with the acquisition parameters
Sun et al. [70]	SFC	Difficulties in identifying the loose matrix, fibrocellular and adipose fat due to the similar T2 values of these components
Xu et al. [68]	MMS	The complexity of the Mean Shift algorithm increases when the feature space dimensionality also increase
Supervised classification		
Anderson et al. [77]	RIPNet	Need for one model for each component; Also, different set of variables is used in each model
Clarke et al. [78]	Minimum Distance	Minimum distance classifier may be sensitive to variations on the data
Clarke et al. [79]	Maximum Likelihood	Hemorrhage and necrotic-core are similar according to the MR signals
Hofman et al. [80]	ANN, Bayes and K-NN	The low number of pixels used for calcification may explain the worst results; Slight overlapping may also have affected the results
van Engelen et al. [81]	Linear Discriminant	Large number of input values; Difficulty in differentiating fibrous tissue and necrotic core components; Validation on in-vivo image is necessary
van Engelen et al. [82]	Linear Discriminant	Quite number of input values for each pixel is necessary for classification
van 't Klooster et al. [83]	Linear Discriminant	Similarity of the signal intensities of calcifications close to the lumen with other components have contributed for the poor results; Also, more images with calcifications should be included in the training step to overcome this problem

*AC = Active Contour; HU = Hounsfield Unit; LS= Level Set; GB = GentleBoost; FC = Fuzzy Clustering; SFC = Spatial Fuzzy C-Means; MMS = Modified Mean-Shift.

50

for neurological events is still a problem in many studies dealing with the segmentation of atherosclerotic plaques. The main cause of this is the similar intensities of these components. Fuzzy C-Means algorithm proved to be effective in segmenting regions with similar intensities. In addition, spatial fuzzy C-Means allows to overcome the presence of local noise not treated with the traditional fuzzy C-Means. The combination of clustering with active contours could provide the correct identification and delineation of the components on atherosclerotic plaques.

Regarding the assessment of the atherosclerotic plaque from an expert systems development point of view, future researches addressing the classification of the disease progression are required to allow the development of medical decision-making systems for providing an efficient and complementary diagnosis for planning the adequate treatment. Since the accuracy of the automated classification depends on the information attained from the segmented structures in images, the extraction of the most relevant features from atherosclerotic plaques and their components is one of the most important task to be considered in future studies for allowing the accurate assessment of carotid diseases. Such features could allow the accuracy improvement of the most existing methodologies applied to the classification of the symptomatic or asymptomatic atherosclerosis. To the best of our knowledge, no one study presents an expert system for the assessment of the atherosclerotic lesion type based on the AHA classification standard. Therefore, as the main contribution that can be attained with the application of expert systems concerning the study of atherosclerotic plaques, we suggest the use of the most efficient classifiers addressed in the literature in order to perform the classification of the lesion type, particularly based on the referred standard.

Acknowledgements

References

[1] S. Mendis, P. Puska, and B. Norrving. *Global atlas on cardiovascular disease prevention and control*. World Health Organization, 2011. ISBN 978-92-4-156437-3.

[2] K. Furie, S. Smimakis, W. Koroshetz, and J. Kistler. Stroke due to large artery atherosclerosis. In K. L. Furie and P. J. Kelly, editors, *Handbook of Stroke Prevention in Clinical Practice*, Current Clinical Neurology, pages 151–165. Humana Press, 2004. ISBN 978-1-4684-9856-1. doi: 10.1007/978-1-59259-769-7_10.

[3] D. O. Wiebers, V. L. Feigin, and R. Brown. *Handbook of Stroke*. Board Review Series. Lippincott Williams & Wilkins, Philadelphia, PA, 2nd edition, 2006. ISBN 978-0-7817-8658-4.

[4] J. P. Schadé. *The Complete Encyclopedia of Medicine & Health*. Foreign Media Books, 2006. ISBN 978-1-6013-6001-4.

[5] B. Widder, K. Paulat, J. Hackspacher, H. Hamann, S. Hutschenreiter, C. Kreutzer, F. Ott, and J. Vollmar. Morphological characterization of carotid artery stenoses by ultrasound duplex scanning. *Ultrasound in Medicine & Biology*, 16(4):349–354, 1990. ISSN 0301-5629. doi: 10.1016/0301-5629(90)90064-J.

[6] T. T. de Weert, M. Ouhlous, E. Meijering, P. E. Zondervan, J. M. Hendriks, M. R. van Sambeek, D. W. Dippel, and A. van der Lugt. In vivo characterization and quantification of atherosclerotic carotid plaque components with multidetector computed tomography and histopathological correlation. *Arteriosclerosis, thrombosis, and vascular biology*, 26(10):2366–2372, 2006. ISSN 1079-5642. doi: 10.1161/01.ATV.0000240518.90124.57.

[7] J. M. Serfaty, L. Chaabane, A. Tabib, J. M. Chevallier, A. Briguet, and P. C. Douek. Atherosclerotic plaques: classification and characterization with T2-weighted high-spatial-resolution MR imaging– an in vitro study. *Radiology*, 219(2):403–410, 2001. ISSN 0033-8419. doi: 10.1148/radiology.219.2.r01ma15403.

[8] D. J. Brenner and E. J. Hall. Computed tomography - an increasing source of radiation exposure. *New England Journal of Medicine*, 357(22):2277–2284, 2007. ISSN 1533-4406. doi: 10.1056/NEJMra072149.

[9] A. Sodickson, P. F. Baeyens, K. P. Andriole, L. M. Prevedello, R. D. Nawfel, R. Hanson, and R. Khorasani. Recurrent CT, cumulative radiation exposure, and associated

radiation-induced cancer risks from CT of adults. *Radiology*, 251(1):175–184, 2009. ISSN 0033-8419. doi: 10.1148/radiol.2511081296.

[10] X. Li and D. Liu. Ultrasound image enhancement using dynamic filtering. In *Proceedings of the 4th International Conference on Image and Graphics (ICIG)*, pages 106–109, August 2007. ISBN 978-0-7695-2929-5. doi: 10.1109/ICIG.2007.43.

[11] H. Yin and D. Liu. Lateral resolution enhancement of ultrasound image using neural networks. In *Proceedings of the 3rd International Conference on Bioinformatics and Biomedical Engineering (ICBBE)*, pages 1–4, June 2009. ISBN 978-1-4244-2901-1. doi: 10.1109/ICBBE.2009.51630110.

[12] L. Zhao and F. Jolesz. Navigation with the integration of device tracking and medical imaging. In F. A. Jolesz, editor, *Intraoperative Imaging and Image-Guided Therapy*, pages 259–276. Springer New York, 2014. ISBN 978-1-4614-7656-6. doi: 10.1007/978-1-4614-7657-3_18.

[13] M. K. Salem, R. D. Sayers, M. J. Bown, K. West, D. Moore, A. Nicolaides, T. G. Robinson, and A. R. Naylor. Patients with recurrent ischaemic events from carotid artery disease have a large lipid core and low GSM. *European Journal of Vascular and Endovascular Surgery*, 43(2):147–153, 2012. ISSN 10785884. doi: 10.1016/j.ejvs.2011.11.008.

[14] NASCET. Beneficial Effect of Carotid Endarterectomy in Symptomatic Patients with High-Grade Carotid Stenosis. *New England Journal of Medicine*, 325(7):445–453, 1991. ISSN 0028-4793. doi: 10.1056/NEJM199108153250701.

[15] C. Warlow. MRC european carotid surgery trial: interim results for symptomatic patients with severe (70-99%) or with mild (0-29%) carotid stenosis. *The Lancet*, 337(8752):1235–1243, 1991. doi: 10.1016/0140-6736(91)92916-P.

[16] B. K. Lal, R. W. Hobson, M. Hameed, P. J. Pappas, F. T. Padberg, Z. Jamil, and W. N. Durán. Noninvasive identification of the unstable carotid plaque. *Annals of Vascular Surgery*, 20(2):167–174, 2006. ISSN 08905096. doi: 10.1007/s10016-006-9000-8.

[17] R. Sztajzel. Ultrasonographic assessment of the morphological characteristics of the carotid plaque. *Swiss Medical Weekly*, 135(43/44):635–643, 2005. ISSN 14247860. doi: 2005/43/smw-11038.

[18] C. M. Steffen, A. C. Gray-Weale, K. E. Byrne, and R. J. Lusby. Carotid artery atheroma: ultrasound appearance in symptomatic and asymptomatic vessels. *The*

Australian and New Zealand Journal of Surgery, 59(7):529–534, 1989. ISSN 0004-8682. doi: 10.1111/j.1445-2197.1989.tb01625.x.

[19] G. Geroulakos, G. Ramaswami, A. Nicolaides, K. James, N. Labropoulos, G. Belcaro, and M. Holloway. Characterization of symptomatic and asymptomatic carotid plaques using high-resolution real-time ultrasonography. *British Journal of Surgery*, 80(10):1274–1277, October 1993. ISSN 00071323. doi: 10.1002/bjs.1800801016.

[20] J. K. Lovett, P. J. Gallagher, L. J. Hands, J. Walton, and P. M. Rothwell. Histological correlates of carotid plaque surface morphology on lumen contrast imaging. *Circulation*, 110(15):2190–2197, 2004. ISSN 00097322. doi: 10.1161/01.CIR.0000144307.82502.32.

[21] G. M. Biasi, P. M. Mingazzini, L. Baronio, M. R. Piglionica, S. A. Ferrari, T. S. Elatrozy, and A. N. Nicolaides. Carotid plaque characterization using digital image processing and its potential in future studies of carotid endarterectomy and angioplasty. *Journal of Endovascular Surgery*, 5(3):240–246, 1998. ISSN 1074-6218. doi: 10.1583/1074-6218(1998)005<0240:CPCUDI>2.0.CO;2.

[22] N. El-Barghouty, G. Geroulakos, A. Nicolaides, A. Androulakis, and V. Bahal. Computer-assisted carotid plaque characterisation. *European Journal of Vascular and Endovascular Surgery*, 9(4):389–393, 1995. ISSN 10785884. doi: 10.1016/S1078-5884(05)80005-X.

[23] T. Elatrozy, A. Nicolaides, T. Tegos, and M. Griffin. The objective characterisation of ultrasonic carotid plaque features. *European Journal of Vascular and Endovascular Surgery*, 16(3):223–230, September 1998. ISSN 10785884. doi: 10.1016/S1078-5884(98)80224-4.

[24] L. M. Pedro, M. M. Pedro, I. Gonçalves, T. F. Carneiro, C. Balsinha, R. Fernandes e Fernandes, and J. Fernandes e Fernandes. Computer-assisted carotid plaque analysis: characteristics of plaques associated with cerebrovascular symptoms and cerebral infarction. *European Journal of Vascular and Endovascular Surgery*, 19 (2):118–123, February 2000. ISSN 1078-5884. doi: 10.1053/ejvs.1999.0952.

[25] J. K. Grogan, W. E. Shaalan, H. Cheng, B. Gewertz, T. Desai, G. Schwarze, S. Glagov, L. Lozanski, A. Griffin, M. Castilla, and H. S. Bassiouny. B-mode ultrasonographic characterization of carotid atherosclerotic plaques in symptomatic and asymptomatic patients. *Journal of Vascular Surgery*, 42(3):435–441, 2005. ISSN 07415214. doi: 10.1016/j.jvs.2005.05.033.

[26] M. K. Salem, M. J. Bown, R. D. Sayers, K. West, D. Moore, A. Nicolaides, T. G. Robinson, and A. R. Naylor. Identification of patients with a histologically unstable carotid plaque using ultrasonic plaque image analysis. *European Journal of Vascular and Endovascular Surgery*, 48(2):118–125, August 2014. ISSN 1532-2165. doi: 10.1016/j.ejvs.2014.05.015.

[27] J. M. Seeger, E. Barratt, G. A. Lawson, and N. Klingman. The relationship between carotid plaque composition, plaque morphology, and neurologic symptoms. *The Journal of Surgical Research*, 58(3):330–336, 1995. ISSN 0022-4804; 0022-4804. doi: 10.1006/jsre.1995.1051.

[28] N. Takaya, C. Yuan, B. Chu, T. Saam, H. Underbill, J. Cai, N. Tran, N. L. Polissar, C. Isaac, M. S. Ferguson, G. A. Garden, S. C. Cramer, K. R. Maravilla, B. Hashimoto, and T. S. Hatsukami. Association between carotid plaque characteristics and subsequent ischemic cerebrovascular events: A prospective assessment with MRI - Initial results. *Stroke*, 37(3):818–823, 2006. ISSN 00392499. doi: 10.1161/01.STR.0000204638.91099.91.

[29] C. Herbert, A. Chandler, and R. Dinsmore. A Definition of Advanced Types of Atherosclerotic Lesions and a Histological Classification of Atherosclerosis. *Circulation*, 92(5):1355–1374, 1995. ISSN 0009-7322. doi: 10.1161/01.CIR.92.5.1355.

[30] E. B. Diethrich, K. Irshad, and D. B. Reid. Virtual histology and color flow intravascular ultrasound in peripheral interventions. *Seminars in Vascular Surgery*, 19(3): 155–162, September 2006. ISSN 0895-7967. doi: 10.1053/j.semvascsurg.2006.06. 001.

[31] W. Koenig and N. Khuseyinova. Biomarkers of Atherosclerotic Plaque Instability and Rupture. *Arteriosclerosis, Thrombosis, and Vascular Biology*, 27:15–26, 2007. ISSN 10795642. doi: 10.1161/01.ATV.0000251503.35795.4f.

[32] J.-M. Cai. Classification of Human Carotid Atherosclerotic Lesions With In Vivo Multicontrast Magnetic Resonance Imaging. *Circulation*, 106(11):1368–1373, August 2002. ISSN 00097322. doi: 10.1161/01.CIR.0000028591.44554.F9.

[33] A. Kampschulte, M. S. Ferguson, W. S. Kerwin, N. L. Polissar, B. Chu, T. Saam, T. S. Hatsukami, and C. Yuan. Differentiation of intraplaque versus juxtaluminal hemorrhage/thrombus in advanced human carotid atherosclerotic lesions by in vivo magnetic resonance imaging. *Circulation*, 110(20):3239–3244, November 2004. ISSN 1524-4539. doi: 10.1161/01.CIR.0000147287.23741.9A.

[34] T. Saam, J. Cai, L. Ma, Y.-Q. Cai, M. S. Ferguson, N. L. Polissar, T. S. Hatsukami, and C. Yuan. Comparison of symptomatic and asymptomatic atherosclerotic carotid plaque features with in vivo MR imaging. *Radiology*, 240(2):464–472, 2006. ISSN 0033-8419. doi: 10.1148/radiol.2402050390.

[35] E. I. Bluth, D. Kay, C. R. B. Merritt, M. Sullivan, G. Farr, N. L. Mills, M. Foreman, K. Sloan, M. Schlater, and J. Stewart. Sonographic characterization of carotid plaque: Detection of hemorrhage. *American Journal of Roentgenology*, 146(5): 1061–1065, 1986. ISSN 0361803X. doi: 10.2214/ajr.146.5.1061.

[36] G. Schulte-Altedorneburg, D. W. Droste, N. Haas, V. Kemény, D. G. Nabavi, L. Füzesi, and E. B. Ringelstein. Preoperative B-mode ultrasound plaque appearance compared with carotid endarterectomy specimen histology. *Acta Neurologica Scandinavica*, 101(3):188–194, 2000. ISSN 0001-6314. doi: 10.1034/j.1600-0404. 2000.101003188.x.

[37] A. Nair. Coronary Plaque Classification With Intravascular Ultrasound Radiofrequency Data Analysis. *Circulation*, 106(17):2200–2206, October 2002. ISSN 00097322. doi: 10.1161/01.CIR.0000035654.18341.5E.

[38] J. F. Granada, D. Wallace-Bradley, H. K. Win, C. L. Alviar, A. Builes, E. I. Lev, R. Barrios, D. G. Schulz, A. E. Raizner, and G. L. Kaluza. In vivo plaque characterization using intravascular ultrasound-virtual histology in a porcine model of complex coronary lesions. *Arteriosclerosis, Thrombosis, and Vascular Biology*, 27 (2):387–393, March 2007. ISSN 1524-4636. doi: 10.1161/01.ATV.0000253907. 51681.0e.

[39] B. K. Lal, R. W. Hobson, P. J. Pappas, R. Kubicka, M. Hameed, E. Y. Chakhtura, Z. Jamil, F. T. Padberg, P. B. Haser, and W. N. Durán. Pixel distribution analysis of B-mode ultrasound scan images predicts histologic features of atherosclerotic carotid plaques. *Journal of Vascular Surgery*, 35(6):1210–1217, June 2002. ISSN 07415214. doi: 10.1067/mva.2002.122888.

[40] J. F. Toussaint, G. M. LaMuraglia, J. F. Southern, V. Fuster, and H. L. Kantor. Magnetic resonance images lipid, fibrous, calcified, hemorrhagic, and thrombotic components of human atherosclerosis in vivo. *Circulation*, 94(5):932–938, 1996. ISSN 0009-7322. doi: 10.1161/01.CIR.94.5.932.

[41] C. Yuan, L. M. Mitsumori, M. S. Ferguson, N. L. Polissar, D. Echelard, G. Ortiz, R. Small, J. W. Davies, W. S. Kerwin, and T. S. Hatsukami. In vivo accuracy of

multispectral magnetic resonance imaging for identifying lipid-rich necrotic cores and intraplaque hemorrhage in advanced human carotid plaques. *Circulation*, 104 (17):2051–2056, 2001. ISSN 0009-7322. doi: 10.1161/hc4201.097839.

[42] T. Saam, M. S. Ferguson, V. L. Yarnykh, N. Takaya, D. Xu, N. L. Polissar, T. S. Hatsukami, and C. Yuan. Quantitative evaluation of carotid plaque composition by in vivo MRI. *Arteriosclerosis, Thrombosis, and Vascular Biology*, 25(1):234–239, 2005. ISSN 10795642. doi: 10.1161/01.ATV.0000149867.61851.31.

[43] B. Chu, A. Kampschulte, M. S. Ferguson, W. S. Kerwin, V. L. Yarnykh, K. D. O'Brien, N. L. Polissar, T. S. Hatsukami, and C. Yuan. Hemorrhage in the atherosclerotic carotid plaque: a high-resolution MRI study. *Stroke*, 35(5):1079–1084, May 2004. ISSN 1524-4628. doi: 10.1161/01.STR.0000125856.25309.86.

[44] C. Yuan. Identification of fibrous cap rupture with magnetic resonance imaging is highly associated with recent transient ischemic attack or stroke. *Circulation*, 105 (2):181–185, January 2002. ISSN 00097322. doi: 10.1161/hc0202.102121.

[45] Y. Watanabe, M. Nagayama, A. Sakata, A. Okumura, Y. Amoh, T. Ishimori, S. Nakashita, and Y. Dodo. Evaluation of fibrous cap rupture of atherosclerotic carotid plaque with thin-slice source images of Time-of-Flight MR Angiography. *Annals of Vascular Diseases*, 7(2):127–133, January 2014. ISSN 1881-641X. doi: 10.3400/avd.oa.13-00101.

[46] C. P. Loizou, S. Petroudi, C. S. Pattichis, M. Pantziaris, T. Kasparis, and A. Nicolaides. Segmentation of atherosclerotic carotid plaque in ultrasound video. In *Proceedings of the Annual International Conference of the IEEE Engineering in Medicine and Biology Society (EMBS)*, pages 53–56, 2012. ISBN 978-1-4244-4119-8. doi: 10.1109/EMBC.2012.6345869.

[47] C. P. Loizou, S. Petroudi, M. Pantziaris, A. N. Nicolaides, and C. S. Pattichis. An integrated system for the segmentation of atherosclerotic carotid plaque ultrasound video. *IEEE Transactions on Ultrasonics, Ferroelectrics, and Frequency Control*, 61(1):86–101, 2014. ISSN 08853010. doi: 10.1109/TUFFC.2014.6689778.

[48] F. Molinari, W. Liboni, E. Pavanelli, P. Giustetto, S. Badalamenti, and J. S. Suri. Accurate and automatic carotid plaque characterization in contrast enhanced 2-D ultrasound images. In *Proceedings of the 29th Annual International Conference of the IEEE Engineering in Medicine and Biology Society (EMBS)*, pages 335–338, 2007. ISBN 1424407885. doi: 10.1109/IEMBS.2007.4352292.

[49] F. Molinari, W. Liboni, P. Giustetto, E. Pavanelli, A. Marsico, and J. S. Suri. Carotid plaque characterization with contrast-enhanced ultrasound imaging and its histological validation. *Journal for Vascular Ultrasound*, 34(4):175–184, 2010. ISSN 1544-3167.

[50] S. Delsanto, F. Molinari, P. Giustetto, W. Liboni, S. Badalamenti, and J. Suri. Characterization of a completely user-independent algorithm for carotid artery segmentation in 2D ultrasound images. *IEEE Transactions on Instrumentation and Measurement*, 56(4):1265–1274, 2007. ISSN 0018-9456. doi: 10.1109/TIM.2007.900433.

[51] W. S. Kerwin, C. Han, B. Chu, D. Xu, Y. Luo, J.-N. Hwang, T. Hatsukami, and C. Yuan. A Quantitative Vascular Analysis System for evaluation of atherosclerotic lesions by MRI. In W. Niessen and M. Viergever, editors, *Medical Image Computing and Computer-Assisted Intervention (MICCAI) 2001*, volume 2208 of *Lecture Notes in Computer Science*, pages 786–794. Springer Berlin Heidelberg, 2001. ISBN 978-3-5404-2697-4. doi: 10.1007/3-540-45468-3_94.

[52] F. Liu, D. Xu, M. S. Ferguson, B. Chu, T. Saam, N. Takaya, T. S. Hatsukami, C. Yuan, and W. S. Kerwin. Automated in vivo segmentation of carotid plaque MRI with Morphology-Enhanced probability maps. *Magnetic Resonance in Medicine*, 55 (3):659–668, March 2006. ISSN 0740-3194. doi: 10.1002/mrm.20814.

[53] W. Kerwin, D. Xu, F. Liu, T. Saam, H. Underhill, N. Takaya, B. Chu, T. Hatsukami, and C. Yuan. Magnetic resonance imaging of carotid atherosclerosis: plaque analysis. *Topics in Magnetic Resonance Imaging*, 18(5):371–378, 2007. ISSN 0899-3459. doi: 10.1097/rmr.0b013e3181598d9d.

[54] P. Brigger, J. Hoeg, and M. Unser. B-spline snakes: a flexible tool for parametric contour detection. *IEEE Transactions on Image Processing*, 9(9):1484–1496, 2000. ISSN 1057-7149. doi: 10.1109/83.862624.

[55] M. A. de Graaf, A. Broersen, P. H. Kitslaar, C. J. Roos, J. Dijkstra, B. P. F. Lelieveldt, J. W. Jukema, M. J. Schalij, V. Delgado, J. J. Bax, J. H. C. Reiber, and A. J. Scholte. Automatic quantification and characterization of coronary atherosclerosis with computed tomography coronary angiography: cross-correlation with intravascular ultrasound virtual histology. *The International Journal of Cardiovascular Imaging*, 29 (5):1177–1190, June 2013. ISSN 1875-8312. doi: 10.1007/s10554-013-0194-x.

[56] D. Vukadinovic, T. V. Walsum, S. Rozie, T. D. Weert, R. Manniesing, A. V. D. Lugt, and W. Niessen. Carotid artery segmentation and plaque quantification in CTA. In

Proceedings of the IEEE International Symposium on Biomedical Imaging: From Nano to Macro (ISBI '09), pages 835–838, 2009. ISBN 978-1-4244-3932-4. doi: 10.1109/ISBI.2009.5193182.

[57] D. Vukadinovic, T. van Walsum, R. Manniesing, S. Rozie, A. van der Lugt, and W. J. Niessen. Region based level set segmentation of the outer wall of the carotid bifurcation in CTA. In *SPIE Medical Imaging*, pages 79623P–1–79623P–8. International Society for Optics and Photonics, March 2011. doi: 10.1117/12.878114.

[58] M. Wintermark, S. S. Jawadi, J. H. Rapp, T. Tihan, E. Tong, D. V. Glidden, S. Abedin, S. Schaeffer, G. Acevedo-Bolton, B. Boudignon, B. Orwoll, X. Pan, and D. Saloner. High-resolution CT imaging of carotid artery atherosclerotic plaques. *American Journal of Neuroradiology*, 29(5):875–882, May 2008. ISSN 1936-959X. doi: 10.3174/ajnr.A0950.

[59] L. W. Goldman. Principles of CT and CT technology. *Journal of Nuclear Medicine Technology*, 35:115–128, 2007. ISSN 0091-4916. doi: 10.2967/jnmt.107.042978.

[60] J. Bushberg. *The Essential Physics of Medical Imaging*. Lippincott Williams & Wilkins, Philadelphia, PA, 2nd edition, 2002. ISBN 9780683301182.

[61] M. G. Dalager, M. Bøttcher, G. Andersen, J. Thygesen, E. M. Pedersen, L. Dejbjerg, O. Gøtzsche, and H. E. Bøtker. Impact of luminal density on plaque classification by CT coronary angiography. *The International Journal of Cardiovascular Imaging*, 27(4):593–600, April 2011. ISSN 1875-8312. doi: 10.1007/s10554-010-9695-z.

[62] D. Vukadinovic, S. Rozie, M. Van Gils, T. Van Walsum, R. Manniesing, A. Van Der Lugt, and W. J. Niessen. Automated versus manual segmentation of atherosclerotic carotid plaque volume and components in CTA: Associations with cardiovascular risk factors. *International Journal of Cardiovascular Imaging*, 28(4):877–887, 2012. ISSN 15695794. doi: 10.1007/s10554-011-9890-6.

[63] I. M. Adame, R. J. Van Der Geest, B. A. Wasserman, M. A. Mohamed, J. H. C. Reiber, and B. P. F. Lelieveldt. Automatic segmentation and plaque characterization in atherosclerotic carotid artery MR images. *Magnetic Resonance Materials in Physics, Biology and Medicine*, 16(5):227–234, 2004. ISSN 09685243. doi: 10.1007/s10334-003-0030-8.

[64] I. M. Adame, R. J. van der Geest, B. A. Wasserman, M. Mohamed, J. H. C. Reiber, and B. P. F. Lelieveldt. Automatic plaque characterization and vessel wall segmentation in magnetic resonance images of atherosclerotic carotid arteries. In *Medical*

Imaging 2004, pages 265–273. International Society for Optics and Photonics, May 2004. doi: 10.1117/12.532471.

[65] V. V. Itskovich, D. D. Samber, V. Mani, J. G. S. Aguinaldo, J. T. Fallon, C. Y. Tang, V. Fuster, and Z. A. Fayad. Quantification of human atherosclerotic plaques using spatially enhanced cluster analysis of multicontrast-weighted magnetic resonance images. *Magnetic Resonance in Medicine*, 52(3):515–523, September 2004. ISSN 0740-3194. doi: 10.1002/mrm.20154.

[66] C. Karmonik, P. Basto, and J. D. Morrisett. Quantification of carotid atherosclerotic plaque components using feature space analysis and magnetic resonance imaging. In *Proceedings of the 28th Annual International Conference of the IEEE Engineering in Medicine and Biology Society (EMBS'06)*, volume 1, pages 3102–3105, 2006. ISBN 1-4244-0032-5. doi: 10.1109/IEMBS.2006.260318.

[67] C. Karmonik, P. Basto, K. Vickers, K. Martin, M. J. Reardon, G. M. Lawrie, and J. D. Morrisett. Quantitative segmentation of principal carotid atherosclerotic lesion components by feature space analysis based on multicontrast MRI at 1.5 T. *IEEE Transactions on Biomedical Engineering*, 56(2):352–360, February 2009. ISSN 1558-2531. doi: 10.1109/TBME.2008.2003100.

[68] D. X. D. Xu, J.-N. H. J.-N. Hwang, and C. Y. C. Yuan. Atherosclerotic plaque segmentation at human carotid artery based on multiple contrast weighting MR images. In *Proceedings of the International Conference on Image Processing*, volume 2, pages 849–852, 2001. ISBN 0-7803-6725-1. doi: 10.1109/ICIP.2001.958627.

[69] B. Sun, D. P. Giddens, R. Long, W. R. Taylor, D. Weiss, G. Joseph, D. Vega, and J. N. Oshinski. Characterization of coronary atherosclerotic plaque using multicontrast MRI acquired under simulated in vivo conditions. *Journal of Magnetic Resonance Imaging*, 24:833–841, 2006. ISSN 10531807. doi: 10.1002/jmri.20687.

[70] B. Sun, D. P. Giddens, R. Long, W. R. Taylor, D. Weiss, G. Joseph, D. Vega, and J. N. Oshinski. Automatic plaque characterization employing quantitative and multicontrast MRI. *Magnetic Resonance in Medicine*, 59:174–180, 2008. ISSN 07403194. doi: 10.1002/mrm.21279.

[71] K. Fukunaga and L. Hostetler. The estimation of the gradient of a density function, with applications in pattern recognition. *IEEE Transactions on Information Theory*, 21(1):32–40, January 1975. ISSN 0018-9448. doi: 10.1109/TIT.1975.1055330.

[72] U. R. Acharya, O. Faust, S. V. Sree, A. P. C. Alvin, G. Krishnamurthi, J. C. R. Seabra, J. Sanches, and J. S. Suri. Atheromatic^{TM}: Symptomatic vs. asymptomatic classification of carotid ultrasound plaque using a combination of HOS, DWT & texture. In *Proceedings of the Annual International Conference of the IEEE Engineering in Medicine and Biology Society (EMBS)*, pages 4489–4492, 2011. ISBN 978-1-4244-4121-1. doi: 10.1109/IEMBS.2011.6091113.

[73] U. R. Acharya, V. Sree S., F. Molinari, L. Saba, A. Nicolaides, S. Shafique, and J. S. Suri. Carotid ultrasound symptomatology using atherosclerotic plaque characterization: A class of Atheromatic systems. In *Proceedings of the Annual International Conference of the IEEE Engineering in Medicine and Biology Society (EMBS)*, pages 3199–3202, 2012. ISBN 978-1-4244-4119-8. doi: 10.1109/EMBC.2012.6346645.

[74] C. I. Christodoulou, C. S. Pattichis, M. Pantziaris, and A. Nicolaides. Texture-based classification of atherosclerotic carotid plaques. *IEEE Transactions on Medical Imaging*, 22(7):902–912, July 2003. ISSN 0278-0062. doi: 10.1109/TMI.2003.815066.

[75] E. Kyriacou, C. S. Pattichis, M. S. Pattichis, A. Mavrommatis, S. Panagiotou, C. I. Christodoulou, S. Kakkos, and A. Nicolaides. Classification of atherosclerotic carotid plaques using gray level morphological analysis on ultrasound images. *Artificial Intelligence Applications and Innovations*, 204:737–744, 2006. doi: 10.1007/0-387-34224-9_87.

[76] E. Kyriacou, M. S. Pattichis, C. S. Pattichis, A. Mavrommatis, C. I. Christodoulou, S. Kakkos, and A. Nicolaides. Classification of atherosclerotic carotid plaques using morphological analysis on ultrasound images. *Applied Intelligence*, 30(1):3–23, 2009. ISSN 0924669X. doi: 10.1007/s10489-007-0072-0.

[77] R. W. Anderson, C. Stomberg, C. W. Hahm, V. Mani, D. D. Samber, V. V. Itskovich, L. Valera-Guallar, J. T. Fallon, P. B. Nedanov, J. Huizenga, and Z. A. Fayad. Automated classification of atherosclerotic plaque from magnetic resonance images using predictive models. *Bio Systems*, 90(2):456–466, 2006. ISSN 0303-2647. doi: 10.1016/j.biosystems.2006.11.005.

[78] S. E. Clarke, R. R. Hammond, J. R. Mitchell, and B. K. Rutt. Quantitative assessment of carotid plaque composition using multicontrast MRI and registered histology. *Magnetic Resonance in Medicine*, 50(6):1199–1208, 2003. ISSN 07403194. doi: 10.1002/mrm.10618.

[79] S. E. Clarke, V. Beletsky, R. R. Hammond, R. A. Hegele, and B. K. Rutt. Validation of automatically classified magnetic resonance images for carotid plaque compositional analysis. *Stroke*, 37(1):93–97, January 2006. ISSN 1524-4628. doi: 10.1161/01.STR.0000196985.38701.0c.

[80] J. M. A. Hofman, W. J. Branderhorst, H. M. M. ten Eikelder, V. C. Cappendijk, S. Heeneman, M. E. Kooi, P. A. J. Hilbers, and B. M. ter Haar Romeny. Quantification of atherosclerotic plaque components using in vivo MRI and supervised classifiers. *Magnetic Resonance in Medicine*, 55(4):790–799, April 2006. ISSN 0740-3194. doi: 10.1002/mrm.20828.

[81] A. van Engelen, W. J. Niessen, S. Klein, H. C. Groen, H. J. M. Verhagen, J. J. Wentzel, A. van der Lugt, and M. de Bruijne. Multi-feature-based plaque characterization in ex vivo MRI trained by registration to 3D histology. *Physics in Medicine and Biology*, 57(1):241–256, January 2012. ISSN 1361-6560. doi: 10.1088/0031-9155/57/1/241.

[82] A. van Engelen, W. J. Niessen, S. Klein, H. C. Groen, H. J. M. Verhagen, J. J. Wentzel, A. Van Der Lugt, and M. De Bruijne. Supervised in-vivo plaque characterization incorporating class label uncertainty. In *Proceedings of the 9th IEEE International Symposium on Biomedical Imaging*, pages 246–249, 2012. ISBN 978-1-4577-1858-8. doi: 10.1109/ISBI.2012.6235530.

[83] R. van 't Klooster, O. Naggara, R. Marsico, J. H. C. Reiber, J. F. Meder, R. J. Van Der Geest, E. Touzé, and C. Oppenheim. Automated versus manual in vivo segmentation of carotid plaque MRI. *American Journal of Neuroradiology*, 33:1621–1627, 2012. ISSN 01956108. doi: 10.3174/ajnr.A3028.

[84] T. F. Chan and L. A. Vese. Active contours without edges. *IEEE Transactions on Image Processing*, 10(2):266–277, 2001. ISSN 1057-7149. doi: 10.1109/83.902291.

[85] O. Michailovich and A. Tannenbaum. Segmentation of medical ultrasound images using active contours. In *Proceedings of the IEEE International Conference on Image Processing (ICIP)*, volume 5, pages V − 513–V − 516, September 2007. ISBN 978-1-4244-1436-9. doi: 10.1109/ICIP.2007.4379878.

[86] Z. Ma, J. M. R. S. Tavares, R. N. Jorge, and T. Mascarenhas. A review of algorithms for medical image segmentation and their applications to the female pelvic cavity.

Computer Methods in Biomechanics and Biomedical Engineering, 13(2):235–246, 2010. ISSN 1025-5842. doi: 10.1080/10255840903131878.

[87] H. Tang, T. van Walsum, R. Hameeteman, M. Schaap, A. van der Lugt, L. J. van Vliet, and W. J. Niessen. Lumen segmentation of atherosclerotic carotid arteries in CTA. In *Proceedings of the 9th IEEE International Symposium on Biomedical Imaging (ISBI)*, pages 274–277, May 2012. ISBN 978-1-4577-1858-8. doi: 10.1109/ISBI.2012.6235537.

[88] A. M. F. Santos, R. M. dos Santos, P. M. A. C. Castro, E. Azevedo, L. Sousa, and J. M. R. S. Tavares. A novel automatic algorithm for the segmentation of the lumen of the carotid artery in ultrasound B-mode images. *Expert Systems with Applications*, 40(16):6570–6579, November 2013. ISSN 09574174. doi: 10.1016/j.eswa.2013.06.003.

[89] A. R. Abdel-Dayem and M. R. El-Sakka. Fuzzy C-Means clustering for segmenting carotid artery ultrasound images. In M. Kamel and A. Campilho, editors, *Image Analysis and Recognition*, pages 935–948. 2007. ISBN 978-3-540-74258-6. doi: 10.1007/978-3-540-74260-9_83.

[90] H. Moftah, W. Elmasry, N. El-Bendary, A. Hassanien, and K. Nakamatsu. Evaluating the effects of k-means clustering approach on medical images. In *Proceedings of the 12th International Conference on Intelligent Systems Design and Applications (ISDA)*, pages 455–459, November 2012. ISBN 978-1-4673-5119-5. doi: 10.1109/ISDA.2012.6416581.

[91] H. Hooda, O. P. Verma, and T. Singhal. Brain tumor segmentation: A performance analysis using k-means, fuzzy C-Means and region growing algorithm. In *Proceedings of the International Conference on Advanced Communication Control and Computing Technologies (ICACCCT)*, pages 1621–1626, May 2014. ISBN 978-1-4799-3914-5. doi: 10.1109/ICACCCT.2014.7019383.

[92] J. C. Bezdek, R. Ehrlich, and W. Full. FCM: The fuzzy c-means clustering algorithm. *Computers & Geosciences*, 10(2):191–203, 1984. ISSN 00983004. doi: 10.1016/0098-3004(84)90020-7.

[93] S. Z. Beevi, M. M. Sathik, K. Senthamaraikannan, and J. H. J. Yasmin. A robust fuzzy clustering technique with spatial neighborhood information for effective medical image segmentation: An efficient variants of fuzzy clustering technique with

spatial information for effective noisy medical image segmentation. In *Proceedings of the Second International Conference on Computing, Communication and Networking Technologies (ICCCNT)*, pages 1–8. IEEE, July 2010. ISBN 978-1-4244-6591-0. doi: 10.1109/ICCCNT.2010.5591787.

[94] B. N. Li, C. K. Chui, S. Chang, and S. H. Ong. Integrating spatial fuzzy clustering with level set methods for automated medical image segmentation. *Computers in Biology and Medicine*, 41(1):1–10, January 2011. ISSN 1879-0534. doi: 10.1016/j.compbiomed.2010.10.007.

[95] S. Krinidis and V. Chatzis. A robust fuzzy local information C-Means clustering algorithm. *IEEE Transactions on Image Processing*, 19(5):1328–1337, May 2010. ISSN 1941-0042. doi: 10.1109/TIP.2010.2040763.

[96] M. Hassan, A. Chaudhry, A. Khan, and J. Y. Kim. Carotid artery image segmentation using modified spatial fuzzy c-means and ensemble clustering. *Computer Methods and Programs in Biomedicine*, 108(3):1261–1276, December 2012. ISSN 1872-7565. doi: 10.1016/j.cmpb.2012.08.011.

[97] R. Beale and T. Jackson. *Neural Computing: An Introduction*. IOP Publishing Ltd., Bristol, UK, 1990. ISBN 0-85274-262-2.

[98] T. Serrano-Gotarredona, B. Linares-Barranco, and A. G. Andreou. *Adaptive Resonance Theory Microchips: Circuit Design Techniques*. Kluwer Academic Publishers, Norwell, MA, USA, 1998. ISBN 0-7923-8231-5.

Part B - Article 2:

Lumen segmentation in magnetic resonance images of the carotid artery

Danilo Samuel Jodas, Aledir Silveira Pereira, João Manuel R. S. Tavares

Abstract

Investigation of the carotid artery plays an important role in the diagnosis of cerebrovascular events. Segmentation of the lumen and vessel wall in Magnetic Resonance (MR) images is the first step towards evaluating any possible cardiovascular diseases like atherosclerosis. However, the automatic segmentation of the lumen is still a challenge due to the low quality of the images and the presence of other elements such as stenosis and malformations that compromise the accuracy of the results. In this article, a method to identify the location of the lumen without user interaction is presented. The proposed method uses the modified mean roundness to calculate the circularity index of the regions identified by the K-means algorithm and return the one with the maximum value, i.e. the potential lumen region. Then, an active contour is employed to refine the boundary of this region. The method achieved an average Dice coefficient of 0.78 ± 0.14 and 0.61 ± 0.21 in 181 3D-T1-weighted and 181 proton density-weighted MR images, respectively. The results show that this method is promising for the correct identification and location of the lumen even in images corrupted by noise.

Keywords: Magnetic Resonance Imaging, K-means algorithm, Deformable model, Subtractive clustering, Circularity index

1   Introduction

The segmentation of medical images is an important diagnostic tool to detect and/or to follow-up various diseases. An examination of the arterial system allows the identification of pathologies associated to cardiovascular diseases [1, 2]. One of the main cardiovascular diseases is atherosclerosis, which is when fatty components, calcium, cholesterol and fibrous tissues form plaques on the artery walls. Consequently, atherosclerosis reduces or blocks the blood flow through the artery, which can cause amaurosis fugax and strokes [3–5]. Several imaging modalities are able to identify atherosclerosis in a non-invasive way, allowing treatment planning before the onset or recurrence of symptoms.

Magnetic Resonance Imaging (MRI) of the carotid artery has been widely used in studies to identify the atherosclerotic plaques and their main components in order to analyze the progression of the disease [6]. However, the correct identification of the lumen and vessel boundaries is an important step before segmenting the atherosclerotic plaque components, since atherosclerosis is located between those boundaries. The automatic/semi-automatic segmentation of the lumen and vessel wall has been proposed

in several studies and in most cases it is considered as the first step to identify and evaluate atherosclerosis [7–12]. However, this task is not always performed automatically and therefore, in several studies, the boundaries of the lumen and vessel wall in the images have to be delineated manually [9, 13]. Typically, the lumen boundary is located inside the vessel wall. Hence, the lumen boundary can be extended until it reaches the vessel wall boundary [8].

Three-dimensional ultrasound (3D-US) is also an interesting imaging modality to envisage the anatomy of the carotid artery [14–16]. However, the segmentation of lumen and wall boundaries in 3D-US images is a challenge because of the poor contrast and weak boundaries caused by shadows that are due to calcifications; however, several studies have been proposed to overcome such difficulties [17, 18].

The segmentation of the lumen and wall of the carotid artery is a strong focus of research due to the lack of automation. Although the refinement of the lumen boundary can be easily achieved by deformable models [19–21], finding the region corresponding to the lumen is the most important step towards a fully automatic segmentation.

The semiautomatic segmentation of the lumen and wall of the carotid artery was tackled by Adame et al. [22, 23]. In those studies, ellipse fitting was used to detect the vessel wall boundary, while fuzzy clustering was applied to identify the lumen and carotid plaques. Although the segmentation results had high correlation with the manual segmentations, the method requires user interaction to determine the centre point of the lumen.

Another study carried out by Saba et al. [8] proposed the segmentation of the lumen and wall of the carotid artery based on the level set algorithm. The radial expansion from a specific point is used to define the initial contour of the lumen. The final contour of the lumen, which is expanded by two pixels, is then used to initialize the contour of the carotid wall.

An attempt to automatically segment the lumen in transverse ultrasound images of the carotid artery was undertaken by Yang et al. [24]. The proposed method used the Canny algorithm to find the edges in the input image and the morphological closing operation was used to find and fill the region corresponding to the lumen.

Gao et al. [25] proposed a method to identify the media-adventitia and lumen regions on intravascular ultrasound (IVUS) images by applying an adaptive region growing algorithm and the combination of the K-means and 2D Otsu algorithms to identify the lumen inside the media-adventitia region. The algorithms were applied individually and the minimization of the curvature was used to obtain the region with the least curvature variation, which is the best representation of the lumen.

Santos et al. [26, 27] addressed the segmentation of the lumen and bifurcation of the common carotid artery in B-mode ultrasound images. After a limiarization process,

the binary image containing the region corresponding to the lumen was used to generate the masks that were applied in the segmentation of the lumen and bifurcation boundaries. The Chan-Vese segmentation algorithm correctly detected the inferior and superior lumen walls. Although the segmentation was fully automatic, the method is only for longitudinal B-mode ultrasound images.

This study proposes a fully automatic method to identify the location of the lumen in MR images of the carotid artery. This method relies on the analysis of the regions in the input image to identify the ones corresponding to the potential lumen. We hypothesized that, since the lumen is a low intensity region with an approximately circular shape on axial MR images, the use of the mean roundness index would allow the identification of the region with the maximum circularity that may represent the potential lumen. In addition, an active contour method is applied to refine the region boundaries. In order to evaluate the method, a comparison between the computer and manual segmentations was made to attain a quantitative analysis.

The article is organized as follows: the steps of the proposed method are described in Section 2. The results of the segmentation, as well as the comparison with the manual segmentation, are presented in Section 3. Section 4 points out the advantages and limitations of the proposed method. Finally, the conclusions are drawn in Section 5.

2 Materials and Methods

2.1 Image acquisition

The MR images of the carotid artery selected for this study were used in research by van Engelen et al. [9] and kindly provided by the authors on request. The proposed method was performed on images that are the regions of interest surrounding the carotid arteries. A registration procedure was previously performed to match the original MR images with the corresponding histology images, which only contained the region of the artery under study [9]. Once the matching was completed, the MR images were cropped to obtain only the part that matched the histology images [9]. The original dataset was composed of five MRI scans acquired from thirteen patients: T1-weighted (T1W), Proton Density Weighted (PDW), Time-of-Flight (TOF) and two 3D-T1W scans. The first three MRI scans were acquired without administration of intravenous (IV) contrast media, whereas the 3D-T1W scan was acquired with and without contrast media. The post-contrast 3D-T1W scan was performed 4.6 ± 3.4 minutes after the administration of the contrast media. Each MRI scan is composed of approximately 17.7 ± 4.8 slices per patient; each slice has a pixel size of 0.25 mm x 0.25 mm. Computer Tomography Angiography (CTA) images

were also acquired to provide details for the registration with the histology images and to facilitate the manual segmentation of the lumen, vessel wall and plaque components. Manually drawn contours of the lumen and arterial wall were also provided for many of the MR slices. The manual delineations of the lumen and vessel wall were performed by one expert based on the combination of the CTA, PDW and post-contrast 3D-T1W scans with visual assessment of additional *in vivo* MRI scans [9]. More details about the MRI scans are available in van Engelen et al. [9].

From the original image dataset, we used all MR images with their corresponding ground truth, i.e. one reference contour of the lumen and another one for the vessel wall manually delineated in the slice under analysis; hence, 181 3D-T1W and 181 PDW MR images were used in the experiments.

2.2 Methodology

The proposed method is made up of three main stages, as shown in Figure 1.
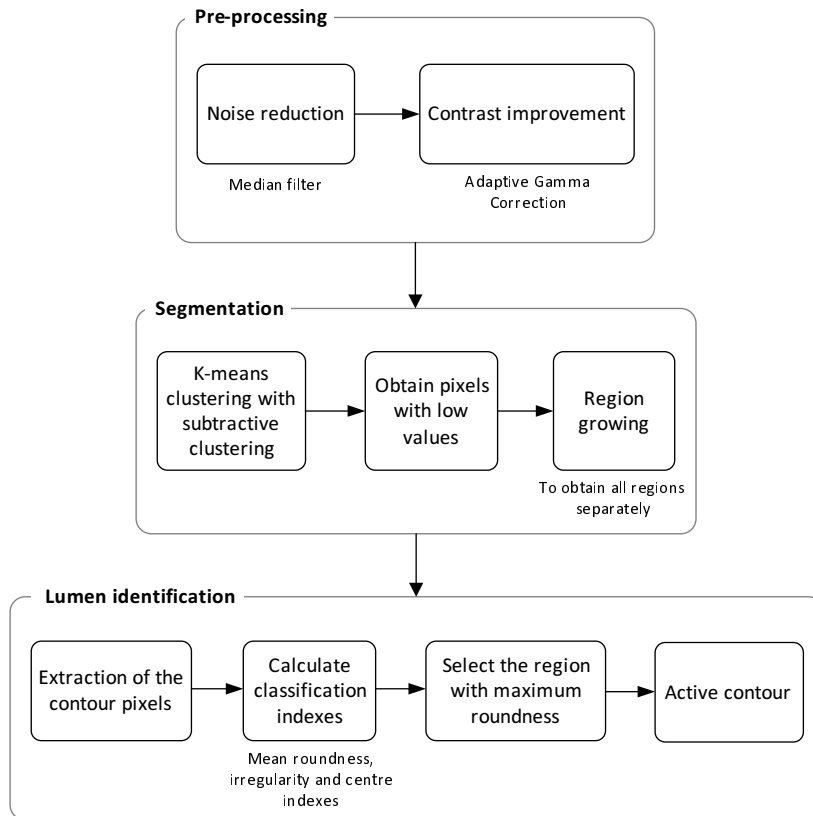

Figure 1: Diagram of the proposed segmentation method.

The pre-processing stage is necessary to minimize noise and improve the quality of the input images. Then, the enhanced images are submitted to the segmentation stage in

order to separate the regions with low pixel values, which include the background and the lumen regions. The lumen identification stage uses three classification indexes to identify the region corresponding to the lumen of the artery, which is then inputted to an active contour algorithm for further refinement of the boundary.

2.2.1 Pre-processing

The first step of the pre-processing stage is the use of a median filter with a mask of 5*x*5 to minimize the noise effects in the original images. The median filter was chosen due to its ability to remove noise without compromising the boundaries of the regions of interest.

The contrast enhancement step improves the brightness of the dark regions of the input images. The transformed-based gamma correction algorithm used here is a contrast enhancement algorithm belonging to the group of histogram modification-based algorithms [28]. In order to overcome the under- and over-estimation problems of the common gamma correction and histogram equalization algorithms, Huang et al. [28] proposed a gamma correction-based method to avoid the overestimation of regions with low-level intensities. The method relies on the probability density function (PDF) and the cumulative density function (CDF) of the intensity values:

$$T(l) = l_{max} \times (l/l_{max})^{1-CDF(l)}, \tag{1}$$

where *CDF(l)* is the cumulative density function of the intensity value *l* and l_{max} is the highest possible intensity value. The output intensity *T(l)* progressively increases as the CDF increases. Also, a weighting distribution is used to avoid an overestimation of low-level intensities. The weighting PDF is proposed as:

$$pdf_w(l) = pdf_{max} \times \left(\frac{pdf(l) - pdf_{min}}{pdf_{max} - pdf_{min}} \right)^{\alpha}, \tag{2}$$

where *l* is the intensity value, pdf_{min} is the minimum probability of the PDF function, pdf_{max} is the maximum probability and α is a parameter. The weighting CDF is defined as:

$$cdf_w(l) = \sum_{l=0}^{l_{max}} \frac{pdf_w(l)}{\sum pdf_w}, \tag{3}$$

where l_{max} is the highest possible intensity value and $\sum pdf_w = \sum_{l=0}^{l_{max}} pdf_w(l)$. The adaptive gamma correction with weighting distribution (AGCWD) [28] is:

$$T(l) = l_{max} \times (l/l_{max})^{1-cdf_w(l)}. \tag{4}$$

The amount of contrast enhancement depends on the value of the α parameter. The larger α is, the greater the enhancement will be.

Since the correct contrast enhancement plays an important role in the segmentation accuracy, the AGCWD is used in this study to avoid overestimating the brightness of the input images. However, a potential loss of important information can occur due to this image processing. Therefore, the analysis of the grayscale intensity is important to automatically determine whether the contrast correction is necessary or not. Hence, an automatic determination technique of the contrast enhancement of images based on the PDF of the grayscale intensities is proposed here. The PDF of the grayscale intensities is partitioned into two halves: the first halve represents the low intensity pixels of the image, whereas the second one represents the high intensity pixels. The difference between the accumulated probabilities of both halves is calculated. If the difference is low, the input image has a good contrast. The Otsu threshold is used to separate the probability density function. The following equation represents the basis of the automatic contrast correction:

$$D = \sum_{i=1}^{t} PDF_{min_i} - \sum_{j=t+1}^{N} PDF_{max_j},\qquad(5)$$

where PDF_{min} and PDF_{max} represent the probabilities of the low and high intensities of the input image, respectively, t is the value obtained by the Otsu threshold algorithm and N is the highest possible intensity value. If D is equal or less than a threshold, the contrast correction is not necessary. Here, a threshold value of 0.1 was found to be the one that led to good contrast enhancements without compromising the structures under analysis.

2.2.2 Segmentation

The K-means clustering algorithm is a well-known method to separate regions with similar characteristics (of intensity, for instance) in images. However, the correct use of the cluster centroids used in the K-means algorithm is a challenging task because different images have different cluster centroids. Additionally, trial and error is not an adequate approach because it is time consuming. Therefore, an automatic method to determine the cluster centroids is necessary.

The inconsistency results of the Fuzzy C-means algorithms are caused by different membership values generated by several executions. Thus, different cluster centroids can be generated because they are calculated from the membership values.

Subtractive clustering [29] has been proposed as an alternative approach to avoid the instability of the Fuzzy C-means algorithms. The adequate number of cluster centroids is calculated from the potential of each pixel in the neighbourhood as:

$$P_i = \sum_{j=1}^{n} e^{\frac{-4\left\|x_i - x_j\right\|^2}{r_a^2}}, \tag{6}$$

where $\left\|x_i - x_j\right\|$ represents the distance between pixels x_i and x_j, r_a is the radius representing the neighbourhood and n is the number of pixels in the input image. Equation 6 gives the initial potential of each pixel; then, the pixel having the highest potential is selected as the first cluster centroid. The next centroids are found according to:

$$P_i = P_i - P_j \times e^{\frac{-4\left\|x_i - x_j\right\|^2}{r_b^2}}, \tag{7}$$

where P_j represents the highest potential, x_j is the pixel with highest potential and r_b is the radius representing the neighbourhood. Equation 7 reduces the potential of the neighbouring pixels; then, the next pixel with the highest potential is selected as the next cluster centroid and the process is repeated until all the centroids have been found.

The advantage of the subtractive clustering algorithm is that the cluster centroids do not change in different runs. This is due to the fact that the potential function relies on the pixel values only (or another feature calculated from the pixels of the input image).

After the cluster centroids have been found, a clustering algorithm may be applied. The combination of the K-means algorithm with the subtractive clustering proposed by Dhanachandra et al. [30] was used in this study. Considering the fact that regions having similar grayscale intensities can be merged into one cluster, the choice of the number of clusters plays an important role to determine the correct segmentation of the lumen. The merging of the lumen region with pixels of the background can occur in arteries with a thin and low intensity wall. The lower the number of clusters, the higher the probability that the lumen and the background regions become one cluster. Based on several experiments, four clusters were found to be a stable choice to correctly identify the region corresponding to the lumen in the images tested.

Because the lumen and the background usually have low intensities in MR images, the next step selects the regions belonging to the cluster with low intensity. An image with such regions is returned as a binary image, in which the regions are represented as white and the background as black. The image is then submitted to the region growing algorithm in order to obtain all regions of the image separately. Here, the region growing is performed on the image corresponding to the cluster with low intensity values to obtain a set with all regions of interest. The white pixels have been chosen as the seed of the region growing algorithm, and the regions are merged when the pixels in the neighbourhood do not belong to another region previous identified and have the same intensity as

the seed. When a region is found, another pixel not belonging to the identified region is chosen as the seed and the process continues until all regions have been found. Although the region growing algorithm has been chosen to separate the regions, the connected component labelling algorithm could also be used to perform the same task without loss of performance. Examples of the segmentation stage with and without previous contrast enhancement are depicted in Figures 2 and 3.
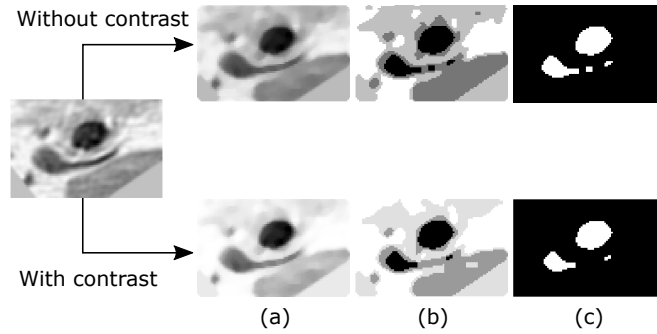

Figure 2: Example of the segmentation stage obtained from the 3D-T1W image with and without previous contrast enhancement; the image obtained from the median filter is shown in (a); the clustered image is shown in (b); and finally, the clusters of the low intensity pixels found are shown in (c).
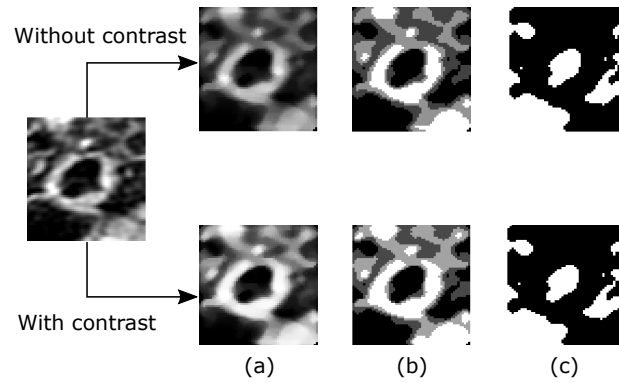

Figure 3: Example of the segmentation stage obtained from the PDW image with and without previous contrast enhancement; the image obtained from the median filter is shown in (a); the clustered image is shown in (b); and finally, the clusters of the low intensity pixels found are shown in (c).

2.2.3 Lumen identification

The lumen identification stage is the kernel of this study, which uses measures to evaluate each region of interest obtained in the previous stage. Since the lumen is a region similar to a circle, a set of indexes that maximize the function representing the roundness of the

possible region corresponding to the lumen is calculated. Hence, three indexes are found for each region in the segmented image:

- Circularity index (*MR*);

- Irregularity index (*Ir*);

- Centre index (*d*).

The process to identify the lumen requires maximizing a function composed of the above-mentioned indexes. In order to avoid additional processing and increase the performance of the method, regions with less than 1.5% of the total number of pixels of the input image are discarded since they are usually associated to noise. The indexes of all remaining regions are calculated.

Circularity indexes have been proposed in several studies [31–33] to quantify the roundness of regions in images. Ritter and Cooper [32] proposed a new index for determining the circularity of objects in images. The new index is called mean roundness, which represents the ratio between the average radius and the distance between the radius of each border pixel and the average radius:

$$MR = \frac{1}{N} \sum_{i=1}^{N} \frac{\bar{r}_b}{|r_i - \bar{r}_b| + \bar{r}_b}. \tag{8}$$

The larger the mean roundness *(MR)* index is, the more circular the object under analysis is. The proposed circularity index is independent of the image resolution [32].

An additional term was added to the mean roundness index to avoid pixels at the border of the input image:

$$MR = \frac{1}{N} \left(\sum_{i=1}^{N} \frac{\bar{r}_b}{|r_i - \bar{r}_b| + \bar{r}_b} \right) - n_b, \tag{9}$$

where n_b is the number of pixels of the region that are located at the border of the image. The modified *MR* index tries to reduce the circularity index of regions at the border of the input image. Also, since no rotation, translation or scaling transforms are performed in the proposed method, the location of the regions on the input image does not change.

In addition to the mean roundness index, the irregularity index has also been proposed to avoid regions with irregular contours. The following irregularity index was used in this study:

$$Ir = P * \left(\frac{1}{SD} - \frac{1}{GD} \right), \tag{10}$$

where *P* is the number of pixels of the contour, *SD* is the shortest diameter and the *GD* is the largest diameter [34]. If the difference between *SD* and *GD* is equal to 0 (zero) or close to it, the *Ir* index decreases, which means that the boundary is more regular.

In addition, a centre index (*d*) is used to identify the correct location of the lumen. In general, the lumen is located close to the centre of the image. Hence, the distances between the centre of the image and the centre of each region are calculated and used to maximize the final index function. Hence, the inverse of the irregularity and centre indexes are then used to maximize the proposed circularity index for each region accordingly to:

$$E = MR + \frac{1}{Ir} + \frac{1}{d}. \tag{11}$$

The irregularity and centre indexes are used to penalize the mean roundness index of regions with irregular borders and those far from the centre of the input image, respectively. The lower the irregularity index is, the larger its inverse will be. The same concept is also applied to the inverse of the centre index. Therefore, regions with high *MR*, irregularity and centre index values have a high probability of being the lumen.

The region that maximizes the circularity index is then submitted to the Chan-Vese active contour algorithm [20] in order to refine the contours previously found. The binary image representing the lumen region may not fit the true boundary of the lumen in the MR image. Hence, the contour of such a region is used as the input of the Chan-Vese active contour model, which is applied to the original image in order to fit the contour to the true boundary. This refinement step plays an important role to avoid under- or over-estimation of the contour, leading the contour closer to the true boundary of the lumen under analysis and, consequently, better results.

The Chan-Vese active contour was proposed by Chan and Vese [20] to segment the boundaries of objects in images based on the level set and Mumford-Shah models. The Chan-Vese active contour model is based on the energy minimization of the variations inside and outside the region as a level set problem, which can deal successfully with topological variations. Since the gradient of the image is not used in the Chan-Vese model, the method is recommended for the segmentation of medical images which commonly have weak boundaries of the structures under analysis.

2.3   Quantitative analysis

The proposed method was validated by evaluating the contours and the areas of the regions found. The following measures were used to compare the segmentations of the new method and the manual method:

- Dice coefficient;

- Polyline distance;

- Hausdorff distance.

The Dice coefficient represents the overlap between two regions, which is a ratio between the intersection and the union of the regions. Here, this metric is important to assess the under- or over-segmentation of the region identified by the automatic method with respect to the corresponding manual method.

The polyline distance represents the average minimum distance between two sets of points, i.e. image pixels, whereas the Hausdorff distance provides the maximum between the greatest distances between such points.

Under- and over-estimation of the lumen affect the value of the Dice coefficient, since it represents the ratio between the intersection and union of the regions under analysis. However, the centroid difference between the manually segmented and the automatically segmented lumen is low when the algorithm finds the correct location of the lumen, even when the Dice coefficient is reduced. Therefore, the difference between the centroids of the regions corresponding to the manual segmentation and the automatically segmented lumen is calculated by using the Euclidean distance. The higher the Euclidean distance, the farthest the regions are from each other.

3   Results

The proposed method was performed on each slice of the post-contrast 3D-T1W and PDW images with the ground truths provided. The following parameters were used to perform the automated segmentation: the mask of the median filter was set to 5x5; when it was necessary to adjust the contrast, the value of α in Equation 2 was defined as equal to the difference between the probabilities of the low and high intensities, as described by Equation 5; the radius r_a and r_b used in the subtractive clustering were set to 1.2 and 1.8, respectively; the percentage of disregarded regions was set at 1.5%; and the number of iterations of the Chan-Vese active contour algorithm was set to 200. The 5x5 mask was empirically determined as the most suitable template for removing noise from the images without disturbing the edges of the regions of interest. The radius values r_a and r_b of the subtractive clustering were empirically determined through several tests as the most appropriate parameters for separating the regions of the input images. In addition, the percentage of the disregarded regions was also experimentally found as the most suitable one for the resolution of the images under evaluation. A higher percentage value could

remove a region corresponding to the lumen, particularly in images where the lumen is small. The values of all parameters were kept constant in the experiments. Examples of the segmentation results and corresponding manual segmentation are shown in Figure 4.

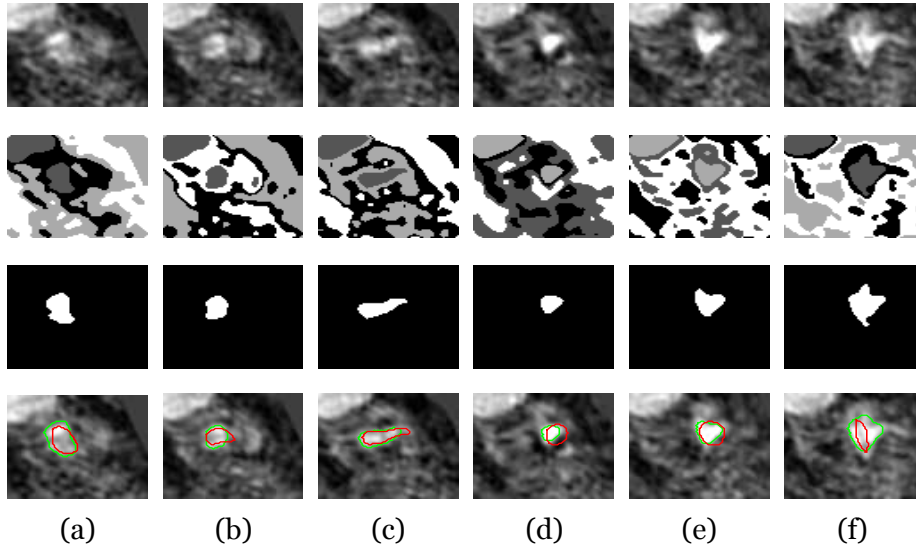
| (a) | (b) | (c) | (d) | (e) | (f) |

Figure 4: Examples of segmentation results obtained from the 3D-T1W images: Each column represents one image belonging to patient 1, which is composed of six slices with ground truth; the first row contains the input images; the second row represents the results of the K-means with subtractive clustering; the third row shows the images with the lumen that was identified by taking into account the modified mean roundness index; and finally, the forth row shows the refined contour in green and the manual one in red.

In Figure 4, the green contours represent the results of the proposed method, whereas the red contours represent the manual results. The lumen was correctly identified by the proposed method as shown by the two results. The values of the validation measures corresponding to the results shown in this figure (Figure 4) are given in Table 1.

Table 1: Values of the validation measures for the images in Figure 4.

	Dice	PD(px)	HD(px)	CD(px)
slice 1	0.75	2.05	5	2.03
slice 2	0.77	1.51	4.12	1.90
slice 3	0.80	1.26	5	3.59
slice 4	0.56	2.56	5	3.75
slice 5	0.78	1.58	4.24	2.82
slice 6	0.51	3.62	9.22	2.72

*PD = Polyline distance; HD = Hausdorff distance; CD = Centroid distance; px = pixels.

The automatic segmentation obtained for slice 6 of patient 1 in Figure 4f, shows that the result was overestimated compared to the manual one; however, it should be understood that the centroids of both regions were well matched.

In order to show the impact of the centre index and the regions on the border of the input image on the segmentation results, the images obtained with and without taking this index and these regions into account are shown in Figure 5.
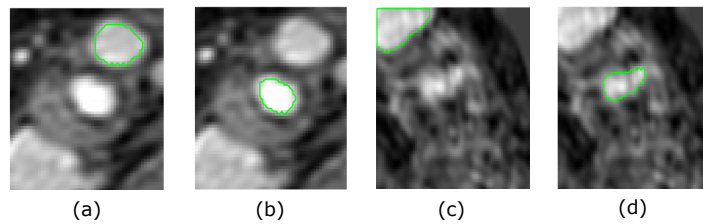

Figure 5: Impact of the centre index (a - not taken into account and b - taken into account) and of the regions on the border of the input image (c - not taken into account and d - taken into account) on the segmentation of the lumen region.

The identified region in Figure 5a does not correspond to the correct location of the lumen, despite its high value of mean roundness index. The correct lumen is represented by the brightest circular area close to the centre of the image. In this case, the centre index penalizes the value of the mean roundness index of the region close to the right top of the image, reducing the value of this index. The result obtained with the centre index activated is shown in Figure 5b. For the cases with regions that include pixels on the border of the input image, the impact of the number of these pixels on the mean roundness index is illustrated in Figures 5c and 5d. Here the number of these pixels contributes to reduce the mean roundness index of such regions, which leads to good segmentation results (Figure 5d).

Figure 6 illustrates the influence of the refinement process of the segmentation contour on the final result. In this figure, the red contour represents the contour of the binary mask of the lumen identification step, whereas the green contour is the result of the Chan-Vese active contour, i.e. the result of the refinement process from the red contour. In all cases shown in this figure, the initial contour (in red) underestimated the true boundary of the lumen, which was then corrected by the Chan-Vese model (green contour).

In order to illustrate the influence of the number of clusters, the images resulting from the segmentation step taking into account three and four clusters are shown in Figure 7.

As shown in Figure 7a-c, the lumen boundary leaked across the vessel wall when three clusters were used. This is due to the low intensity and the thinness of the vessel wall in the regions where the leakage occurred. The segmentation of the image shown in Figure
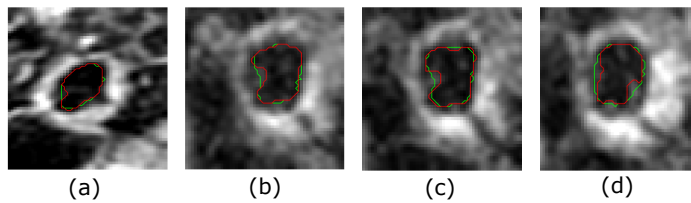
Figure 6: Impact of the Chan-Vese active contour on the final segmentation result: The red contour is the one obtained in the lumen identification step, and the green contour is the one obtained by the refinement process of the red one.
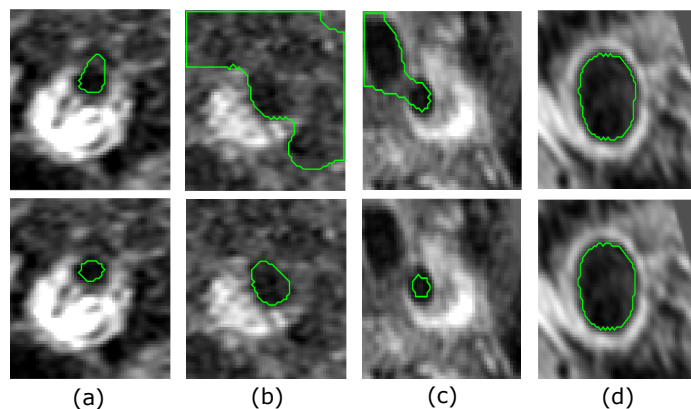

Figure 7: Influence of the number of clusters on the final lumen segmentation: The first row represents the segmentation obtained using three clusters, whereas the second row shows the segmentation obtained using four clusters.

7d was not affected by the number of clusters due to the higher grayscale intensity and thickness of the vessel wall.

The average values of the Dice similarity, polyline distance, Hausdorff distance and centroid distance of the automatically segmented lumens in comparison to the manual ones are shown in Tables 2 and 3 for each patient, respectively. For each metric, the average standard deviation was calculated using the pooled standard deviation formula.

The average measures obtained for the 3D-T1W images were better than those obtained for the PDW images, reaching Dice coefficients ranging from 0.67 ± 0.18 to 0.91 ± 0.04 (Table 2). The maximum Dice coefficient for the PDW images was 0.74 ± 0.16. This not-so-good result is due to the poor quality of the PDW images when compared to the 3D-T1W images. The polyline and Hausdorff distances were used to assess the difference between the manual and automatic segmentations regarding the contours obtained. For the 3D-T1W images, the polyline distance ranged from 1.06 ± 0.28 to 4.13 ± 5.69 pixels, whereas for the Hausdorff distance the differences ranged from 2.58 ± 1.02 to 9.97 ± 9.65 pixels. On the other hand, for the PDW images, the distances calculated by the polyline distance ranged from 1.44 ± 0.59 to 7.01 ± 4.98 pixels, whereas for the

Table 2: Average measures obtained for the 3D-T1W images.

	Dice $\pm$ std	PD $\pm$ std (px)	HD $\pm$ std (px)	CD $\pm$ std (px)
Patient 1	0.70 ± 0.13	2.10 ± 0.88	5.43 ± 1.90	2.80 ± 0.77
Patient 2	0.90 ± 0.02	1.33 ± 0.15	2.78 ± 0.37	0.53 ± 0.20
Patient 3	0.68 ± 0.11	1.36 ± 0.48	2.99 ± 1.80	1.79 ± 0.98
Patient 4	0.67 ± 0.18	2.25 ± 2.88	6.98 ± 9.93	3.42 ± 5.14
Patient 5	0.71 ± 0.22	1.98 ± 2.16	4.77 ± 4.41	1.39 ± 1.49
Patient 6	0.76 ± 0.16	2.17 ± 2.16	8.08 ± 9.85	3.83 ± 4.60
Patient 7	0.77 ± 0.20	1.75 ± 1.42	4.42 ± 4.15	1.98 ± 2.24
Patient 8	0.85 ± 0.15	1.07 ± 0.36	2.58 ± 1.02	1.26 ± 0.81
Patient 9	0.82 ± 0.07	1.30 ± 0.27	3.33 ± 1.71	1.39 ± 1.16
Patient 10	0.74 ± 0.11	1.41 ± 0.96	4.00 ± 3.15	1.77 ± 1.78
Patient 11	0.85 ± 0.08	1.39 ± 0.98	3.78 ± 5.04	1.52 ± 2.98
Patient 12	0.73 ± 0.16	4.13 ± 5.69	9.97 ± 9.65	5.52 ± 7.46
Patient 13	0.91 ± 0.04	1.06 ± 0.28	3.17 ± 1.07	1.08 ± 0.60
Average	0.78 ± 0.14	1.79 ± 2.13	4.79 ± 5.42	2.18 ± 3.22

*PD=Polyline distance; HD=Hausdorff distance; CD=Centroid distance; px=pixels; std=standard deviation.

Table 3: Average measures obtained for the PDW images.

	Dice $\pm$ std	PD $\pm$ std (px)	HD $\pm$ std (px)	CD $\pm$ std (px)
Patient 1	0.62 ± 0.12	3.14 ± 1.14	7.34 ± 3.52	2.23 ± 1.64
Patient 2	0.65 ± 0.25	3.35 ± 2.48	8.58 ± 5.90	3.89 ± 3.05
Patient 3	0.68 ± 0.10	1.44 ± 0.59	3.74 ± 2.42	2.07 ± 1.21
Patient 4	0.68 ± 0.21	1.64 ± 1.30	4.91 ± 4.11	2.14 ± 1.42
Patient 5	0.66 ± 0.14	1.89 ± 1.34	5.12 ± 2.87	1.81 ± 0.93
Patient 6	0.69 ± 0.15	4.43 ± 5.75	10.64 ± 11.55	5.13 ± 5.72
Patient 7	0.74 ± 0.16	1.52 ± 0.93	3.60 ± 2.07	2.19 ± 1.49
Patient 8	0.71 ± 0.26	1.94 ± 1.63	5.21 ± 4.83	2.66 ± 2.86
Patient 9	0.52 ± 0.23	3.15 ± 1.99	8.61 ± 6.08	3.74 ± 3.03
Patient 10	0.60 ± 0.25	2.81 ± 3.22	7.48 ± 7.78	3.58 ± 4.24
Patient 11	0.20 ± 0.26	6.89 ± 3.76	13.39 ± 6.27	5.21 ± 2.41
Patient 12	0.69 ± 0.24	2.70 ± 3.19	7.78 ± 8.96	3.42 ± 5.00
Patient 13	0.42 ± 0.23	7.01 ± 4.98	14.91 ± 7.62	6.53 ± 4.37
Average	0.61 ± 0.21	3.22 ± 3.05	7.79 ± 6.47	3.43 ± 3.35

*PD=Polyline distance; HD=Hausdorff distance; CD=Centroid distance; px=pixels; std=standard deviation.

Hausdorff distance the differences ranged from 3.60 ± 2.07 to 14.91 ± 7.62 pixels.

As indicated by Table 3, the lower Dice coefficient obtained for patient 11 was due to the fact that the lumen was not well characterized, as shown in Figure 8.

Figure 8 shows that the K-means algorithm was not able to correctly separate the whole region into clusters corresponding to the low intensity value because the region be-
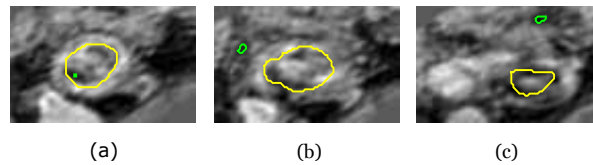
(a)   (b)   (c)

Figure 8: PDW images of patient 11 with the lumen not well characterized (the yellow colour represents the manual delineation, i.e. the correct region of interest).

longing to the lumen under analysis was corrupted by high intensity values. As mentioned earlier, the high quality of the 3D-T1W images and the good lumen characterization contributed to the good performance of the proposed method. Some segmentation examples of PDW images with the lumen properly characterized are shown in Figure 9.
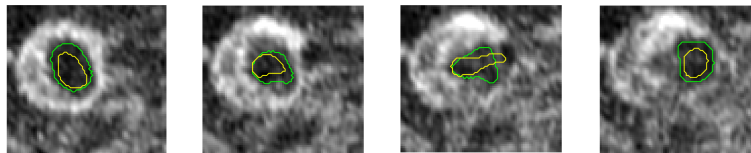

Figure 9: Segmentation of PDW images with the lumen properly characterized (the yellow colour represents the manual delineation, i.e. the correct region of interest).

4   Discussion

The development of automatic methods to correctly identify and segment the lumen in MR images is a challenge considering the low quality of input images, the presence of stenosis and malformations of this structure. In this work an automatic method to segment the lumen in MR images was presented. Since the lumen is approximately circular in axial MR images, our method automatically evaluated the circularity of the regions segmented by the K-means algorithm. In addition, an active contour algorithm was applied to further refine the boundary of the identified region.

The proposed method has several advantages compared to the other methods found in the literature. The main advantages are that the method is easily implemented and does not need any kind of user interaction. Also, by using a circularity index, the region corresponding to the lumen is identified without the use of complex algorithms. Although the parameters were tuned taking into account the characteristics of the dataset used in this article, most of these characteristics are commonly found in other related datasets, making the chosen parameters also suitable for these datasets without needing to make any significant changes in their values. In terms of the parameters of the pre-processing step, the mask of the median-filter used is a suitable choice to attenuate the noise usually found

in medical images without leading to excessive smoothing of the borders of the structures of interest, and is commonly adopted in such studies. The amount of contrast enhancement is determined by the value of the α parameter in Equation 2, which is automatically calculated by using the PDF of the grayscale intensities of the input image. The most important parameters are the ones related to the segmentation step. The number of clusters that are defined has an important role in the proposed method. The grayscale intensity of the lumen in carotid MR images is well-defined and distinguishable from other structures in the images. Hence, the number of clusters proposed here is suitable to be used in other image datasets. Moreover, the number of clusters was defined by taking into account that the thin and low intensity walls of the carotid arteries can cause the lumen boundary to leak. Moreover, since this is a common characteristic found in MR images of carotid arteries, the value of this parameter is appropriate to separate the regions without loss of performance. On using the subtractive clustering algorithm, the r_a and r_b parameters may affect the number of clusters to be generated [35]. However, since the subtractive clustering is only used to generate the centroids of the expected number of clusters, the values of these parameters can be used in other related image datasets to successfully identify the regions presented according to the same expected number.

Several difficulties that can affect the segmentation accuracy have been addressed in this study. Although the mean roundness measure is an easy and efficient index to identify circular shapes in images, the use of the mean radius also identifies regions not corresponding to a circular pattern, such as the ones that include the border of the input MR image. Hence, additional indexes are employed to penalize the mean roundness index in such cases. Depending on the imaging examination angle, two circular regions corresponding to the internal and external carotid arteries or the jugular vein can appear in the input image, compromising the segmentation result when the circular pattern of such regions is greater than the one of the lumen under study. Therefore, since the lumen is commonly located close to the centre of the input image, the centre index is used to penalize circular regions far from the centre. Consequently, the segmentation results are improved.

The results of the quantitative analysis show the superior quality of the 3D-T1W images which produced better results compared to the PDW images. The centroid distance showed that the location of the segmented lumen corresponds well to the location of the associated manual segmentation, even when there is an under- or over-estimation of the segmented lumen. The maximum average Dice coefficient was 0.91 ± 0.04 for the 181 3D-T1W images, whereas for the 181 PDW images, the maximum average was 0.74 ± 0.16 . On the other hand, the minimum average Dice was 0.67 ± 0.18 and 0.20 ± 0.26 for the same images, respectively. It should be pointed out that the segmen-

tation errors relating to patient 11 contributed to the minimum Dice calculated from the PDW images. The poor quality of the PDW images and the malformation of the lumen contributed to the majority of the segmentation errors found. In addition, the incorrect adjustment of the manual segmentations with respect to the real location of the lumen could distort the quantitative analysis. Since the manual segmentations were based on a combination of several imaging modalities, a misalignment can exist between such images and the images evaluated here (3D-T1W and PDW MR images). A new set of manual segmentations should be built in order to measure the accuracy of the proposed method against improved manual delineations. Nevertheless, the proposed method was able to identify the correct location of the lumen even in noisy images and in images of only reasonable quality.

The proposed method achieved a total average Dice similarity of 0.78 ± 0.14 for the 181 3D-T1W images and of 0.61 ± 0.21 for the 181 PDW images. Although the validation measures and the type of images used in the majority of related studies are different from the ones presented here, our method is in accordance with the works that have been published. According to Pratt's Figure of Merit (FOM), the method proposed by Yang et al. [24] achieved a similarity of 0.705 between the manually delineated and the segmented lumen contours. Although a complete and simple automatic method to segment the lumen has been proposed by Yang et al. [24], an analysis of the regions in the input images and the application of deformable models may improve the segmentation accuracy. Also, this method presents the following limitations: the applied morphological operations can distort the region corresponding to the lumen, the used gradient based method is not efficient to identify the desired edges on homogeneous regions, and additional algorithms should be employed to refine the boundary found. On the other hand, the method proposed by Adame et al. [22] achieved a correlation coefficient r of 0.94 between the manually delineated and the segmented lumen contours. However, all regions of the input image are processed to find the correct lumen, instead of evaluating only the regions limited by the wall boundary. In addition, the method proposed by Gao et al. [25] achieved a correlation coefficient r equal to 0.99 in the segmentation of the lumen in IVUS images. However, the lumen segmentation is performed after the identification of the region corresponding to the media-adventitia layer.

Manual editing could be considered to improve the results of the proposed method by manually adjusting the detected contour towards the real boundary of the lumen, leading to lower segmentation errors and, consequently, higher Dice coefficients. However, this would lead to a more time-consuming and subjective solution.

In spite of the potential offered by the proposed method, some limitations exist. Since the images showed regions of interest (ROI) acquired from the MRI exam, no additional

pre-processing or delineation to limit the ROI was performed in the input images. However, the cropping of medical images represents an important step to generate the regions surrounding the structures of interest. Since the MRI scan of carotid arteries is performed using a large field of view, covering the whole region of the neck, the cropping of the images becomes necessary to remove undesirable structures. Centerline tracking algorithms [36, 37] represent an alternative to find the centre of the artery in each slice and crop the image in order to obtain the region surrounding that artery. The success of the segmentation depends on correctly setting up the parameters of the proposed method, mainly the percentage of disregarded regions, which depends on the resolution of the input image. Since small regions corresponding to noisy artifacts can also appear as circular regions in some cases, the proposed method can fail to identify the correct lumen in these cases. The higher the image resolution is, the higher the percentage of disregarded regions should be. However, special attention must be taken when the lumen appears as a small region in the input image since it can also be discarded when a high percentage of disregarded regions is adopted. Although morphological operations could be effective to remove noisy regions from the input image, the choice of the shape and size of the structuring element is relevant to remove any noise efficiently and avoid the distortion of the region corresponding to the lumen. A more efficient approach will be considered in the future in order to correctly identify regions corresponding to noise without having to use 'disregarding percentages'.

5 Conclusions

The development of a fully automatic segmentation method of the lumen and vessel wall is an-ongoing and intensive focus of research. In this article a novel method was presented for the automatic lumen segmentation in MR images of the carotid artery without user interaction. The proposed method proved to be promising to identify the correct location of the lumen.

The low quality of the input images and the malformation of the lumen, as well as the misalignment and lack of manual interventions, contributed to the majority of the segmentation errors found. Nevertheless, the results showed that a good overlap and low point distances between the automatically segmented lumen and the associated manual results can be achieved by the proposed method even in the presence of noise.

Future studies will be conducted to reduce the number of parameters used in the proposed method and to tune automatically their values based on features of the input image.

In addition, the segmentation of the vessel wall is going to be addressed in the next step of our research.

Acknowledgements

References

[1] L. C. Sousa, C. F. Castro, C. C. António, A. Santos, R. Santos, P. Castro, E. Azevedo, and J. M. R. S. Tavares. Haemodynamic conditions of patient-specific carotid bifurcation based on ultrasound imaging. *Computer Methods in Biomechanics and Biomedical Engineering: Imaging & Visualization*, 2(3):157–166, September 2014. ISSN 2168-1163. doi: 10.1080/21681163.2013.875486.

[2] L. C. Sousa, C. F. Castro, C. C. António, A. M. F. Santos, R. M. Santos, P. M. A. C. Castro, E. Azevedo, and J. M. R. S. Tavares. Toward hemodynamic diagnosis of carotid artery stenosis based on ultrasound image data and computational modeling. *Medical & Biological Engineering & Computing*, 52(11):971–983, November 2014. ISSN 1741-0444. doi: 10.1007/s11517-014-1197-z.

[3] K. L. Furie, S. M. Smimakis, W. J. Koroshetz, and J. P. Kistler. Stroke due to large artery atherosclerosis. In K. L. Furie and P. J. Kelly, editors, *Handbook of Stroke Prevention in Clinical Practice*, Current Clinical Neurology, pages 151–165. Humana Press, 2004. ISBN 978-1-4684-9856-1.

[4] J. P. Schadé. *The Complete Encyclopedia of Medicine & Health*. Foreign Media Books, 2006. ISBN 9781601360014.

[5] D. O. Wiebers, V. L. Feigin, and R. Brown. *Handbook of Stroke*. Board Review Series. Lippincott Williams & Wilkins, Philadelphia, PA, 2nd edition, 2006. ISBN 9780781786584.

[6] D. S. Jodas, A. S. Pereira, and J. M. R. S. Tavares. A review of computational methods applied for identification and quantification of atherosclerotic plaques in images. *Expert Systems with Applications*, 46:1 – 14, 2016. ISSN 0957-4174. doi: 10.1016/j.eswa.2015.10.016.

[7] W. Kerwin, D. Xu, F. Liu, T. Saam, H. Underhill, N. Takaya, B. Chu, T. Hatsukami, and C. Yuan. Magnetic resonance imaging of carotid atherosclerosis: plaque analysis. *Topics in Magnetic Resonance Imaging*, 18:371–378, 2007. ISSN 0899-3459. doi: 10.1097/rmr.0b013e3181598d9d.

[8] L. Saba, H. Gao, E. Raz, S. V. Sree, L. Mannelli, N. Tallapally, F. Molinari, P. P. Bassareo, U. R. Acharya, H. Poppert, and J. S. Suri. Semiautomated analysis of carotid artery wall thickness in MRI. *Journal of Magnetic Resonance Imaging*, 39 (6):1457–1467, 2014. ISSN 1522-2586. doi: 10.1002/jmri.24307.

[9] A. van Engelen, W. J. Niessen, S. Klein, H. C. Groen, H. J. M. Verhagen, J. J. Wentzel, A. van der Lugt, and M. de Bruijne. Atherosclerotic plaque component segmentation in combined carotid MRI and CTA data incorporating class label uncertainty. *PLoS ONE*, 9(4):1–14, April 2014. ISSN 1932-6203. doi: 10.1371/journal.pone.0094840.

[10] D. Vukadinovic, T. Van Walsum, S. Rozie, T. de Weert, R. Manniesing, A. van der Lugt, and W. Niessen. Carotid artery segmentation and plaque quantification in CTA. In *IEEE International Symposium on Biomedical Imaging: From Nano to Macro*, pages 835–838, June 2009. ISBN 978-1-4244-3931-7. doi: 10.1109/ISBI. 2009.5193182.

[11] D. Vukadinovic, T. Van Walsum, R. Manniesing, S. Rozie, R. Hameeteman, T. de Weert, A. van der Lugt, and W. Niessen. Segmentation of the outer vessel wall of the common carotid artery in CTA. *IEEE Transactions on Medical Imaging*, 29(1):65–76, January 2010. ISSN 0278-0062. doi: 10.1109/TMI.2009.2025702.

[12] R. van 't Klooster, A. J. Patterson, V. E. Young, J. H. Gillard, J. H. C. Reiber, and R. J. van der Geest. An Objective Method to Optimize the MR Sequence Set for Plaque Classification in Carotid Vessel Wall Images Using Automated Image Segmentation. *PLoS ONE*, 8:1–7, 2013. ISSN 19326203. doi: 10.1371/journal. pone.0078492.

[13] A. van Engelen, W. J. Niessen, S. Klein, H. C. Groen, H. J. Verhagen, J. J. Wentzel, A. van der Lugt, and M. de Bruijne. Supervised in-vivo plaque characterization

incorporating class label uncertainty. In *9th IEEE International Symposium on Biomedical Imaging (ISBI)*, pages 246–249. IEEE, 2012. ISBN 978-1-4577-1858-8. doi: 10.1109/ISBI.2012.6235530.

[14] B. Chiu, V. Shamdasani, R. Entrekin, C. Yuan, and W. S. Kerwin. Characterization of carotid plaques on 3-dimensional ultrasound imaging by registration with multi-contrast magnetic resonance imaging. *Journal of Ultrasound in Medicine: Official Journal of the American Institute of Ultrasound in Medicine*, 31(10):1567–1580, 2012. ISSN 1550-9613. doi: 10.7863/jum.2012.31.10.1567.

[15] A. Fenster, A. Landry, D. B. Downey, R. A. Hegele, and J. D. Spence. 3D ultrasound imaging of the carotid arteries. *Current Drug Targets - Cardiovascular & Hematological Disorders*, 4(2):161–175, 2004. ISSN 1568-0061. doi: 10.2174/1568006043336311.

[16] A. Fenster, G. Parraga, and J. Bax. Three-dimensional ultrasound scanning. *Interface Focus*, 1(4):503–519, 2011. ISSN 2042-8901. doi: 10.1098/rsfs.2011.0019.

[17] M. M. Hossain, K. AlMuhanna, L. Zhao, B. K. Lal, and S. Sikdar. Three dimensional level set based semiautomatic segmentation of atherosclerotic carotid artery wall volume using 3D ultrasound imaging. *Medical Physics*, 9034(4):90344B–1–90344B–8, 2014. ISSN 16057422. doi: 10.1117/12.2043975.

[18] E. Ukwatta, J. Awad, A. Ward, J. Samarabandu, A. Krasinski, G. Parraga, and A. Fenster. Segmentation of the lumen and media-adventitia boundaries of the common carotid artery from 3D ultrasound images. In *Progress in Biomedical Optics and Imaging - Proceedings of SPIE*, volume 7963, pages 79630G–1–79630G–8, 2011. ISBN 9780819485052. doi: 10.1117/12.877722.

[19] V. Caselles, R. Kimmel, and G. Sapiro. Geodesic active contours. In *Proceedings of IEEE International Conference on Computer Vision*, pages 694–699. IEEE Comput. Soc. Press, 1995. ISBN 0-8186-7042-8. doi: 10.1109/ICCV.1995.466871.

[20] T. F. Chan and L. A. Vese. Active contours without edges. *IEEE Transactions on Image Processing*, 10(2):266–277, 2001. ISSN 1057-7149. doi: 10.1109/83.902291.

[21] Z. Ma, J. M. R. S. Tavares, R. N. Jorge, and T. Mascarenhas. A review of algorithms for medical image segmentation and their applications to the female pelvic cavity. *Computer Methods in Biomechanics and Biomedical Engineering*, 13(2):235–246, 2010. doi: 10.1080/10255840903131878.

[22] I. M. Adame, R. J. van der Geest, B. A. Wasserman, M. Mohamed, J. H. Reiber, and B. P. Lelieveldt. Automatic plaque characterization and vessel wall segmentation in magnetic resonance images of atherosclerotic carotid arteries. In *Medical Imaging 2004*, pages 265–273. International Society for Optics and Photonics, 2004. doi: 10.1117/12.532471.

[23] I. M. Adame, R. J. van der Geest, B. A. Wasserman, M. A. Mohamed, J. H. Reiber, and B. P. Lelieveldt. Automatic segmentation and plaque characterization in atherosclerotic carotid artery MR images. *Magnetic Resonance Materials in Physics, Biology and Medicine*, 16(5):227–234, 2004. ISSN 1352-8661. doi: 10.1007/s10334-003-0030-8.

[24] X. Yang, M. Ding, L. Lou, M. Yuchi, W. Qiu, and Y. Sun. Common carotid artery lumen segmentation in B-mode ultrasound transverse view images. *International Journal of Image, Graphics and Signal Processing (IJIGSP)*, 3(5):15–21, 2011. ISSN 2074-9074. doi: 10.5815/ijigsp.2011.05.03.

[25] Z. Gao, W. K. Hau, M. Lu, W. Huang, H. Zhang, W. Wu, X. Liu, and Y.-T. Zhang. Automated Framework for Detecting Lumen and Media–Adventitia Borders in Intravascular Ultrasound Images. *Ultrasound in Medicine & Biology*, 41(7):2001–2021, July 2015. ISSN 03015629. doi: 10.1016/j.ultrasmedbio.2015.03.022.

[26] A. M. F. Santos, J. M. R. S. Tavares, L. Sousa, R. Santos, P. Castro, and E. Azevedo. Automatic segmentation of the lumen of the carotid artery in ultrasound B-mode images. *Proc. SPIE*, 8670:86703I–1–86703I–16, 2013. doi: 10.1117/12.2007259.

[27] A. M. F. Santos, R. M. dos Santos, P. M. A. Castro, E. Azevedo, L. Sousa, and J. M. R. S. Tavares. A novel automatic algorithm for the segmentation of the lumen of the carotid artery in ultrasound B-mode images. *Expert Systems with Applications*, 40 (16):6570–6579, November 2013. ISSN 09574174. doi: 10.1016/j.eswa.2013.06.003.

[28] S.-C. Huang, F.-C. Cheng, and Y.-S. Chiu. Efficient Contrast Enhancement Using Adaptive Gamma Correction with Weighting Distribution. *IEEE Transactions on Image Processing*, 22(3):1032–1041, March 2013. ISSN 1057-7149. doi: 10.1109/TIP.2012.2226047.

[29] K. Bataineh, M. Naji, and M. Saqer. A comparison study between various fuzzy clustering algorithms. *Editorial Board*, 5(4):335–343, 2011. ISSN 1995-6665.

[30] N. Dhanachandra, K. Manglem, and Y. J. Chanu. Image Segmentation Using K - means Clustering Algorithm and Subtractive Clustering Algorithm. *Procedia Computer Science*, 54:764–771, 2015. ISSN 18770509. doi: 10.1016/j.procs.2015.06. 090.

[31] Y. Kehong, Z. Jiying, F. Shu, D. Chaijie, B. Shanglian, and C. Qiansheng. Roundness curve for classification of cell phase on microscopic image. In *International Conference on Technology and Applications in Biomedicine (ITAB)*, pages 70–73, May 2008. ISBN 9781424422555. doi: 10.1109/ITAB.2008.4570653.

[32] N. Ritter and J. Cooper. New Resolution Independent Measures of Circularity. *Journal of Mathematical Imaging and Vision*, 35(2):117–127, October 2009. ISSN 0924-9907. doi: 10.1007/s10851-009-0158-x.

[33] A. M. Herrera-Navarro, H. Jiménez Hernández, H. Peregrina-Barreto, F. Manríquez-Guerrero, and I. R. Terol-Villalobos. A New Measure of Circularity Based on Distribution of the Radius. *Computación y Sistemas*, 17(4):515–526, December 2013. ISSN 14055546. doi: 10.13053/CyS-17-4-2013-005.

[34] S. Jain, V. Jagtap, and N. Pise. Computer Aided Melanoma Skin Cancer Detection Using Image Processing. *Procedia Computer Science*, 48:735–740, 2015. ISSN 18770509. doi: 10.1016/j.procs.2015.04.209.

[35] S. L. Chiu. Fuzzy model identification based on cluster estimation. *Journal of Intelligent & Fuzzy Systems*, 2(3):267–278, May 1994. ISSN 1064-1246.

[36] M. M. G. Macedo, C. Mekkaoui, and M. P. Jackowski. *Vessel Centerline Tracking in CTA and MRA Images Using Hough Transform*, pages 295–302. Springer Berlin Heidelberg, Berlin, Heidelberg, 2010. ISBN 978-3-642-16687-7. doi: 10.1007/ 978-3-642-16687-7_41.

[37] H. Tang, T. van Walsum, R. S. van Onkelen, S. Klein, R. Hameeteman, M. Schaap, Q. J. A. van den Bouwhuijsen, J. C. M. Witteman, A. van der Lugt, L. J. van Vliet, and W. J. Niessen. Multispectral MRI centerline tracking in carotid arteries. In *SPIE Medical Imaging*, volume 7962, pages 79621N–1–79621N–7, 2011. doi: 10.1117/ 12.877817.

Part B - Article 3:

Automatic segmentation of the lumen region in intravascular images of the coronary artery

Danilo Samuel Jodas, Aledir Silveira Pereira, João Manuel R. S. Tavares

Abstract

Image assessment of the arterial system plays an important role in the diagnosis of cardiovascular diseases. The segmentation of the lumen and media-adventitia in intravascular (IVUS) images of the coronary artery is the first step towards the evaluation of the morphology of the vessel under analysis and the identification of possible atherosclerotic lesions. In this study, a fully automatic method for the segmentation of the lumen in IVUS images of the coronary artery is presented. The proposed method relies on the K-means algorithm and the mean roundness to identify the region corresponding to the potential lumen. An approach to identify and eliminate side branches on bifurcations is also proposed to delimit the area with the potential lumen regions. Additionally, an active contour model is applied to refine the contour of the lumen region. In order to evaluate the segmentation accuracy, the results of the proposed method were compared against manual delineations made by two experts in 326 IVUS images of the coronary artery. The average values of the Jaccard measure, Hausdorff distance, percentage of area difference and Dice coefficient were 0.88 ± 0.06, 0.29 ± 0.17 mm, 0.09 ± 0.07 and 0.94 ± 0.04, respectively, in 324 IVUS images successfully segmented. Additionally, a comparison with the studies found in the literature showed that the proposed method is slight better than the majority of the related methods that have been proposed. Hence, the new automatic segmentation method is shown to be effective in detecting the lumen in IVUS images without using complex solutions and user interaction.

Keywords: Medical Imaging, Intravascular Ultrasound, Image Pre-processing, Image Segmentation

1   Introduction

According to the World Health Organization (WHO), coronary artery diseases were responsible for the death of 7.3 million people around the world in 2008 [1]. Atherosclerosis is an underlying disease responsible for the occurrence of heart attacks and strokes. Atherosclerotic plaques are formed when fatty material and cholesterol are deposited inside the lumen of the artery, reducing the blood flow through the vessel and increasing the risk of blood clots that can cause heart attacks and strokes. Thus, in order to prevent such risks a treatment plan or even stenting procedures should be established based on image-based technologies.

Technological advances in computerized systems for imaging-based diagnosis are able to detect and analyze cardiovascular diseases. Intravascular Ultrasound (IVUS) is

an imaging procedure that allows the evaluation of the arterial morphology by means of the introduction of a catheter equipped with an ultrasound transducer inside the vessel to be studied. The catheter slides through a guidewire placed in the blood vessel near the segment of interest in order to acquired images of the affected region. Images acquired from IVUS imaging systems allow experts to envisage atherosclerotic lesions and the shape and size of the vessels under analysis.

The segmentation of IVUS images plays an important role in evaluating the morphology of the vessel under study and obtaining important information such as the area and diameter of the lumen, the presence and volume of atherosclerotic plaques and the identification of the atherosclerotic plaque components [2–5]. Since a large number of image frames are acquired from a single IVUS exam, the manual identification of the structures of interest becomes a time-consuming and laborious task. Therefore, the automatic segmentation of IVUS images is demanded for expediting the assessment of the morphology of the vessel and the treatment planning of atherosclerotic lesions.

The segmentation of the lumen and media-adventitia regions in IVUS images has been an intensive focus of research [6]. The presence of calcifications, shadows, transducer reflection, speckle noises and bifurcations, as well as the variations of the grayscale intensities inside the same structure, represent a challenge to the development of a fully automatic segmentation method. The presence of the first two artefacts, i.e. calcifications and shadows, is an obstacle to the efficient segmentation of the media-adventitia region, whereas the transducer reflection and speckle noises represent a challenge to identify the region corresponding to the lumen successfully. Additionally, the segmentation of the lumen in bifurcation regions represents a challenge due to the extension of the low-intensity values from the lumen region to the borders of the IVUS image.

This article proposes a method to automatically detect the lumen boundary in IVUS images of coronary arteries. An initial version of this method was applied in the segmentation of the lumen in magnetic resonance (MR) images of carotid arteries [7]. The approach was based on the assumption that the lumen is a low-intensity region with an approximately circular shape. Thus, a circularity index, combined with a centre index and the number of regions at the border of the image were used to find the region corresponding to the lumen under analysis. In the current study, besides the assessment concerning the suitability of the method to detect the lumen boundary of coronary arteries in IVUS images using the same parameters as were established for the MR images, the method has been improved in order to enhance its robustness, efficiency, automaticity and competency. Hence, a new approach was developed to identify and remove side branches of bifurcation regions so only the regions that potentially correspond to the lumen are selected for further processing, avoiding bifurcation parts at the border of the image and

enhancing therefore, the robustness of the method. Moreover, the regions at the border are now discarded before computing the circularity index of each potential lumen region, which boosts the performance of the method. Additionally, noisy regions are now automatically eliminated without the use of any predefined parameter, which increases the automaticity. Finally, a post-processing step has now been added to smooth the contour found for the lumen region, which leads to better segmentation results.

The remainder of the article is organized as follow: Section 2 presents the previous studies related to the segmentation of IVUS images. Section 3 provides a detailed description of the proposed automatic lumen segmentation method. The results of the segmentation, as well as the comparison with the manual delineations and related methods found in the literature, are given in Section 4. The advantages and limitations of the proposed method are pointed out in Section 5. Finally, the conclusions are drawn up in Section 6.

2   Previous studies

Several studies have been proposed to address the segmentation of the lumen and media-adventitia in IVUS images acquired using different ranges of frequencies and with several artefacts that hamper the segmentation successful. In summary, the studies can be divided into approaches based on machine learning, probabilistic functions, deformable models, region growing, thresholding and morphological operations.

Lo Vercio et al. [8] proposed a learning machine-based approach to segment the lumen and media-adventitia regions in IVUS images of coronary arteries. From the input images, a set of features obtained using noise-reduction filters, texture and edge detector operators was acquired and used as input to a Support Vector Machine (SVM) classifier, which classify the likelihood of the pixels to belong to the lumen and background regions. Hence, the classification between lumen and non-lumen, as well as between background and non-background, was performed to determine the correct location of the lumen and media-adventitia contours.

Another learning machine-based approach to segment the lumen and media-adventitia contours in IVUS images of coronary arteries was tackled by Su et al. [9]. Two Artificial Neural Networks (ANN) are used to classify the pixels inside a region of interest (ROI) as belonging to the media-adventitia region. The first ANN is used to perform the initial classification, whereas the second one performs the classification of the binary image resultant from the first ANN in order to remove noises and refine the results. Then, the pixels inside the region corresponding to the identified media-adventitia are classified as

lumen and non-lumen by using the same ANNs. The contours of the regions are then submitted to the Snake active contour model proposed by Kass et al. [10] in order to adjust them to the true boundary of each region.

A study carried out by Destrempes et al. [11] proposed a fast-marching method (FMM) to segment the lumen and media-adventitia boundaries in IVUS images of coronary arteries. The proposed method relies on the minimization of a function that uses the gradient of the image and the probability of the pixels to belong to a region corresponding to one of the structures of the coronary artery: lumen, media, adventitia, and surrounding tissues.

Mendizabal-Ruiz et al. [12] proposed an approach to find the lumen contour in IVUS images of coronary arteries based on probabilistic functions. After the transformation of the IVUS images into the polar coordinates domain, the probabilities of the pixels belonging to the lumen region are used to find the correct contour by means of the minimization of a cost function. The probabilities are calculated by using a sigmoid function and an SVM classifier that receives texture features from Law's filters, which are used to deal with pixel intensities that increase due to the catheters with higher frequencies.

A parametric active contour model for the segmentation of lumen and media-adventitia contours in IVUS images of coronary arteries was proposed by Vard et al. [13]. For the lumen contour segmentation, a method based on the short-term autocorrelation (STA) is used to remove speckle noise from the lumen region. The proposed STA method, called normalized cumulative STA (NCSTA), is then used to produce a new grayscale IVUS image without noise in the lumen region. The image resulting from the NCSTA method generates a pressure force for a parametric active contour model that is used to find the lumen contour.

A 3D-FMM method was proposed by Cardinal et al. [14] to segment the lumen and media-adventitia contours in IVUS images of femoral arteries. The 3D-FMM method is based on the Rayleigh probability density function (PDF) and a gradient function to find the correct contour of each region, i.e. lumen and media-adventitia, by means of the refinement of contours manually defined. Another study tackled by Cardinal et al. [15] combines the PDF and gradient intensity obtained from the input images in order to calculate the propagation speed of the 3D-FMM. In addition, the proposed method automatically detects the initial contours of the lumen and media-adventitia borders to be used by the 3D-FMM method.

Taki et al. [16] proposed a method based on thresholding and deformable models to identify the contours of the lumen and media-adventitia regions in IVUS images. Regarding the lumen contour identification, the evaluation of the pixels in the polar coordinates domain is made in order to identify the ones with intensities higher than a pre-defined

threshold T. If $I(r, \theta) > T$, then the pixel is assumed to belong to the lumen border. The initial contour of the lumen is then submitted to a parametric active contour and a geometric model to adjust it to the true borders of the corresponding lumen region.

The combination of fuzzy clustering with morphological operation was proposed by dos Santos et al. [17] to identify the lumen region in IVUS images. The fuzzy clustering defined with two clusters was applied to the images after the transformation into the polar coordinates domain. Then, the morphological closing operation was performed to obtain more regular borders. The extracted contour was converted into the Cartesian coordinate domain and overlapped with the IVUS images to present the final segmentation result. Segmentation methods based on the Otsu's threshold algorithm and morphological operations for the identification of the lumen region in IVUS image were also proposed by Sofian et al. [18] and Moraes and Furuie [19].

Most of the above mentioned studies still required manual interventions, re-training of the learning-based model and the transformation of the image into the polar coordinates domain. In addition, the use of threshold values as proposed by Taki et al. [16] can fail to identify the initial contour of the lumen in different datasets due to the usual variability of the grayscale intensities. Hence, the development of a more robust, efficient, automated and less complex solution was the goal of this study.

3 Materials and Methods

3.1 IVUS images used

This study was accomplished by using the IVUS images of coronary arteries selected for the IVUS Segmentation Challenge described in Balocco et al. [20] that were kindly provided by the authors. The images were acquired using a Si5 imaging system (Volcano Corporation) equipped with an Eagle Eye catheter operating at a frequency of 20 MHz [20]. A total of 326 images with ground truths provided were selected for validating the proposed method. The manual delineations of the contours corresponding to the lumen and media-adventitia regions were performed by two experts, and one of them repeated the manual delineations about one week after the first delineations [20]. The images have a resolution of 384x384 pixels and the pixel size is 0.026 mm x 0.026 mm. More details about the IVUS images are available in Balocco et al. [20].
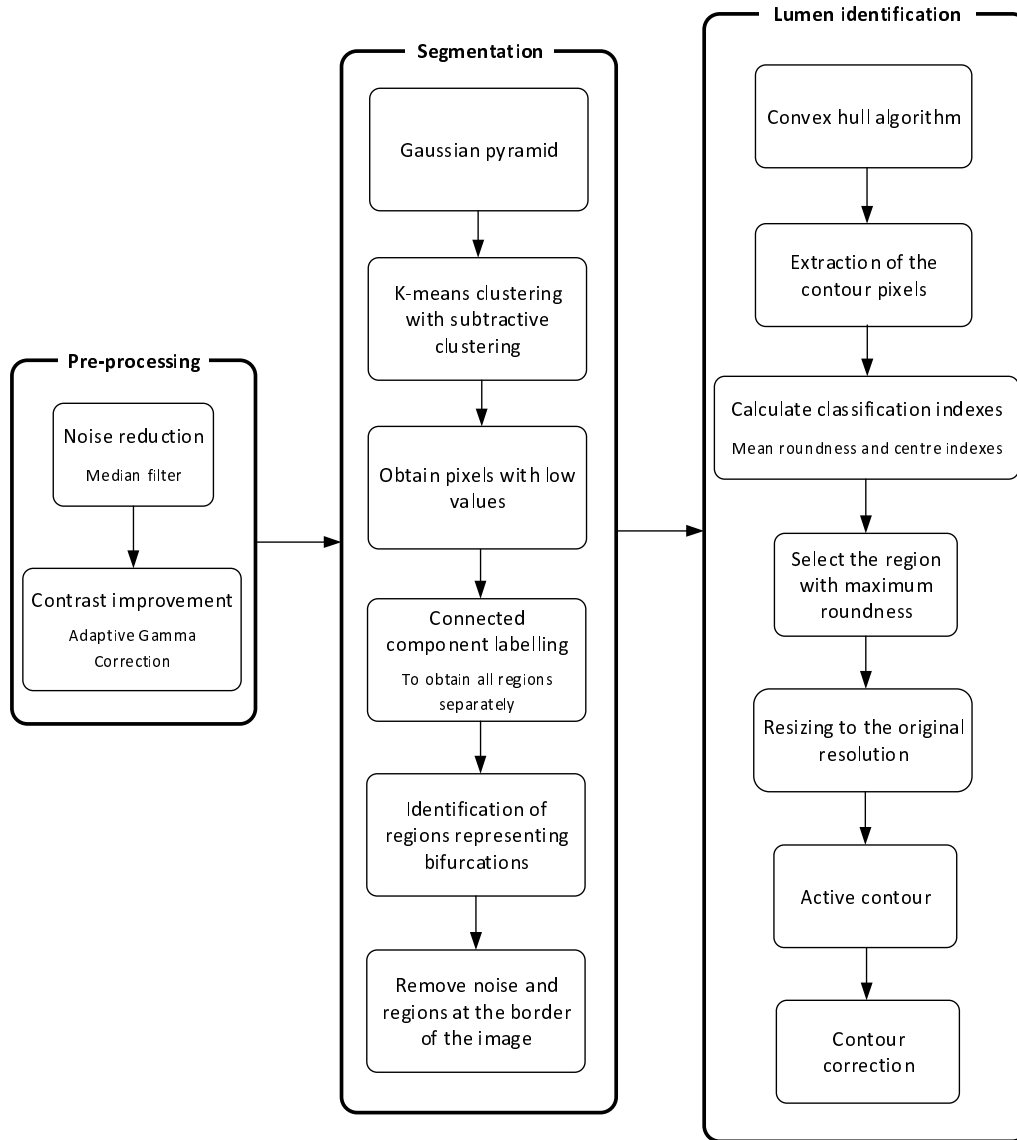
Figure 1: Diagram of the proposed method.

3.2 Proposed method

The proposed lumen segmentation method is made up of three main stages: pre-processing, segmentation and lumen identification. The diagram of the proposed method is shown in Figure 1.

The pre-processing stage is necessary to minimize noise and adjust the contrast of the input image. Then, the enhanced image is submitted to the segmentation stage in order to separate the regions with low pixel values, which include the background and the lumen. Relatively to the initial version [7], the method has three new steps in this stage: the Gaussian pyramid, which is adopted to reduce the resolution of the input image; the

elimination of regions at the border of the image; and the identification and removal of side branches at the bifurcation regions. Additionally, connected component labelling is employed here to separate all regions of the binary image corresponding to the low intensity values instead of using the region growing algorithm proposed in the initial version. The lumen identification stage uses two classification indexes to identify the region corresponding to the lumen of the artery under analysis, which is then inputted to an active contour algorithm for further refinement of the boundary. A post-processing step is now included in the method in order to smooth the contour resultant from the active contour algorithm, which leads to better segmentation results.

3.2.1 Pre-processing

The first step of the pre-processing stage is the use of a median filter with a mask of 5x5 to minimize the noise in the original image. The median filter was chosen due to its ability to remove noise without compromising the boundaries of the regions of interest.

The contrast enhancement step improves the brightness of the dark regions of the input image. The gamma correction-based method proposed by Huang et al. [21] was employed to avoid the overestimation of regions with low-level intensities. The method relies on the probability density function (PDF) and the cumulative density function (CDF) of the intensity values as:

$$T(l) = l_{max} \times (l/l_{max})^{1-cdf_w(l)},\qquad(1)$$

where $cdf_w(l)$ is the weighting CDF of the intensity value l and l_{max} is the highest possible intensity value. The weighting PDF (pdf_w) and weighting CDF (cdf_w) are defined as:

$$cdf_w(l) = \sum_{l=0}^{l_{max}} \frac{pdf_w(l)}{\sum pdf_w},\qquad(2)$$

and

$$pdf_w(l) = pdf_{max} \times \left(\frac{pdf(l) - pdf_{min}}{pdf_{max} - pdf_{min}} \right)^{\alpha},\qquad(3)$$

where pdf_{min} is the minimum probability of the PDF, pdf_{max} is the maximum probability of the PDF, $\sum pdf_w = \sum_{l=0}^{l_{max}} pdf_w(l)$ and α is a parameter that controls the amount of contrast enhancement. The value of the α parameter is determined by partitioning the PDF of the grayscale intensities as proposed in our previous work [7]:

$$\alpha = \sum_{i=1}^{t} PDF_{min_i} - \sum_{j=t+1}^{N} PDF_{max_j},\qquad(4)$$

where PDF_{min} and PDF_{max} represent the probabilities of the low and high intensities of the input image, respectively, t is the value obtained by the Otsu's threshold algorithm and N is the highest possible intensity value. Here, if the value of α is less than 0 (zero), the contrast correction is not necessary since there are more pixels with high intensities.

3.2.2 Segmentation

The K-means clustering algorithm is a well-known method to separate regions with similar characteristics (of intensity, for instance) in images. Finding the correct cluster centroids to be used in the K-means algorithm is a challenging task because different images have different cluster centroids. Subtractive clustering [22, 23] has been proposed as an alternative approach to find the adequate number of cluster centroids based on the potential of each pixel in the neighbourhood. The advantage of the subtractive clustering algorithm is that the cluster centroids do not change in different runs. This is due to the fact that the potential function relies on the pixel values only (or on another feature calculated from the pixels of the input image).

Although subtractive clustering has been widely used in image segmentation and classification problems, the computational complexity of $O(d^2, N^2)$, with N representing the number of data points and d the dimensional number, has limited its application to large-scale problems [24]. Hence, a reduction in the number of data points, i.e. pixels, is necessary to reduce the computational time of the subtractive clustering algorithm. Here, the Gaussian pyramid is applied to the input IVUS image in order to reduce its resolution and consequently, the number of pixels to be used in the subtractive clustering algorithm.

The Gaussian pyramid is an image processing technique used to reduce the resolution of images in repeated steps [25]. Pattern recognition, texture analysis and image compression are examples for the use of the Gaussian pyramid. The pyramid is a sequence of copies of the original image generated by recursively smoothing the image with a low-pass filter and reducing its resolution by half. The following equation represents the basis of the Gaussian pyramid:

$$g_l(i,j) = \sum_{m=-2}^{2} \sum_{n=-2}^{2} w(m,n)g_{l-1}(2i+m, 2j+n), \tag{5}$$

where l is a level of the pyramid, i and j are the pixel coordinates at the lth level, g_{l-1} is the smoothed image at the level $l-1$ and $w(m,n)$ is a 5x5 low-pass filter applied to the neighbourhood of the pixel (i,j). The original image is represented by g_0, i.e. the image at the level $l=0$. The image at the level $l=1$ is generated by smoothing g_0 with $w(m,n)$ followed by downsampling the resulting image by a factor of two. The image at the level

$l = 2$ is obtained by applying the same procedure on the image g_1, i.e. the image at the level $l = 1$. The process is repeated until the desired number of levels is reached. The final result is a pyramid in which the base is the original image and the top represents the smoothed image with the smallest resolution. The smoothing of the image is necessary to avoid the aliasing effect generated when the resolution is reduced. An example of the application of the Gaussian pyramid in order to reduce the resolution of an IVUS image and accelerate the use of the subtractive clustering algorithm is shown in Figure 2.
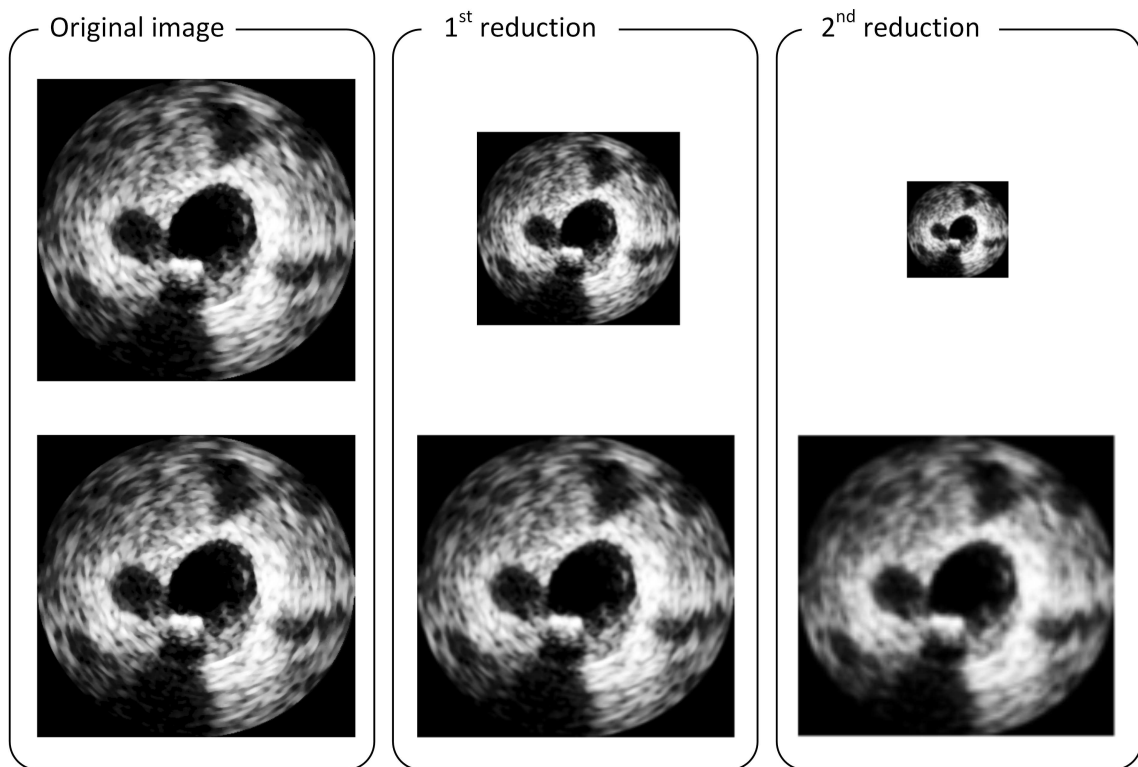

Figure 2: Example of the Gaussian pyramid applied two times on a pre-processed IVUS image (the second row shows the Gaussian pyramid results expanded to the size of the original image).

Although the most common use of the Gaussian pyramid is compressing an input image and multiscale processing at lower resolutions, here the goal is to generate a pyramid of lower resolution images for the input image in order to select the one with the smallest resolution, i.e. the image at the top of the pyramid, where the subtractive clustering algorithm is then applied with lower computational time than if it was applied on the original image. Here, the number of reductions performed by the Gaussian pyramid is defined as equal to 2, leading to a pyramid with three levels in which the base is represented by the input IVUS image with 384x384 pixels of resolution and the top represents the

IVUS image with the smallest resolution of 96x96 pixels that is inputted to the subtractive clustering algorithm. Thereafter, the subsequent steps of the proposed method are performed on the image with the smallest resolution in order to obtain a binary image with the identified lumen, which is then restored to the input image resolution without performing any processing on the higher resolution images of the pyramid. The choice of the Gaussian pyramid was due to its simple implementation and ability to reduce the input image resolution without losing important information about the structure of interest.

After the downsampling of the input image, the K-means algorithm with subtractive clustering suggested in Dhanachandra et al. [26] is employed to separate the regions of the image according to the grayscale intensity. The centroid of each cluster is found by means of the subtractive clustering algorithm. After the centroids have been found, the K-means clustering is applied to separate the regions of the image. As proposed in our previous study, four clusters are used here to correctly identify the region corresponding to the lumen. Since the lumen and background regions have low intensities in IVUS images, the same approach employed is used to find the cluster having the regions with low-intensity pixels for identifying the one representing the correct lumen. A binary image with such regions is returned, in which the identified regions are represented by white pixels and the background by black pixels. The image is then submitted to the connected component labelling algorithm in order to obtain all regions of the image separately. Here, the connected component labelling is performed on the image corresponding to the cluster with low-intensity values to obtain a set with all regions of interest. Firstly, the algorithm performs a pixel-by-pixel scan of the binary image from the top to bottom and left to right in order to identify a white pixel and assign a label to it that relies on the evaluation of the adjacent pixels that share the same intensity. If none of the neighbour pixels have until then been labelled, a new label is assigned to the pixel under analysis. Otherwise, the pixel under analysis receives a label assigned to a neighbour pixel. The process continues until all pixels of the binary image have been labelled. Then, pixels having the same label are merged to form a single region. Thereafter, each region is used as the input to the lumen identification stage in order to find the one that represents the lumen.

3.2.3 Lumen identification

In our previous work, a set of measures was used to evaluate each region of interest obtained by the region growing algorithm in order to identify the one corresponding to the lumen in the MR images of carotid arteries. Hence, the mean roundness (MR), irregularity (Ir) and centre (d) indexes are included in the following circularity function, which is used to evaluate each region of the binary image:

$$E = MR + \frac{1}{Ir} + \frac{1}{d}. \tag{6}$$

The *MR* was proposed to determine the circularity of objects in images [27]. It consists of calculating the ratio between the average radius and the distance between the radius of each border pixel of the object and the average radius. The mean roundness is calculated according to:

$$MR = \frac{1}{N} \sum_{i=1}^{N} \frac{\bar{r}_b}{|r_i - \bar{r}_b| + \bar{r}_b}, \tag{7}$$

where N is the number of pixels of the contour of the object under analysis, $\bar{r}_b$ is the average radius of the object, and r_i is the radius at the contour pixel i. The larger the mean roundness (*MR*) index is, the more circular the object under analysis is.

The following irregularity index is used to avoid regions with irregular contours:

$$Ir = P * \left(\frac{1}{SD} - \frac{1}{GD} \right), \tag{8}$$

where P is the number of pixels of the contour, SD is the shortest diameter and GD is the greatest diameter [28].

A centre index is also used to identify the correct location of the lumen. As described in our previous work, the lumen is a circular-shaped region located close to the centre of the input MR image. Hence, the distances between the centre of the image and the centre of each region are calculated and used to penalize those far from the centre of the MR image. The same concept can also be applied here due to the fact that the lumen is also located close to the centre of an IVUS image.

The segmentation of the lumen close to bifurcations represents a challenge due to the extension of the low-intensity values from the lumen region to the border of the input image, which causes the establishment of a region representing this extension when the cluster corresponding to the low-intensity values is built. Hence, in the initial version of the proposed method, these regions were not assessed in the subsequent processing steps, since the regions at the border of the image are discarded before the identification of the lumen. Therefore, a new approach was developed to identify regions representing bifurcations in order to distinguish these regions from the ones at the border of the binary images corresponding to low-intensity values. The proposed approach is based on the generation of circles surrounding the regions of possible lumens, like the approach proposed in de Macedo et al. [29]. However, here, the distances from the centres of the input image to the pixels of the bifurcation regions at the borders are used to define the radius of the circles, instead of the distance transform suggested in de Macedo et al. [29].

Hence, the regions obtained by the connected component labelling algorithm are evaluated to identify the one that is in the centre of the input image. Then, the number of pixels of this region that are at the border are computed in order to verify if the region represents a bifurcation. Once the region is identified as a bifurcation, the distances between the centre of the image and each pixel of the region at the border are calculated. The radius of the circle is then calculated according to:

$$r = min(dist(Cp, Bp)) - min(dist(Cp, Rp)), \qquad (9)$$

where Cp is the pixel at the centre of the IVUS image, Bp is the set of pixels of the bifurcation region that are at the border of the image and Rp is the set of all pixels of the contour of the bifurcation. The circle generated is centred at the centre of the IVUS image and the region outside this circle is removed from the binary image corresponding to the low-intensity values. An example of the proposed approach applied to an IVUS image with a bifurcation region is illustrated in Figure 3.
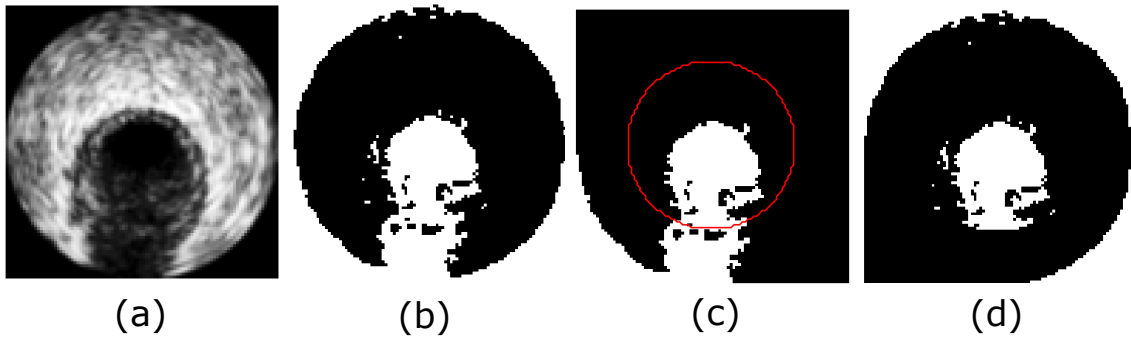

(a)　　　　(b)　　　　(c)　　　　(d)

Figure 3: Example of the identification and removal of the side branch of a bifurcation region: a) Image pre-processed and reduced by the Gaussian pyramid; b) Binary image corresponding to the cluster with low-intensity pixels; c) Binary image with the identified bifurcation region (the circle generated by the proposed approach is shown in red); d) Binary image without the part of the bifurcation region on the border.

As depicted in Figure 3c, the bifurcation region can be divided into two parts, i.e. one inside the circle and the other outside. Since the part inside the circle contains the regions with the possible lumen, the regions outside the circle are removed from the binary image corresponding to the low-intensity values, leading to a new binary image that is then submitted to the subsequent steps of the lumen identification stage.

Concavities, irregularities and holes inside the regions of the binary image corresponding to the cluster with low-intensity values may be present due to high intensity values inside the lumen under analysis. Since the high intensity values are identified as belonging to another cluster when the K-means algorithm is applied, such artefacts are generated

in the regions of the binary image. In order to attenuate the effect of these artefacts, the convex hull algorithm is used here. The use of the convex hull algorithm instead of morphological operations is to avoid underestimation and cutting of parts of the region of interest when concavities are presented.

The convex hull of a set of points *S* is the smallest convex polygon containing all the points of *S* [30]. The definition of convex hull relies on the concept of a convex set, which is a region defined in a way that for every pair of points $[a,b]$ belonging to a region, the line joining such points must be totally inside the region. Here, for each region present in the binary image obtained by the connected component labelling algorithm a correspondent convex hull is generated i.e., the set of pixels representing the convex polygon that includes all the white pixels of the region, before calculating the classification indexes used to find the lumen region. An example of the application of the convex hull algorithm is shown in Figure 4.
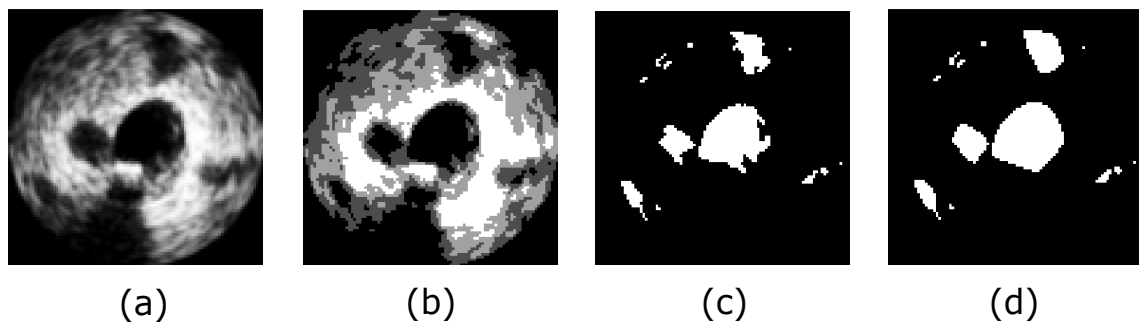

<center>(a) (b) (c) (d)</center>

Figure 4: Example of the application of the convex hull algorithm: a) Image pre-processed and reduced by the Gaussian pyramid; b) Result of the K-means with the subtractive clustering algorithm; c) Binary image corresponding to the cluster with low-intensity pixels (regions at the border corresponding to the background were previously removed); d) Result of the convex hull algorithm applied to each region (white pixels) of the binary image.

As depicted in Figure 4, the regions become more regular after the application of the convex hull algorithm. Hence, the irregularity index is now redundant and the function defined by Equation 6 is therefore, simplified to:

$$E = MR + \frac{1}{d}. \tag{10}$$

In the initial version of the proposed method, the regions with less than 1.5% of the total number of pixels of the input image were discarded from the lumen identification procedure, since these regions usually represent small regions associated to noise. However, this empirically defined discarding criterion is not always robust. Hence, a new approach based on the morphological opening operation was developed in order to identify

and disregard the small regions associated to noise. The morphological opening operation is the erosion followed by the dilation of an image *I* by a structuring element *SE*. When applied to binary images, the opening operation can smooth the borders of the regions represented by white pixels, split regions connected by thin bridges and remove small regions that represent noisy artefacts. The choice of the shape and size of the structuring element is usually based on the shape of the regions of interest, and it plays an important role in effectively achieving the desired results. Since the lumen is a circular-shaped region in IVUS images, a disk-shaped structuring element is used to perform the opening operation. In addition, the size of the structuring element is adaptively defined according to the approach proposed by Gao et al. [31] and formulated as:

$$S_o = \frac{1}{2}\sqrt{\frac{A_r}{\pi}}, \tag{11}$$

where A_r is the area of the region under analysis. The opening operation with the adaptive structuring element is applied to each region obtained by the connected component labelling algorithm. Hence, a region is not considered in the lumen identification step if its size is equal or less than the size of the structuring element, and the region is removed by the opening operation. Here, the morphological opening operation is only employed to identify small regions corresponding to noise. Therefore, the smoothing of the regions is not performed by the opening operation since the convex hull is previously applied to correct the shape of the regions under analysis. A region identified as noise and removed from the binary image by the opening operation is not selected for calculating the circularity index defined in Equation 10.

Although the terms in Equation 10 are defined in different contexts, the objective of using the centre index in the proposed circularity index is to penalize regions with larger values of roundness that are distant from the centre of the input image. The value of the circularity index proposed in Equation 10 is calculated for each region resultant after the opening operation and the one with the maximum value is considered to be the lumen of the artery under study. This region is resized to the original resolution of the input IVUS image and then submitted to the Chan-Vese active contour algorithm [32] for further refinement of the contour. The binary image representing the lumen region may not fit the true boundary of the lumen in the IVUS image. Hence, the contour of such a region is used as the input of the Chan-Vese active contour model, which is applied to the original IVUS image in order to fit the contour to the true boundary. This refinement step plays an important role in avoiding under- or over-estimating the contour, leading the contour closer to the true boundary of the lumen under analysis and, consequently, to better results. Since the gradient of the image is not used in the Chan-Vese model, the

method is recommended for the segmentation of medical images which commonly have weak boundaries of the structures of interest [33–36].

The post-processing step consists in smoothing the lumen contour by using the morphological opening and dilation operations. The morphological opening operation was employed to smooth the boundaries of the lumen region generated from the result of the Chan-Vese active contour. A binary image is generated from the lumen contour such that the region inside the contour is represented by white pixels. Then, the region is smoothed by first applying the opening operation. Finally, the morphological dilation operation is performed on the resulting region in order to restore its size as close as possible to the size of the original region. The sizes of the structuring elements are defined according to the size of the region under analysis and formulated as:

$$S_o = \frac{1}{2}\sqrt{\frac{A_l}{\pi}}, S_d = \frac{1}{N}\sum_{i=1}^{N}\sqrt{(Co_i - Cr_k)^2}, \tag{12}$$

where S_o and S_d are the sizes of the structuring element used in the morphological opening and dilation operations, respectively, A_l is the area of the lumen region, C_o is the contour of the region resulting from the opening operation, C_r is contour of the region obtained from the lumen contour and N is the number of pixels of the contour C_o. Co_i is the *ith* pixel of *Co*, and Cr_k is the *kth* pixel of *Cr* closest to Co_i. The size S_o was proposed by Gao et al. [31], whereas S_d is defined as the average distance between the contours C_o and C_r.

The steps performed in the automatic segmentation of the lumen in one IVUS image are depicted in Figure 5.

3.3   Quantitative analysis

The contours obtained by the proposed method and the related manual delineations were compared based on four measures: Jaccard measure (*JM*), Dice coefficient (*DC*), Hausdorff distance (*HD*) and percentage of area difference (*PAD*).

The Jaccard measure is calculated by means of the ratio between the size of the intersection and the size of the union of the regions corresponding to the automatic (S_{auto}) and manual (S_{manual}) segmentations:

$$JM = \frac{|S_{auto} \cap S_{manual}|}{|S_{auto} \cup S_{manual}|}. \tag{13}$$

The Jaccard measure is important to assess the overlap of the region identified by the proposed method with respect to the corresponding manual delineation. Similarly,
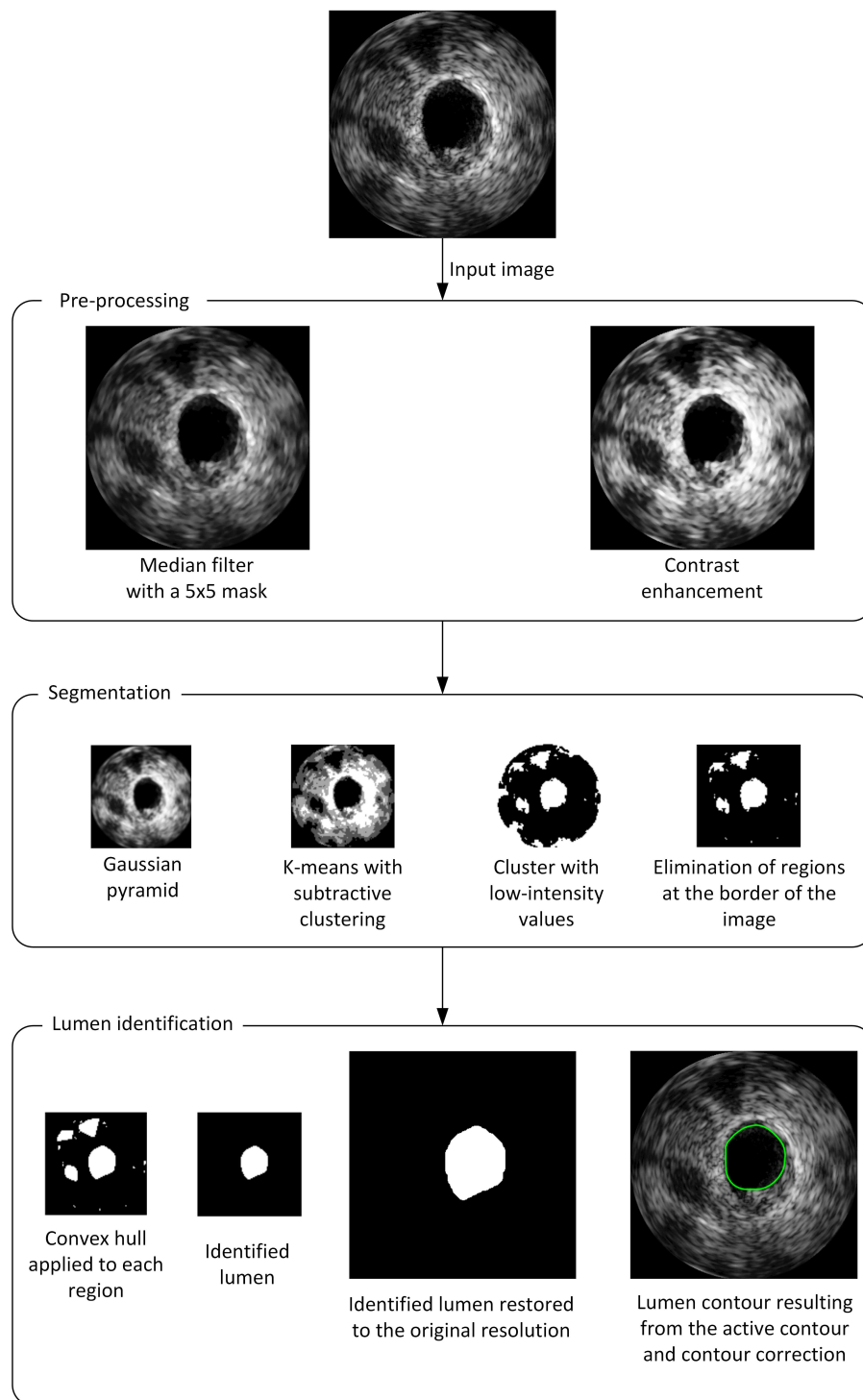
Figure 5: Example of the output images resulting from each step of the automatic segmentation of the lumen in one IVUS image (the green contour in the image on the right of the lumen identification step represents the final segmentation result). (The identification of the bifurcation region step is not illustrated in this example since there was no side branch in the IVUS image used.)

the Dice coefficient is used to calculate the overlap between the automatic and manual segmentations:

$$DC = \frac{2 * |S_{auto} \cap S_{manual}|}{|S_{auto}| + |S_{manual}|}. \tag{14}$$

The Hausdorff distance is important to assess the closeness of two contours, and it is defined here as the maximum between the greatest distances between the pixels of the automatic (C_a) and manual (C_m) contours:

$$HD(C_a, C_m) = max\{\max_{a \in Ca} \min_{b \in Cm} d(a,b), \max_{b \in Cm} \min_{a \in Ca} d(a,b)\}, \tag{15}$$

where a and b are the pixels of contours C_a and C_m, respectively, and $d(a,b)$ is the Euclidean distance between these pixels.

The percentage of area difference (*PAD*) represents the difference between the areas of the contour obtained from the automatic segmentation (A_{auto}) and the corresponding manual delineation (A_{manual}) with respect to the area of the manual delineation:

$$PAD = \frac{|A_{auto} - A_{manual}|}{A_{manual}}. \tag{16}$$

The lumen area and the average lumen diameter of the automatic and manual segmentations were also calculated to compare the segmentation results by means of the regression analysis and Bland-Altman analysis. The lumen area is the area inside the contour of the lumen and the average lumen diameter (*ALD*) is defined as:

$$ALD = \frac{1}{N} \sum_{i=1}^{N} 2 * r_i, \tag{17}$$

where N is the number of pixels of the contour of the lumen and r_i is the radius of the *ith* pixel.

4   Results

The proposed method was implemented in MATLAB software (The Mathworks Inc., Natick, USA) and executed in a desktop computer equipped with an Intel i7-4700 HQ processor (2.4 GHz) and 16 GB of RAM memory. A comparison between the contours obtained from the proposed method and those generated by manual delineations was performed in order to evaluate the accuracy of the segmentation results. In addition, the results of the proposed method were also compared with the ones reported in related studies found in the literature. The details about the datasets and the validation measures of the studies

used here to compare the segmentation results of the new automatic segmentation method are shown in Table 1.

Table 1: Details about the datasets and the validation measures of the studies used to compare the segmentation results of the proposed method.

Authors	Catheter's frequency	Number of frames	Validation measure(s)
Lo Vercio et al. [8]	20 MHz	149	*JM* and *PAD*
Su et al. [9]	20 MHz	461	*JM* and *HD*
Sofian et al. [18]	20 MHz	30	*JM*, *HD*, *PAD* and *DC*
Destrempes et al. [11]	40 MHz	3207	*HD*
Mendizabal-Ruiz et al. [12]	20 MHz and 40 MHz	585	*JM*, *HD* and *DC*
Cardinal et al. [15]	20 MHz	1593	*HD*
Vard et al. [13]	30 MHz	40	*HD*
Taki et al. [16]	30 MHz	60	*HD*

*JM = Jaccard measure; HD = Hausdorff distance; PAD = percentage of area difference; DC = Dice coefficient; MHz = Megahertz

Since there are not any common validation measures in the studies indicated in Table 1, all measures described in Section 3.3 were calculated and the ones used in each of these studies were selected to compare the performance of the proposed automatic lumen segmentation.

The proposed automatic lumen segmentation was also compared with the results obtained from the eight participant groups of the IVUS Segmentation Challenge held in the 2011 Computing and Visualization for (Intra)Vascular Imaging (CVII) workshop of the Medical Image Computing & Computer Assisted Intervention (MICCAI) conference.

The results of the proposed method with the contrast enhancement activated and deactivated were also taken into account in order to evaluate the improvement obtained by adjusting the contrast of the input image.

4.1 Initialization of the parameters

The following parameters were defined to perform the automatic segmentation: the size of the mask of the median filter was set to 5x5, which proved to be the most suitable template for removing noise without affecting the edges of the lumen; when the contrast enhancement was necessary, the value of the α parameter was defined as the difference between the probability of the low and high intensities of the image, as described by Equation 4; the number of reductions performed by the Gaussian pyramid was automatically defined as equal to 2, leading to images with a resolution of 96x96 to be processed by the K-means with subtractive clustering; the radius r_a and r_b of the subtractive clustering

algorithm were set to 1.2 and 1.8, respectively; and the number of iterations of the Chan-Vese active contour algorithm was set to 500, which was higher when compared to our previous study using MR images (200 iterations) due to the higher resolution of the IVUS images under analysis.

4.2 Performance of the proposed method

Examples of the segmentation results and corresponding manual delineations are shown in Figure 6.
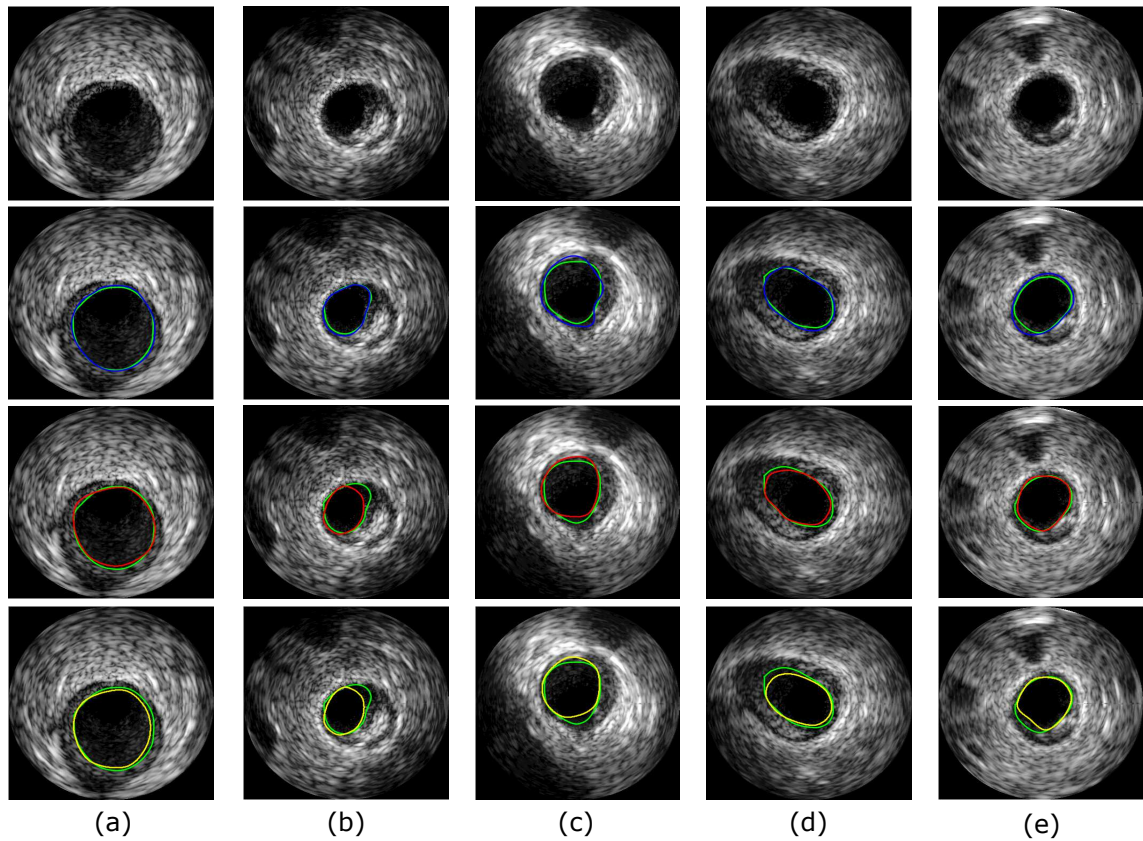

(a) (b) (c) (d) (e)

Figure 6: Examples of segmentation results obtained by the automatic segmentation method (a-e): The original IVUS images are shown in the first row, and the subsequent rows depict the segmentation results and the corresponding manual delineations, respectively. (The contours in green are the ones generated by the proposed method, whereas the blue, red and yellow contours represent the manual delineations.)

In Figure 6, the green contours are the results obtained by the proposed method, whereas the blue, red and yellow contours represent the related manual delineations. The lumen was correctly identified in all images and is very close to the corresponding manual delineations. Due to the subjective analysis of each expert, the automatically segmented

contour is very close to corresponding manual delineation in some cases, while small differences were produced in other cases as shown in Figure 6b.

The effect of the post-processing step on the lumen contour resulting from the Chan-Vese active contour is shown in Figure 7.

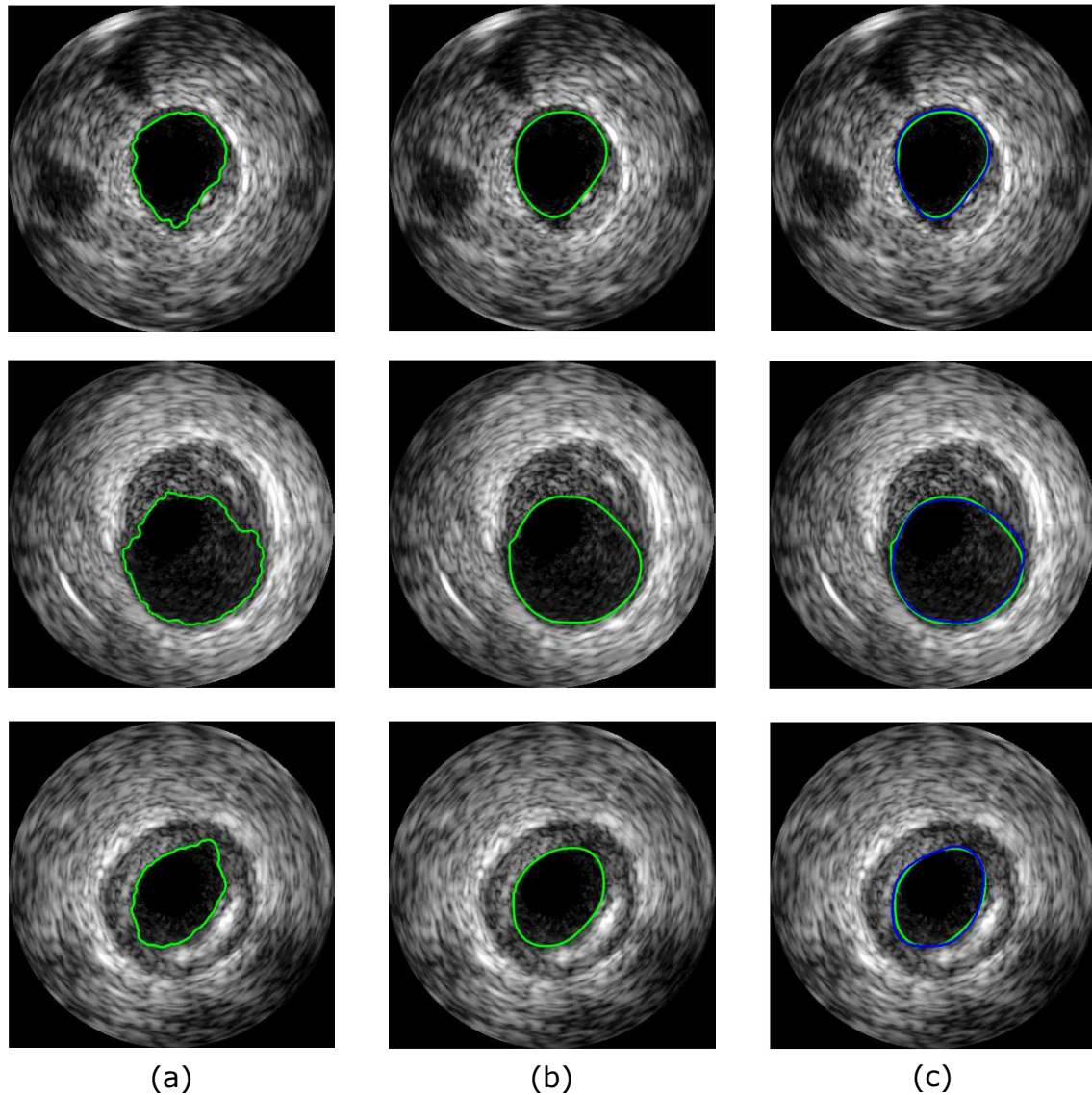| (a) | (b) | (c) |

Figure 7: Illustration of the post-processing step on the lumen contour: a) The contour resulting from the Chan-Vese active contour; b) The result of the smoothing of the contour; c) The smoothed contour (in green) along with a corresponding manual delineation (in blue).

As shown in Figure 7a, the automatically segmented lumen contour can be somewhat irregular and leak from the true boundary as depicted in the image of the third row. However, the lumen contours became more regular and smooth after the final post-processing step, which leads to results very similar to the manual delineations (Figure 7c).

The effectiveness of the proposed approach to identify and eliminate side branches of bifurcation regions is apparent in Figure 8.

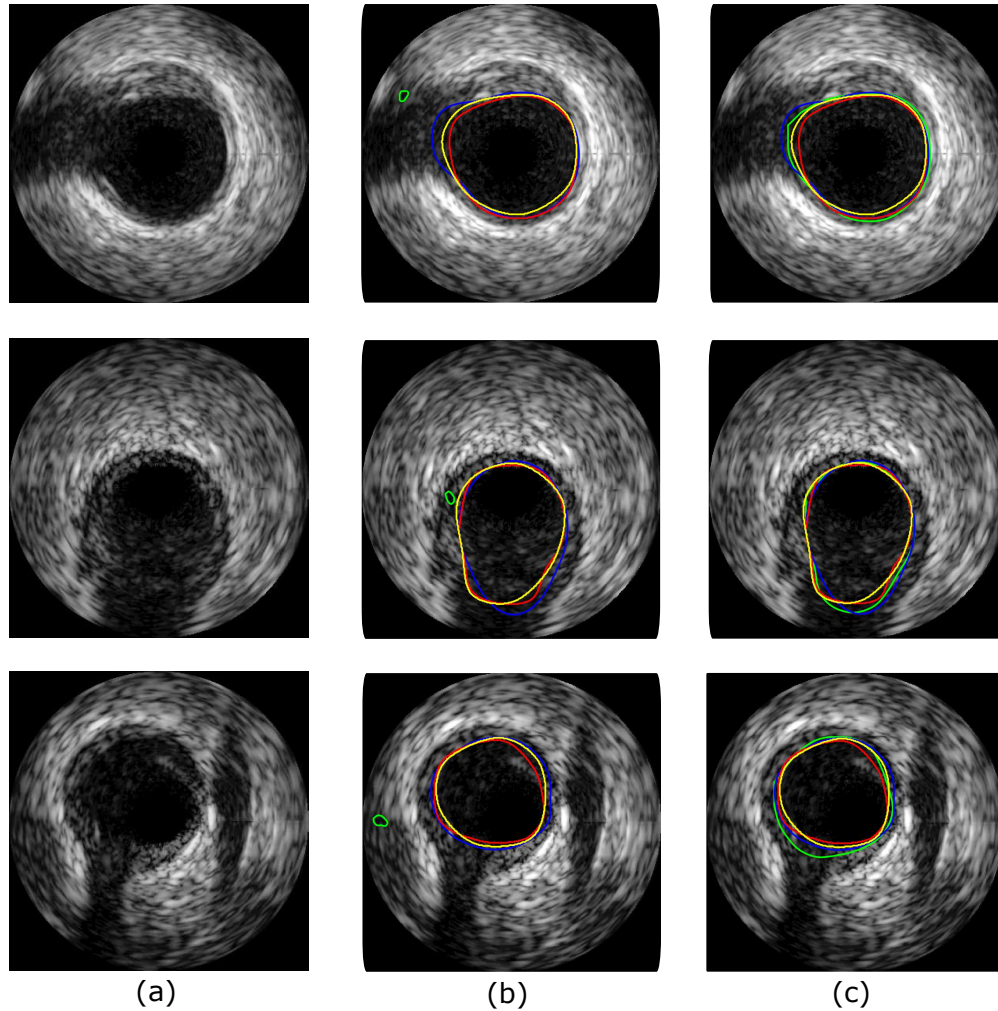(a)   (b)   (c)

Figure 8: Examples of segmentation results after applying the proposed approach to identify bifurcation regions: a) The original IVUS images; b) The result of the automatic lumen segmentation (in green) along with the corresponding manual delineations (in blue, red and yellow) before the identification of the bifurcation region; c) The result of the automatic lumen segmentation (in green) along with the corresponding manual delineations (in blue, red and yellow) after the identification of the bifurcation region.

As shown in Figure 8b, the segmentation errors resulting from the automatic lumen segmentation are due to the removal of the whole bifurcation region from the binary image representing the low-intensity values before applying the circularity index in Equation 10, leading to the identification of another region as belonging to the potential lumen. However, as shown in Figure 8c, the lumen was successfully segmented after applying the proposed approach to identify and split the bifurcation region.

From the 326 IVUS images used in the experiments, the proposed method successfully segmented 324 images. The average values of the Jaccard measure, Hausdorff distance, percentage of area difference and Dice coefficient of the automatically segmented lumen in comparison with the three manual delineations of the correctly segmented images are indicated in Tables 2 and 3. Additionally, the average values of the same four measures obtained from the intra- and inter-observer analysis are indicated in Table 4.

Table 2: Average values of the Jaccard measure (JM), Hausdorff distance (HD), Percentage of area difference (PAD) and Dice coefficient (DC) obtained by the proposed method without the application of the contrast enhancement.

	Manual delineation 1	Manual delineation 2	Manual delineation 3	Average
JM	0.86±0.07	0.88±0.07	0.88±0.07	**0.87±0.07**
HD	0.30±0.17	0.29±0.18	0.30±0.19	**0.30±0.18**
PAD	0.12±0.08	0.08±0.07	0.08±0.08	**0.09±0.08**
DC	0.92±0.05	0.93±0.04	0.93±0.04	**0.93±0.04**

*The values of the Hausdorff distance (HD) are presented in millimeters; Manual delineation 1 represents the tracing done by the expert 1, whereas the manual delineations 2 and 3 are the first and second tracings of the expert 2, respectively.

Table 3: Average values of the Jaccard measure (JM), Hausdorff distance (HD), Percentage of area difference (PAD) and Dice coefficient (DC) obtained by the proposed method with the application of the contrast enhancement.

	Manual delineation 1	Manual delineation 2	Manual delineation 3	Average
JM	0.87±0.06	0.88±0.06	0.88±0.06	**0.88±0.06**
HD	0.29±0.15	0.29±0.17	0.29±0.18	**0.29±0.17**
PAD	0.11±0.07	0.08±0.07	0.08±0.08	**0.09±0.07**
DC	0.93±0.04	0.94±0.04	0.94±0.04	**0.94±0.04**

*The values of the Hausdorff distance (HD) are presented in millimeters; Manual delineation 1 represents the tracing done by the expert 1, whereas the manual delineations 2 and 3 are the first and second tracings of the expert 2, respectively.

As shown in Tables 2 and 3, the average values of the Jaccard measure, percentage of area difference and Dice coefficient for the manual delineations 2 and 3 are better than those obtained in comparison to the manual delineation 1. However, the results of the Hausdorff distance are similar to almost all the manual delineations, except in the case where the adjustment of the contrast of the images was not applied (Table 2), leading to a decrease of the Hausdorff distance for the manual delineation 2. As shown in Table 3, the average value of the Jaccard measure increased from 0.87 ± 0.07 to 0.88 ± 0.06 after the application of the contrast enhancement. Additionally, an increase of the average value of the Dice coefficient from 0.93 ± 0.04 to 0.94 ± 0.04 was also obtained after adjusting

Table 4: Average values of the Jaccard measure (*JM*), Hausdorff distance (*HD*), Percentage of area difference (*PAD*) and Dice coefficient (*DC*) obtained from the intra- and inter-observer analysis.

	Exp 1 vs Exp 2 (1st)	Exp 1 vs Exp 2 (2nd)	Exp 2 (1st) vs Exp 2 (2nd)	Average
JM	0.88 ± 0.05	0.87 ± 0.05	0.93 ± 0.05	**0.89 $\pm$ 0.05**
HD	0.28 ± 0.13	0.30 ± 0.13	0.17 ± 0.13	**0.25 $\pm$ 0.13**
PAD	0.11 ± 0.08	0.13 ± 0.08	0.04 ± 0.05	**0.09 $\pm$ 0.07**
DC	0.94 ± 0.03	0.93 ± 0.03	0.96 ± 0.03	**0.94 $\pm$ 0.03**

*Exp stands for Expert; 1st and 2nd indicate the first and second delineations of Expert 2, respectively; the values of the Hausdorff distance (*HD*) are expressed in millimeters.

the contrast of the images. The Hausdorff distance also decreased from 0.30 ± 0.18 mm to 0.29 ± 0.17 mm after adjusting the contrast of the images. In terms of the intra- and inter-observer variability, the results of Table 4 show that the proposed method is also in accordance with the average values computed from the comparison between Expert 1 and Expert 2. The average values of the Jaccard measure, Hausdorff distance, percentage of area difference and Dice coefficient between both experts were 0.89 ± 0.05, 0.25 ± 0.13 mm, 0.09 ± 0.07 and 0.94 ± 0.03, respectively, which are very similar to the results obtained by our method (see Tables 2 and 3).

The mean values of the lumen area and average lumen diameter calculated for each manual delineation and for the corresponding automatically detected lumen are shown in Table 5.

Table 5: Mean values of the lumen area (*LA*) and average lumen diameter (*ALD*) for the manual delineations and the automatically segmented lumen after adjusting the contrast of the images.

	Manual delin. 1	Manual delin. 2	Manual delin. 3	Proposed method
Mean *LA* (mm^2)	8.75 ± 3.73	8.03 ± 3.56	7.94 ± 3.55	7.93 ± 3.63
Mean *ALD* (mm)	3.11 ± 0.63	3.10 ± 0.68	3.08 ± 0.68	3.07 ± 0.71

*Manual delin. 1 represents the delineation done by Expert 1, whereas manual delin. 2 and manual delin. 3 are the first and second delineations of Expert 2, respectively.

The mean lumen area obtained from the proposed method was 7.93 ± 3.63 mm^2, which is close to the one obtained from the manual delineation 3 (7.94 ± 3.55 mm^2). Additionally, the mean value of the average lumen diameter of the automatically detected lumen was also close to the one obtained from the manual delineation 3 (3.07 ± 0.71 mm and 3.08 ± 0.68 mm, respectively). Although the results of the proposed method were closer to the manual delineation 3, no significant differences were found between

the areas and average diameters of the automatically detected and manually delineated lumen contours.

A comparison between the proposed automatic lumen segmentation and the methods reported in the literature was also carried out, which led to the results shown in Tables 6 and 7.

Table 6: Jaccard measure (*JM*), Hausdorff distance (*HD*) and percentage of area difference (*PAD*) obtained from the general performance of the IVUS Segmentation Challenge for the test images acquired at 20 MHz [20].

	P1	**P2**	**P3**	**P4**	**P5**	**P7**	**P8**
JM	0.81±0.12	0.83±0.08	**0.88±0.05**	0.77±0.09	0.79±0.08	0.84±0.08	0.81±0.09
HD	0.47±0.39	0.51±0.25	**0.34±0.14**	0.47±0.22	0.46±0.30	0.38±0.26	0.42±0.22
PAD	0.14±0.13	0.14±0.12	**0.06±0.05**	0.15±0.12	0.16±0.09	0.11±0.12	0.11±0.11

*P stands for the participant group; Participant group 6 (P6) did not perform the segmentation of the lumen contour and it explains the absence of the average values of this participant group; the values of the Hausdorff (*HD*) distance are presented in millimeters.

Table 7: Average measures obtained from the proposed method and the related ones found in the literature.

Authors	*JM*	*HD*	*PAD*	*DC*
Lo Vercio et al. [8]	0.8300±0.0500	-	0.1800±0.0600	-
Su et al. [9]	0.9182	0.2243	-	-
Sofian et al. [18]	0.8624±0.0193	0.5444±0.1290	0.0645±0.0509	0.9260±0.0111
Destrempes et al. [11]	-	0.3300±0.0700	-	-
Mendizabal-Ruiz et al. [12]§	0.8671±0.0341	0.1398±0.0384	-	0.9283±0.0201
Vard et al. [13]	-	0.3044±0.1853	-	-
Cardinal et al. [15]†	-	0.4300±0.3000	-	-
Taki et al. [16]	-	0.7081±0.2491	-	-
Proposed method	0.8800±0.0600	0.2900±0.1700	0.0900±0.0700	0.9400±0.0400

**JM* = Jaccard measure; *HD* = Hausdorff distance; *PAD* = Percentage of area difference; *DC* = Dice coefficient.
§ Average values of the comparison between the method and the manual delineations of two observers.
† Result from the pre-interventional group. The *HD* for the post-interventional and follow-up groups were 0.46 ± 0.26 and 0.40 ±0.21, respectively. (See the study of Cardinal et al. [15] for more details.)

Table 6 shows the average measures of the general performance calculated from each participant group of the IVUS Segmentation Challenge proposed at the MICCAI 2011 CVII workshop [20]. Table 6 demonstrates that the method proposed by Participant group 3 outperformed all the others presented at the challenge. The performance of our method is comparable to the one proposed by this group. Regarding the results obtained after

adjusting the contrast of the input images, the average value of the Jaccard measure obtained from the proposed automatic lumen segmentation was 0.88 ± 0.06 against 0.88 ± 0.05 presented by Participant group 3 at the IVUS Segmentation Challenge; the average Hausdorff distance of our method was 0.29 ± 0.17 mm against 0.34 ± 0.14 mm of this participant group; and the average percentage of area difference obtained from our method was 0.09 ± 0.07 against 0.06 ± 0.05 of the same group.

Table 7 shows the comparison between our automatic lumen segmentation approach and related methods proposed in the literature. The comparison shows that our method is in accordance with the ones proposed in the studies found, achieving results comparable or even better than the ones of those methods.

The computational cost of the most important procedures in the segmentation and identification stages of the proposed method when applied to each image of the dataset used in this study is shown in Table 8.

Table 8: Computational cost of the most important procedures of the proposed method when applied to each image (in seconds).

	K-means	Chan-Vese active contour	Smoothing of the contour	Total time
Average	1.5279	3.8694	0.3192	5.7165
Std	0.2322	1.1645	0.1452	1.5419

*Std = Standard deviation

The execution time of the Chan-Vese active contour is the highest among the other algorithms involved, representing about 68% of the total time. The K-means with subtractive clustering represents about 27% of the total time, whereas the smoothing of the contour takes only 6% of the whole segmentation and identification of the lumen.

Linear regression analysis for the lumen area and average lumen diameter showed a high correlation between the automatic segmentations and manual delineations, as shown in Figures 9 and 10.

For the lumen area, the correlation coefficients of the proposed method compared to the manual delineations 1, 2 and 3 were 0.985096, 0.975378 and 0.974440, respectively, before adjusting the contrast of the input images; while for the case when the contrast adjustment was applied, the correlation coefficients were 0.985729, 0.974483 and 0.974314, respectively. A slight improvement in the correlation coefficients between the automatic segmentations and the manual delineations of Expert 1 was obtained after the application of the contrast enhancement. Regarding the average lumen diameter, the correlation coefficients between the automatic segmentations and manual delineations 1, 2 and 3 were 0.977080, 0.972486 and 0.971514, respectively, before adjusting the contrast of the input images. When the contrast enhancement was applied, the correlation coefficients were
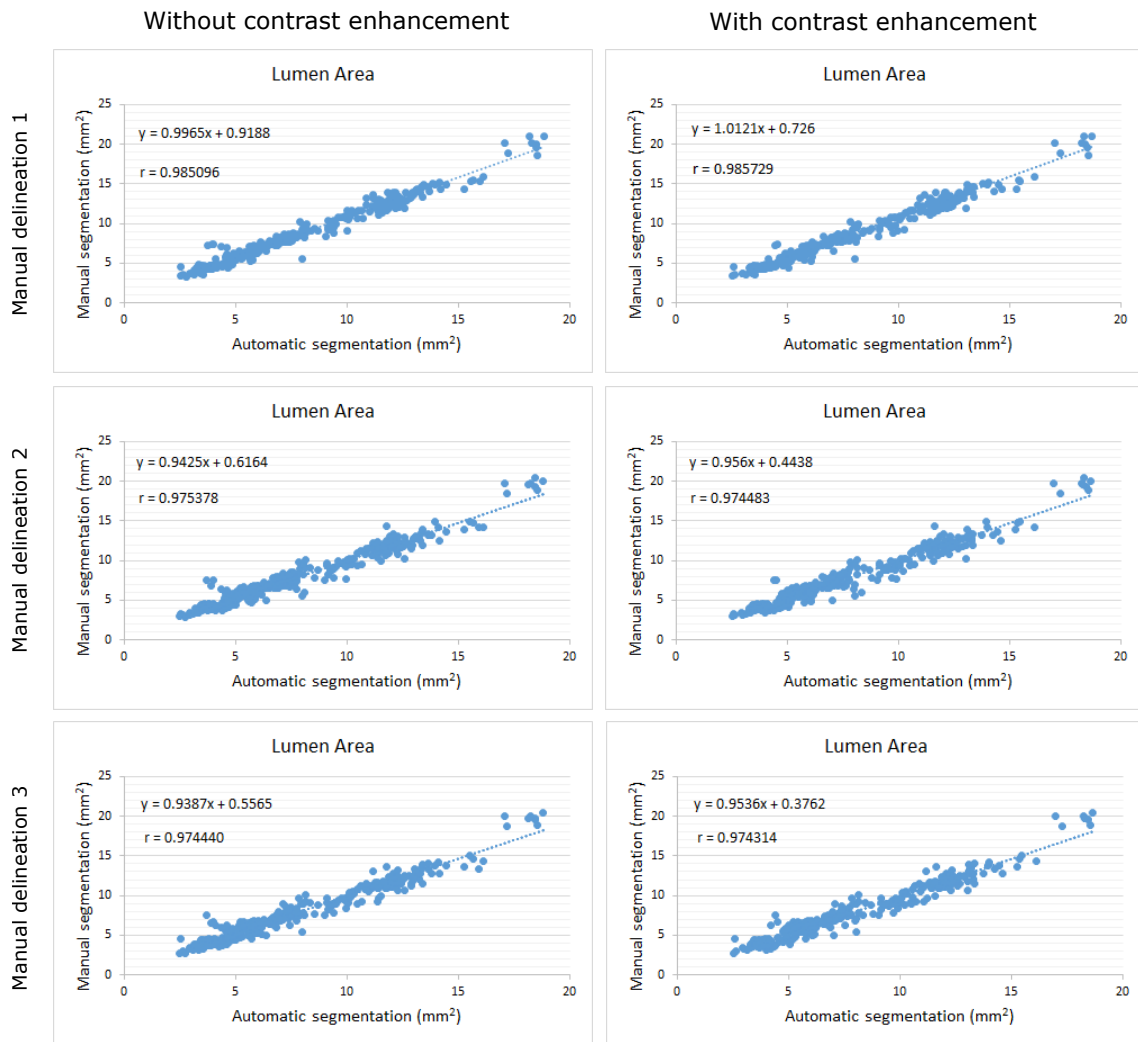
Figure 9: Area of the automatically segmented lumen versus the three corresponding manual delineations before and after adjusting the contrast of the input images.

0.977346, 0.972354 and 0.971756, respectively. Similar to the lumen area, a slight improvement in the correlation coefficients of the average lumen diameter between the automatic segmentations and manual delineations 1 and 3 was also achieved after adjusting the contrast of the input images.

The difference between the area calculated by the automatically segmented lumen and the ones obtained from the three manual delineations is depicted in Figure 11 by Bland-Altman plots. For the average lumen diameter, the difference between the automatic and manual segmentations is represented in Figure 12.

Figure 11 shows a significant underestimation of the lumen area of the automatic segmentation compared to the manual delineation 1, leading to average differences of -0.89136 mm^2 and -0.82174 mm^2 before and after adjusting the contrast of the input images, respectively. In contrast, the average difference between the automatically seg-
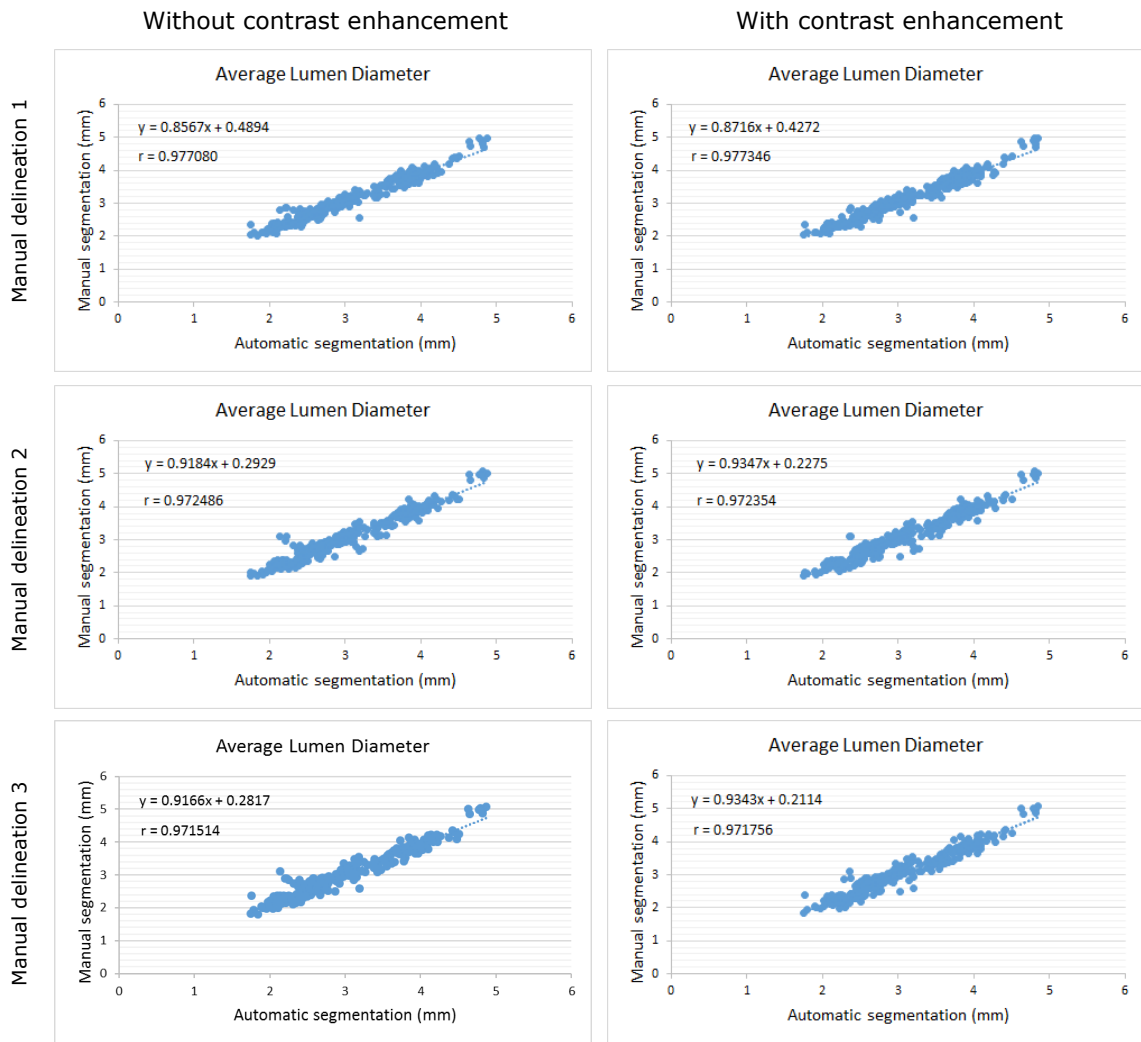
Figure 10: Average lumen diameter of the automatically segmented lumen versus the three manual delineations before and after adjusting the contrast of the input images.

mented lumen and the manual delineations 2 and 3 is small. The average differences of the lumen area between the automatically segmented lumen and the manual delineation 2 were -0.16389 mm^2 and -0.09497 mm^2 before and after adjusting the contrast of the images, respectively. For the manual delineation 3, the average differences were -0.07421 mm^2 and -0.00808 mm^2 before and after the adjustment of the contrast, respectively.

Regarding the average lumen diameter, a slight average difference was found between the automatic and manual segmentations. For the manual delineation 1, the average differences were -0.05160 mm and -0.03283 mm before and after the contrast enhancement of the input images, respectively; for the manual delineation 2, the average differences were -0.04473 mm and -0.02680 mm before and after the contrast enhancement, respectively; and for the manual delineation 3, the average differences were -0.02701 mm and -0.00963 mm before and after the contrast enhancement, respectively.
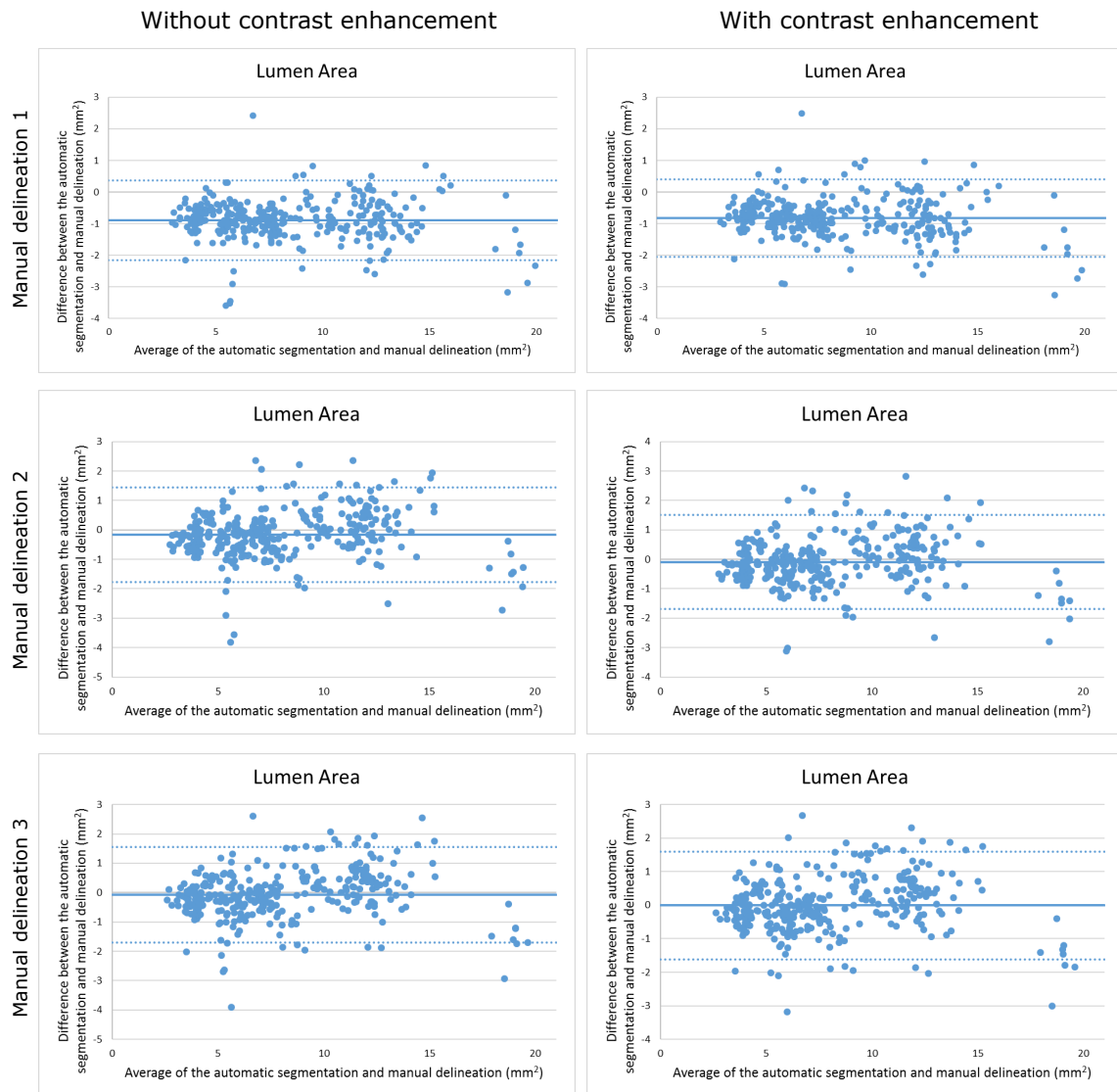
Figure 11: Bland-Altman plots of the lumen area of the automatically segmented lumen and the three corresponding manual delineations.

The linear regression and Bland-Altman analysis obtained from the delineations of the two experts is depicted in Figure 13.

5 Discussion

The development of automatic segmentation methods applied to medical images plays an important role in providing experts with auxiliary diagnosis tools for identifying various types of pathological conditions. For example, the segmentation of the lumen and media-adventitia regions in IVUS images represents an important step to quickly identify and quantify possible atherosclerosis in arteries.
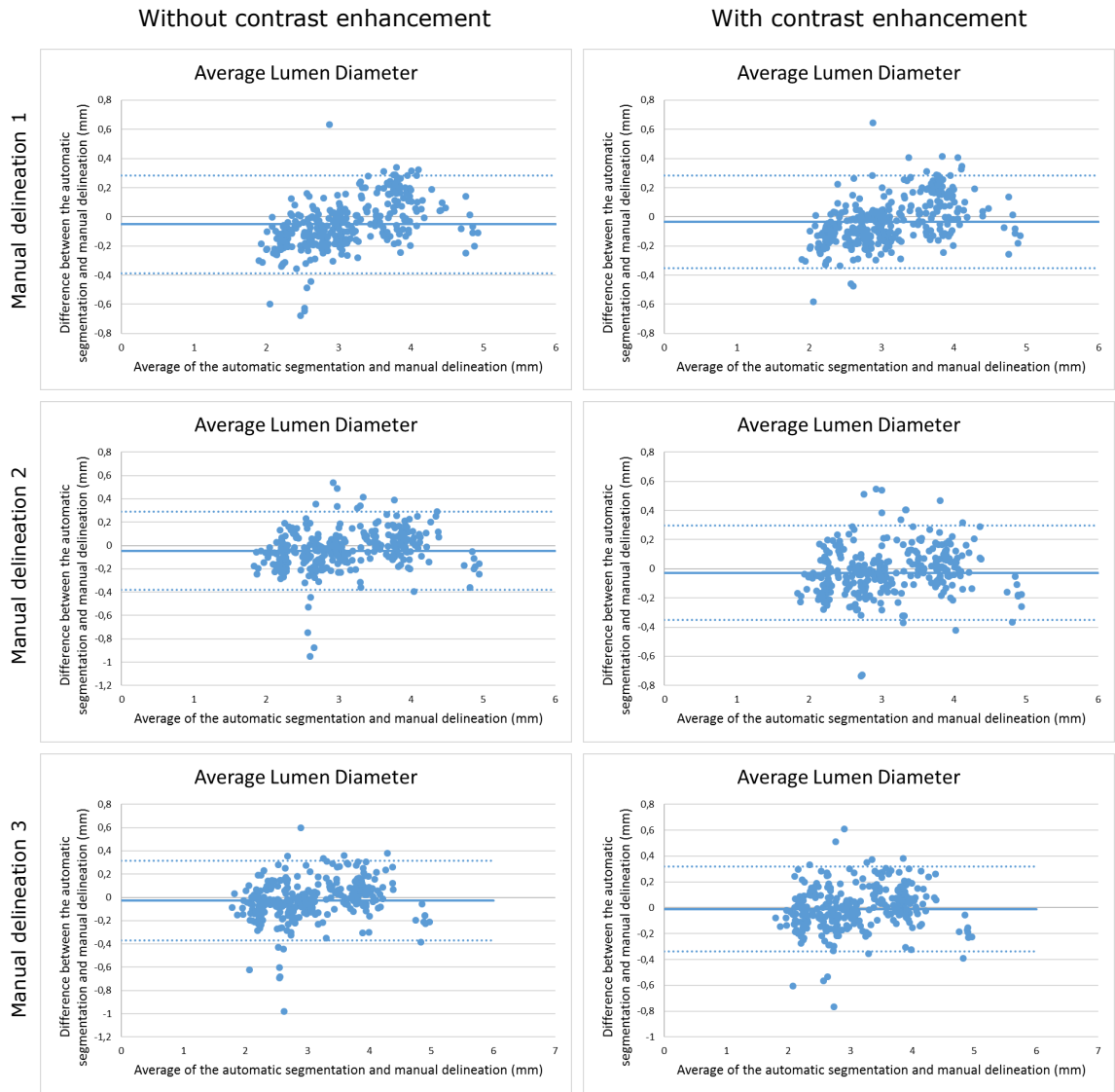
Figure 12: Bland-Altman plots of the average lumen diameter of the automatically segmented lumen and the three corresponding manual delineations.

The automatic segmentation of the lumen region in IVUS images of coronary arteries was successfully tackled in this study. The use of unsupervised classification and circularity index to identify the lumen region is the kernel of the proposed method. In our previous work, the initial version of the proposed method was applied to identify the lumen region in MR images of carotid arteries. Based on the fact that the lumen is a circular-shaped region with low-intensity values in axial black-blood MR images, the use of a circularity index was proposed to identify the region corresponding to the correct lumen among those obtained from the subtractive clustering algorithm. One goal of this study was to assess the viability of the method for segmenting the lumen in IVUS images of coronary arteries. Additionally, improvements were developed to make the method more
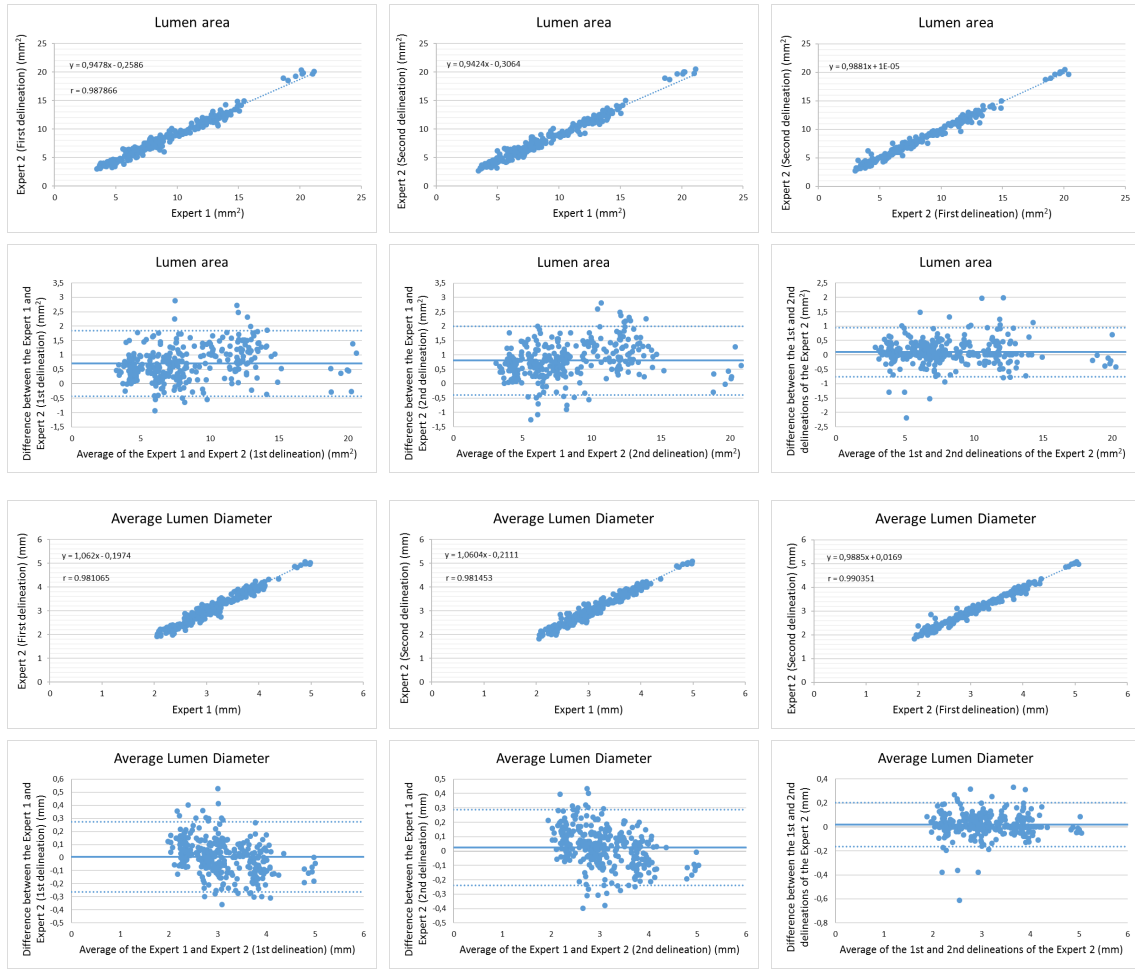
Figure 13: Linear regression and Bland-Altman analysis concerning the lumen area and average lumen diameter obtained from the delineations of the two experts.

robust, flexible, efficient and competent. Briefly, the original empirical criterion concerning noise was redefined, side branches in bifurcations regions are now successfully tackle, and the segmentation accuracy has been considerably improved.

5.1   Initialization of the parameters

The values of the parameters adopted in our previous study concerning MR images were also employed here to show the ability of the proposed method in segmenting the lumen in IVUS images. The mask of the median-filter used has also been used in many studies related to medical image segmentation; which therefore, indicates that it is a suitable choice to attenuate the noise present in the input images without leading to excessive smoothing of the borders of the structures of interest. The value of the α parameter in Equation 3 is automatically calculated by using the difference between the probabilities of the low and high grayscale intensities of the input image as given by Equation 4. Hence, the

adjustment of the contrast is not necessary if more pixels with high grayscale intensities are present in the input image. The number of clusters that are defined has an important role in the proposed method. In most cases, the grayscale intensity of the lumen in IVUS images is well-defined and distinguishable from other structures in the images. Hence, the number of clusters initially proposed in our previous study is also suitable in the segmentation of the lumen in IVUS images. On using the subtractive clustering algorithm, the r_a and r_b parameters may affect the number of clusters to be generated [23]. However, since the subtractive clustering is only used to generate the centroids of the expected number of clusters, the values of these parameters can also be used to separate the regions in IVUS images according to the same expected number. Regarding the downsampling of the resolution of the input IVUS image, the Gaussian pyramid was implemented in such way that it is automatically performed until the total number of pixels of the input image is equal or less than 22500, which was found as appropriate to reduce the computational cost of the subtractive clustering algorithm. Since all the IVUS images used have the same resolution (384x384), the downsampling process was performed twice, leading to a final image resolution of 96x96 (9216 pixels).

5.2   Performance of the proposed method

When compared to the related studies found in the literature, the proposed automatic segmentation of the lumen does not require any kind of user interaction and is easily implemented without using complex algorithms. The K-means with subtractive clustering is used to separate the regions of the input IVUS image according to the expected number of clusters. The subtractive clustering is only used as a prior step to find the appropriate initial centroids to be used in the K-means clustering algorithm. Different results could be produced when the centroids are randomly selected and used in the K-means clustering algorithm. Since the result of the K-means clustering algorithm depends on the selection of the initial centroids, we decided to use the subtractive clustering due to its stability to find the same initial centroids even when the algorithm is executed several times. Additionally, the subtractive clustering algorithm is easily implemented, although the computational time increases in images with higher resolution. Once the initial centroids are found, the traditional K-means clustering algorithm is applied to the input image.

Because the low-intensity values are associated to the lumen and background regions, the connected component labelling algorithm is applied to obtain all regions of the cluster belonging to the low-intensity values as a binary image. The regions corresponding to the background of the IVUS image are at the border of the generated binary image. In our previous work, a term representing the number of pixels of the region at the border of the

image was added to reduce its circularity index. Here, the region is simply discarded from the binary image to avoid additional processing. Additionally, the morphological opening operation with adaptive size of the structuring element is proposed to remove noisy artefacts without the need of a heuristic criterion as in the initial version. The morphological operations in the new post-processing step of the proposed method revealed that they were effective in smoothing the lumen contour resulting from the Chan-Vese active contour and removing possible irregularities.

An important contribution of this study is an effective approach to identify regions corresponding to side branches in the input IVUS images. The low-intensity values of the side branch extend from the lumen region to the border of the IVUS images when a bifurcation is presented. Hence, the bifurcation is represented by a single region with pixels at the border of the input image when the cluster with low-intensity values is generated by the K-means clustering algorithm. In order to avoid the elimination of this region in the lumen identification step, an approach based on the delimitation of the potential lumen region by a circle centred on the centre of the input IVUS image is proposed to separate and remove the branch of the bifurcation region. The proposed approach proved to be effective in eliminating the side branches of bifurcation regions and therefore, in decreasing the number of erroneous segmentations.

The average values of the measures described in Section 3.3 were obtained from the 324 IVUS images successfully segmented by the proposed method. The contrast enhancement of the IVUS images can improve the brightness of the region corresponding to the intima layer, allowing a better distinction between this region and the lumen. Hence, the segmentation accuracy obtained before and after adjusting the contrast of the input image were compared. A slight improvement in the average values of the Jaccard measure and Dice coefficient was found when the contrast enhancement was applied. The average value of the Jaccard measure was 0.87 ± 0.07 before adjusting the contrast of the images, whereas a slight increasing to 0.88 ± 0.06 was achieved after the application of the contrast. Additionally, the Hausdorff distance decreased from 0.30 ± 0.18 mm to 0.29 ± 0.17 mm after adjusting the contrast. Regarding the Bland-Altman analysis, the average differences between the area calculated from the proposed method and the ones obtained from the manual delineations reduced when the contrast enhancement was applied. Similar reductions of the bias were also obtained for the average lumen diameter. When compared to the manual delineation 3, a reduction of the bias from -0.02701 mm to -0.00963 mm was obtained before and after adjusting the contrast, respectively, leading to an average distance less than one pixel between the automatic and manual segmentations.

The high complexity ($O(d^2, N^2)$) of the subtractive clustering algorithm makes it unfeasible to be applied in images with higher resolutions due to the high number of pixels

to be processed to find the centroids of the clusters. Hence, the reduction of the resolution of the input image in order to decrease the computational cost of the subtractive clustering algorithm was tackled in this study. The Gaussian pyramid proved to be the most suitable choice due to its simple implementation and effective reduction of the resolution of the input image without losing important information on the structure of interest. The effectiveness of the Gaussian pyramid can be perceived from the data in Table 8, which indicates that the execution time of the K-means with the subtractive clustering algorithm is low when compared to the average total time and the time required by the Chan-Vese algorithm. This is due to the reduction of the number of pixels to be processed by the subtractive clustering algorithm when the Gaussian pyramid was applied. The computational cost of the Chan-Vese active contour was greater than that of the other algorithms. Since re-initialization of the signed distance function of the contour is necessary at every step of the contour evolution, the time consumed by the algorithm increases when applied to images of higher resolution. However, it was decided to apply the Chan-Vese active contour to the original IVUS image in order to take into account all the pixels of the lumen region available in the full resolution of the input image.

5.3 Comparison with the intra- and inter-observer variability

In terms of the inter-observer variability, i.e. the comparison between the manual delineations of Expert 1 and Expert 2, the results are close to the ones computed from our method. The average values of the Jaccard measure, Hausdorff distance, percentage of area difference and Dice coefficient of Expert 1 in comparison to the first delineation of Expert 2 were 0.88 ± 0.05, 0.28 ± 0.13 mm, 0.11 ± 0.08 and 0.94 ± 0.03, respectively. The average values for the same measures obtained from the comparison between the proposed method after adjusting the contrast of the input images and the first delineation of Expert 2 (represented by the manual delineation 2 in Table 3) were 0.88 ± 0.06, 0.29 ± 0.17 mm, 0.08 ± 0.07 and 0.94 ± 0.04, respectively. Regarding the comparison between the manual delineation of Expert 1 and the second delineation of Expert 2, the average values of the Jaccard measure, Hausdorff distance, percentage of area difference and Dice coefficient were 0.87 ± 0.05, 0.30 ± 0.13 mm, 0.13 ± 0.08 and 0.93 ± 0.03, respectively. The results of the proposed method for the same measures obtained from the comparison with the second delineation of Expert 2 (represented by the manual delineation 3 in Table 3) were 0.88 ± 0.06, 0.29 ± 0.18 mm, 0.08 ± 0.08 and 0.94 ± 0.04, respectively, which were slightly better than the ones obtained between Expert 1 and Expert 2 (second delineation).

The regression analysis showed that the segmentation results of the proposed method are also close to ones obtained from the intra- and inter-observer variability. In terms of the lumen area, the Pearson correlation coefficients between Expert 1 and the first and second delineations of Expert 2 were 0.987866 and 0.986466, respectively. The regression analysis of the intra-observer variability showed a correlation coefficient of 0.992330 between the lumen areas of the first and second delineations of Expert 2. After the application of the contrast enhancement, the automatic segmentation method obtained a correlation coefficient of 0.985729, 0.974483 and 0.974314 with the lumen area calculated from the manual delineations of Expert 1 and the first and second delineations of Expert 2, respectively. For the average lumen diameter, the correlation coefficients between Expert 1 and the first and second delineations of Expert 2 were 0.981065 and 0.981453, respectively, whereas the correlation coefficient between the first and second delineations of Expert 2 was 0.990351. After adjusting the contrast of the input images, the automatic segmentation of the lumen obtained a correlation coefficient of 0.977346, 0.972354 and 0.971756 with the average lumen diameter of the manual delineations of Expert 1 and the first and second delineations of Expert 2, respectively. The Bland-Altman analysis showed similar results between the proposed method and the intra- and inter-observer variability. For the lumen area, the bias between Expert 1 and the first delineation of Expert 2 were 0.708995 mm^2, whereas for the second delineation of Expert 2 the bias was 0.803415 mm^2. The Bland-Altman analysis of the lumen area with respect to the intra-observer variability showed a bias of 0.094420 mm^2 between the first and second delineations of Expert 2. The bias between the proposed method after adjusting the contrast of the images and the first delineation of Expert 2 was -0.09497 mm^2, which is closer to zero when compared to the bias between Expert 1 and the same delineation of Expert 2 (0.708995 mm^2). For the average lumen diameter, the bias between Expert 1 and the first delineation of Expert 2 was 0.006241 mm, whereas for the second delineation of Expert 2 the bias was 0.024817 mm. For the intra-observer variability, the bias of the average lumen diameter between the first and second delineations of Expert 2 was 0.018575 mm. The bias of the average lumen diameter between the proposed method after adjusting the contrast of the images and the three manual delineations were -0.03283 mm, -0.02680 mm and -0.00963 mm. Compared to the manual delineations, the proposed method underestimated the average lumen diameter. However, the results were similar to the intra- and inter-observer variability.

5.4   Comparison with other methods

A comparison with related studies found in the literature was carried out in order to validate the accuracy of the proposed lumen segmentation method. The first comparison was performed against the results obtained in the IVUS Segmentation Challenge [20]. The average values described in Table 6 showed that the method proposed by Participant group 3 outperformed the ones obtained from the other participant groups. A slight improvement of the Hausdorff distance was obtained from our method when compared to the one of Participant group 3 of the challenge (0.29 ± 0.17 mm vs 0.34 ± 0.14 mm, respectively). Although no significant improvements were achieved when compared to the results of this participant group, the segmentation of the lumen performed by our method is fully automatic and there is no need for an initial user interaction. In contrast, the method proposed by this group requires the initialization of a number of points to generate the initial contours.

The results shown in Table 7 indicate that our method outperformed many of the studies found in the literature. The value of the Dice coefficient of our method (0.9400 ± 0.0400) is better than the values obtained by Sofian et al. [18] and Mendizabal-Ruiz et al. [12] (0.9260 ± 0.0111 and 0.9283 ± 0.0201, respectively). The value of the Jaccard measure (0.8800 ± 0.0600) was also better than the ones obtained from the studies under comparison, except for the value obtained by Su et al. [9] (0.9182). The value of the Hausdorff distance (0.2900 ± 0.1700 mm) is only greater than the ones obtained from Su et al. [9] and Mendizabal-Ruiz et al. [12] (0.2243 mm and 0.1398 ± 0.0384 mm, respectively). Finally, the value of the percentage of area difference (0.0900 ± 0.0700) is only greater than the one obtained from Sofian et al. [18] (0.0645 ± 0.0509).

Although the results presented by Su et al. [9] are better than the ones obtained from our method, a ROI surrounding the region corresponding to the media-adventitia region must be delineated in the input image before the classification by the two ANN. In addition, the elimination of noise of the binary image resulting from the first classification is performed by a second ANN. In contrast, morphological operations and the convex hull algorithm are used here to identify noise and refine the regions to be evaluated instead of using a complex ANN. In addition, the method proposed performs the lumen segmentation in the whole image. Although the value of the percentage of area difference of the method proposed by Sofian et al. [18] is less than the one obtained from the proposed method, the authors only used 30 IVUS images randomly selected from the dataset provided by Balocco et al. [20] to perform the experiments. In the study tackled by Mendizabal-Ruiz et al. [12], IVUS images acquired from catheters operating at frequencies of 20 MHz and 40 MHz were taken into account. However, if only the images

acquired from the frequency of 20 MHz were considered, then the average values of the Dice, Jaccard and Hausdorff distance would be 0.9215 ± 0.0217, 0.8555 ± 0.0363 and 0.1421 ± 0.0371 mm, respectively.

In terms of the computational cost, the average total time of the proposed method is also in accordance with the related studies found in the literature. The average total time of the proposed method to process each one of the 326 IVUS images was 5.7165 ± 1.5419 seconds. Gao et al. [31] reported an average total time of 8.13 ± 6.05 seconds for the lumen segmentation step of their automated framework. The average total time of the lumen segmentation carried out by Mendizabal-Ruiz et al. [12] was 4.51 seconds.

5.5   Limitations

The proposed method has two limitations. The first limitation regards the number of parameters of the clustering algorithm. The K-means algorithm with subtractive clustering used requires three parameters: the number of clusters and the radius r_a and r_b representing the neighbourhood of the pixels under analysis. Although the proposed method with the same parameters adopted in our previous study for MR images was able to identify the lumen region in IVUS images, a fully automatic segmentation without any empirical parameters increases the reliability and robustness of the method. Hence, future studies will be conducted to effectively separate the regions present in the input images without any kind of parameter.

The second limitation regards the segmentation of IVUS images acquired from a frequency of 40 MHz. Since speckle noise in these images is higher when compared to IVUS images acquired at a frequency of 20 MHz, the application of most efficient filters to minimize the effects of such noisy artefacts will be considered in future research projects to enable segmentation on images acquired from catheters operating at different frequencies. In addition, texture analysis will also be considered instead of using only the grayscale intensity of the pixels in the K-means algorithm.

6   Conclusions

The segmentation of the lumen and media-adventitia regions in IVUS images is an intensive focus of research and plays an important role in assessing the presence and progression of atherosclerosis. A fully automatic segmentation of the lumen in IVUS images of coronary arteries was proposed in this article. Compared to our previous study, new solutions were developed to enhance the robustness, efficiency and automaticity of the proposed method. Additionally, a new approach to successfully identify and remove side

branches of bifurcation regions was also proposed to avoid the elimination of the potential lumen regions from the subsequent processing steps. The improved method proved to be effective in identifying the regions corresponding to the lumen without user interaction and any change in the values of the method parameters.

Modifications were also accomplished to improve the shape of the lumen contour and the segmentation accuracy. The qualitative analysis showed that the visual shape of the lumen contour produced by the new contour correction step was better than the one obtained from the Chan-Vese active contour algorithm, leading to smoother and more regular final contours. The quantitative analysis demonstrated that the segmentation results of the new automatic segmentation method are in accordance with the manual delineations performed by two experts. Additionally, the proposed method showed results close to the ones obtained from the inter-observer variability.

An effective approach to reduce the number of parameters of the subtractive clustering algorithm, as well as the application of the method proposed here to IVUS images acquired from catheters operating at different frequencies, are expected to be addressed in future research work.

Acknowledgements

References

[1] S. Mendis, P. Puska, and B. Norrving. *Global atlas on cardiovascular disease prevention and control*. World Health Organization, 2011. ISBN 978-92-4-156437-3.

[2] A. Nair, B. D. Kuban, E. M. Tuzcu, P. Schoenhagen, S. E. Nissen, and D. G. Vince. Coronary plaque classification with intravascular ultrasound radiofrequency data analysis. *Circulation*, 106(17):2200–2206, 2002. ISSN 0009-7322. doi: 10.1161/01.CIR.0000035654.18341.5E.

[3] E. B. Diethrich, K. Irshad, and D. B. Reid. Virtual histology and color flow intravascular ultrasound in peripheral interventions. *Seminars in vascular surgery*, 19(3): 155–162, September 2006. ISSN 0895-7967. doi: 10.1053/j.semvascsurg.2006.06. 001.

[4] A. König and V. Klauss. Virtual histology. *Heart*, 93(8):977–982, 2007. ISSN 1355-6037. doi: 10.1136/hrt.2007.116384.

[5] A. Broersen, M. A. de Graaf, J. Eggermont, R. Wolterbeek, P. H. Kitslaar, J. Dijkstra, J. J. Bax, J. H. C. Reiber, and A. J. Scholte. Enhanced characterization of calcified areas in intravascular ultrasound virtual histology images by quantification of the acoustic shadow: validation against computed tomography coronary angiography. *The International Journal of Cardiovascular Imaging*, 32(4):543–552, 2016. ISSN 1573-0743. doi: 10.1007/s10554-015-0820-x.

[6] A. Katouzian, E. D. Angelini, S. G. Carlier, J. S. Suri, N. Navab, and A. F. Laine. A state-of-the-art review on segmentation algorithms in intravascular ultrasound (IVUS) images. *IEEE Transactions on Information Technology in Biomedicine*, 16 (5):823–834, September 2012. ISSN 1089-7771. doi: 10.1109/TITB.2012.2189408.

[7] D. S. Jodas, A. S. Pereira, and J. M. R. S. Tavares. Lumen segmentation in magnetic resonance images of the carotid artery. *Computers in Biology and Medicine*, 79: 233–242, 2016. ISSN 0010-4825. doi: 10.1016/j.compbiomed.2016.10.021.

[8] L. Lo Vercio, J. I. Orlando, M. del Fresno, and I. Larrabide. Assessment of image features for vessel wall segmentation in intravascular ultrasound images. *International Journal of Computer Assisted Radiology and Surgery*, 11(8):1397–1407, August 2016. ISSN 1861-6410. doi: 10.1007/s11548-015-1345-4.

[9] S. Su, Z. Hu, Q. Lin, W. K. Hau, Z. Gao, and H. Zhang. An artificial neural network method for lumen and media-adventitia border detection in IVUS. *Computerized Medical Imaging and Graphics*, November 2016. ISSN 08956111. doi: 10.1016/j. compmedimag.2016.11.003. (in press).

[10] M. Kass, A. Witkin, and D. Terzopoulos. Snakes: Active contour models. *International Journal of Computer Vision*, 1(4):321–331, 1988. ISSN 09205691. doi: 10.1007/BF00133570.

[11] F. Destrempes, M.-H. Roy Cardinal, L. Allard, J.-C. Tardif, and G. Cloutier. Segmentation method of intravascular ultrasound images of human coronary arteries.

Computerized Medical Imaging and Graphics, 38(2):91–103, March 2014. ISSN 08956111. doi: 10.1016/j.compmedimag.2013.09.004.

[12] E. G. Mendizabal-Ruiz, M. Rivera, and I. A. Kakadiaris. Segmentation of the luminal border in intravascular ultrasound B-mode images using a probabilistic approach. *Medical Image Analysis*, 17(6):649–670, 2013. ISSN 1361-8415. doi: 10.1016/j.media.2013.02.003.

[13] A. Vard, K. Jamshidi, and N. Movahhedinia. An automated approach for segmentation of intravascular ultrasound images based on parametric active contour models. *Australasian Physical & Engineering Sciences in Medicine*, 35(2):135–150, 2012. ISSN 1879-5447. doi: 10.1007/s13246-012-0131-7.

[14] M. H. R. Cardinal, J. Meunier, G. Soulez, R. L. Maurice, E. Therasse, and G. Cloutier. Intravascular ultrasound image segmentation: a three-dimensional fast-marching method based on gray level distributions. *IEEE Transactions on Medical Imaging*, 25(5):590–601, May 2006. ISSN 0278-0062. doi: 10.1109/TMI.2006. 872142.

[15] M.-H. R. Cardinal, G. Soulez, J.-C. Tardif, J. Meunier, and G. Cloutier. Fast-marching segmentation of three-dimensional intravascular ultrasound images: a pre- and post-intervention study. *Medical Physics*, 37(7):3633–3647, 2010. ISSN 2473-4209. doi: 10.1118/1.3438476.

[16] A. Taki, Z. Najafi, A. Roodaki, S. K. Setarehdan, R. A. Zoroofi, A. Konig, and N. Navab. Automatic segmentation of calcified plaques and vessel borders in IVUS images. *International Journal of Computer Assisted Radiology and Surgery*, 3(3): 347–354, 2008. ISSN 1861-6429. doi: 10.1007/s11548-008-0235-4.

[17] E. dos Santos, M. Yoshizawa, A. Tanaka, Y. Saijo, and T. Iwamoto. Detection of luminal contour using fuzzy clustering and mathematical morphology in intravascular ultrasound images. In *IEEE 27th Annual Conference Engineering in Medicine and Biology*, pages 3471–3474, 2005. ISBN 0-7803-8741-4. doi: 10.1109/IEMBS.2005.1617226.

[18] H. Sofian, J. T. C. Ming, and N. M. Noor. Detection of the lumen boundary in the coronary artery disease. In *2015 IEEE International WIE Conference on Electrical and Computer Engineering (WIECON-ECE)*, pages 143–146. IEEE, December 2015. ISBN 978-1-4673-8786-6. doi: 10.1109/WIECON-ECE.2015.7443882.

[19] M. C. Moraes and S. S. Furuie. Automatic coronary wall segmentation in intravascular ultrasound images using binary morphological reconstruction. *Ultrasound in Medicine & Biology*, 37(9):1486–1499, September 2011. ISSN 03015629. doi: 10.1016/j.ultrasmedbio.2011.05.018.

[20] S. Balocco, C. Gatta, F. Ciompi, A. Wahle, P. Radeva, S. Carlier, G. Unal, E. Sanidas, J. Mauri, X. Carillo, T. Kovarnik, C.-W. Wang, H.-C. Chen, T. P. Exarchos, D. I. Fotiadis, F. Destrempes, G. Cloutier, O. Pujol, M. Alberti, E. G. Mendizabal-Ruiz, M. Rivera, T. Aksoy, R. W. Downe, and I. A. Kakadiaris. Standardized evaluation methodology and reference database for evaluating IVUS image segmentation. *Computerized Medical Imaging and Graphics*, 38(2):70–90, 2014. ISSN 0895-6111. doi: 10.1016/j.compmedimag.2013.07.001. Special Issue on Computing and Visualisation for Intravascular Imaging.

[21] S.-C. Huang, F.-C. Cheng, and Y.-S. Chiu. Efficient contrast enhancement using adaptive gamma correction with weighting distribution. *IEEE Transactions on Image Processing*, 22(3):1032–1041, March 2013. ISSN 1057-7149. doi: 10.1109/TIP.2012.2226047.

[22] K. Bataineh, M. Naji, and M. Saqer. A comparison study between various fuzzy clustering algorithms. *Editorial Board*, 5(4):335–343, 2011. ISSN 1995-6665.

[23] S. L. Chiu. Fuzzy model identification based on cluster estimation. *Journal of Intelligent & Fuzzy Systems*, 2(3):267–278, May 1994. ISSN 1064-1246.

[24] Z.-H. Sun, X.-H. Wei, and W.-H. Zhou. A nyström-based subtractive clustering method. In *2012 International Conference on Wavelet Active Media Technology and Information Processing (ICWAMTIP)*, pages 74–77, December 2012. ISBN 978-1-4673-1684-2. doi: 10.1109/ICWAMTIP.2012.6413443.

[25] E. H. Adelson, C. H. Anderson, J. R. Bergen, P. J. Burt, and J. M. Ogden. Pyramid methods in image processing. *RCA Engineer*, 29(6):33–41, 1984.

[26] N. Dhanachandra, K. Manglem, and Y. J. Chanu. Image segmentation using K-means clustering algorithm and subtractive clustering algorithm. *Procedia Computer Science*, 54:764–771, 2015. ISSN 18770509. doi: 10.1016/j.procs.2015.06.090.

[27] N. Ritter and J. Cooper. New resolution independent measures of circularity. *Journal of Mathematical Imaging and Vision*, 35(2):117–127, October 2009. ISSN 0924-9907. doi: 10.1007/s10851-009-0158-x.

[28] S. Jain, V. Jagtap, and N. Pise. Computer aided melanoma skin cancer detection using image processing. *Procedia Computer Science*, 48:735–740, 2015. ISSN 18770509. doi: 10.1016/j.procs.2015.04.209.

[29] M. M. G. de Macedo, C. K. Takimura, P. A. Lemos, and M. A. Gutierrez. A robust fully automatic lumen segmentation method for in vivo intracoronary optical coherence tomography. *Research on Biomedical Engineering*, 32(1):35–43, March 2016. ISSN 2446-4740. doi: 10.1590/2446-4740.0759.

[30] M. d. Berg, O. Cheong, M. v. Kreveld, and M. Overmars. *Computational Geometry: Algorithms and Applications*. Springer-Verlag TELOS, Santa Clara, CA, USA, 3rd edition, 2008. ISBN 3540779736, 9783540779735.

[31] Z. Gao, W. K. Hau, M. Lu, W. Huang, H. Zhang, W. Wu, X. Liu, and Y.-T. Zhang. Automated framework for detecting lumen and media–adventitia borders in intravascular ultrasound images. *Ultrasound in Medicine & Biology*, 41(7):2001–2021, July 2015. ISSN 03015629. doi: 10.1016/j.ultrasmedbio.2015.03.022.

[32] T. F. Chan and L. A. Vese. Active contours without edges. *IEEE Transactions on Image Processing*, 10(2):266–277, February 2001. ISSN 1057-7149. doi: 10.1109/83.902291.

[33] Z. Ma, J. M. R. S. Tavares, R. N. Jorge, and T. Mascarenhas. A review of algorithms for medical image segmentation and their applications to the female pelvic cavity. *Computer Methods in Biomechanics and Biomedical Engineering*, 13(2):235–246, 2010. ISSN 1025-5842. doi: 10.1080/10255840903131878.

[34] X.-F. Wang, D.-S. Huang, and H. Xu. An efficient local Chan-Vese model for image segmentation. *Pattern Recognition*, 43(3):603–618, 2010. ISSN 0031-3203. doi: 10.1016/j.patcog.2009.08.002.

[35] A. M. F. Santos, R. M. dos Santos, P. M. A. Castro, E. Azevedo, L. Sousa, and J. M. R. S. Tavares. A novel automatic algorithm for the segmentation of the lumen of the carotid artery in ultrasound B-mode images. *Expert Systems with Applications*, 40 (16):6570–6579, November 2013. ISSN 09574174. doi: 10.1016/j.eswa.2013.06.003.

[36] C. Huang and L. Zeng. An active contour model for the segmentation of images with intensity inhomogeneities and bias field estimation. *PLOS ONE*, 10(4):1–24, April 2015. doi: 10.1371/journal.pone.0120399.

Part B - Article 4:

Using a distance map and an active contour model to segment in proton density weighted magnetic resonance images the carotid artery boundary from the lumen contour

Danilo Samuel Jodas, Maria Francisca Monteiro da Costa, Tiago A. A. Parreira, Aledir Silveira Pereira, João Manuel R. S. Tavares

Abstract

Segmentation methods have assumed an important role in image-based diagnostic of several cardiovascular diseases. Particularly, the segmentation of the boundary of the carotid artery is demanded in the detection and characterization of atherosclerosis and assessment of the disease progression. In this article, a fully automatic approach for the segmentation of the carotid artery boundary in Proton Density Weighted Magnetic Resonance Images is presented. The approach relies on the expansion of the lumen contour based on a distance map built using the gray-weighted distance relatively to the centre of the identified lumen region in the image under analysis. Then, the Snake model with a modified weighted external energy based on the combination of a balloon force along with a Gradient Vector Flow based external energy is applied to the expanded contour towards the correct boundary of the carotid artery. The average values of the Dice coefficient, Polyline distance, mean contour distance and centroid distance found in the segmentation of 139 carotid arteries were 0.83 ± 0.11, 2.70 ± 1.69 pixels, 2.79 ± 1.89 pixels and 3.44 ± 2.82 pixels, respectively. The segmentation results of the proposed approach were also compared against the ones obtained by related approaches found in the literature, which confirmed the outstanding of the new approach. Additionally, the proposed weighted external energy for the Snake model shown to be robust to carotid arteries with large thickness and weak boundary edges.
Keywords: Medical imaging, Magnetic resonance imaging, Image segmentation, Snake model, Gray-weighted distance

1   Introduction

Cardiovascular diseases are the leading cause of death and disability in the world. The most common underlying disease process is atherosclerosis, which is still the most dangerous disease that affects the majority of people around the world [1]. The accumulation of fatty material and cholesterol in the walls of the arterial system is the underlying condition to the formation of the so called atherosclerotic plaques, which can progressively obstruct the blood through the artery and lead to heart attacks and strokes. The rupture of atherosclerotic plaques lodged in the carotid artery might lead to acute thrombus formation with acute carotid occlusion and/or generating embolic debris to the intracranial circulation, two factors that might lead to a stroke. Therefore, an early diagnostic is important to rapidly establish a treatment planning for preventing the onset or recurrence of symptoms.

Magnetic resonance imaging (MRI) has been widely used in non-invasive image-based diagnostic of the carotid artery. Particularly, magnetic resonance (MR) images have been successfully used in the characterization of atherosclerotic plaques, enabling the assessment of the disease progression [2]. Computer-aided methods for the analysis of the carotid artery in MR images play an important role to expedite the identification and assessment of possible atherosclerosis and, consequently, the design of the best treatment planning to prevent future symptomatic events. The quantification of atherosclerotic plaques and their main components allows the experts to evaluate the progression and regression of the disease, the establishment of the mostly suitable treatment for the patient and evaluate the necessity for a surgical or endovascular procedure. Additionally, the evaluation of the atherosclerotic plaque components plays an important role in identifying patients with higher risk for future symptomatic events [3–5].

Usually, the identification of the carotid artery is the first step towards the quantitative evaluation of the morphology of the vessel wall and the evaluation of the presence and progression of atherosclerosis. However, the manual delineation of the lumen and carotid wall boundaries is a laborious and time-consuming task taking into account the high number of slices acquired in a single imaging exam. Approaches based on surface graph cuts [6, 7], ellipse fitting [8, 9], difference of Gaussian [10] and active contour models [11–18] were proposed in the literature for the segmentation of the lumen and carotid wall boundaries in MR images. However, the main limitation of the aforementioned methods is the necessity for manual interventions and the expansion of the lumen contour according to a fixed value as in Ladak et al. [12], van 't Klooster et al. [15], Saba et al. [17] and Gao et al. [18]. In images with different resolutions, a heuristic value can fail to appropriately dilate the contour outward the lumen region. Additionally, the gradient information usually adopted in active contour models is insufficient to overcome weak boundaries commonly found on MR images of the carotid artery. Therefore, the expansion of the lumen contour without using any heuristic value is required for the fully automatic segmentation of the lumen and carotid wall boundaries, which is highly demanded to rapidly provide to the clinical experts the region of the vessel to be evaluated. The use of the image intensity in the external energy commonly adopted in active contour models is also important to improve the segmentation in carotid arteries with weak boundaries.

This article proposes a novel fully automatic approach to segment the lumen and outer boundaries of the carotid artery in Proton Density Weighted (PDW) MR images. The proposed approach performs the segmentation of the carotid artery boundaries using a gray-weighted distance map and the Snake model with a modified external energy that relies on Gradient Vector Flow and balloon forces. Briefly, the first step of the new approach is the identification of the lumen contour using the mean roundness criterium proposed in Jodas

et al. [19]. Then, since the magnitude of the gradient along the lumen region prevents the lumen contour to reach the boundary of the carotid artery, the gray-weighted distance map is employed to expand the contour outward the lumen region towards the carotid artery boundary. Then, the region inside the expanded contour is discarded and the contour is used to initiate the Snake model in order to segment the carotid artery boundary. Since the Snake model is a particular case of deformable models, the identified lumen contour might be deformed and moved using the concept of curve evolution to find the boundary of the carotid artery based on geometrical properties and image information.

This study provides three main contributions: The use of a gray-weighted distance map to automatically expand the lumen contour outward the lumen region; the combination of a balloon force along with a Gradient Vector Flow based external energy in the Snake model to handle the segmentation of the boundaries of carotid arteries with large thickness and weak edges; the detailed assessment of the accuracy of the proposed approach using a challenge PDW MR image dataset.

The remainder of this article is organized as follow: Section 2 describes the proposed automatic segmentation approach. Section 3 presents segmentation results obtained by the proposed approach and their comparison against the corresponding manual delineations. The advantages and limitations of the proposed approach are identified in Section 4. Finally, the conclusions are drawn in Section 5.

2   Materials and Methods

2.1   MR images used

The MR images of the carotid artery selected for this study were used in research by van Engelen et al. [20] and kindly provided by the authors on request. The proposed segmentation approach was performed on images that are the regions of interest surrounding the carotid arteries. A registration procedure was previously performed to match the original MR images with the corresponding histology images, which only contained the region of the artery under study [20]. Once the matching was completed, the MR images were cropped to obtain only the part that matched the histology images [20]. The original dataset was composed of five MRI scans acquired from thirteen patients: T1-weighted (T1W), Proton Density Weighted (PDW), Time-of-Flight (TOF) and two 3D-T1W scans. The first three MRI scans were acquired without administration of intravenous (IV) contrast media, whereas the 3D-T1W scan was acquired with and without contrast media. The post-contrast 3D-T1W scan was performed 4.6 ± 3.4 minutes after the administration of the contrast media. Each MRI scan is composed of approximately 17.7 ± 4.8 slices

per patient; each slice has a pixel size of 0.25 mm x 0.25 mm. CTA images were also acquired to provide details for the registration with the histology images and to facilitate the manual segmentation of the lumen, vessel wall and plaque components. More details about the MRI scans are available in van Engelen et al. [20].

In order to overcome the lack of manual delineations in the original dataset and misalignments of the provided contour with the PDW MR images resulting from the registration step described in van Engelen et al. [20] that may affect the quantitative analysis on the segmentation accuracy, the lumen and carotid walls were manually delineated on the 230 PDW MR images of the thirteen patients. The new manual delineations were made by a physician of the Neuroradiology Department from the Centro Hospitalar São João, in Porto, Portugal, with the supervision of an experienced physician from the same department. The manual contours for the lumen and carotid walls of the images belonging to eight patients were established based on the PDW MR images only; the delineations of the images belonging to four patients were made with the additional visual examination of the corresponding 3D-T1W MR images; and the PDW MR images of one patient were not manually segmented due to their low quality and the presence of strong noise artefacts; additionally, the images of patients 11 and 13 were not used due to the impossibility of identifying the structures of interest. Hence, 185 PDW MR images with manual delineations of the lumen and carotid boundaries were used in this study.

2.2   Proposed approach

The diagram of the proposed automatic approach for segmenting the carotid wall boundary in PDW MR images is depicted in Figure 1.

Here, the segmentation of the lumen boundary was performed using the method proposed in our previous study [19], which relies on the circularity index calculated from each region identified by the K-means algorithm with subtractive clustering. The identified lumen contour is then submitted to the vessel wall segmentation stage to expand it to the outer boundary of the carotid artery. In the vessel wall segmentation stage, the lumen contour is expanded in two iterations: the first iteration consists in expanding the contour outward the lumen region by means of the application of the Snake active contour with ellipse constraint in the grayscale distance map of the input MR image; and the second iteration completes the expansion to the true boundary of the carotid artery based on the Snake active contour with a weighted external energy.
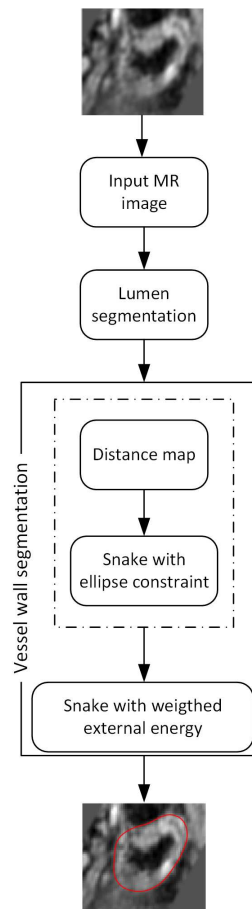
Figure 1: Diagram of the proposed approach for segmenting the carotid artery boundaries in PDW MR images.

2.2.1 Distance map

Edge detector operators rely on the gradient of the input image to find significant variations on the grayscale intensities of the regions under analysis. In Black-Blood MR images of the carotid artery, the lumen is a region with low intensity values surrounded by high intensity values corresponding to the region of the vessel wall. Hence, significant variations of the grayscale intensity between the lumen and vessel wall regions represent a challenge to expand the lumen contour towards the boundary of the carotid artery.

External energies used in the Snake model usually rely on the magnitude of the gradient vectors to decrease the evolution of the initial contours towards the boundaries of the structures of interest. However, the high magnitude of the gradient vectors around the lumen region can hinder the expansion of the identified lumen contour towards the boundary of the carotid artery under analysis. Approaches based on heuristic values in order to expand the lumen contour in the direction of the boundary of the carotid artery may still fail due to the lack of robustness against changes in the resolution of the input image.

Therefore, an efficient and dynamic approach to avoid the edges between the lumen and carotid wall is proposed in this study.

Distance transform is a method applied to binary or grayscale images to assign a value to each pixel of the object of interest that represents the nearest distance to the pixels of the image background. The distance transform has been successfully used in many image processing and analysis problems such as in skeletonization [21], edge detection [22] and minimal path extraction [23] problems.

Geodesic time represents the gray-weighted distance between two pixels p and q in a grayscale image and it is defined as the sum of the pixel intensities along the minimum cost path connecting these two pixels (p and q). The geodesic time was proposed by Soille [24] and it is calculated as the mean of two adjacent pixels of the grayscale image f along the minimum path:

$$t_f(P) = \sum_{i=1}^{l} \frac{f(p_i - 1) + f(p_i)}{2},$$ (1)

where $f(p_i - 1)$ and $f(p_i)$ are the intensity of two adjacent pixels along the minimum cost path $t_f(P)$, and l is the length of the path P. Starting from the pixel p, the minimum cost relatively to the pixel q is calculated from a 3x3 neighborhood of each pixel along the path according to Equation 1. The geodesic time assures that there is only one path with minimum cost between p and q. Hence, the geodesic time is the smallest amount of time, i.e., cost, between the pixels p and q:

$$t_f(p,q) = min\{t_f(P)|P \text{ connects } p \text{ and } q\}.$$ (2)

Figure 2 illustrates an example of the gray-weighted distance calculated from a centre pixel to each pixel at the border of a 5x5 matrix.

As shown in Figure 2, the distance along the path connecting the centre pixel to each pixel at the border of the matrix increases according to the intensity values. The higher the pixel intensities along the path, the larger will be the distance from the starting pixel to the ending pixel. Considering the low intensity of the lumen region of the carotid artery in Black-Blood MR images, the distances from the centre of the lumen to all pixels at the border of the input image start to increase significantly as the paths reach the edge between the lumen and the vessel wall regions. Hence, the expansion of the identified lumen contour beyond the boundary of the lumen region can be performed by decreasing the contour evolution as the values of the distance map increase. Examples of the gray-weighted distance applied to PDW MR images of carotid arteries are illustrated in Figure 3.

17	24	1	8	15
23	5	7	14	16
4	6	13	20	22
10	12	19	21	3
11	18	25	2	9

(a)

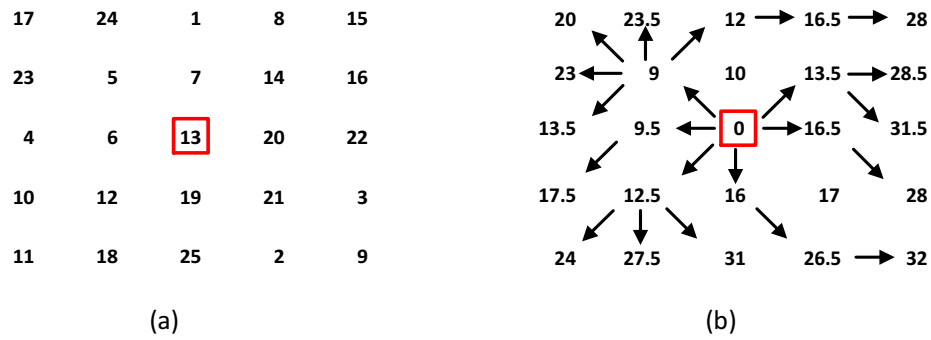| 20	23.5	12	16.5	28
23	9	10	13.5	28.5
13.5	9.5	0	16.5	31.5
17.5	12.5	16	17	28
24	27.5	31	26.5	32

(b)

Figure 2: Example of the gray-weighted distance applied to a 5x5 matrix: a) A 5x5 matrix with grayscale intensities; b) The gray-weighted distance calculated from the pixel highlighted in red to each pixel at the border of the matrix. (The arrows indicates the path with minimum cost.)
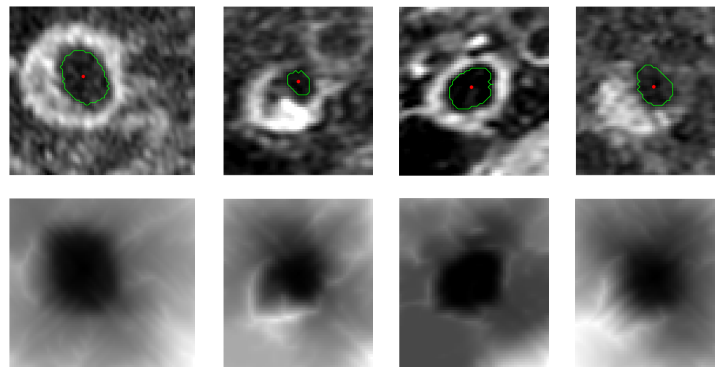

Figure 3: Examples of the gray-weighted distance applied to PDW MR images of carotid arteries: The first row shows the images with the segmented lumen contours represented in green (the starting points of the gray-weighted distance are the red dots that represent the centres of the lumen contours). The second row shows the distance maps calculated by Equation 1.

As shown in Figure 3, the grayscale intensities of the images corresponding to the distance maps (second row) represent the distances from the centres of the lumen contours to all pixels at the border of the images. The higher the intensity values are, the larger will be the distances from the centre of the lumen. The distances inside the lumen region start to increase close to the edge of the lumen boundary.

2.2.2 Active contour model

Deformable models have been widely used in the segmentation of boundaries of structures presented in medical images [25–29]. Active contours, or Snakes, were proposed by Kass et al. [30] to find boundaries of regions in images through the evolution of curves,

i.e., contours, controlled by internal and external energies. Hence, active contour models combine geometrical properties, image information and constraints to move contours towards the true boundaries of the structures of interest [31]. The active contour model proposed by Kass et al. [30] performs the evolution of the curve C(s) = [x(s),y(s)], s ∈ [0,1] based on the minimization of the energy function defined as:

$$E(C) = \int_0^1 E_{int}(C(s)) + E_{ext}(C(s)) + E_{con}(C(s)) \, ds, \tag{3}$$

where E_{int} is the internal energy of the contour, E_{ext} is the external energy calculated from the input image and E_{con} is a constraint energy restricting the evolution of the contour. The internal energy E_{int} controls the elasticity and curvature of the contour, and it is defined as:

$$E_{int}(C(s)) = \int_0^1 \frac{1}{2} \left(\alpha |C'(s)|^2 + \beta |C''(s)|^2 \right), \tag{4}$$

where $C'(s)$ and $C''(s)$ are the first and second derivatives of the contour $C(s)$, respectively, and α and β are weights that control the elasticity and curvature of the contour, respectively. The external energy E_{ext} forces the contour to move towards the boundary of the structure of interest based on the image information. In the absence of external energies, the geometrical properties controlled by the internal energy is responsible to evolve the contour.

The active contour model proposed by Kass et al. [30] has been extensively used in tasks of image processing and analysis, particularly in the segmentation of medical images. However, the gradient of the input image commonly used as external energy provides limited capture range and poor convergence to concavities. Hence, the initial contour needs to be placed close to the boundary of the structure of interest. Balloon forces [32] have been proposed to increase the amplitude and range of the contour to be evolved:

$$F_{balloon} = kn(s), \tag{5}$$

where $n(s)$ is a unit vector perpendicular to each point of the contour to be deformed, and k is a weight that defines the amplitude of the unit vector force. The sign of k defines the orientation of the contour, i.e., the ability to inflate or deflate around the structure of interest. A positive value of k will make the contour to inflate until it fits the boundary of interest, whereas a negative value will be responsible to deflate the contour. Balloon forces have been successfully applied to increase the pressure force of active contour models, leading the contours to fit the boundaries of interest even when the initial contours are

distant from the structures. However, balloon forces may cause the segmentation contour to leak weak edges due to the amplitude and strengthen of the unit vectors.

Xu and Prince [33] proposed a new external force called Gradient Vector Flow (GVF) to increase the capture range and handle with concavities in the structures of interest by diffusing the gradient vectors of an edge map calculated from the input image. Although successfully used as an external energy for active contour models, the main disadvantage of the GVF method is the inability to deal with weak edges that can cause the contour to leak the true boundary. Liu and Bovik [34] proposed an new external energy for the Snake model based on the decomposition of the Laplacian operator. The new external energy is called Neighbourhood-Extending and Noise-Smoothing Gradient Vector Flow (NNGVF), which is based on the convolution of two templates used to maintain the low-frequency components of the image obtained by a gradient operator, suppress noisy artefacts and increase the edge-preservation. Since the convolution is performed in larger neighbourhoods, the NNGVF performs the noise reduction and the capturing of more information to calculate the diffusion vectors in regions with weak edges.

Although the NNGVF provides better results when compared to the GVF, the evolution of the contour in structures with large areas is still the most challenge in the segmentation of medical images. Examples of segmentation results obtained by the Snake model with the NNGVF applied to PDW MR images of carotid arteries are shown in Figure 4.
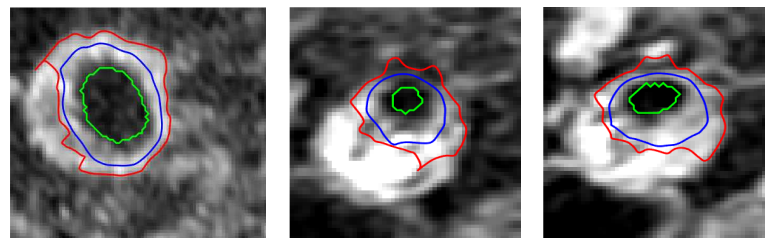

Figure 4: Examples of incomplete convergence of the lumen contours to the boundaries of carotid arteries resulting from the Snake model with the NNGVF applied to PDW MR images. (The identified lumen contours are depicted in green, the blue contours represent the lumen contours expanded beyond the boundaries of the lumen regions by using the images resulting from the gray-weighted distance, and the red contours are the results of the Snake model with the NNGVF initialized with the blue contours.)

In Figure 4, the contours in red represent the results of the Snake model with the NNGVF. The incomplete convergence of the initial contours represented in blue to the true boundaries of the carotid arteries is due to the variations of the grayscale intensities inside the carotid wall and the high distance to the boundaries of interest.

In order to overcome the limited range covered by the GVF, Khadidos et al. [35] proposed a new external energy for the Snake model based on the combination of the

GVF and balloon based forces. Hence, a weighted factor based on the intensity of the magnitude of the gradient and the difference between the directions of the balloon forces and the gradient vectors is introduced to control the evolution of the initial contour [35]:

$$E_{ext} = (F_{balloon} * (1 - \Omega)) + (F_{GVF} * \Omega), \tag{6}$$

where $F_{balloon}$ is the balloon force calculated from the contour to be deformed, F_{GVF} is the external energy calculated from the GVF based force and Ω is defined as:

$$\Omega = h^{1-(AD-\varepsilon)}. \tag{7}$$

The value of h at each pixel (x,y) of the contour to be deformed is defined as the average value of the intensities inside a semi-circular region centered at (x,y):

$$h(x,y) = \frac{1}{N} \sum_{(i,j) \in S} f(i,j), \tag{8}$$

where $f(i,j)$ is the intensity value at pixel (i,j) of the image with the edges detected by a gradient operator, S is the region inside the semi-circle centred at the contour pixel (x,y), and N is the number of pixels of the region S.

The value of AD at each contour pixel (x,y) is defined as the average of the difference between the angle of the balloon force and the angle of each gradient vector inside a cone-shaped region ahead the contour pixel (x,y) under analysis:

$$AD(x,y) = \frac{1}{M * \pi} \sum_{(i,j) \in T} \theta(i,j), \tag{9}$$

where $\theta(i,j)$ is the angle between the balloon force at the contour pixel (x,y) and the gradient vector at the pixel (i,j), T contains the pixels ahead the contour pixel (x,y) that are inside the cone-shaped region, and M is the number of pixels of this cone-shaped region.

Given an edge map image f obtained by a gradient operator with edges represented by high intensity values and non-edge regions represented by low intensity values, the basic idea of the external energy proposed by Khadidos et al. [35] is to apply the balloon forces to continue the evolution of the contour when a homogeneous region with low intensities is found. In contrast, when an edge is found, the GVF based force is applied to fit the contour to this edge.

The weighted external energy was proposed to force the expansion of the contour in homogeneous regions, and attenuate the evolution in heterogeneous regions close to the desired boundary. However, the leakage of the contour remains a major challenge due

to low intensity values in regions with weak edges. Since the average value h of the intensities inside the semi-circular region tends to zero close to weak edges, the balloon forces predominate the external energy proposed in Equation 6, leading the contour to leak the true boundary of the region of interest. Hence, a modification of the weighted external energy defined in Equation 6 is proposed in this study to improve the results in weak boundaries. The modification consists in replacing the average value h by the entropy of the intensity values ahead the contour pixel (x, y) of the contour to be deformed by using the following formulation:

$$h(x, y) = 1 - \frac{1}{entropy(P) + 1}, \tag{10}$$

where *entropy(P)* is the entropy of the pixels inside the semi-circle centred at the contour pixel P located on the (x, y) coordinates:

$$entropy = -\sum_{i=1}^{N} p_i * log_2(p_i), \tag{11}$$

where N is the highest possible intensity value, and p_i is the probability of occurrence of the intensity value i. An entropy close or equal to zero represents a homogeneous region; whereas an entropy greater than zero, indicates a heterogeneous region. Hence, in homogeneous region the value of h tends to 0 (zero) and the balloon force is prevalent on the weighted external energy. On the other hand, the value of h tends to 1 (one) when the region is heterogeneous, leading to the application of the GVF in Equation 6. Unlike the average of the grayscale intensities, the entropy is more sensitive to the variation of the intensities inside the region ahead the pixel of the contour to be deformed. Hence, the GVF in Equation 6 tends to be applied in regions with high entropy, leading the contour to stop in weak boundaries. Besides the use of the entropy, a weighting factor is proposed to decrease the evolution of the contour when regions with low intensities are found:

$$A(x, y) = \frac{1}{N} \sum_{i,j \in S} f(i, j), \tag{12}$$

where N is the number of pixels inside the semi-circular region S, and (x, y) is a pixel of the contour. In Black-Blood MR images, the region outside the vessel wall is composed of low intensity values. Therefore, the proposed weighting factor attenuates the evolution in regions with low intensities, while maintaining the evolution in regions with high intensity pixels. The GVF in Equation 6 was replaced by the NNGVF to handle more efficiently with regions corrupted by noise, and the following modified weighted external energy is proposed to find the boundaries of carotid arteries:

$$E_{ext} = A * ((F_{balloon} * (1 - \Omega)) + (F_{NNGVF} * \Omega)), \tag{13}$$

where A is the weighting factor calculated for each contour pixel as defined in Equation 12. The regions S and T used to calculate the values of AD and h defined in Equations 9 and 10 were defined as semi-circular shaped regions to improve the capture range of the pixels ahead the pixel of the contour to be expanded towards the boundary of the carotid artery.

2.2.3 Ellipse constraint

Variations in the intensities of the input image can be responsible for fitting the identified lumen contour in local regions and hindering its evolution beyond the boundary of the lumen region, leading the contour to assume an irregular shape. Parts of the lumen contour with incomplete evolution still remain inside or close to the boundary of the lumen region, which could impede the evolution towards the true boundary of the carotid artery. Therefore, a geometrical constraint is employed here to force the lumen contour to completely expand beyond the boundary of the lumen region and avoid local incomplete evolutions in regions with non-uniform grayscale intensity.

The constraint E_{con} in Equation 3 is employed to control the geometrical shape of the contour. In this study, the ellipse constraint proposed in Ray et al. [36] and Wang et al. [31] is used to maintain the ellipsoid shape of the expanded contour:

$$
\begin{aligned}
x_i - \lambda \left(c_x + r_1 * cos(\theta_i - \theta_m) * cos(\theta_m) - r_2 * sin(\theta_i - \theta_m) * sin(\theta_m) \right), \\
y_i - \lambda \left(c_y + r_1 * cos(\theta_i - \theta_m) * sin(\theta_m) + r_2 * sin(\theta_i - \theta_m) * cos(\theta_m) \right),
\end{aligned} \tag{14}
$$

where $[c_x, c_y]$ is the centroid of the contour, θ_m is the angle of the major axis of the contour with respect to x-axis, $r1$ and $r2$ are the radius of the major and minor axis of the contour, respectively, θ_i is the angle of the ith pixel of the contour with respect to its major axis, and x_i and y_i are the ith pixels of the contour. The employed constraint penalizes the pixels of contours that are assuming non-ellipsoid shapes.

The Equation 14 is integrated into the Snake model defined by Equation 3, which is applied to the images resulting from the gray-weighted distance proposed in Equation 1 to expand the lumen contour beyond the boundaries of the lumen region. Examples of the expansion of the lumen contour performed by the Snake model with the ellipse constraint are shown in Figures 5 and 6.

As shown in Figure 5b, the lumen and carotid wall boundaries in the images representing the distance maps progressively increase the magnitudes and convergence of the gradient vectors. It is due to the fact that the gradient magnitude of the distance map
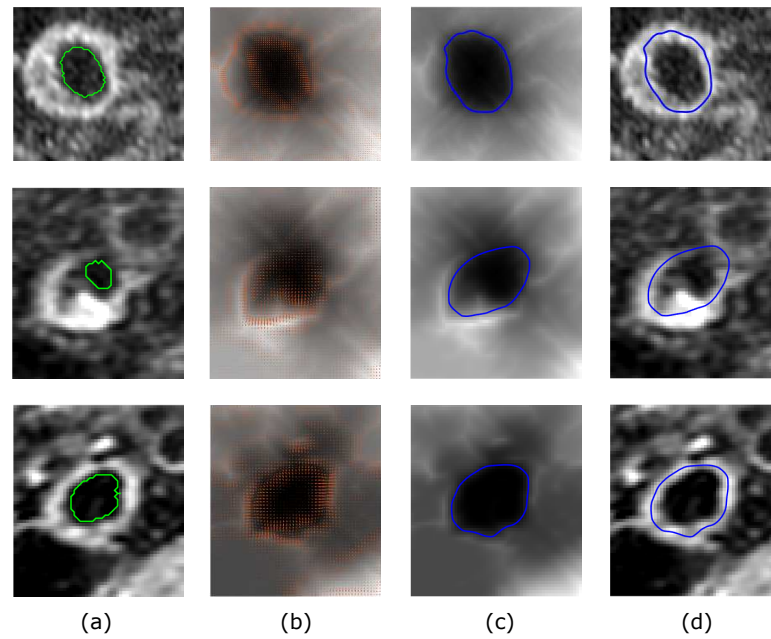
(a)   (b)   (c)   (d)

Figure 5: Examples of the expansion of lumen contours resulting from the Snake model with ellipse constraint applied to images obtained based on the gray-weighted distance: a) Original MR images with the segmented lumen contours in green; b) The gradient vectors (in orange) calculated from the images obtained based on the gray-weighted distance; c) The expanded lumen contours (in blue) overlapped on the images representing the distance maps; d) The expanded lumen contours overlapped on the original MR images.
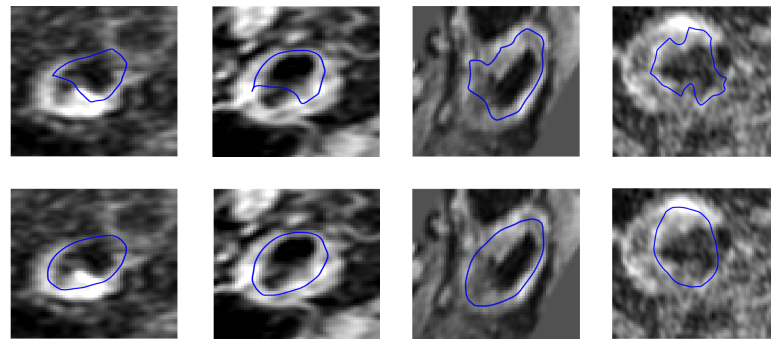

Figure 6: Examples of the expansion of lumen contours performed by the Snake model without (first row) and with (second row) taking into account the ellipse constraint.

image is proportional to the distance value associated to each pixel [37]. Therefore, the magnitude of the gradient vectors tends to increase at regions with higher distances calculated with respect to the centre of the lumen region, leading the contour to expand beyond the boundaries of the lumen region as shown in Figure 5d.

In Figure 6, the contours generated by the Snake model without taking into account the ellipse constraint were trapped by grayscale intensity variations inside the carotid wall. Particularly, the examples shown in the first row of Figure 6 depicted an incomplete

evolution of the contours caused by gradient vectors with high magnitudes in the low intensities regions close to the lumen boundary. However, after the employment of the ellipse constraint, the contours overcome the regions with high intensity variations and maintain their shapes more regular when compared to the ones obtained by the Snake model without taking into account the ellipse constraint.

2.3   Validation measures

The contours segmented by the proposed approach and the corresponding manual delineations were compared based on four measures: Dice coefficient (DC), Polyline distance (PD), mean contour distance (MCD) and centroid distance (CD). The Dice coefficient is used to calculate the overlap between the automatic (S_{auto}) and manual (S_{manual}) segmentations:

$$DC = \frac{2 * |S_{auto} \cap S_{manual}|}{|S_{auto}| + |S_{manual}|}. \tag{15}$$

The Polyline distance represents the average minimum distance between two sets of points, i.e., image pixels, and indicates how far one set is from the other one, being calculated as:

$$D_s(B_1, B_2) = \frac{d(B_1, B_2) + d(B_2, B_1)}{N(B_1) + N(B_2)}, \tag{16}$$

where B_1 and B_2 are the two sets of points under comparison, $N(B_1)$ and $N(B_2)$ are the number of points in B_1 and B_2, respectively, and $d(B_1, B_2) = \sum_{v \in B_1} min\{d(v, s)\}$ and $d(B_2, B_1) = \sum_{s \in B_2} min\{d(s, v)\}$.

An under- and over-estimation of the segmented region may affect the values calculated by the Dice coefficient. However, the centroid difference between the contour segmented by the proposed approach and the corresponding manual delineation is low when the approach finds the correct location of the region. Therefore, the centroid difference was also employed according to:

$$CD = \sqrt{(x_s - x_g)^2 + (y_s - y_g)^2}, \tag{17}$$

where (x_s, y_s) and (x_g, y_g) represent the centroids of the segmented region and of the corresponding manual delineation, respectively. The higher the centroid distance, the greater the distance between the regions.

The lumen area, total carotid area, average lumen diameter, average carotid diameter and vessel wall thickness of the automatic and manual segmentations of the lumen and

carotid artery contours were also calculated to compare the segmentation results by means of the linear regression analysis and Bland-Altman analysis. The lumen area and the total carotid area are the absolute areas inside the contours of the lumen and carotid artery, respectively, and the average diameter (AVD) of the segmented contours is defined as:

$$AVD = \frac{1}{N} \sum_{i=1}^{N} 2 * r_i, \tag{18}$$

where N is the number of pixels of the contour and r_i is the radius of pixel i^{th}. The vessel wall thickness is defined as the mean distance between the segmented contours of the lumen and carotid artery.

3   Experimental results

A comparison between the contours obtained by the proposed approach and the corresponding ones generated by manual delineations was performed in order to evaluate the accuracy of the segmentation results.

3.1   Initialization of the parameters

The parameters used to segment the boundaries of the carotid arteries in the experimental image dataset are indicated in Table 1.

Table 1: Values of the parameters used in the segmentation of the carotid artery boundaries under analysis.

Parameter	1st step	2nd step
α	0.05	0.05
β	0	1
μ	0.02	0.02
κ	1	1
σ	1	1
Radius of the semi-circle	5	5
Number of iterations	150	500

The value of parameter α was set to 0.05 to avoid the contour to become too rigid in regions with large areas. The value of β was set to 1 (one) in the second step of the proposed approach in order to the final contour of the carotid artery may be more smooth. The value of κ was also set to 1 (one) to avoid the excessive amplitude of the balloon force defined in Equation 5. The value of σ was set to 1 (one) to avoid the excessive smoothing of the boundaries of interest and consequently, the weakening and displacement of the

gradient vectors obtained by the NNGVF. The value of μ and the radius of the semi-circle defined in Equations 9 and 10 were defined experimentally by combining and testing a set of values on the images of three patients randomly selected. In this tuning process, the values chosen for μ varied from 0.01 to 0.07 with intervals of 0.01, whereas the values selected for the radius of the semi-circle were between 2 and 10. The mean Polyline distance was calculated for each combination of the values of μ and the radius of the semi-circle. The value of μ and the corresponding radius that provided the minimum average Polyline distance for the images of the three patients were chosen to be the best for the dataset under study. Due to the high computational cost of the ellipse constraint, the number of iterations used in the first step of the proposed approach was lower than the one used in the second step. However, the value chosen here was able to successfully expand the lumen contour beyond the boundary of the lumen region. Table 2 shows the average values of the Polyline distance for each combination of the parameter μ with the radius of the semi-circle. The average values found for the Dice coefficient, Polyline distance, mean contour distance and centroid distance that led the best combination of μ and the radius of the semi-circle are shown in Table 3.

Table 2: The average values of the Polyline distance (in pixels) for each combination of parameter μ and the radius of the semi-circular region. (The value in bold is the minimum average Polyline distance obtained from the images of the three patients used for tuning these parameters.)

Radius μ	2	3	4	5	6	7	8	9	10
0.01	4.0117	2.8806	2.6332	2.4892	2.5602	2.5722	2.6396	2.7048	2.7265
0.02	3.4291	2.6974	2.5738	**2.4675**	2.598	2.7162	2.7595	2.8254	2.8547
0.03	3.203	2.6762	2.5468	2.5519	2.7642	2.8216	2.8431	2.9811	3.0341
0.04	3.0366	2.6938	2.5171	2.7535	2.9772	3.1496	3.1824	3.1831	3.327
0.05	2.9615	2.5438	2.6402	2.9168	3.1949	3.3402	3.4034	3.5569	3.6093
0.06	2.717	2.7496	2.9286	3.9539	3.4282	3.6216	3.6871	3.7895	3.8347
0.07	2.9005	3.0912	3.3454	3.6456	3.8288	3.9332	3.9784	3.9583	4.0072

Table 3: Average values found for the Dice coefficient, Polyline distance, mean contour distance and centroid distance that led to the best combination of μ and the radius of the semi-circle.

Validation measure	Weighted external energy	NNGVF
Dice coefficient	0.8625 ± 0.0863	0.7666 ± 0.1202
Polyline distance (px)	2.4675 ± 1.7135	4.001 ± 2.7791
Mean contour distance (px)	2.4561 ± 1.6779	3.2355 ± 1.5508
Centroid distance (px)	2.9309 ± 2.6268	5.2198 ± 2.9887

*NNGVF=Neighbourhood-Extending and Noise-Smoothing Gradient Vector Flow; px=pixels.

3.2 Performance of the proposed method

Examples of carotid artery boundaries segmented by the proposed approach and the corresponding manual delineations are shown in Figure 7.
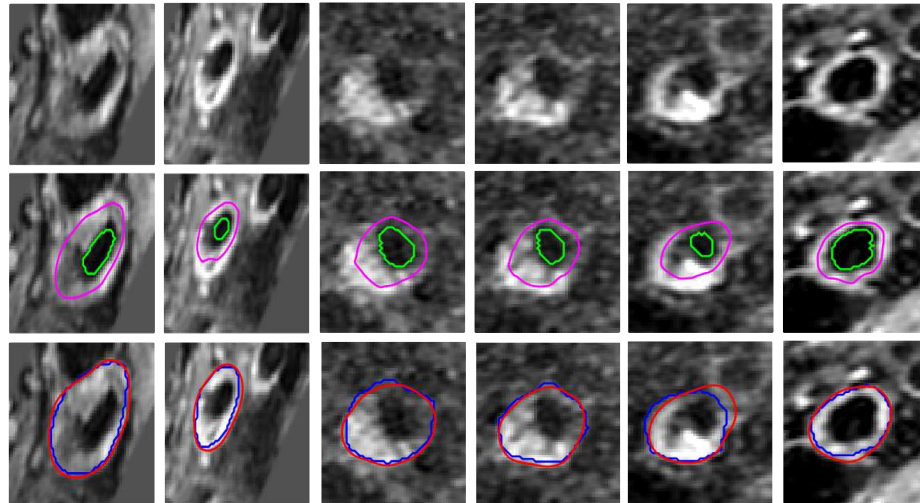

Figure 7: Examples of carotid artery boundaries segmented by the proposed approach: In the first row, original PDW MR images; in the second row, lumen contours (in green) along with the contours expanded based on the images obtained by the gray-weighted distance (in magenta) which were then used to initiate the segmentation of the carotid artery boundaries; in the third row, carotid artery boundaries segmented by the Snake model with the proposed weighted external energy (in red) and the corresponding manual delineations (in blue).

The lumen contours shown in green in the second row of Figure 7 were obtained by the automatic method proposed in Jodas et al. [19] for the segmentation of the lumen region, whereas the ones obtained from these contours by their expansion, using the Snake model with the ellipse constraint on the images obtained by the gray-weighted distance, are represented in magenta. In the third row of the same figure, the contours illustrated in red are the carotid artery boundaries found by the Snake model with the proposed weighted external energy, and the contours shown in blue are the corresponding manual delineations. From the images shown, it is possible to notice that the carotid artery boundaries were correctly segmented in all images, being the automated results very close to the corresponding manual delineations.

The comparison performed between the carotid artery boundaries obtained by the Snake model with the proposed weighted external energy and those generated by only taking into account the forces calculated by the NNGVF is depicted in Figure 8.

As shown in the second row of Figure 8, the proposed approach is effective to expand the lumen contour to the true boundary of the carotid artery. The incomplete evolution
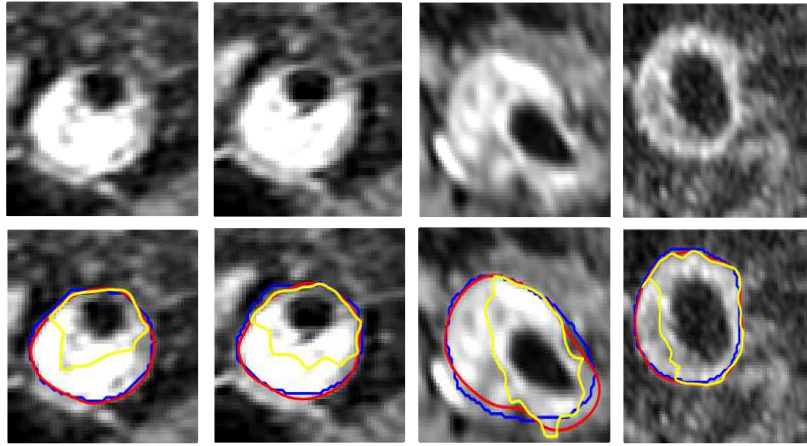
Figure 8: Comparison between the carotid artery boundaries obtained by the Snake model with the proposed weighted external energy (in red) and the ones generated by only taking into account the forces calculated by the NNGVF (in yellow). (The corresponding manual delineations are shown in blue; the original PDW MR images are shown in the first row.)

of the lumen contour when only the forces calculated by the NNGVF are used owes to the large thickness and grayscale intensity variations inside the wall of the carotid artery under analysis.

Regarding the quantitative analysis, the Dice coefficients between the carotid artery boundaries obtained by the Snake model with the proposed weighted external energy (in red) and the corresponding manual delineations (in blue) shown in the second row of Figure 8 were 0.97, 0.96, 0.93 and 0.97, respectively. In contrast, the Dice coefficients between the Snake model with the NNGVF (in yellow) and the corresponding manual delineations (in blue) were 0.65, 0.72, 0.71 and 0.87, respectively. The distribution of the Dice coefficients calculated from the segmented lumen and carotid artery regions and the corresponding manual delineations are depicted according to intervals of 0.2 in Figures 9 and 10, respectively.

In terms of the lumen segmentation results, the interval of Dice coefficients between 0 and 0.20 includes the images erroneously segmented. From the 185 PDW MR images used in the experiments, the lumen region was successfully segmented in 139 images. As depicted in Figure 9, the images with Dice coefficients between 0 and 0.20 represent 26% (49 images) of the total segmentation results. The images with Dice coefficients ranging from 0.21 to 0.40 (4 images) and from 0.41 to 0.60 (11 images) represent only 2% and 6%, respectively, of the total segmentation of the lumen regions. In contrast, the resultant images with Dice coefficients ranging from 0.61 to 0.80 (42 images) and from 0.81 to 1.00 (79 images) represent 23% and 43% of the total segmented images, respectively, reaching in total the greatest percentage of the total number of images used
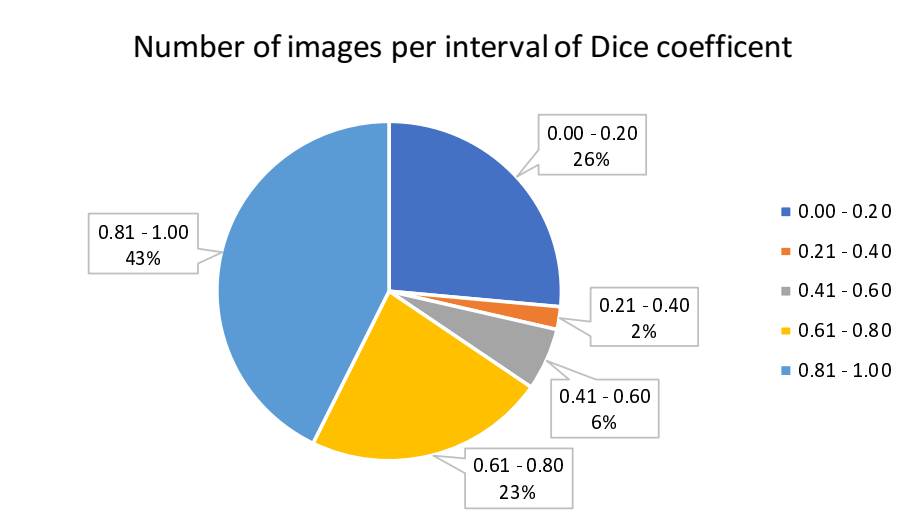
Number of images per interval of Dice coefficent

Figure 9: Intervals of Dice coefficients calculated from the segmented lumen regions and the corresponding manual delineations.
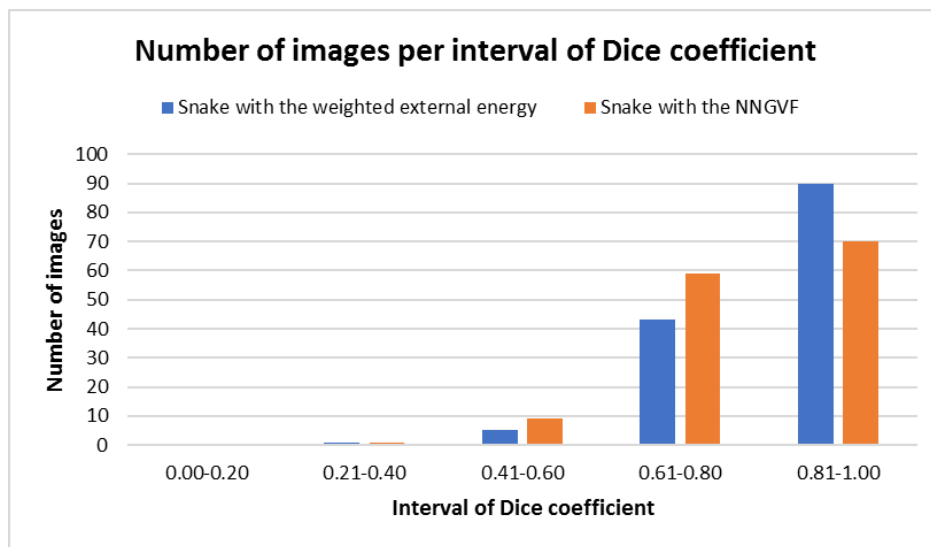

Figure 10: Intervals of Dice coefficients calculated from the segmented carotid artery regions and the corresponding manual delineations.

in the experiments. Regarding the segmentation of the carotid artery boundaries, the number of images having Dice coefficients between 0.81 and 0.90 is higher for the Snake model with the proposed weighted external energy in comparison with the Snake model with only the forces calculated by the NNGVF. As shown in Figure 10, 90 images with Dice coefficients between 0.81 and 1.00 were successfully segmented. In contrast, the number of images with Dice coefficients in the same interval decreased to 76 when the Snake model with only the NNGVF forces was employed.

The average values found for the Dice coefficient, Polyline distance, mean contour

distance and centroid distance of the segmented lumen contours in comparison with the corresponding manual delineations are indicated in Table 4. Additionally, the average values of the same quantitative measures calculated from the segmented carotid artery boundaries and the corresponding manual delineations are indicated in Table 5.

Table 4: Average values found for the Dice coefficient, Polyline distance (PD), mean contour distance (MCD) and centroid distance (CD) concerning the lumen segmentation.

	Dice $\pm$ std	PD $\pm$ std (px)	MCD $\pm$ std (px)	CD $\pm$ std (px)
Patient 1	0.86 ± 0.06	1.50 ± 0.57	1.39 ± 0.51	1.95 ± 1.03
Patient 2	0.71 ± 0.17	2.65 ± 1.26	2.60 ± 1.70	3.30 ± 2.51
Patient 3	0.81 ± 0.17	1.24 ± 1.28	0.77 ± 0.50	1.49 ± 1.88
Patient 4	0.48 ± 0.21	2.24 ± 0.30	1.63 ± 0.67	1.63 ± 0.05
Patient 5	0.82 ± 0.10	0.78 ± 0.27	0.69 ± 0.18	0.96 ± 0.42
Patient 6	0.75 ± 0.15	2.51 ± 2.81	2.62 ± 3.62	3.24 ± 4.92
Patient 7	0.78 ± 0.11	1.16 ± 0.29	1.11 ± 0.37	1.55 ± 0.63
Patient 8	0.83 ± 0.12	1.15 ± 0.59	1.18 ± 0.68	1.22 ± 0.74
Patient 9	0.73 ± 0.22	1.14 ± 0.67	1.03 ± 0.85	1.45 ± 0.95
Patient 10	0.69 ± 0.22	1.81 ± 2.38	1.90 ± 2.99	2.03 ± 3.32
Patient 12	0.69 ± 0.21	2.07 ± 2.60	2.09 ± 3.14	2.43 ± 3.15
Average	0.76 ± 0.17	1.49 ± 1.53	1.40 ± 1.81	1.80 ± 2.20

*px = pixels; std = standard deviation.

In terms of the lumen segmentation results, the average values of the Dice coefficient obtained from patient 1 are greater than the ones obtained from the other patients, as indicated in Table 4. In contrast, the averages values of the Polyline, mean contour and centroid distances are lower for patient 5 relatively to the averages values of the other patients. As indicated in Table 5, the results obtained using the Snake model with the proposed weighted external energy for the segmentation of the carotid artery boundaries are better than the majority obtained using the Snake model with the NNGVF. Regarding the average values of the validation measures, the Dice coefficient increased from 0.80 ± 0.11 to 0.83 ± 0.11 when the proposed weighted external energy was used in the Snake model. The averages values of the Polyline distance decreased from 3.01 ± 2.05 pixels to 2.70 ± 1.69 pixels after the usage of the Snake model with the proposed weighted external energy. Additionally, the average value of the centroid distance obtained for the proposed approach is lower than the one obtained for the Snake model with the NNGVF (3.44 ± 2.82 pixels against 4.18 ± 2.97, respectively).

The Linear regression and Bland-Altman analysis concerning the lumen area and the average lumen diameter showed a good correlation between the segmented lumen contours and the corresponding manual delineations, as can be observed in Figure 11. The linear regression and Bland-Altman analysis for the total carotid area, average carotid diameter and vessel wall thickness calculated concerning the segmented carotid artery boundaries and the corresponding manual delineations are depicted in Figures 12 and 13.

Table 5: Averages values found for the Dice coefficient, Polyline distance (PD), mean contour distance (MCD) and centroid distance (CD) regarding the segmentation of the carotid artery boundaries.

	Method	Dice ± std	PD ± std (px)	MCD ± std (px)	CD ± std (px)
Patient 1	Proposed weighted external energy	0.80 ± 0.08	4.36 ± 1.91	4.09 ± 1.66	5.45 ± 2.84
	NNGVF	0.79 ± 0.07	4.49 ± 1.84	4.07 ± 1.28	6.35 ± 2.52
Patient 2	Proposed weighted external energy	0.77 ± 0.11	3.51 ± 1.68	3.62 ± 2.13	4.92 ± 3.30
	NNGVF	0.75 ± 0.11	3.56 ± 1.49	3.69 ± 1.49	4.81 ± 3.05
Patient 3	Proposed weighted external energy	0.92 ± 0.04	1.19 ± 0.55	1.20 ± 0.52	1.23 ± 1.21
	NNGVF	0.80 ± 0.12	3.72 ± 3.88	2.38 ± 1.37	4.80 ± 3.55
Patient 4	Proposed weighted external energy	0.85 ± 0.06	2.07 ± 1.02	2.23 ± 1.14	2.76 ± 2.44
	NNGVF	0.78 ± 0.02	2.72 ± 0.56	2.77 ± 1.00	4.27 ± 1.08
Patient 5	Proposed weighted external energy	0.76 ± 0.14	3.06 ± 1.85	3.17 ± 1.94	4.08 ± 3.45
	NNGVF	0.81 ± 0.12	2.29 ± 1.40	2.36 ± 1.32	3.56 ± 3.20
Patient 6	Proposed weighted external energy	0.77 ± 0.12	3.99 ± 2.37	4.41 ± 3.07	5.86 ± 4.32
	NNGVF	0.81 ± 0.12	2.93 ± 2.13	3.24 ± 2.76	5.08 ± 4.20
Patient 7	Proposed weighted external energy	0.88 ± 0.05	2.09 ± 0.90	2.20 ± 1.01	2.88 ± 1.73
	NNGVF	0.82 ± 0.10	2.88 ± 1.66	2.83 ± 1.45	3.97 ± 2.62
Patient 8	Proposed weighted external energy	0.87 ± 0.06	2.05 ± 0.83	2.20 ± 0.95	2.25 ± 1.23
	NNGVF	0.88 ± 0.05	1.69 ± 0.63	1.88 ± 0.78	2.26 ± 1.28
Patient 9	Proposed weighted external energy	0.83 ± 0.09	2.82 ± 1.34	2.93 ± 1.57	3.40 ± 2.44
	NNGVF	0.72 ± 0.13	4.04 ± 1.71	3.70 ± 1.49	5.07 ± 2.56
Patient 10	Proposed weighted external energy	0.82 ± 0.10	2.43 ± 1.64	2.50 ± 1.85	2.97 ± 2.03
	NNGVF	0.80 ± 0.11	2.44 ± 1.38	2.61 ± 1.65	3.54 ± 2.87
Patient 12	Proposed weighted external energy	0.77 ± 0.19	3.19 ± 2.17	3.18 ± 2.36	4.26 ± 4.04
	NNGVF	0.77 ± 0.18	3.10 ± 2.02	3.16 ± 2.21	4.46 ± 3.77
Average ± Std	Proposed weighted external energy	0.83 ± 0.11	2.70 ± 1.69	2.79 ± 1.89	3.44 ± 2.82
	NNGVF	0.80 ± 0.11	3.01 ± 2.05	2.87 ± 1.67	4.18 ± 2.97

*NNGVF = Neighbourhood-Extending and Noise-Smoothing Gradient Vector Flow; std = standard deviation; px = pixels.

As shown in Figure 11a, the Spearman correlation between the segmented lumen contours and the corresponding manual delineations was high and similar for both measures, reaching a value of 0.8811 and 0.8764 for the lumen area and average lumen diameter, respectively. For the segmentation of the carotid artery boundaries, the Spearman correlation between the total carotid areas obtained from the Snake model with the proposed weighted external energy and the corresponding areas generated from the manual delineations was 0.7956, which is higher in comparison with the correlation coefficient of the segmentation results obtained by the Snake model with the NNGVF (0.7338). Regarding the average carotid diameter, the Spearman correlation between the segmentations obtained by the proposed approach and the corresponding manual delineations was 0.7974, which is also better than the one obtained from the comparison between the Snake model with the NNGVF and the manual delineations (0.7333). Additionally, the Spearman

Lumen area

Average lumen diameter
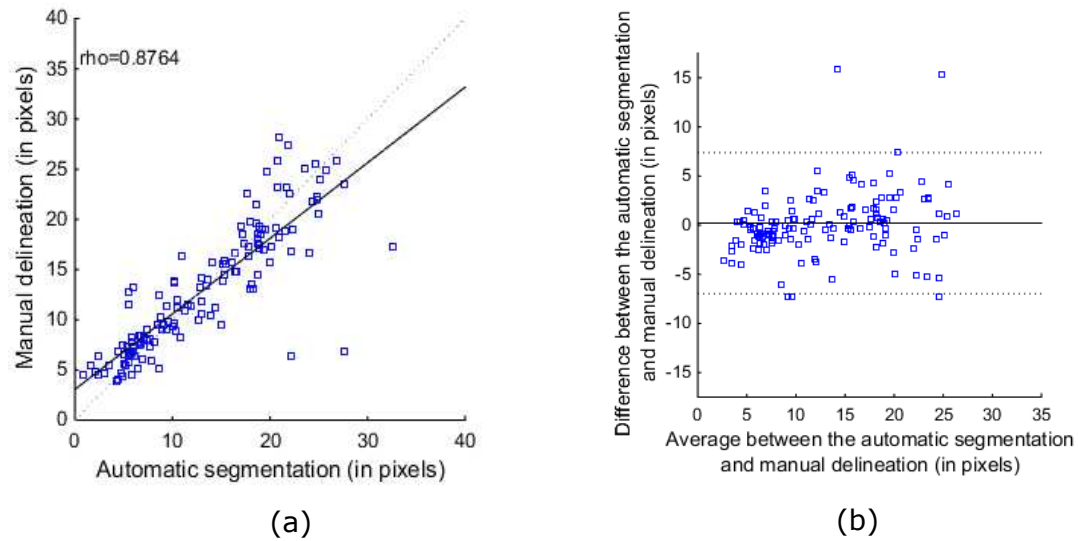

(a)   (b)
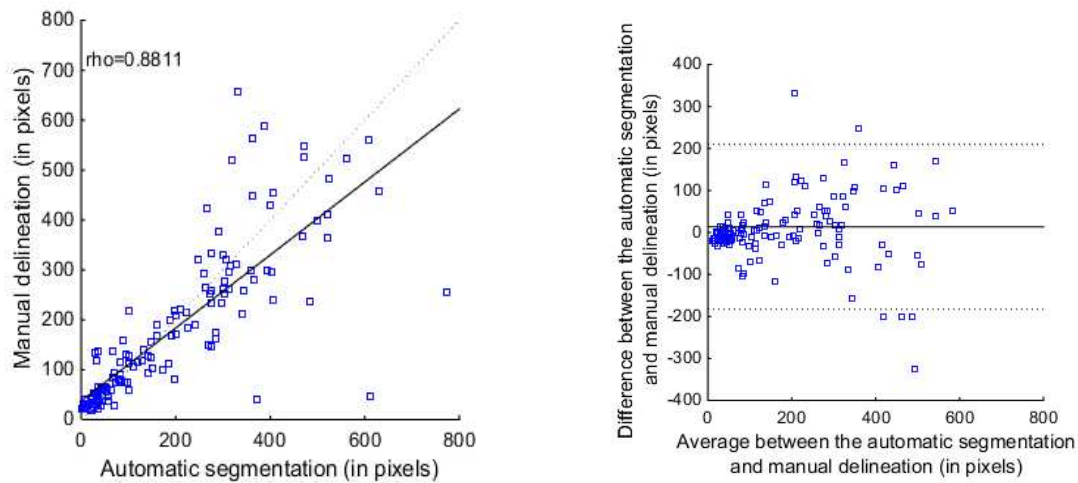
Figure 11: Linear regression (a) and Bland-Altman analysis (b) concerning the lumen area and average lumen diameter calculated from the segmented lumen contours and the corresponding manual delineations.

correlation between the proposed approach and the corresponding manual delineations showed also better results in comparison with the Snake model with the NNGVF regarding the vessel wall thickness (0.6308 and 0.6041, respectively). The differences between the segmented lumen contours and the corresponding manual delineations are shown in the Bland-Altman plots of Figure 11b. The Bland-Altman analysis of the carotid artery boundaries segmented by the Snake model with the proposed weighted external energy
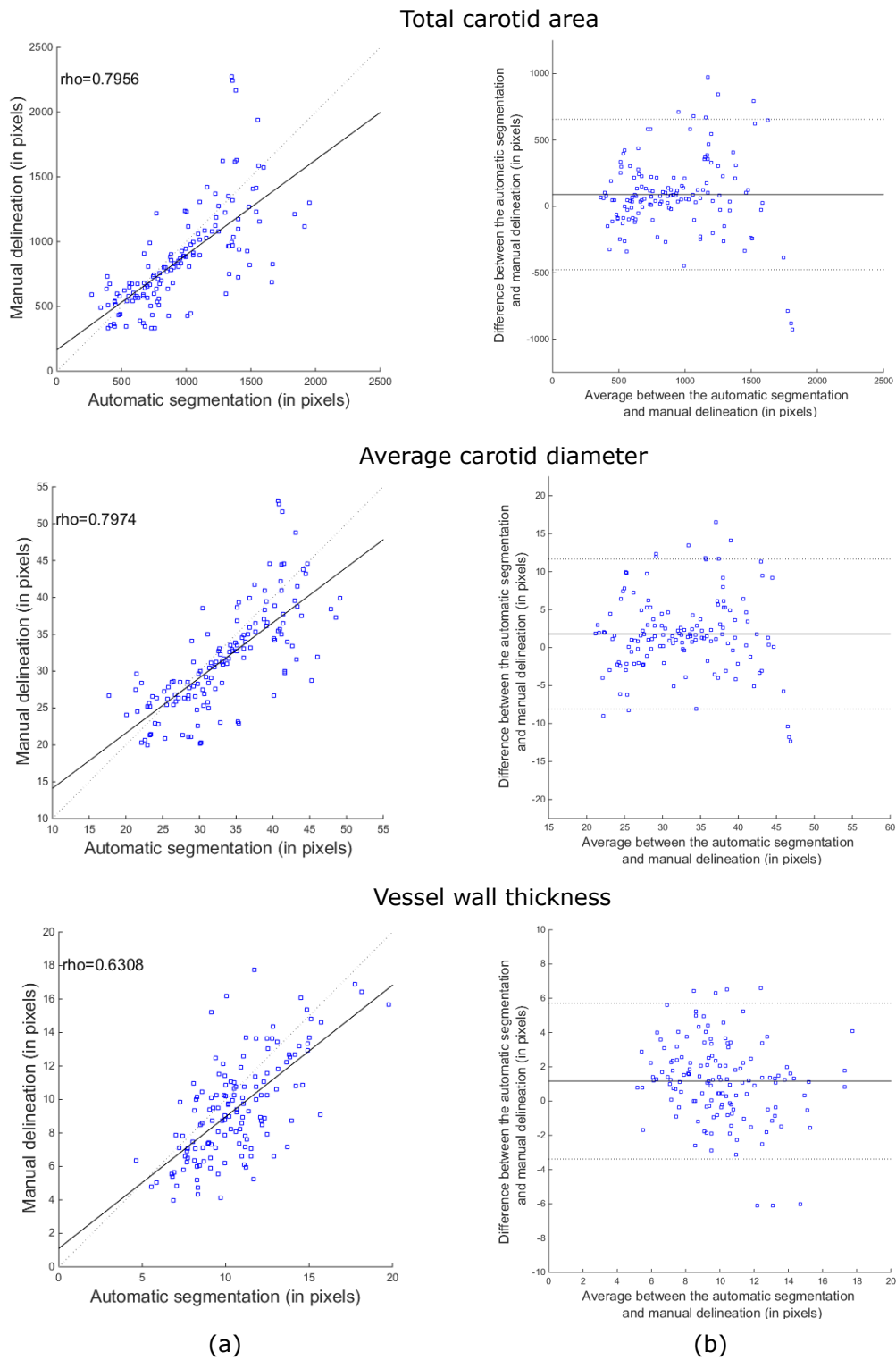
Figure 12: Linear regression (a) and Bland-Altman analysis (b) concerning the total carotid area, average carotid diameter and vessel wall thickness calculated from the carotid artery contours segmented by the Snake model with the proposed weighted external energy and the corresponding manual delineations.
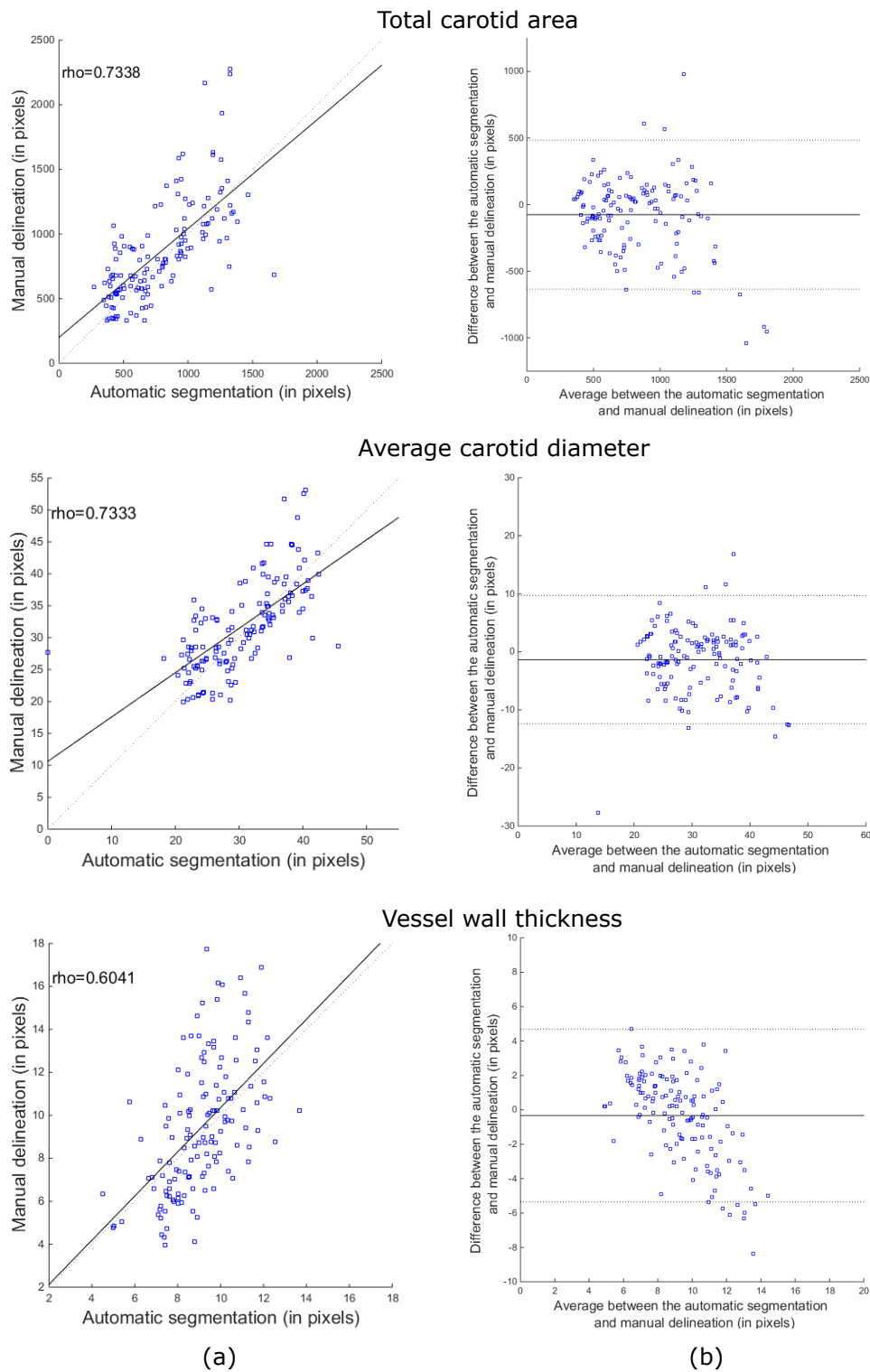
Figure 13: Linear regression (a) and Bland-Altman analysis (b) concerning the total carotid area, average carotid diameter and vessel wall thickness calculated from the carotid artery contours segmented by the Snake model with the NNGVF and the corresponding manual delineations.

and NNGVF are depicted in Figures 12b and 13b, respectively. Regarding the lumen area, the average difference between the segmented lumen contours and the corresponding manual delineations was 13.50 pixels. For the average lumen diameter, the average difference between the segmented and manually delineated lumen contours was 0.21 pixels. For the total carotid area and average carotid diameter, the average differences between the proposed approach and manual delineations were 90 and 1.8 pixels, respectively. The average difference between the vessel wall thickness calculated from the carotid artery boundaries segmented by the proposed approach and the ones calculated from corresponding manual delineations was 1.2 pixels. The high average difference of the total carotid area was due to the similar intensities in regions close to the boundaries of the carotid arteries, which makes the distinction between the carotid boundaries and the image background more difficult. Examples of carotid artery boundaries segmented by the proposed approach in images with background regions having intensities similar to the ones of the carotid artery boundaries are illustrated in Figure 14.

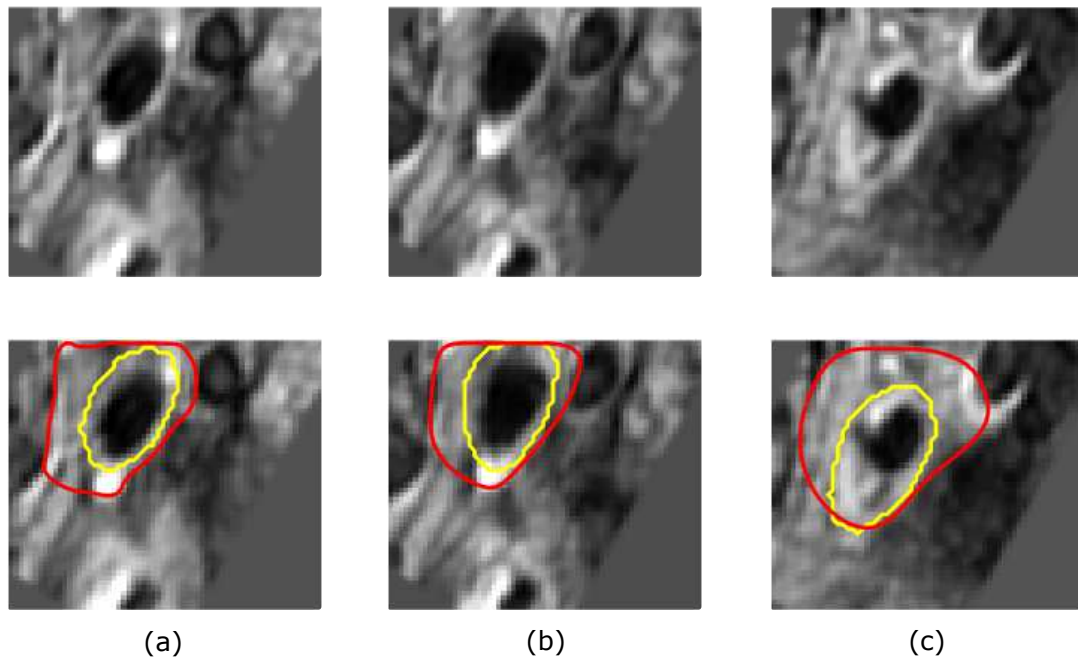| (a) | (b) | (c) |

Figure 14: Examples of carotid artery boundaries segmented by the proposed approach in PDW MR images with indistinguishable boundaries: The first row shows the original PDW MR images and the second row presents the segmented carotid artery boundaries (in red) along with the corresponding manual delineations (in yellow). (The differences found between the areas of the segmented and manually delineated carotid artery boundaries shown in images (a-c) were 399 pixels, 297 pixels and 582 pixels, respectively.)

As depicted in Figure 14, the carotid artery boundaries segmented by the Snake model with the proposed weighted external energy overestimated the corresponding manual de-

lineations due to the similar grayscale intensities surrounding the true boundaries of interest, leading to the increase of the difference between the areas of the automatically segmented and manually delineated carotid artery boundaries.

4   Discussion

The development of automatic segmentation methods dedicated to medical images plays an important role in providing experts with auxiliary diagnosis tools for identifying various types of diseases. For example, the segmentation of the lumen and carotid artery boundaries in MR images represents an important step to quickly identify and quantify possible atherosclerosis in arteries. The segmentation of the carotid artery boundaries in PDW MR images was successfully tackled in this study. The use of the images obtained by the gray-weighted distance to expand the lumen contour beyond the boundary of the lumen region in the input image represents an important contribution to correctly identify the boundary of the carotid artery. Additionally, the usage of the proposed weighted external energy in the Snake model proved to be effective in expanding the lumen contours towards the boundaries of carotid arteries even in cases of large thickness. The modification in the external energy proposed by Khadidos et al. [35] makes the convergence of the lumen contours more robust, stable and appropriate for carotid arteries with weak edges.

4.1   Initialization of the parameters

The convergence of the lumen contour to the boundary of the carotid artery under analysis depends on the value of parameter α defined for the elasticity term of the Snake model. When the value of α decreases, the contour elasticity is increased, leading to an easier evolution towards the boundary of interest. In contrast, the contour becomes more rigid as the value of α increases, leading the contour to deflate even in regions with large capture range provided by the gradient vectors. Hence, it was decided to use a low value for parameter α in order to avoid the swift convergence and shrinking of the lumen contour. Parameter β defined for the curvature term in Equation 3 is employed to control the smoothness and bend of the contour. The higher is the value of β, the more smooth the contour is. In the second step of the proposed approach, the value of β was set to 1 (one) in order to smooth the final contour of the carotid artery boundary. Parameter μ represents a regularization term that controls the tradeoff between the Laplacian operator and the gradient of the image's edge map defined for the NNGVF. The value of the μ depends on the amount of noise in the image under analysis. The higher is the value of μ, more diffuse are the gradient vectors. In this study, the low value of μ determined by

the parameter tuning procedure plays an important role to avoid the excessive diffusion of the gradient vectors and the evolution of the lumen contour beyond the boundary of the carotid artery under analysis. Parameter κ is responsible for the strength of the balloon forces and therefore, used to inflate or deflate the contour to be deformed. When the value of κ increases, the amplitude of the unit vectors defined by the balloon force also increases, leading the contour to pass through weak edges. Since the lumen contour needs to be inflated from the lumen region to the boundary of the carotid artery, the value of κ was set 1 (one) to avoid the excessive amplitude of the balloon forces. Parameter σ is used in the Gaussian filter and has an important role to control the amount of smoothness of the image and the capture range of the gradient vectors. A large value for σ will cause the boundaries to become more smooth and distorted and therefore, the capture range of the gradient vectors will be also increased. In order to avoid excessive distortion of the boundaries of the input image, the value of σ was set to 1 (one). The number of iterations defined for the first step of the carotid artery boundary segmentation was lower than the one of the second step due to the high computational cost imposed by the ellipse constraint. However, the value chosen in this study was sufficient to expand successfully the lumen contour beyond the boundary of the lumen region. The radius of the disk-shaped template used to calculate the values of *AD* and *h* defined in Equations 9 and 10 plays an important role in the correct determination of the carotid artery boundary. Since the entropy of the pixels ahead the lumen contour to be expanded is responsible for the convergence to the carotid artery boundary of interest, a large number of pixels could increase the entropy and lead to a fast and incomplete evolution of the lumen contour. In contrast, a low number of pixels may still decrease the entropy defined in Equation 11 and, consequently, lead the lumen contour to leak the true boundary of the carotid artery. Hence, the parameter tuning procedure was important to determine the best radius for the dataset used in the experiments. The same values for α, β, μ and σ defined for the proposed weighted external energy were also used in the NNGVF formulation.

Although the parameters' values established for the proposed approach were able to efficiently identify the boundaries of the carotid arteries in the images used in this study, the convergence of the lumen contour is mostly dependent on the parameters of the internal energy of the Snake model, the amplitude of the balloon forces and the number of iterations used to perform the convergence of the contour until it fits the desirable boundary. Changing the image resolution may still affect the segmentation results, leading the lumen contour to an incomplete and slow convergence in images with higher resolutions. However, the proposed approach might be easily adapted to initialize and adjust the aforementioned parameters for other MR image datasets.

4.2   Performance of the proposed approach

The distance map proposed in this study proved to be effective in expanding the lumen contour beyond the boundary of the lumen region and therefore, to avoid the gradient vectors that can hinder the contour to converge to the boundary of the carotid artery under analysis. Along with the ellipse constraint, the contour resultant from the Snake model applied to the image representing the distance map becomes more regular and without concavities that may be caused by low intensities regions close to the lumen of the carotid artery.

The modification in the weighted external energy proposed by Khadidos et al. [35] is shown to be successful in converging the lumen contours to the boundaries of carotid arteries with large thickness. The evolution of the lumen contour may still fail due to the diffusion of the gradient vectors in regions with large intensity variations. Balloon forces have been proposed to improve the convergence of the contour based on the strength of the unit vectors in each pixel of the contour to be expanded, leading to a rapid convergence even in regions with large areas. However, the balloon forces still fail in fitting the contour in regions having weak edges, which causes the contour to leak the boundary of interest. Hence, the combination of balloon forces and the GVF based external energy represents an important approach to handle at the same time with the quick evolution of the contour in regions with larges areas and the decrease of the contour evolution in weak edges of the structures under analysis. The use of the entropy instead of the average intensities in Equation 8 improves the convergence of the lumen contour in weak edges of the carotid artery boundary of interest due to the sensitivity of the entropy in regions with high variations of the grayscale intensities. Additionally, the penalty term defined in Equation 12 proved to be effective in decreasing the contour evolution when dark regions corresponding to the background of the image are found.

Regarding the total carotid area, the Bland-Altman analysis depicted in Figures 12b and 13b showed a significant difference between the segmented carotid artery boundaries and the corresponding manual delineations. The bias corresponding to the difference between the total carotid areas calculated from the results obtained by the proposed approach and the ones of the corresponding manual delineations was 89.59 pixels, with a standard deviation of 289.26 pixels. For the average carotid diameter, the bias between the carotid artery boundaries segmented by the proposed approach and the corresponding manual delineations was 1.79 pixels, with standard deviation of 5.04 pixels. The bias between the vessel wall thickness calculated from carotid artery boundaries obtained by the proposed approach and the ones of the corresponding manual delineations was 1.17 pixels with standard deviation of 2.32 pixels. In some cases, the manual delineations can under-

estimate the corresponding carotid artery contours obtained by the Snake model with the proposed weighted external energy. Since the proposed weighted external energy relies on the similarity of the grayscale intensities of the input image, the segmentation error is due to regions with intensities similar to the ones close to the boundary of the carotid artery to be segmented. The gradient vectors of the carotid artery boundary are weaker than the ones of the lumen region, making the segmentation more difficult and susceptible to errors due to the leakage of the contour beyond the true boundary of the carotid artery under analysis.

A comparison with recent studies found in the literature was carried out in order to validate the accuracy of the approach proposed here. Although a direct comparison is hardly possible since the validation measures and the image dataset used in this study are different from the ones used in studies found in the literature, the results obtained from our approach proposed to segment the carotid artery boundaries in PDW MR images are comparable to the ones reported in the related studies found. The average value of the Degree of Similarity (DoS) between the automatic and manual segmentations of the carotid artery boundaries reported by van 't Klooster et al. [15] was 75.3%. The average value of the DoS between the automatic and manual segmentations of the boundaries of the Common Carotid Artery (CCA) reported by Gao et al. [18] was 82.7%. The Jaccard similarity between the automatic and manual segmentations of the boundaries of carotid arteries reported by Saba et al. [17] was 0.71 ± 0.08. The average value of the Dice coefficient between the carotid artery boundaries obtained by our approach and the corresponding contours manually delineated was 0.83 ± 0.11 ($82.61\% \pm 10.84\%$). The Jaccard similarity obtained from the comparison between the carotid arteries segmented by the proposed approach and the corresponding manual delineations was 0.72 ± 0.15. The main limitation of the study carried out by van 't Klooster et al. [15] is that the signal profile vector with a specific length is necessary to find the edges of the lumen and carotid artery boundaries. Additionally, the gradient information is insufficient to handle with weak edges commonly found in MR images of carotid arteries. Although the approach proposed by Saba et al. [17] is similar to the one proposed in this article, its main limitation is the expansion of the lumen contour beyond the boundary of the lumen region by using a heuristic value. Similarly, the method proposed by Gao et al. [18] also relies on the expansion of the lumen contour based on a heuristic value, although the method is fully automatic. In contrast, our proposed approach to segment the boundaries of carotid arteries in PDW MR images is fully automatic and the expansion of the lumen contours is completely performed by using the distance map without any use of heuristic values.

4.3   Limitations

The proposed approach has two limitations. The first one regards the segmentation of carotid arteries with calcifications. Calcifications appears as dark regions in PDW MR images and therefore, the convergence of the lumen contours towards the boundaries of carotid arteries may be compromised due to the strength of the gradient vectors that avoid the expansion of the contour when calcified regions are found. Hence, future studies will be conducted to effectively identify local regions inside the carotid artery that represent possible calcifications. The second limitation regards the segmentation of the lumen and carotid artery boundaries in regions representing bifurcations. Although bifurcation regions have been identified and delineated by the physician in the PDW MR images, the carotid artery boundary manually delineated in the input image having the higher Dice coefficient with the segmented carotid artery boundary was chosen to evaluate the accuracy of the result. Hence, the segmentation of the lumen and carotid artery boundaries in bifurcation regions is expected to be considered in future researches.

5   Conclusions

The segmentation of the lumen and carotid artery boundaries plays an important role in assessing the progression of atherosclerosis. An automatic approach for the segmentation of carotid artery boundaries in PDW MR images was presented in this article. The main contribution of this study is an efficient and robust approach based on the gray-weighted distance map to expand the lumen contour towards the boundary of the carotid artery without the use of any heuristic values. Additionally, the lumen contour expanded by the Snake model with the ellipse constraint applied to the distance map image is used to identify the final boundary of the carotid artery based on the Snake model along with the modified weighted external energy. The proposed approach proved to be also robust in identifying the boundaries of carotid arteries that have large thickness and weak edges.

The comparison between the carotid artery boundaries segmented by the proposed approach and the corresponding manual delineations showed that the usage of the proposed weighted external energy in the Snake model is more effective than if only the NNGVF is used. Additionally, the proposed approach outperformed the results reported in related studies found in the literature.

Futures studies will be conducted to efficiently segment the lumen and carotid artery boundaries in PDW MR images having bifurcations regions. The segmentation of the carotid artery boundaries using other MR image datasets is also expected in order to assess the parameter tuning procedure and the segmentation results in images obtained

with higher resolutions and different acquisition settings. Moreover, the segmentation of the boundaries of carotid arteries having calcified regions is also expected to be addressed in order to avoid the local convergence and incomplete evolution of the segmented lumen contours.

Acknowledgements

References

[1] S. Mendis, P. Puska, and B. Norrving. *Global atlas on cardiovascular disease prevention and control*. World Health Organization, 2011. ISBN 978-92-4-156437-3.

[2] D. S. Jodas, A. S. Pereira, and J. M. R. S. Tavares. A review of computational methods applied for identification and quantification of atherosclerotic plaques in images. *Expert Systems with Applications*, 46:1–14, 2016. ISSN 0957-4174. doi: 10.1016/j.eswa.2015.10.016.

[3] L. Esposito, M. Sievers, D. Sander, P. Heider, O. Wolf, O. Greil, C. Zimmer, and H. Poppert. Detection of unstable carotid artery stenosis using MRI. *Journal of Neurology*, 254(12):1714–1722, December 2007. ISSN 0340-5354. doi: 10.1007/s00415-007-0634-4.

[4] U. R. Acharya, M. R. K. Mookiah, S. Vinitha Sree, D. Afonso, J. Sanches, S. Shafique, A. Nicolaides, L. M. Pedro, J. Fernandes e Fernandes, and J. S. Suri. Atherosclerotic plaque tissue characterization in 2D ultrasound longitudinal carotid scans for automated classification: a paradigm for stroke risk assessment. *Medical & Biological Engineering & Computing*, 51(5):513–523, May 2013. ISSN 0140-0118. doi: 10.1007/s11517-012-1019-0.

[5] L. Esposito-Bauer, T. Saam, I. Ghodrati, J. Pelisek, P. Heider, M. Bauer, P. Wolf, A. Bockelbrink, R. Feurer, D. Sepp, C. Winkler, P. Zepper, T. Boeckh-Behrens,

168

M. Riemenschneider, B. Hemmer, and H. Poppert. MRI plaque imaging detects carotid plaques with a high risk for future cerebrovascular events in asymptomatic patients. *PLoS ONE*, 8(7):e67927, July 2013. ISSN 1932-6203. doi: 10.1371/ journal.pone.0067927.

[6] A. Arias, J. Petersen, A. van Engelen, H. Tang, M. Selwaness, J. C. M. Witteman, A. van der Lugt, W. Niessen, and M. de Bruijne. *Carotid Artery Wall Segmentation by Coupled Surface Graph Cuts*, pages 38–47. Springer Berlin Heidelberg, Berlin, Heidelberg, 2013. ISBN 978-3-642-36620-8. doi: 10.1007/978-3-642-36620-8_5.

[7] A. M. Arias-Lorza, J. Petersen, A. van Engelen, M. Selwaness, A. van der Lugt, W. J. Niessen, and M. de Bruijne. Carotid artery wall segmentation in multispectral MRI by coupled optimal surface graph cuts. *IEEE Transactions on Medical Imaging*, 35 (3):901–911, 2016. ISSN 0278-0062. doi: 10.1109/TMI.2015.2501751.

[8] I. M. Adame, R. J. van der Geest, B. A. Wasserman, M. Mohamed, J. H. Reiber, and B. P. Lelieveldt. Automatic plaque characterization and vessel wall segmentation in magnetic resonance images of atherosclerotic carotid arteries. In *Medical Imaging 2004*, pages 265–273. International Society for Optics and Photonics, 2004. doi: 10.1117/12.532471.

[9] I. M. Adame, R. J. van der Geest, B. A. Wasserman, M. A. Mohamed, J. H. Reiber, and B. P. Lelieveldt. Automatic segmentation and plaque characterization in atherosclerotic carotid artery MR images. *Magnetic Resonance Materials in Physics, Biology and Medicine*, 16(5):227–234, 2004. ISSN 1352-8661. doi: 10.1007/s10334-003-0030-8.

[10] Fang Wang, Qiu Guan, S. Chen, Zhongzhao Teng, U. Sadat, and J. Gillard. Multiscale segmentation of carotid artery wall in MRI images. In *The 2nd International Conference on Information Science and Engineering*, pages 1–4. IEEE, December 2010. ISBN 978-1-4244-7616-9. doi: 10.1109/ICISE.2010.5688938.

[11] C. Yuan, E. Lin, J. Millard, and J. N. Hwang. Closed contour edge detection of blood vessel lumen and outer wall boundaries in black-blood MR images. *Magnetic Resonance Imaging*, 17(2):257–266, 1999. ISSN 0730725X. doi: 10.1016/S0730-725X(98)00162-3.

[12] H. M. Ladak, J. B. Thomas, J. R. Mitchell, B. K. Rutt, and D. A. Steinman. A semi-automatic technique for measurement of arterial wall from black blood MRI. *Medical Physics*, 28(6):1098–1107, 2001. ISSN 0094-2405. doi: 10.1118/1.1368125.

[13] G. Adams, G. W. Vick III, C. Bordelon, W. Insull, and J. Morrisett. An algorithm for quantifying advanced carotid artery atherosclerosis in humans using MRI and active contours. In *Proc. SPIE*, volume 4684, pages 1448–1457. International Society for Optics and Photonics, 2002. doi: 10.1117/12.467110.

[14] H. Tang, R. S. van Onkelen, T. van Walsum, R. Hameeteman, M. Schaap, F. L. Tori, Q. J. A. van den Bouwhuijsen, J. C. M. Witteman, A. van der Lugt, L. J. van Vliet, and W. J. Niessen. *A Semi-automatic Method for Segmentation of the Carotid Bifurcation and Bifurcation Angle Quantification on Black Blood MRA*, pages 97–104. Springer Berlin Heidelberg, Berlin, Heidelberg, 2010. ISBN 978-3-642-15711-0. doi: 10.1007/978-3-642-15711-0_13.

[15] R. van 't Klooster, P. J. de Koning, R. A. Dehnavi, J. T. Tamsma, A. de Roos, J. H. Reiber, and R. J. van der Geest. Automatic lumen and outer wall segmentation of the carotid artery using deformable three-dimensional models in MR angiography and vessel wall images. *Journal of Magnetic Resonance Imaging*, 35(1):156–165, January 2012. ISSN 10531807. doi: 10.1002/jmri.22809.

[16] K. Hameeteman, R. van 't Klooster, M. Selwaness, A. van der Lugt, J. C. M. Witteman, W. J. Niessen, and S. Klein. Carotid wall volume quantification from magnetic resonance images using deformable model fitting and learning-based correction of systematic errors. *Physics in Medicine and Biology*, 58(5):1605–1623, March 2013. ISSN 0031-9155. doi: 10.1088/0031-9155/58/5/1605.

[17] L. Saba, H. Gao, E. Raz, S. V. Sree, L. Mannelli, N. Tallapally, F. Molinari, P. P. Bassareo, U. R. Acharya, H. Poppert, and J. S. Suri. Semiautomated analysis of carotid artery wall thickness in MRI. *Journal of Magnetic Resonance Imaging*, 39 (6):1457–1467, June 2014. ISSN 10531807. doi: 10.1002/jmri.24307.

[18] S. Gao, R. van 't Klooster, A. Brandts, S. D. Roes, R. Alizadeh Dehnavi, A. de Roos, J. J. Westenberg, and R. J. van der Geest. Quantification of common carotid artery and descending aorta vessel wall thickness from MR vessel wall imaging using a fully automated processing pipeline. *Journal of Magnetic Resonance Imaging*, 45 (1):215–228, January 2017. ISSN 10531807. doi: 10.1002/jmri.25332.

[19] D. S. Jodas, A. S. Pereira, and J. M. R. S. Tavares. Automatic segmentation of the lumen region in intravascular images of the coronary artery. *Medical Image Analysis*, 40:60–79, 2017. ISSN 1361-8415. doi: 10.1016/j.media.2017.06.006.

[20] A. van Engelen, W. J. Niessen, S. Klein, H. C. Groen, H. J. M. Verhagen, J. J. Wentzel, A. van der Lugt, and M. de Bruijne. Atherosclerotic plaque component segmentation in combined carotid MRI and CTA data incorporating class label uncertainty. *PLoS ONE*, 9(4):1–14, April 2014. ISSN 1932-6203. doi: 10.1371/journal.pone.0094840.

[21] K. Qian, S. Cao, and P. Bhattacharya. Skeletonization of gray-scale images by gray weighted distance transform. In *AeroSense'97*, pages 224–228. International Society for Optics and Photonics, 1997. doi: 10.1117/12.280625.

[22] D. Baggett, M.-a. Nakaya, M. McAuliffe, T. P. Yamaguchi, and S. Lockett. Whole cell segmentation in solid tissue sections. *Cytometry Part A*, 67(2):137–143, 2005. ISSN 1552-4930. doi: 10.1002/cyto.a.20162.

[23] R. Strand. Minimal paths by sum of distance transforms. In *International Conference on Discrete Geometry for Computer Imagery*, pages 349–358. Springer, 2016. ISBN 978-3-319-32360-2. doi: 10.1007/978-3-319-32360-2_27.

[24] P. Soille. Generalized geodesy via geodesic time. *Pattern Recognition Letters*, 15 (12):1235–1240, 1994. ISSN 0167-8655. doi: 10.1016/0167-8655(94)90113-9.

[25] T. McInerney and D. Terzopoulos. Deformable models in medical image analysis: a survey. *Medical Image Analysis*, 1(2):91–108, 1996. ISSN 1361-8415. doi: 10.1016/S1361-8415(96)80007-7.

[26] Z. Ma, J. M. R. S. Tavares, R. N. Jorge, and T. Mascarenhas. A review of algorithms for medical image segmentation and their applications to the female pelvic cavity. *Computer Methods in Biomechanics and Biomedical Engineering*, 13(2):235–246, 2010. ISSN 1025-5842. doi: 10.1080/10255840903131878.

[27] H. Tang, T. van Walsum, R. Hameeteman, M. Schaap, A. van der Lugt, L. J. van Vliet, and W. J. Niessen. Lumen segmentation of atherosclerotic carotid arteries in CTA. In *9th IEEE International Symposium on Biomedical Imaging (ISBI)*, pages 274–277. IEEE, May 2012. ISBN 978-1-4577-1858-8. doi: 10.1109/ISBI.2012. 6235537.

[28] A. M. F. Santos, R. M. dos Santos, P. M. A. Castro, E. Azevedo, L. Sousa, and J. M. R. S. Tavares. A novel automatic algorithm for the segmentation of the lumen of the carotid artery in ultrasound B-mode images. *Expert Systems with Applications*, 40 (16):6570–6579, November 2013. ISSN 09574174. doi: 10.1016/j.eswa.2013.06. 003.

[29] A. M. F. Santos, J. M. R. S. Tavares, L. Sousa, R. Santos, P. Castro, and E. Azevedo. Automatic segmentation of the lumen of the carotid artery in ultrasound B-mode images. *Proc. SPIE*, 8670:86703I–1–86703I–16, 2013. doi: 10.1117/12.2007259.

[30] M. Kass, A. Witkin, and D. Terzopoulos. Snakes: Active contour models. *International Journal of Computer Vision*, 1(4):321–331, 1988. ISSN 09205691. doi: 10.1007/BF00133570.

[31] Y. Wang, Y. Wu, and Y. Jia. Shape constraints for the left ventricle segmentation from cardiac cine MRI based on snake models. In *Shape Analysis in Medical Image Analysis*, pages 373–412. Springer, 2014. ISBN 978-3-319-03813-1. doi: 10.1007/978-3-319-03813-1_12.

[32] L. D. Cohen. On active contour models and balloons. *CVGIP: Image Understanding*, 53(2):211 – 218, 1991. ISSN 1049-9660. doi: 10.1016/1049-9660(91)90028-N.

[33] C. Xu and J. Prince. Snakes, shapes, and gradient vector flow. *IEEE Transactions on Image Processing*, 7(3):359–369, March 1998. ISSN 10577149. doi: 10.1109/83.661186.

[34] L. Liu and A. C. Bovik. Active contours with neighborhood-extending and noise-smoothing gradient vector flow external force. *EURASIP Journal on Image and Video Processing*, 2012(1):1–6, 2012. ISSN 1687-5281. doi: 10.1186/1687-5281-2012-9.

[35] A. Khadidos, V. Sanchez, and C.-T. Li. Active contours based on weighted gradient vector flow and balloon forces for medical image segmentation. In *2014 IEEE International Conference on Image Processing (ICIP)*, pages 902–906. IEEE, October 2014. ISBN 978-1-4799-5751-4. doi: 10.1109/ICIP.2014.7025181.

[36] N. Ray, S. T. Acton, and K. Ley. Tracking leukocytes in vivo with shape and size constrained active contours. *IEEE Transactions on Medical Imaging*, 21(10):1222–1235, October 2002. ISSN 0278-0062. doi: 10.1109/TMI.2002.806291.

[37] R. Kimmel. *Numerical Geometry of Images: Theory, Algorithms, and Applications*. SpringerVerlag, 2003. ISBN 0387955623.

Part B - Article 5:

Classification of calcified regions in atherosclerotic lesions of the carotid artery in computed tomography angiography images

Danilo Samuel Jodas, Aledir Silveira Pereira, João Manuel R. S. Tavares

Abstract

The identification of atherosclerotic plaque components, extraction and analysis of their morphology represent an important role towards the prediction of cardiovascular events. In this article, the classification of regions representing calcified components in Computed Tomography Angiography (CTA) images of the carotid artery is tackled. The proposed classification model has two main steps: the classification per pixel and the classification per region. Features extracted from each pixel inside the carotid artery are submitted to four classifiers in order to determine the correct class, i.e. calcification or non-calcification. Then, geometrical and intensity features extracted from each candidate region resulting from the pixel classification step are submitted to the classification per region in order to determine the correct regions of calcified components. In order to evaluate the classification accuracy, the results of the proposed classification model were compared against ground truths of calcifications obtained from micro Computed Tomography images of excised atherosclerotic plaques that were registered with *in vivo* CTA images. The average values of the Spearman correlation coefficient obtained by the Linear Discriminant Classifier were higher than 0.80 for the relative volume of the calcified components. Moreover, the average values of the absolute error between the relative volumes of the classified calcium regions and the ones calculated from the corresponding ground truths were lower than 3%. The new classification model seems to be adequate as an auxiliary diagnostic tool for identifying calcifications and allowing their morphology assessment.

Keywords: Medical Imaging, Pattern Recognition, Classification, Atherosclerosis, Computed Tomography Angiography

1 Introduction

Cardiovascular diseases represent one of the main causes of the increasing number of deaths around the world. Therefore, the early diagnosis of pathological conditions is important to minimize clinical cases such as heart attacks, transient ischemic attacks and even the occurrence of strokes. In a broader research study, Mendis et al. [1] revealed alarming numbers regarding cardiovascular disease prevention and control: according to World Health Organization, cardiovascular diseases represented 31% of deaths of people in the world in 2011; and in 2008, cardiovascular diseases were responsible for the death of more than 17 millions of people with less than 60-year-old [1].

Atherosclerosis is an underlying disease responsible for the occurrence of heart attacks and strokes. Atherosclerotic plaques are formed when fatty material and cholesterol are deposited inside the wall of the artery. In an advanced stage, an atherosclerosis is composed by lipid core, fibrous tissue, intraplaque hemorrhage and calcifications. Atherosclerosis reduces the blood flow through the artery, leading to serious complications such as heart attacks and strokes. Hence, in order to prevent such risks, a treatment or rehabilitation plan should be designed based on imaging exams.

Technological advances in computational systems for imaging-based diagnosis allow the detection and assessment of atherosclerotic lesions. Computed Tomography (CT), Magnetic Resonance (MR) and ultrasound are examples of less invasive imaging modalities that have been widely used in evaluating the presence and assess the morphology of atherosclerotic plaques [2–4]. Although x-ray angiography allows the assessment of the lumen diameter, this imaging modality does not provide enough quality to identify the components of atherosclerotic plaques [5]. The correct diagnosis of atherosclerotic plaque components is performed based on images of the carotid artery acquired from ultrasound, CT and MR examinations in a noninvasive way, which allows the visualization of such plaques and the identification of the associated components.

Previous studies [6–11] have confirmed the importance of the atherosclerotic plaque components in evaluating the risks of cerebrovascular diseases. The assessment of the atherosclerotic plaque composition is important to identify risks related to plaque rupture and embolization, as well as risks to transient ischemic attacks, amaurosis fugax and strokes. Although visual analysis has been proposed for quantifying the atherosclerotic plaque composition in images, the intra and intervariability between experts might impair the correct diagnosis. Therefore, the development of computational algorithms plays an important role to expedite the assessment of atherosclerotic plaques and avoid the intervariability between experts.

Computational algorithms have been proposed to segment atherosclerotic plaques and associated components in images [12], which allows the assessment of the plaques in order to predict the risk to cardiovascular and cerebrovascular diseases more quickly. Techniques of image processing, clustering and supervised classification are examples of computational approaches suggested in several studies for identifying the main components of atherosclerotic plaques in a semiautomatic or automatic way [12].

According to several studies, the presence of calcifications represents an advanced stage of the atherosclerosis [13] [14]. Therefore, this article proposes the classification of calcified components in CTA images of the carotid artery. Briefly, the proposed classification model has two main steps: the classification per pixel and the classification per region. In the first step, intensity and distance features extracted from each pixel inside the

carotid artery are submitted to four classifiers in order to obtain the candidate regions representing calcified components. Thereafter, geometrical and intensity features extracted from each candidate region are submitted to the classification per region step in order to determine the regions corresponding to true calcifications.

One of the main contributions of this study is the ability of the proposed model to overcome possible classification errors induced by misalignments of the registration between micro CT images of excised atherosclerotic plaques and related *in vivo* CTA images. Briefly, the used ground truths of the calcified components were obtained from micro CT images. Parts of the lumen and other regions with intensity similar to calcifications in CTA images may affect the classification results, leading to erroneously determination of the calcium regions; however, the proposed classification model seems to be robust to these errors. In addition, since the presence of outliers and the distances of each pixel to the contours of the lumen and carotid artery under analysis can influence the final classification results, a study on these factors was also performed.

The remainder of this article is organized as follow: Section 2 introduces previous studies related to the classification of atherosclerotic plaque components in images acquired by well-know imaging modalities. Section 3 presents a description of the proposed classification model. Section 4 presents the classification results obtained by the proposed classification model and the comparison between these results and the corresponding ground truths. The advantages and limitations of the proposed model are discussed in Section 5. Finally, the conclusions are drawn in Section 6.

2   Previous studies

Several studies have been proposed to identify atherosclerotic plaque components in MR and CTA images of carotid and coronary arteries. Vukadinovic et al. [15] proposed the segmentation of calcium regions in atherosclerotic plaques of the carotid artery in CTA images based on the following steps: a level set approach is used to segment the lumen of the carotid artery in the CTA image under analysis; then, features of the candidate calcium regions are extracted and used to classify them as belonging to calcium or non-calcium components; afterwards, features are extracted to classify the pixels as inside or outside the carotid wall; and then, an ellipse fitting procedure is used to detect the carotid wall boundary. In this work, the lumen and calcium regions are combined to delineate the contour of the carotid wall since the calcium appears in the inner region of the carotid artery.

van Engelen et al. [16] proposed the classification of atherosclerotic plaque components in CTA and MR images of the carotid artery. The main objective of this study was to handle the misalignments between *in vivo* and histological images of atherosclerosis by measuring the probability and dice overlap of each voxel relatively to the corresponding ground truth. The combination of features extracted from each voxel of the CTA and MR images was also addressed. After the registration of the *in vivo* with histological and micro CT images, each component of the ground truth was binarized and blurred with a Gaussian filter in order to create soft labels that indicate the probability of each voxel to belonging to an atherosclerotic plaque component. Additionally, the rejection of outliers was also performed to address the misalignments of the plaque components manually delineated in histological images with the corresponding CTA and MR images. For the classification of the plaque components into calcification, fibrous tissue and lipid-rich necrotic core, 23 features were extracted from each voxel and submitted to a Linear Discriminant Classifier, which provided better results than a Support Vector Machine (SVM) with a Radial Basis Function (RBF) kernel.

Wintermark et al. [17] proposed the identification of atherosclerotic plaque components in CTA images of the carotid artery based on the analysis of the Hounsfield Unit (HU) values. The HU values obtained from a 2x2 mm square template centred at each pixel of the CTA image under analysis are used in a linear mixed model to obtain the appropriate mean HU values for each atherosclerotic plaque component. In terms of the classification results, the calcium regions classified based on the intensity obtained from the CTA images were in perfect accordance with the corresponding ground truths manually delineated in histological images.

de Graaf et al. [18] proposed an automatic method to identify the atherosclerotic plaque components in CTA images of the coronary artery. The extraction of each component was performed by using two approaches: fixed threshold and dynamic threshold. The first approach is based on fixed HU values for extracting each plaque component, whereas the second one defines the cut-off values based on the luminal intensity. The dynamic threshold is based on the fact that the lower the luminal intensity is, the lower will be the HU value of the atherosclerotic plaque. Thus, the HU values of each plaque component are defined based on the luminal attenuation.

The main limitation of the above-mentioned studies regards the usage of fixed HU values for identifying the atherosclerotic plaque components, as in Vukadinovic et al. [15], Wintermark et al. [17] and de Graaf et al. [18]. Additionally, the identification of calcified regions in atherosclerotic lesions can be more effective when features extracted from CTA images are used in the classification process. Hence, instead of using images acquired by different imaging modalities as is suggested in van Engelen et al. [16], the

proposed approach uses only CTA images.

3 Materials and Methods

3.1 CTA images used

The images of the carotid artery selected for this study were used in research by van Engelen et al. [16] and kindly provided by the authors on request. The proposed classification method was performed on images that are regions of interest surrounding the carotid arteries. A registration procedure was previously performed to align the original MR images with the corresponding histological images, which only contained the region of the arteries under study [16]. Once the alignment was completed, the MR images were cropped to obtain only the part that matched the histological images [16]. The original dataset was composed of five MRI scans acquired from thirteen patients: T1-weighted (T1W), Proton Density Weighted (PDW), Time-of-Flight (TOF) and two 3D-T1W scans. The first three MRI scans were acquired without administration of intravenous contrast media, whereas the 3D-T1W scans were acquired with and without contrast media. The post-contrast 3D-T1W scan was performed 4.6 ± 3.4 minutes after the administration of the contrast media. Each MR imaging scan is composed of approximately 17.7 ± 4.8 slices per patient; each slice has a pixel size of 0.25 mm x 0.25 mm. CTA images were also acquired to provide details for the registration of these images with the histological images and to facilitate the manual segmentations of the lumen, vessel wall and plaque components. The manual delineations of the lumen and carotid wall in the CTA and MR images were also provided. More details about the MR and CTA imaging datasets are available in van Engelen et al. [16].

From the original image dataset, we used all CTA images with their corresponding ground truth of the atherosclerotic plaque components and manual delineations of the contours of the lumen and carotid wall made by one expert. In total, 230 CTA images are available with the dataset provided. The ground truths of the atherosclerotic plaque components are available in 177 CTA images and the manual delineations of the lumen and carotid wall are available in 184 CTA images. The manual delineations of the fibrous tissue and lipid-rich necrotic core were made on the histological images, whereas the ground truths of the calcified components were obtained by using a fixed threshold value on the micro CT images acquired from the excised plaques [16].

3.2   Proposed method

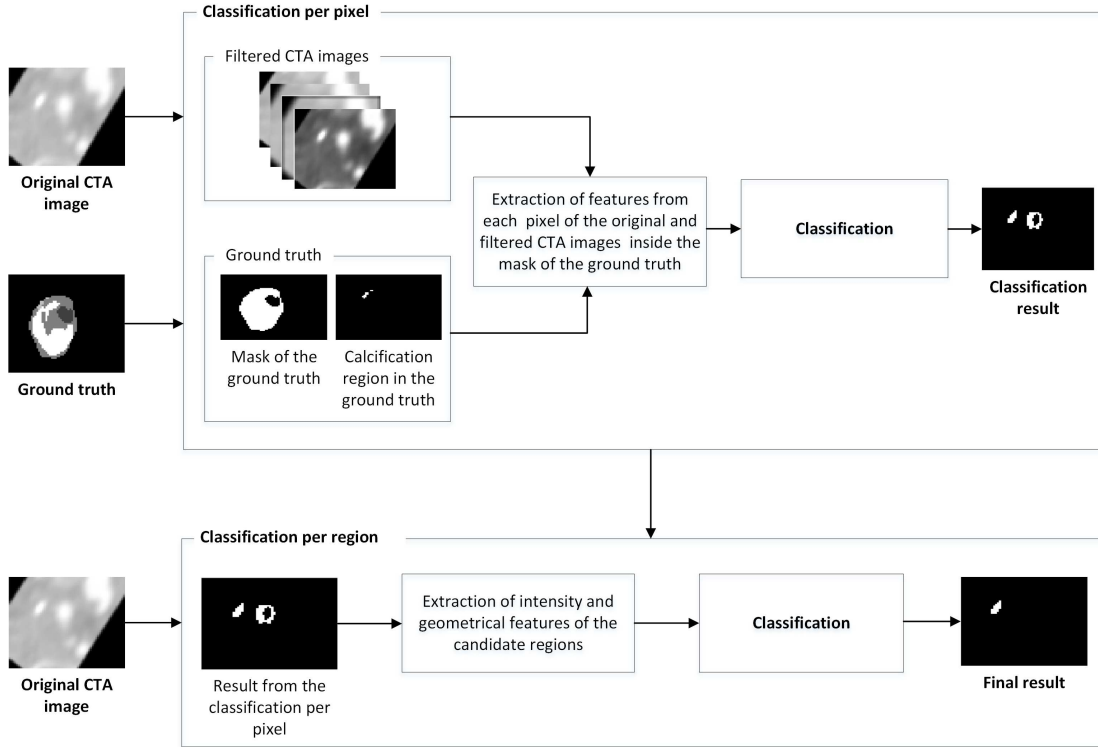The proposed classification model has two main steps, as depicted in Figure 1.

Figure 1: Diagram of the proposed classification model.

The classification per pixel represents the first step of the proposed model and it consists in classifying each pixel inside the carotid wall provided by the ground truth as belonging or not to calcifications. Features extracted from the following CTA images are used in this step: the original image, the original image after been smoothed by a Gaussian filter, the original image after been smoothed by a mean filter and the same input image after the application of a Sigmoid filter. The second step consists in classifying the regions resultant from the previous step in order to determine the ones that represent true calcifications of the atherosclerotic lesions. Hence, geometrical and intensity features of the regions obtained by the first step are extracted and submitted to the second step which performs the classification per region.

3.2.1   Feature extraction

Feature extraction plays an important role in the accuracy of the classification result. Calcifications are characterized as regions having the highest intensity in CTA images. However, features extracted from the lumen region represent a challenge for classifying

the calcified components due to the similarity of their intensity values. Moreover, small regions corresponding to image noise could also be classified as calcifications. Hence, the model proposed in this study takes into account the intensities of the calcium and lumen regions, as well as geometrical features extracted from the candidate regions previously classified in the pixel classification step.

The following filters are applied to highlight the calcium regions relatively to other structures present in the original CTA images: a Gaussian filter with a standard deviation σ; a mean filter with a NxN neighbourhood; and a Sigmoid filter that is applied to highlight a range of intensities and attenuate the intensities outside this range. The Gaussian and mean filters are used to smooth the original CTA images in order to remove noise artefacts, whereas the Sigmoid filter is employed to improve the contrast of regions having high intensities. The Sigmoid filter is based on a pixel-wise function defined as:

$$f(x) = min + \frac{max - min}{1 + e^{\frac{\beta - x}{\alpha}}}, \tag{1}$$

where *min* and *max* are the minimum and maximum intensities of the resultant image $f(x)$, respectively, and α and β are enhancing parameters defined according to the intensities of the structure to be enhanced. Examples of CTA images obtained after the application of the above-mentioned imaging filters are illustrated in Figure 2.

The brightest regions corresponding to the possible calcifications are enhanced by the application of the Sigmoid filter, as one can realize in Figure 2d. For the pixel classification step, the intensity features obtained from each pixel of the original and filtered CTA images are used as inputs for the classifiers. Table 1 indicates the features used in the two steps of the proposed classification model.

Two additional features are used in the pixel classification step: the distances of the pixel under analysis to the boundaries of the lumen and wall of the carotid artery. In addition, the average intensities of the lumen and carotid wall regions in the original CTA image were also used.

3.2.2 Outliers removal

Detection of outliers represents an important task in data analysis and one of the most important pre-processing steps for improving the robustness, performance and accuracy of a classification model. An outlier is characterized as an observation that is far from the remainder ones in a dataset. The presence of outliers often decreases the performance and accuracy of the used classifier due to the increase of the observations variance. Hence, the removal of outliers plays an important role to reduce the observations variance and improve the accuracy of the associated classification model.
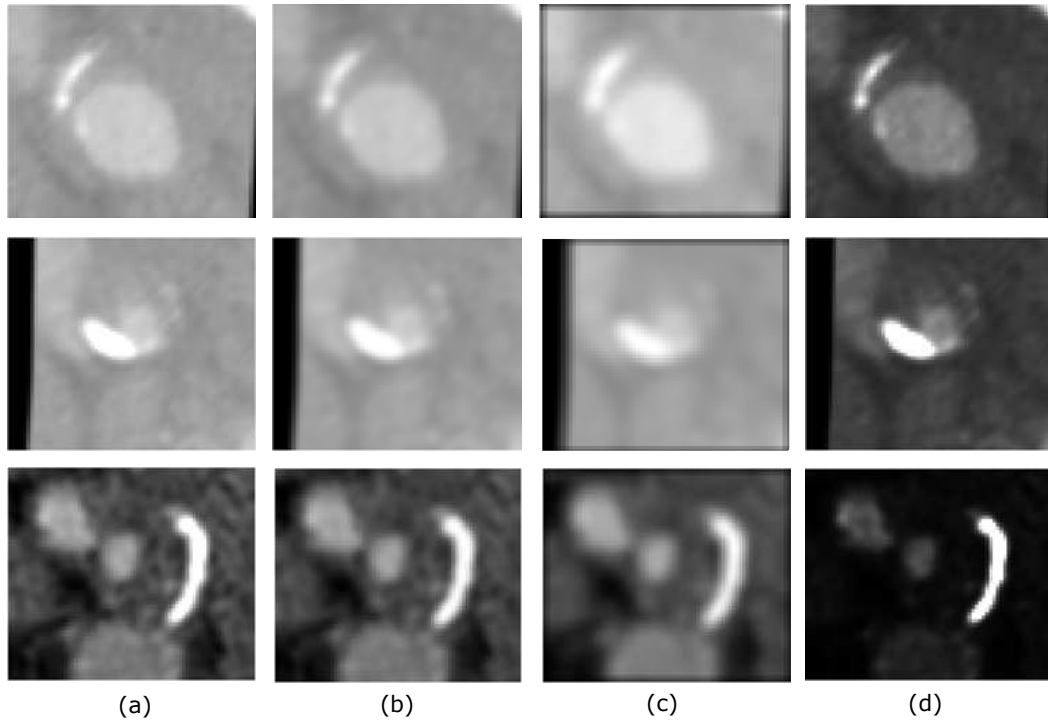
Figure 2: Examples of images resulting from the Gaussian, mean, and Sigmoid filters: a) Original CTA images; b) Images resulting from the original images after applying a Gaussian filter with $\sigma = 2$, c) a mean filter with $N = 3$, and d) a Sigmoid filter with $\alpha = 50$ and $\beta = 256$.

Table 1: Features used in the proposed classification model.

Id.	Classification per pixel	Id.	Classification per region
F1	Intensity of the original image	F21	Percentage of the area relatively to the carotid wall
F2	Intensity of the image (Gaussian filter)	F22	Area of the region
F3	Intensity of the image (Mean filter)	F23	Average intensity of the lumen †
F4	Intensity of the image (Sigmoid filter)	F24	Average intensity of the carotid wall †
F5	Average intensity (Original image)*	F25	Distance of the centroid of the region to the lumen
F6	Average intensity (Gaussian filter)*	F26	Distance of the centroid of the region to the carotid wall
F7	Average intensity (Mean filter)*		
F8	Average intensity (Sigmoid filter)*		
F9	Minimum intensity (Original image)*		
F10	Minimum intensity (Gaussian filter)*		
F11	Minimum intensity (Mean filter)*		
F12	Minimum intensity (Sigmoid filter)*		
F13	Maximum intensity (Original image)*		
F14	Maximum intensity (Gaussian filter)*		
F15	Maximum intensity (Mean filter)*		
F16	Maximum intensity (Sigmoid filter)*		
F17	Average intensity of the lumen †		
F18	Average intensity of the carotid wall †		
F19	Distance of the pixel to the lumen contour		
F20	Distance of the pixel to the carotid wall contour		

*Features extracted from a 3x3 neighbourhood centred at each pixel of the original and filtered CTA images.
†Features extracted from the original CTA image.

Regarding the classification of calcified regions, the outliers are often related to pixels corresponding to misalignments of the histological images with the MR and CTA images

resultant from the registration step [16]. Therefore, the identification and removal of these pixels from the training and testing sets were tackled.

The boxplot analysis is an important statistical tool used to evaluate the distribution and variability of the observations under study. Additionally, abnormal observations can also be identified by means of boxplots. An approach based on boxplots is proposed in this study to detect and remove outliers before the training phase of the classification process. Firstly, the examples of the training set are separated into calcifications and non-calcifications. Then, boxplots of each intensity feature extracted from the pixels of the input CTA image that are inside the carotid wall are generated and combined in order to provide the distribution of the training examples for all features used. An illustration of the combined boxplots built is presented in Figure 3.
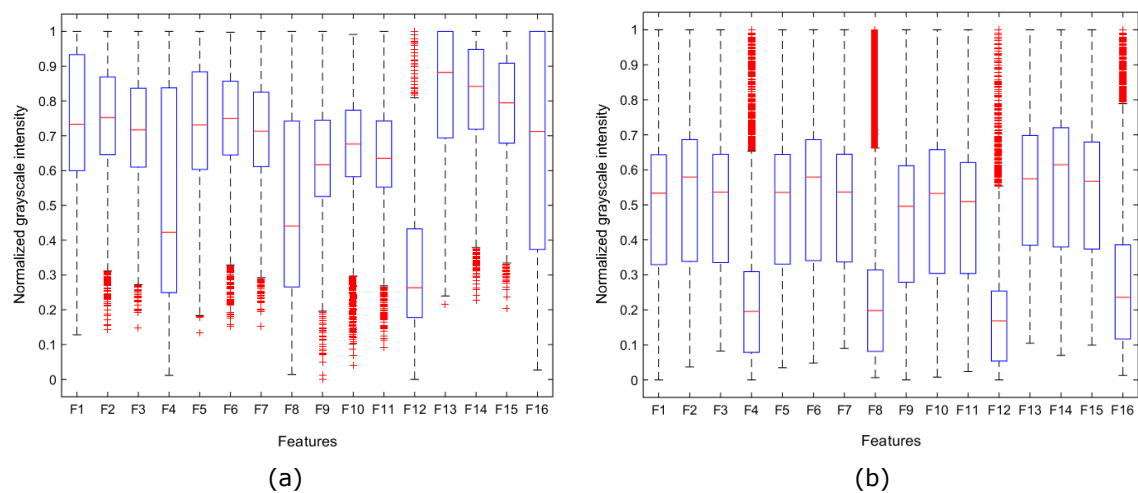

Figure 3: Example of outliers detected by using boxplots built from all features and pixels of the images used in the classification model: a) Boxplot of the calcified examples with the outliers represented in red; b) Boxplot of the non-calcified examples with the outliers represented in red. (The identification of each feature is indicated in Table 1 in column "Classification per pixel".)

From the boxplots in Figure 3, it is possible to notice that the outliers of the features F4, F8, F12 and F16 (see Table 1) in the non-calcified components represented by the highest intensity values might belong to calcified regions (Figure 3b). Likewise, the outliers in the calcified components represented by the lowest intensity values and the ones of the feature F12 represented by the highest intensity values (Figure 3a) may belong to non-calcified regions. The outliers belonging to each class, i.e. calcification and non-calcification subsets, are evaluated in order to find the ones that are present in all features. Then, these outliers are removed from the corresponding subset. The boxplot analysis continues until all outliers have been removed. A new training set without the outliers found is generated and submitted to the classification model.

3.2.3   Training and testing of the classifiers

After selecting the features and removing the outliers, a set of classifiers is used for the classification model. Decision tree, Support Vector Machine (SVM), Naive Bayes and Linear Discriminant Classifier (LDC) were selected to perform the classification of the pixels and, subsequently, the candidate regions representing possible calcified regions in atherosclerotic lesions.

Decision Trees are one of the most simple and effective models used in inductive inference. A decision tree is trained according to a training set and then, other examples are classified according to the same tree model. The graphical representation of the decision tree is composed of lines that are used to identify the decision to be made (for example, "yes" or "no") and nodes to identify the issues to be decided. Each branch formed by lines and nodes ends in a leaf node that identifies the most likely consequence of the sequence of decisions made. The choice of Decision Tree is due to the simple implementation, performance and effectiveness in classifying problems involving sequential decisions.

Support Vector Machines have been adopted for the classification of patterns into two classes separated by a decision hyperplane. The decision hyperplane is a surface that separates the input data into two classes. The goal of a SVM is to find an optimal decision hyperplane, which keeps a maximal gap between the examples under analysis. Building an optimal hyperplane as a decision surface is a fundamental step for increasing the separation between the examples to be classified. However, problems that are not linearly separable are common in many classification problems. Hence, the mapping of the nonlinear training set into a linearly separable space is necessary to determine an optimal decision hyperplane. The linearly separable space is called feature space, which is generated by a kernel function that maps the input examples of the nonlinear space onto a space in which the examples are linearly separable. Linear, polynomial, Radial Basis Function (RBF) and Hyperbolic tangent are examples of kernel functions used in several classification problems tackled by SVMs. SVMs are appropriate for binary classification problems. In this study, a SVM was used with RBF, linear and polynomial based kernels.

The Naive Bayes classifier is one of the most simple and effective probabilistic models used in many types of classification problems. Given an example x in the training phase, the Naive Bayes classifier calculates a distribution $Pr(x|c)$ for each class $c = \{-1, 1\}$, which represents the probability of the example x to belong to class c. In the testing phase, the distribution with the highest probability generated from each example is calculated. The conditional probability used in the Naive Bayes classifier is defined as:

$$P(c_i|x) = \frac{p(c_i)p(x|c_i)}{p(x)}, \qquad (2)$$

where $P(c_i|x)$ is the posterior probability, i.e. the probability of the example x belonging to class c_i, $p(c_i)$ is the probability of occurring class c_i, $p(x|c_i)$ is the probability of occurring the example x given class c_i and $p(x)$ is the probability of occurring the example x. Class c_i with the maximum posterior probability is assigned to the input example x. The Naive Bayes classifier can also be extended to examples having more than one feature; in such cases, example x is represented by a vector of features. Prior probabilities $p(x|c_i)$ of the features are calculated and combined to obtain posterior probability $P(c_i|x)$ of the example x.

The LDC is a simple technique used for detecting the group or class having the average value closer to the one of the test examples. The average of each group is obtained from the features of all examples belonging to that group [19]. The LDC is defined as:

$$\delta_k(x) = x^T \sum{}^{-1} \mu_k - \frac{1}{2} \mu_k^T \sum{}^{-1} \mu_k + log(\pi_k), \tag{3}$$

where $\delta_k(x)$ is the posterior probability, i.e. the probability of the example x belonging to class k, k is the class, x is the vector of features, $\sum$ is the covariance matrix and μ_k is the mean of class k. Likewise the Naive Bayes classifier, the example represented by feature vector x is assigned to class k that have the maximum posterior probability $\delta_k(x)$.

The proposed classification approach has two main steps: the first step concerns the classification of each pixel of the original and filtered CTA images inside the mask of the ground truth, whereas in the second step the classification of the candidate regions resulting from the first step is performed to identify the ones that correspond to true calcified regions. Hence, two models were developed for each step of the classifier under analysis.

Leave-one-out and k-fold cross-validation were performed in the CTA images of the thirteen patients under study. The leave-one-out cross-validation was applied in repeatedly steps, with the images of 12 patients used in the training step and the images of the remaining 13th patient used for testing the classifiers. The k-fold cross-validation method consists in dividing the data set into mutually exclusive subsets of the same size. A subset is used for testing the classifier and the $k-1$ subsets are employed for building the model of the classifier. This process is performed k times by alternating the subset of observations used for testing the classifier.

In order to evaluate the influence of the distance features and of the outliers removal process, the approaches indicated in Table 2 were studied.

Two new sets of training and testing examples were generated from each approach indicated in Table 2 for each iteration of the leave-one-out and k-fold cross-validation techniques. Additionally, the outliers removal was performed in each iteration of the two cross-validation techniques. Hence, four models of each classifier were built in the

Table 2: Approaches adopted to verify the influence of the distance features and of the outliers removal process.

	Outlier removal	Usage of the distances to the lumen and carotid wall
Approach 1	No	Yes
Approach 2	No	No
Approach 3	Yes	Yes
Approach 4	Yes	No

training step of the pixel classification step.

For the training of the classifiers in the pixel classification step, a binary image of the carotid wall obtained from the ground truth corresponding to the atherosclerotic plaque components was built for selecting only the pixels of the CTA images that are inside the carotid artery. Then, the features extracted from each pixel were submitted to the classifier corresponding to each approach indicated in Table 2.

As to the region classification step, the region corresponding to the lipid-rich necrotic core is used as reference for the non-calcified class. The choice of the lipid-rich necrotic core is due to the intensity and geometrical features that differ from the calcium components in CTA images, making it appropriate for a binary classification in the region classification step. The features of the regions of the binary images resultant from each approach of the pixel classification step were extracted and submitted to the classifiers that perform the classification of each potential calcified region.

Regarding the testing of the classifiers under analysis, the pixels inside the manually delineated carotid wall were used for testing and validating the accuracy of the chosen classifiers. The extraction of the pixels inside the binary image representing the carotid wall is illustrated in Figure 4.

For the pixel classification step, the intensity and distance features described in Table 1 were extracted from the original and filtered CTA images belonging to the testing set for the classification process. The intensities of each pixel of the original CTA image inside the previously identified regions along with geometrical features of each candidate region were then submitted to the classifiers that perform the classification per region.

4   Results

The accuracy of the classification solution proposed in this study was evaluated by means of the absolute error and Spearman correlation between the areas and volumes of the classified calcium regions and those calculated from the corresponding ground truths. The relative and absolute areas and volumes of the calcium regions were calculated to
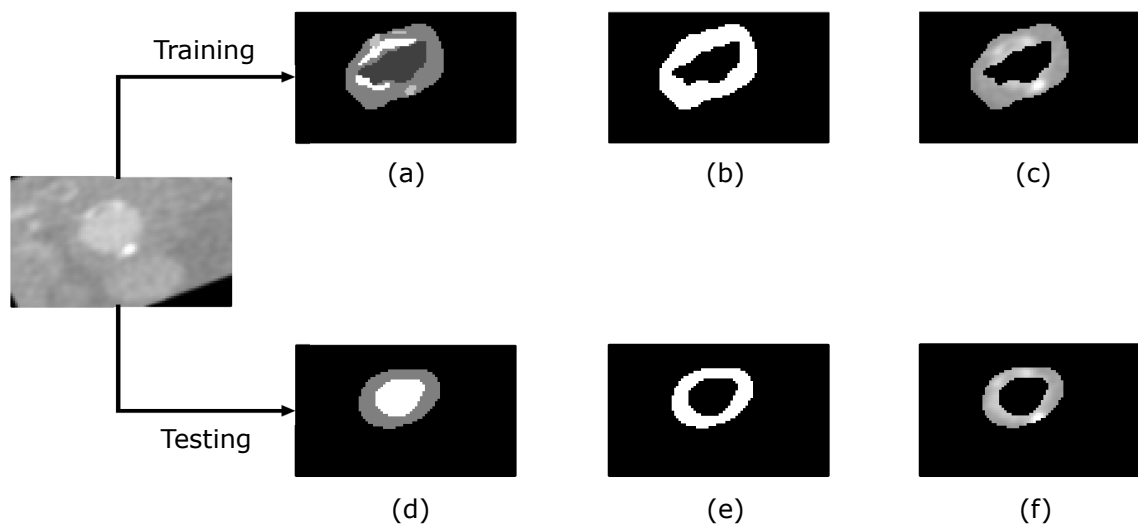
Figure 4: Illustration of the procedure used to select the pixels inside the carotid wall for extracting the features to be used in the pixel classification step of the proposed classification model: a) The ground truth of the atherosclerotic plaque components; b) Binary image of the ground truth with the carotid wall represented in white; c) Part of the original CTA image inside the carotid wall; d) The manual delineations of the lumen and carotid wall; e) Binary image obtained from the manual delineations with the carotid wall represented in white; f) Part of the original CTA image inside the carotid wall.

evaluate the results generated by the classification model. The relative area and volume represent the percentage of the calcium region occupied in the total area and volume of the carotid artery. The absolute area and volume are the total area and volume of the related calcium region, respectively. The evaluation by means of the Area Under the Curve (AUC), sensitivity and specificity was not possible due to the existent misalignment between the ground truths obtained from the micro CT images and the corresponding *in vivo* CTA images.

The following parameters were defined to perform the classification process: the value of parameter σ of the Gaussian filter was defined as equal to 2; the values of α and β parameters of the Sigmoid filter were defined as equal to 50 and 256, respectively; neighbourhood NxN of the mean filter was set to 3x3; the number of iterations to remove outliers of the training and testing sets was defined as equal to 50; the value of k of the k-fold cross-validation approach was set to 10 since this is the most used value in several classification problems; the values of σ and of penalty term C of the RBF kernel were defined as equal to 1 (one) since these values have been commonly used in several studies; and the best order of the polynomial kernel was defined as equal to 3.

Examples of the classification results per pixel and per region obtained by each classifier under analysis are shown in Figure 5.
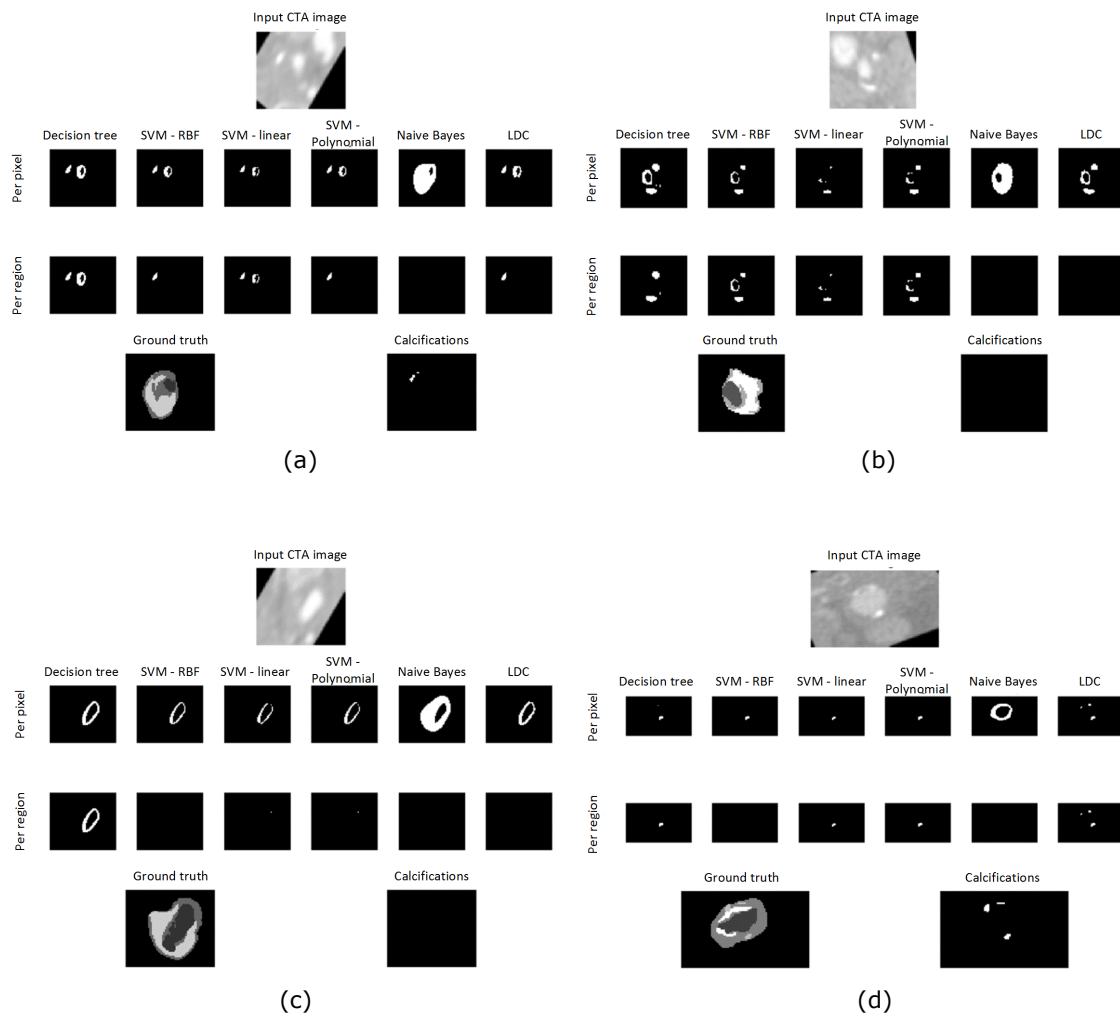
Figure 5: Examples of classification results obtained by each classifier under comparison in the pixel and region classification steps.

As shown in Figure 5a, the lumen region of the CTA image under study overestimated the size of the lumen of the related ground truth obtained from the manual delineation, causing that part of the lumen in the input image be used in the pixel classification step. Hence, the referred part of the lumen was classified as calcification due to the similarity of its grayscale intensity with the grayscale intensity of true calcified regions. In these cases, the region classification step plays an important role to evaluate the geometrical properties of the candidate regions previously classified by the pixel classification step in order to select those that represent true calcifications. After the classification per region, the mentioned part of the lumen was disregarded and only the region corresponding to a calcification remained in the final classification result. The results provided by the SVM with the RBF and polynomial kernels, as well as the results of the LDC classifier, are also in accordance with the ground truth as shown in Figure 5a. The examples illustrated

in Figure 5b-c also show the good accordance of the results obtained by most of the classifiers under analysis with the corresponding ground truths.

Examples resultant from each approach indicated in Table 2 in the pixel classification step are shown in Figure 6.

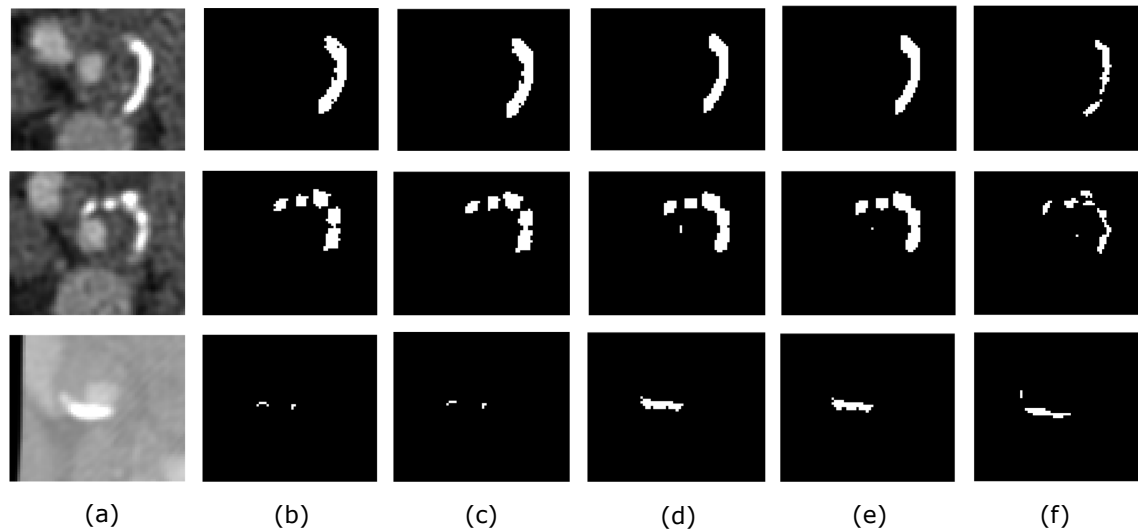<div style="text-align:center">(a)   (b)   (c)   (d)   (e)   (f)</div>

Figure 6: Examples of classification results obtained by each approach indicated in Table 2 in the pixel classification step: a) Original CTA images; b) Classification results obtained by Approach 1; c) Classification results obtained by Approach 2; d) Classification results obtained by Approach 3; e) Classification results obtained by Approach 4; f) Corresponding ground truths of the calcified components.

The classification results were improved after the outliers removal as can be perceived in Figure 6(d-e), mainly in the case of the CTA image shown in the third row.

Regarding the comparison of the computational results with the ground truths, the LDC obtained better results than the remainder classifiers as can be perceived in the examples of Figure 5.

The average error and Spearman correlation between the computational results and the corresponding ground truths as to the k-fold cross-validation technique for each approach and classifier are shown in Figure 7, Figure 8 and Figure 9. In addition, the average bias of the relative areas and volumes are indicated in Tables 3 and 4.

Regarding the relative percentage of the classified calcium regions with respect to the total area of the carotid wall, the average absolute errors decreased for almost of the classifiers after the employment of the classification per region, mainly for Approaches 3 and 4, as can be observed in Figure 7. Additionally, the average absolute errors obtained from the classification performed by the LDC were lower than those obtained from the other classifiers, mainly for Approaches 1 and 2. In terms of the results obtained by Approach 3, the average absolute error of the relative area obtained from the LDC results decreased
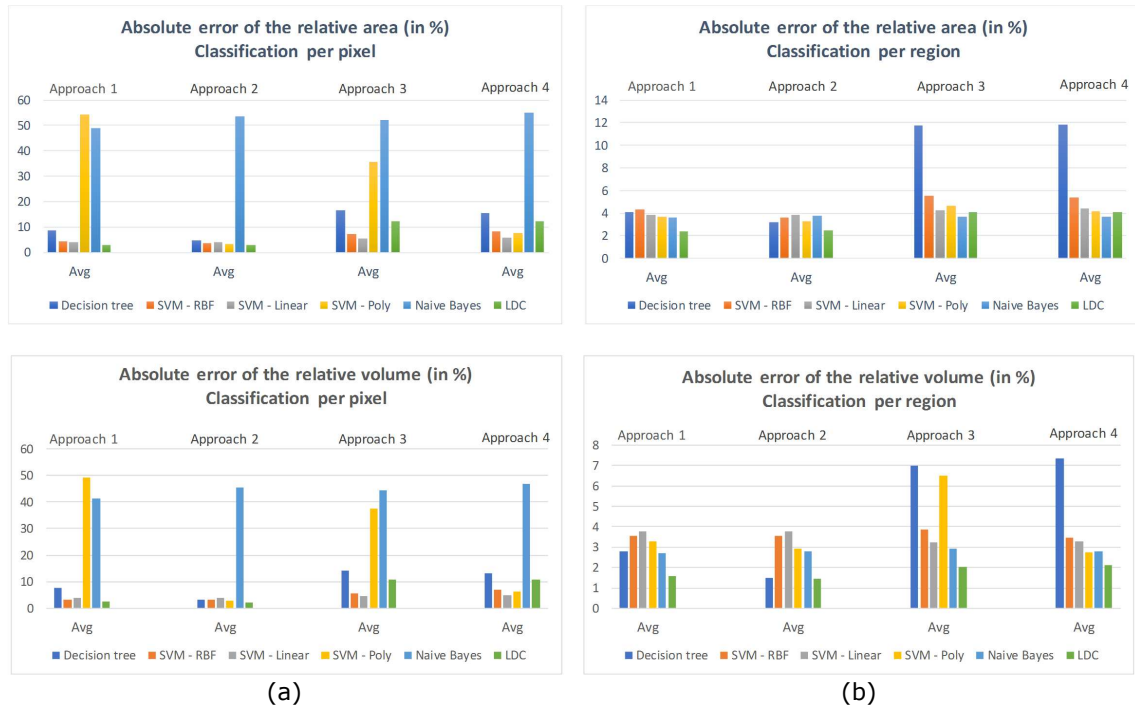
Figure 7: Average absolute errors of the relative areas and volumes obtained from the k-fold cross-validation technique for the classifications (a) per pixel and (b) per region. (The first row represents the average absolute errors for the relative area, and the second row the average absolute errors for the relative volume of the classified calcium regions.)

Table 3: Average bias obtained as to the relative areas of the classified calcium regions in each approach and classifier of the k-fold cross validation technique.

		Decision tree	SVM - RBF	SVM - Linear	SVM - Poly	Naive Bayes	LDC
Approach 1	**Per pixel**	7.19 ± 12.07	-2.08 ± 5.98	-3.82 ± 5.23	54.19 ± 28.29	48.75 ± 42.00	-0.06 ± 4.74
	Per region	1.23 ± 6.43	-2.59 ± 5.81	-3.82 ± 5.23	-2.80 ± 5.06	-2.47 ± 5.56	-1.20 ± 3.96
Approach 2	**Per pixel**	3.55 ± 7.27	-3.29 ± 5.12	-3.82 ± 5.23	-3.15 ± 4.85	53.36 ± 41.70	0.29 ± 4.60
	Per region	0.46 ± 4.90	-3.42 ± 5.17	-3.82 ± 5.23	-3.16 ± 4.86	-2.49 ± 5.73	-0.70 ± 4.05
Approach 3	**Per pixel**	16.18 ± 16.16	2.94 ± 9.87	1.77 ± 7.85	34.79 ± 26.47	52.07 ± 42.17	11.67 ± 11.94
	Per region	8.95 ± 17.19	0.18 ± 7.54	-0.31 ± 6.02	-2.46 ± 9.23	-2.63 ± 5.64	1.89 ± 5.67
Approach 4	**Per pixel**	15.49 ± 15.87	6.92 ± 10.97	3.09 ± 8.16	6.04 ± 9.97	54.99 ± 41.49	11.60 ± 12.18
	Per region	9.55 ± 17.11	0.76 ± 8.05	0.07 ± 6.17	1.59 ± 5.99	-2.58 ± 5.62	1.92 ± 5.55

*The values are expressed in percentage.

from 12.3183% to 4.0718% after the employment of the classification per region on the results obtained from the classification per pixel step. Similar improvements were also obtained for Approach 4, in which the average absolute error of the relative area decreased from 12.219% to 4.0643% after the classification per region. As shown in Figure 7 (plots of the second row), a significant reduction of the absolute errors of the relative volume was also achieved after classifying each region resultant from the pixel classifi-
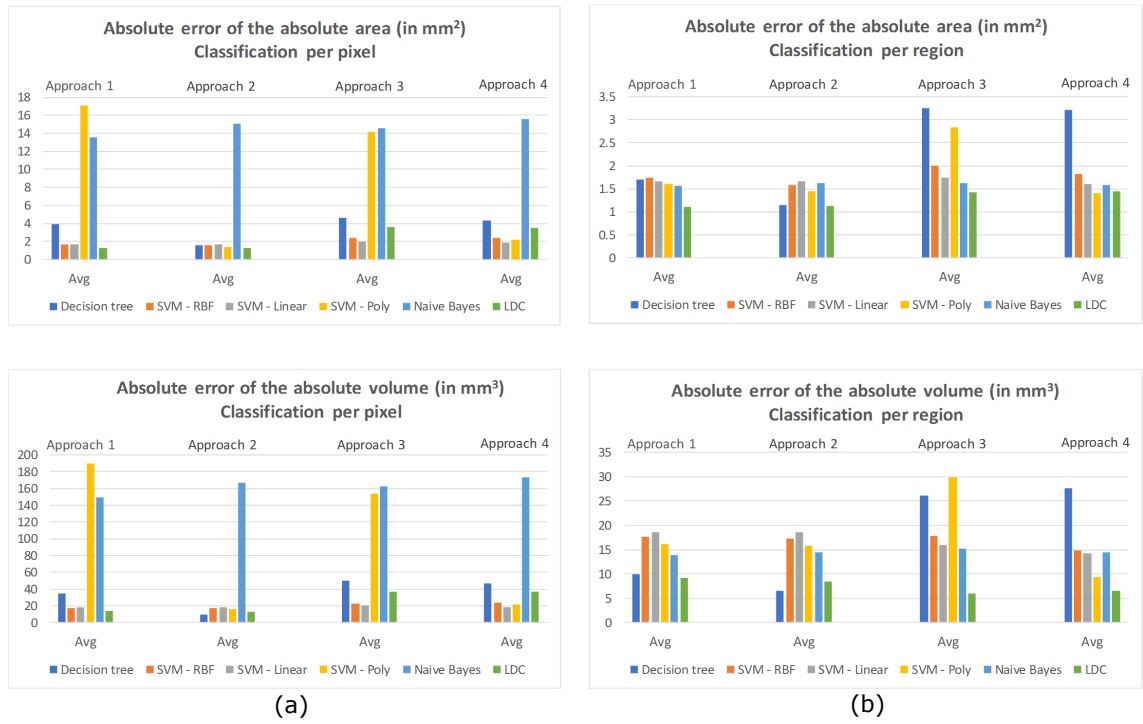
Figure 8: Average absolute errors of the absolute areas and volumes obtained by the k-fold cross-validation technique for the classifications (a) per pixel and (b) per region. (The first row represents the average absolute errors for the absolute area, and the second row the average absolute errors for the absolute volume of the classified calcium regions.)

Table 4: Average bias obtained as to the relative volumes of the classified calcium regions in each approach and classifier of the k-fold cross validation technique.

		Decision tree	SVM - RBF	SVM - Linear	SVM - Poly	Naive Bayes	LDC
Approach 1	**Per voxel**	7.81 ± 10.79	-2.08 ± 4.14	-3.79 ± 3.38	49.13 ± 23.88	41.23 ± 35.88	0.42 ± 3.95
	Per region	1.17 ± 3.55	-2.70 ± 3.92	-3.79 ± 3.39	-2.90 ± 3.65	-2.47 ± 2.87	-1.22 ± 2.34
Approach 2	**Per voxel**	3.10 ± 2.12	-3.08 ± 3.39	-3.79 ± 3.39	-2.89 ± 3.14	45.26 ± 37.04	0.65 ± 3.25
	Per region	0.35 ± 1.72	-3.43 ± 3.31	-3.79 ± 3.39	-2.90 ± 3.15	-2.47 ± 3.02	-0.82 ± 1.87
Approach 3	**Per voxel**	14.06 ± 10.92	2.32 ± 7.54	1.81 ± 6.07	37.39 ± 19.33	44.32 ± 36.55	10.71 ± 8.96
	Per region	6.46 ± 10.19	-0.54 ± 5.10	-0.72 ± 4.31	0.22 ± 9.82	-2.57 ± 3.29	1.74 ± 1.94
Approach 4	**Per voxel**	13.29 ± 10.60	6.08 ± 7.89	2.96 ± 5.85	5.40 ± 7.10	46.76 ± 36.77	10.63 ± 9.10
	Per region	6.92 ± 10.73	-0.22 ± 4.66	-0.62 ± 4.05	1.55 ± 3.30	-2.51 ± 3.06	1.81 ± 1.77

*The values are expressed in percentage.

cation step, leading the absolute error of Approaches 3 and 4 to decrease from 10.9399% and 10.8359% to 2.0247% and 2.1402%, respectively. In terms of the absolute area and volume of the calcifications, similar improvements were also found with the classification per region as shown in Figure 8. Additionally, the average absolute errors of the absolute area and volume of the calcium regions were also lower for the LDC in all approaches (Figure 8b).
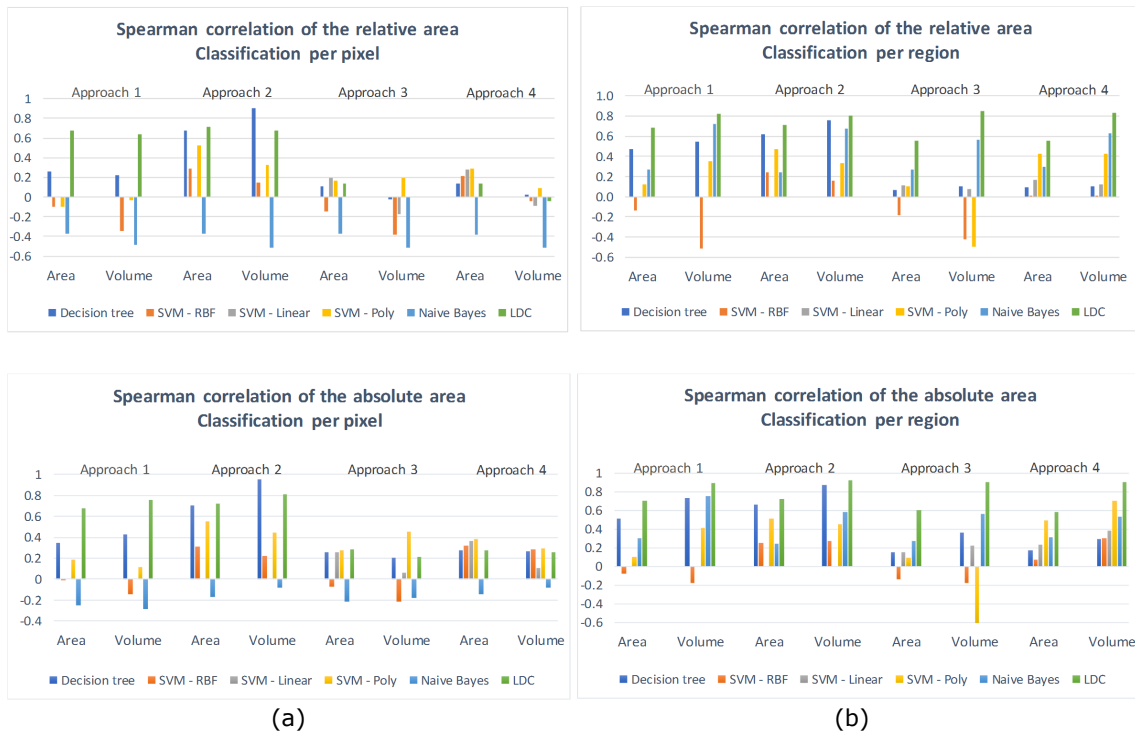
Figure 9: Spearman correlation coefficients of the relative and absolute areas and volumes obtained by the k-fold cross-validation technique for the classifications (a) per pixel and (b) per region. (The first row represents the Spearman correlation coefficients for the relative area and volume of the classified calcium regions, whereas the second row the Spearman correlation coefficient of the absolute area and volume of the same regions.)

Improvements on the Spearman correlation coefficients were also achieved from the classification of the candidate regions resultant from the pixel classification step. As shown in Figure 9b, a significant increase of the correlation coefficients between the area and volume of the classification results and those calculated from the corresponding ground truths was obtained after the region classification step for most of the classifiers used, mainly for Approaches 3 and 4. Moreover, the results obtained by the LDC were also better than the ones obtained from the other classifiers. Regarding the results obtained by the LDC, the Spearman correlation coefficient between the relative area calculated from the classified calcium regions and the ones obtained from the corresponding ground truths was 0.136 for Approach 3 of the pixel classification step. The correlation coefficient for the same approach increased to 0.553 after the application of the classification per region. Regarding the relative volume obtained by using Approach 3, the Spearman correlation coefficient increased from 0 (zero) to 0.850 after the application of the classification per region. With respect to Approach 4, the Spearman correlation coefficients between the relative area and volume of the classification results and those calculated from the ground truths were 0.1415 and -0.044, respectively, for the pixel clas-

sification step. The correlation coefficients increased to 0.557 and 0.828, respectively, after the classification of the candidate regions obtained from the pixel classification step. Similar improvements in the Spearman correlation coefficients of the absolute area and volume of the calcium regions were also achieved for all approaches and classifiers as shown in Figure 9 (plots of the second row).

Similar results were also achieved by means of the leave-one-out cross-validation technique as illustrated in Figure 10, Figure 11 and Figure 12. In addition, the average bias of the relative area and volume obtained from the leave-one-out cross-validation technique are indicated in Tables 5 and 6.
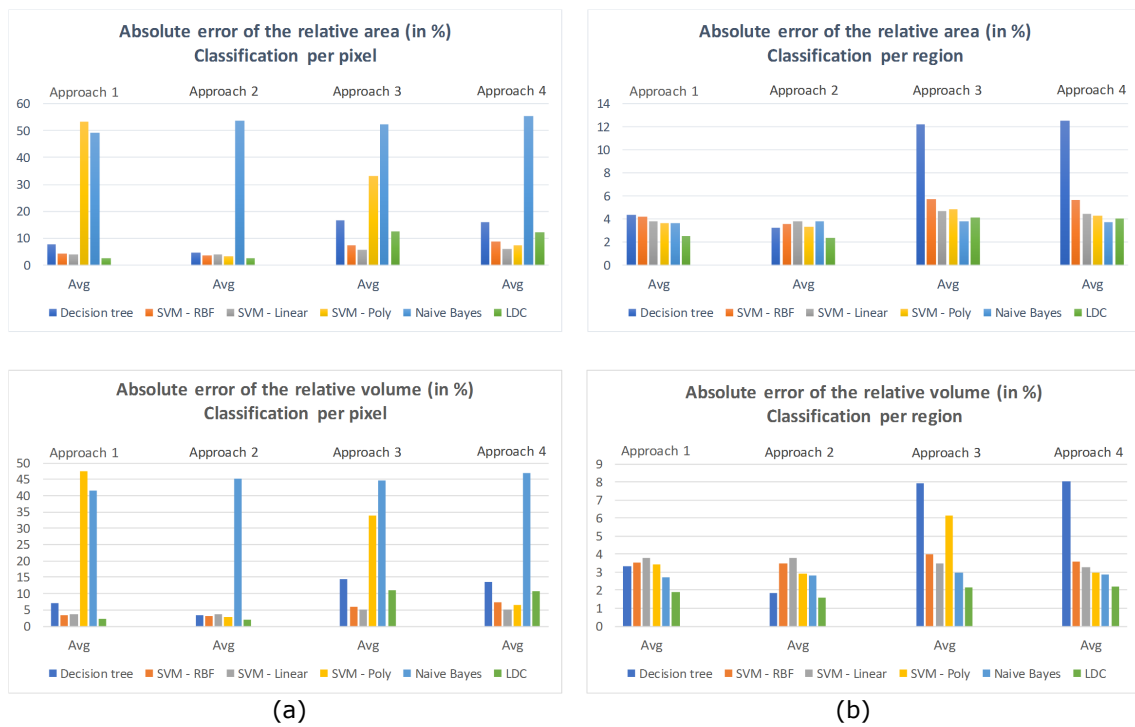

Figure 10: Average absolute errors of the relative areas and volumes obtained from the leave-one-out cross-validation technique for the classifications (a) per pixel and (b) per region. (The first row represents the average absolute errors for the relative area, and the second row the average absolute errors for the relative volume of the classified calcium regions.)

Similar to the k-fold cross-validation technique, the results obtained by the LDC were also better than the ones generated by the remainder classifiers. In terms of the relative area, the average absolute errors obtained by the LDC in the pixel classification step were 2.4926%, 2.4578%, 12.479% and 12.270% for Approaches 1, 2, 3 and 4, respectively. After the application of the classification per region, the average absolute errors were 2.557%, 2.379%, 4.0989% and 4.0659% for the same Approaches, respectively. It is possible to notice a significant reduction of the average absolute errors of the relative area
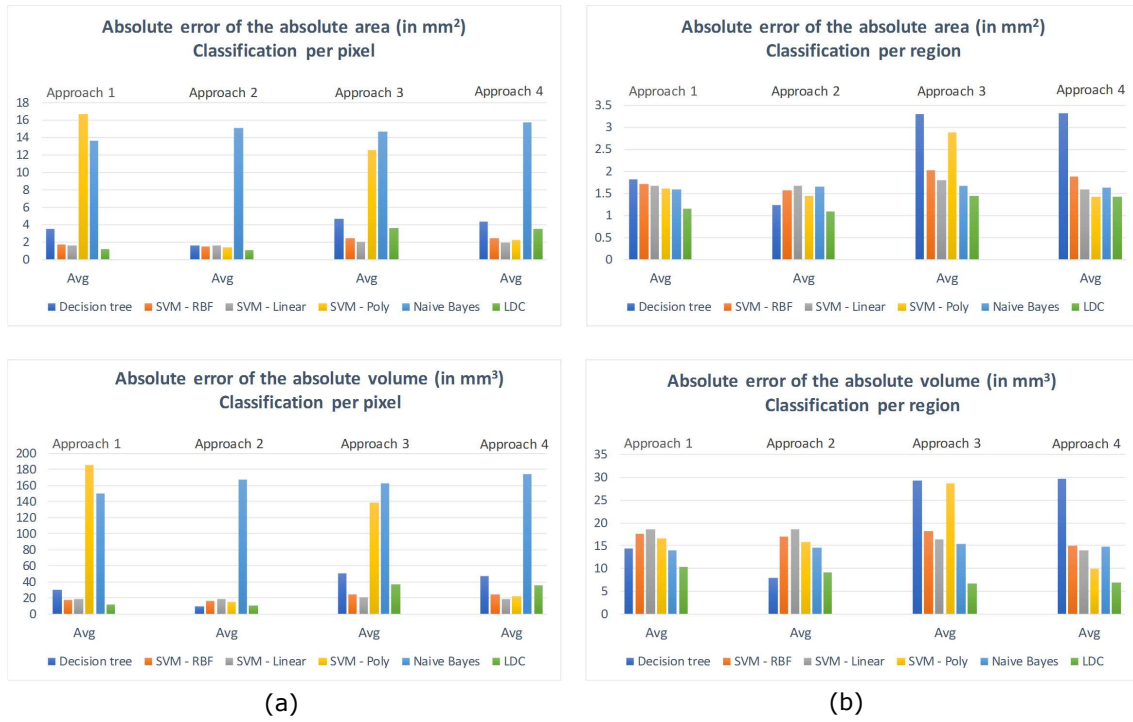
Figure 11: Average absolute errors of the absolute areas and volumes obtained from the leave-one-out cross-validation technique for the classifications (a) per pixel and (b) per region. (The first row represents the average absolute errors for the absolute area, and the second row the average absolute errors for the absolute volume of the classified calcium regions.)

Table 5: Average bias obtained as to the relative areas of the classified calcium regions in each approach and classifier of the leave-one-out cross validation technique.

		Decision tree	SVM - RBF	SVM - Linear	SVM - Poly	Naive Bayes	LDC
Approach 1	Per pixel	6.06 ± 10.00	-2.05 ± 5.95	-3.82 ± 5.23	53.32 ± 31.08	48.94 ± 41.87	-0.44 ± 4.08
	Per region	1.31 ± 6.76	-2.63 ± 5.70	-3.82 ± 5.23	-3.04 ± 4.96	-2.41 ± 5.64	-0.99 ± 4.18
Approach 2	Per pixel	3.32 ± 7.38	-3.25 ± 5.09	-3.82 ± 5.23	-3.08 ± 4.95	53.41 ± 41.62	-0.08 ± 4.03
	Per region	0.33 ± 4.98	-3.38 ± 5.14	-3.82 ± 5.23	-3.09 ± 4.96	-2.43 ± 5.79	-0.53 ± 3.88
Approach 3	Per pixel	16.56 ± 16.62	3.30 ± 10.27	2.26 ± 8.35	32.92 ± 26.41	52.31 ± 42.02	11.84 ± 12.44
	Per region	9.73 ± 17.42	0.39 ± 8.04	0.09 ± 6.76	-2.13 ± 9.42	-2.56 ± 5.76	2.03 ± 5.63
Approach 4	Per pixel	15.83 ± 16.56	7.24 ± 11.24	3.20 ± 8.32	6.20 ± 10.08	55.16 ± 41.36	11.67 ± 12.50
	Per region	10.38 ± 17.40	1.01 ± 8.50	0.24 ± 6.39	1.74 ± 6.11	-2.51 ± 5.72	2.03 ± 5.49

*The values are expressed in percentage.

obtained from Approaches 3 and 4 after the region classification step. For the absolute error of the relative volume, the average values obtained from Approaches 1, 2, 3 and 4 were 2.1309%, 1.8922%, 10.996% and 10.804%, respectively, for the pixel classification step. After the classification per region, the average absolute errors decreased to 1.9087%, 1.5630%, 2.1509% and 2.1866%, respectively, for the same Approaches. A significant
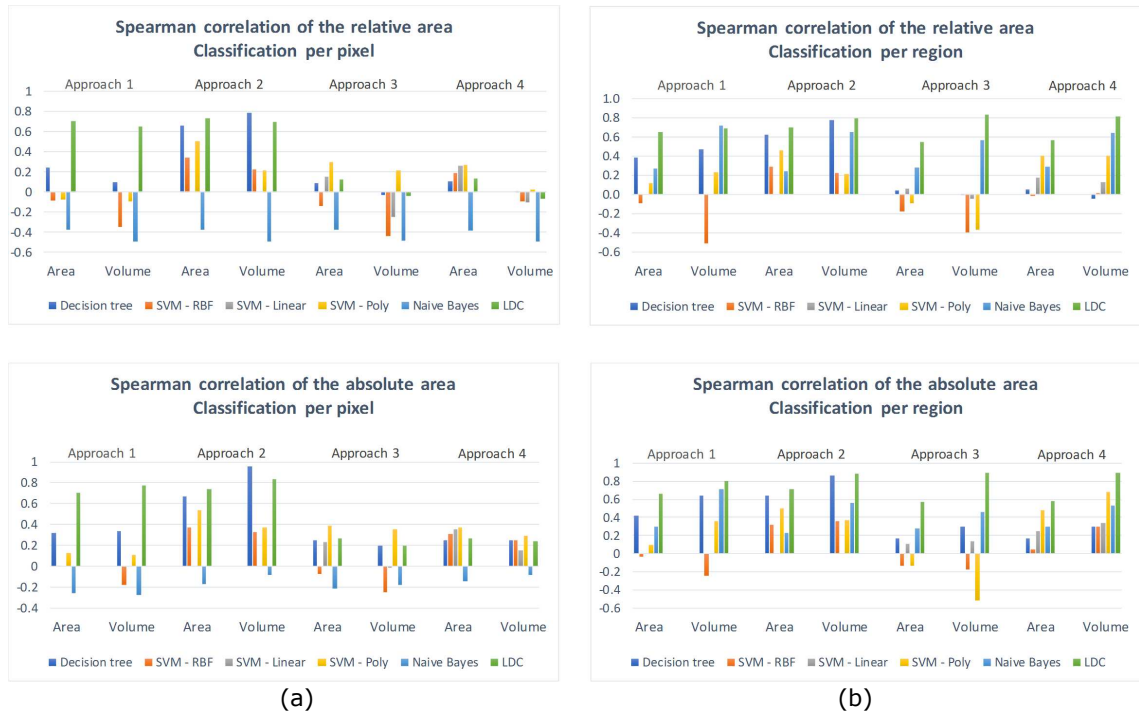
Figure 12: Spearman correlation coefficients of the relative and absolute areas and volumes obtained from the leave-one-out cross-validation technique for the classifications (a) per pixel and (b) per region. (The first row represents the Spearman correlation coefficients for the relative area and volume of the classified calcium regions, whereas the second row the Spearman correlation coefficients of the absolute area and volume.)

Table 6: Average bias obtained as to the relative volumes of the classified calcium regions in each approach and classifier of the leave-one-out cross validation technique.

		Decision tree	SVM - RBF	SVM - Linear	SVM - Poly	Nave Bayes	LDC
Approach 1	**Per voxel**	6.53 ± 9.37	-2.02 ± 4.19	-3.79 ± 3.39	47.41 ± 27.00	41.47 ± 35.81	-0.03 ± 3.32
	Per region	1.18 ± 4.30	-2.69 ± 3.95	-3.79 ± 3.39	-3.19 ± 3.48	-2.39 ± 2.95	-1.02 ± 2.66
Approach 2	**Per voxel**	3.16 ± 2.39	-3.04 ± 3.39	-3.79 ± 3.39	2.81 ± 3.29	45.33 ± 36.95	0.19 ± 2.70
	Per region	0.27 ± 2.19	-3.40 ± 3.32	-3.79 ± 3.39	-2.82 ± 3.29	-2.40 ± 3.08	-0.61 ± 2.11
Approach 3	**Per voxel**	14.43 ± 11.36	2.69 ± 7.71	2.19 ± 6.15	34.00 ± 20.27	44.60 ± 36.45	10.80 ± 9.48
	Per region	7.25 ± 9.96	-0.41 ± 5.23	-0.49 ± 4.48	0.54 ± 9.69	-2.51 ± 3.38	1.87 ± 1.91
Approach 4	**Per voxel**	13.57 ± 11.34	6.37 ± 8.04	3.00 ± 5.88	5.53 ± 7.14	46.95 ± 36.64	10.63 ± 9.46
	Per region	7.71 ± 10.43	0.01 ± 4.91	-0.48 ± 4.06	1.67 ± 3.38	-2.47 ± 3.14	1.91 ± 1.77

*The values are expressed in percentage.

reduction of the absolute error was also achieved for Approaches 3 and 4. As shown in Figure 11, regarding the average absolute errors for the absolute area and volume of the calcium regions, a similar decreasing behaviour was found after the classification per region step.

The Spearman correlation coefficients obtained from the leave-one-out cross-validation technique were similar to the ones calculated for the k-fold cross-validation technique, showing the stability of the suggested classification model. The LDC classifier also showed better results than the other classifiers. The Spearman correlation coefficients between the relative areas of the classification results and the ones calculated from the corresponding ground truths were 0.6991, 0.7310, 0.1234 and 0.1352, for Approaches 1, 2, 3 and 4, respectively, in the pixel classification step. The Spearman correlation coefficients obtained from the region classification step were 0.6530, 0.7002, 0.5410 and 0.5630 for the same Approaches, leading to a significant increase of the correlation coefficients for Approaches 3 and 4. Similar improvements were also obtained from the relative volumes. The correlation coefficients between the relative volumes of the classification results and the ones calculated from the corresponding ground truths were 0.6465, 0.6960, -0.0385 and -0.0660 for Approaches 1, 2, 3 and 4, respectively, in the pixel classification step. On the other hand, the correlation coefficients obtained after the classification per region step were 0.6850, 0.7900, 0.8280 and 0.8060 for the same Approaches. Likewise the relative area, significant improvements in the absolute areas of the classified calcium regions were also achieved for Approaches 3 and 4 after the region classification step as can be perceived in Figure 12 (plots of the second row).

5 Discussion

The characterization of atherosclerotic plaque components plays an important role towards the evaluation of the disease progression. The composition of atherosclerotic plaques has been addressed as an important factor for evaluating the risks of plaque rupture, as well as risks for embolization and neurological events. Previous studies suggested that the presence of calcified components in atherosclerotic plaques represents an advanced stage of the disease.

The classification of calcium regions in CTA images of the carotid artery was successfully tackled in this study. Firstly, the proposed classification model performs the classification of each pixel inside the carotid artery in order to obtain the candidate regions representing the calcifications of the atherosclerosis. Then, the regions previously identified are submitted to the region classification step in order to identify the ones that represent true calcifications based on geometrical and intensity features extracted from each region. Misalignments between the histological images and the corresponding *in vivo* CTA images resulting from the used registration procedure might affect the classification results due to the selection of parts of the lumen and other regions having intensity similar to the

one of calcified components. Hence, pixels belonging to regions corresponding to other structures of the carotid artery may affect the accuracy of the results. Hence, a second step to identify and maintain only the regions correctly representing calcifications was included in the proposed classification model, leading to results significantly better than the ones exclusively obtained by the classification per pixel step.

Besides the assessment of regions that do not correspond to true calcifications of the atherosclerotic lesions, the removal of outliers represents an important approach to increase the performance of the classifiers and provide a better separation of the pixels belonging to each class, i.e. calcium and non-calcium regions. The presence of outliers decreases the ability of the classifiers in separating the classes and determining the correct class of the input pixel, leading to errors in the classification results and, consequently, the decreasing of the accuracy of the classification model. Hence, an approach to remove outliers of the pixels selected for training and testing the classifiers in each cross-validation iteration was proposed in this study. The boxplots of the pixels belonging to each class was generated and evaluated to determine the presence of outliers in the experimental dataset based on all intensity features extracted from each pixel to be classified. Hence, common pixels representing outliers in all features were removed before the training and testing processes. The outliers removal approach proposed here proved to be effective in determining the correct class of each pixel and improving the shapes of the calcified regions to make them as close as possible to the ones of the corresponding ground truths.

The areas and volumes of the calcium regions in the CTA images used in this study are often larger than the ones of the corresponding calcifications in the ground truth. The ground truth of the calcified components was obtained using micro CT images of the excised plaques as described in van Engelen et al. [16]. According to van Engelen et al. [16], the blooming artefacts often present in CTA images may cause the overestimation of the calcium components. The bias of the areas and volumes resulting from Approaches 3 and 4 showed a positive value when compared to Approaches 1 and 2. The average bias of the relative area obtained from the classification per region in Approaches 1, 2, 3 and 4 were -1.20 ± 3.96%, -0.70 ± 4.05%, 1.89 ± 5.67% and 1.92 ± 5.55%, respectively, for the classification results of the LDC in the k-fold cross-validation technique. In terms of the relative volume, the average bias obtained from the LDC in the k-fold cross-validation technique in the region classification step were -1.22 ± 2.34%, -0.82 ± 1.87%, 1.74 ± 1.94% and 1.81 ± 1.77% for Approaches 1, 2, 3 and 4, respectively. Regarding the leave-one-out cross validation technique, the average bias of the relative areas obtained by the LDC for Approaches 1, 2, 3 and 4 were -0.99 ± 4.18%, -0.53 ± 3.88%, 2.03 ± 5.63% and 2.03 ± 5.49%, respectively, for the region classification step. Similarly, the average bias of the relative volumes obtained from the same Approaches were -1.02

$\pm$ 2.66%, -0.61 $\pm$ 2.11%, 1.87 $\pm$ 1.91% and 1.91 $\pm$ 1.77%, respectively, concerning the results generated by the LDC in the region classification step. Similarly to the k-fold cross validation technique, the average bias of Approaches 3 and 4 overestimated the ground truth relatively to Approaches 1 and 2. The outliers removal is responsible for the overestimation of the calcium regions classified by Approaches 3 and 4. After removing the outliers from the training and testing sets in each iteration of the cross-validation technique, the good separation of the examples belonging to each class induces the classifier to assign the correct class to the pixels under analysis. Hence, the calcified components tend to overestimate the corresponding ground truths since all pixels of the calcium regions are correctly classified.

The Spearman correlation of the relative and absolute areas of the classified calcium regions decreased in Approaches 3 and 4 in comparison to the results obtained from Approaches 1 and 2 in the region classification step. As previously discussed, the overestimation of the calcifications after the outliers removal is responsible for affecting the size of the classified components, leading the area of the calcified regions to increase significantly in some cases. Since the areas of the classified calcium regions increase in comparison to the correspondent ground truths, the Spearman correlation coefficients also decreased. As to the distance features, no significant differences were found when the distances of each pixel to the lumen and carotid wall contours were removed from the classification process. Hence, the classification model could be designed with only 18 intensity features in the pixel classification step.

The classification results obtained by the LDC are better than those obtained by the other classifiers that are often used in many classification problems. The results obtained by van Engelen et al. [16] also indicated the better performance of the LDC in comparison to a SVM with a RBF kernel. Other studies have also indicated the superior performance of the LDC in classifying atherosclerotic plaque components in images [20] [21] [22]. Although decision trees have been widely used in several studies dealing with different classification problems, the large number of decisions makes the tree more complex and prone to overfitting. Additionally, small changes in the input values may still cause significant changes in the model of the decision tree. As shown in Figure 9 and Figure 12, the Spearman correlation coefficients obtained from the decision tree were better for Approaches 1 and 2 of the pixel and region classification steps, achieving results equivalent to the ones of the LDC. However, the correlation coefficients obtained from the decision tree decreased significantly in Approaches 3 and 4. Improvements in the results obtained by the Naive Bayes classifier were also achieved after applying the region classification step. However, the results are still of lower quality than those of the LDC. Although the Naive Bayes classifier is simple and independent of irrelevant features, an important

condition for better results is that the features might be conditionally independent for the given class. The results of the LDC were stable in all approaches, which indicates that this classifier is more effective to classify atherosclerotic plaque components, particularly the calcified regions as proposed in this study.

The main limitation of the proposed classification model is the number of features used to perform the identification of calcified and non-calcified regions. Dimensionality reduction is often used to decrease the computational cost of the classifiers and represents an important step towards the selection of the relevant features to be used in classification models. The outliers removal has been performed to avoid the incorrect assignment of the correct class to each pixel due to the misalignments between the ground truths manually delineated in histological images and the input CTA images. However, the number of pixels of the calcified components is significantly lower than the ones belonging to the non-calcified regions. The relative area of the calcified components is low with respect to the total area of the carotid wall and the outliers removal might decrease the number of examples of the calcified components. Hence, manual delineations made directly in the CTA images represent an effective approach to avoid the removal of pixels with important information for the classification process.

Despite the above-mentioned limitation, the classification in two steps of calcium regions in CTA images of the carotid artery seems to be effective in eliminating regions not belonging to the true calcifications of the atherosclerotic lesions.

6   Conclusions

The characterization of atherosclerosis is an intensive focus of research and represents an important step in evaluating the progression of the disease. The classification of calcified components in CTA images of carotid arteries was proposed in this article. In the proposed classification model, the original CTA images are submitted to a step that processes the classification of each pixel inside the carotid artery wall. Then, the candidate regions are submitted to the next step that performs the classification per region in order to identify those ones corresponding to true calcified components. Additionally, the proposed outliers removal approach proved to be effective in improving the separation of the pixels belonging to each class, i.e. calcified and non-calcified regions, leading the shapes of the classified calcium regions close to the ones of the corresponding ground truths.

In this study, the region classification step was proposed to effectively handle the incorrect classification of regions resultant from misalignments of the ground truths with the corresponding *in vivo* CTA images. The method proved to be effective in eliminating

regions that do not correspond to true calcified components, leading to improvements of the classification results and, consequently, a more efficient, reliable and accurate classification model.

Acknowledgements

References

[1] S. Mendis, P. Puska, and B. Norrving. *Global atlas on cardiovascular disease prevention and control*. World Health Organization, 2011. ISBN 978-92-4-156437-3.

[2] B. Widder, K. Paulat, J. Hackspacher, H. Hamann, S. Hutschenreiter, C. Kreutzer, F. Ott, and J. Vollmar. Morphological characterization of carotid artery stenoses by ultrasound duplex scanning. *Ultrasound in Medicine & Biology*, 16(4):349–354, 1990. ISSN 0301-5629. doi: http:10.1016/0301-5629(90)90064-J.

[3] T. T. de Weert, M. Ouhlous, E. Meijering, P. E. Zondervan, J. M. Hendriks, M. R. van Sambeek, D. W. Dippel, and A. van der Lugt. In vivo characterization and quantification of atherosclerotic carotid plaque components with multidetector computed tomography and histopathological correlation. *Arteriosclerosis, Thrombosis, and Vascular Biology*, 26(10):2366–2372, 2006. ISSN 1079-5642. doi: 10.1161/01.ATV.0000240518.90124.57.

[4] J. M. Serfaty, L. Chaabane, A. Tabib, J. M. Chevallier, A. Briguet, and P. C. Douek. Atherosclerotic plaques: classification and characterization with T2-weighted high-spatial-resolution MR imaging– an in vitro study. *Radiology*, 219(2):403–410, 2001. ISSN 0033-8419. doi: 10.1148/radiology.219.2.r01ma15403.

[5] Z. A. Fayad and V. Fuster. Characterization of atherosclerotic plaques by magnetic resonance imaging. *Annals of the New York Academy of Sciences*, 902:173–186, 2000. ISSN 0077-8923. doi: 10.1111/j.1749-6632.2000.tb06312.x.

[6] J. M. Seeger, E. Barratt, G. A. Lawson, and N. Klingman. The relationship between carotid plaque composition, plaque morphology, and neurologic symptoms. *The Journal of Surgical Research*, 58(3):330–336, 1995. ISSN 0022-4804. doi: 10. 1006/jsre.1995.1051.

[7] C. Yuan. Identification of Fibrous Cap Rupture With Magnetic Resonance Imaging Is Highly Associated With Recent Transient Ischemic Attack or Stroke. *Circulation*, 105(2):181–185, January 2002. ISSN 00097322. doi: 10.1161/hc0202.102121.

[8] J. N. E. Redgrave, J. K. Lovett, P. J. Gallagher, and P. M. Rothwell. Histological assessment of 526 symptomatic carotid plaques in relation to the nature and timing of ischemic symptoms: the Oxford plaque study. *Circulation*, 113(19):2320–2328, May 2006. ISSN 1524-4539. doi: 10.1161/CIRCULATIONAHA.105.589044.

[9] N. Takaya, C. Yuan, B. Chu, T. Saam, H. Underbill, J. Cai, N. Tran, N. L. Polissar, C. Isaac, M. S. Ferguson, G. A. Garden, S. C. Cramer, K. R. Maravilla, B. Hashimoto, and T. S. Hatsukami. Association between carotid plaque characteristics and subsequent ischemic cerebrovascular events: A prospective assessment with MRI - Initial results. *Stroke*, 37(3):818–823, 2006. ISSN 00392499. doi: 10.1161/01.STR.0000204638.91099.91.

[10] R. M. Kwee, R. J. van Oostenbrugge, W. H. Mess, M. H. Prins, R. J. van der Geest, J. W. ter Berg, C. L. Franke, A. G. Korten, B. J. Meems, J. M. van Engelshoven, J. E. Wildberger, and M. E. Kooi. MRI of carotid atherosclerosis to identify TIA and stroke patients who are at risk of a recurrence. *Journal of Magnetic Resonance Imaging*, 37(5):1189–1194, May 2013. ISSN 10531807. doi: 10.1002/jmri.23918.

[11] M. K. Salem, M. J. Bown, R. D. Sayers, K. West, D. Moore, A. Nicolaides, T. G. Robinson, and A. R. Naylor. Identification of patients with a histologically unstable carotid plaque using ultrasonic plaque image analysis. *European Journal of Vascular and Endovascular Surgery*, 48(2):118–125, August 2014. ISSN 1532-2165. doi: 10.1016/j.ejvs.2014.05.015.

[12] D. S. Jodas, A. S. Pereira, and J. M. R. S. Tavares. A review of computational methods applied for identification and quantification of atherosclerotic plaques in images. *Expert Systems with Applications*, 46:1–14, 2016. ISSN 0957-4174. doi: 10.1016/j.eswa.2015.10.016.

[13] C. Herbert, A. Chandler, and R. Dinsmore. A Definition of Advanced Types of Atherosclerotic Lesions and a Histological Classification of Atherosclerosis. *Circulation*, 92:1355–1374, 1995. ISSN 0009-7322. doi: 10.1161/01.CIR.92.5.1355.

[14] H. Huang, R. Virmani, H. Younis, A. P. Burke, R. D. Kamm, and R. T. Lee. The impact of calcification on the biomechanical stability of atherosclerotic plaques. *Circulation*, 103(8):1051–1056, 2001. ISSN 0009-7322. doi: 10.1161/01.CIR.103.8.1051.

[15] D. Vukadinovic, T. van Walsum, R. Manniesing, S. Rozie, R. Hameeteman, T. T. de Weert, A. van der Lugt, and W. J. Niessen. Segmentation of the outer vessel wall of the common carotid artery in CTA. *IEEE Transactions on Medical Imaging*, 29 (1):65–76, January 2010. ISSN 1558-254X. doi: 10.1109/TMI.2009.2025702.

[16] A. van Engelen, W. J. Niessen, S. Klein, H. C. Groen, H. J. M. Verhagen, J. J. Wentzel, A. van der Lugt, and M. de Bruijne. Atherosclerotic plaque component segmentation in combined carotid MRI and CTA data incorporating class label uncertainty. *PLoS ONE*, 9(4):1–14, April 2014. doi: 10.1371/journal.pone.0094840.

[17] M. Wintermark, S. S. Jawadi, J. H. Rapp, T. Tihan, E. Tong, D. V. Glidden, S. Abedin, S. Schaeffer, G. Acevedo-Bolton, B. Boudignon, B. Orwoll, X. Pan, and D. Saloner. High-resolution CT imaging of carotid artery atherosclerotic plaques. *American Journal of Neuroradiology*, 29(5):875–882, May 2008. ISSN 0195-6108. doi: 10.3174/ajnr.A0950.

[18] M. A. de Graaf, A. Broersen, P. H. Kitslaar, C. J. Roos, J. Dijkstra, B. P. F. Lelieveldt, J. W. Jukema, M. J. Schalij, V. Delgado, J. J. Bax, J. H. C. Reiber, and A. J. Scholte. Automatic quantification and characterization of coronary atherosclerosis with computed tomography coronary angiography: cross-correlation with intravascular ultrasound virtual histology. *The International Journal of Cardiovascular Imaging*, 29 (5):1177–1190, June 2013. ISSN 1875-8312. doi: 10.1007/s10554-013-0194-x.

[19] H. Yan and Y. Dai. The comparison of five discriminant methods. In *International Conference on Management and Service Science*, pages 1–4, August 2011. ISBN 978-1-4244-6579-8. doi: 10.1109/ICMSS.2011.5999201.

[20] R. Van 't Klooster, O. Naggara, R. Marsico, J. H. C. Reiber, J. F. Meder, R. J. Van Der Geest, E. Touzé, and C. Oppenheim. Automated versus manual in vivo segmentation of carotid plaque MRI. *American Journal of Neuroradiology*, 33: 1621–1627, 2012. ISSN 01956108. doi: 10.3174/ajnr.A3028.

[21] A. van Engelen, W. J. Niessen, S. Klein, H. C. Groen, H. J. M. Verhagen, J. J. Wentzel, A. van der Lugt, and M. de Bruijne. Multi-feature-based plaque characterization in ex vivo MRI trained by registration to 3D histology. *Physics in Medicine and Biology*, 57(1):241–256, January 2012. ISSN 1361-6560. doi: 10.1088/0031-9155/57/1/241.

[22] A. van Engelen, W. Niessen, S. Klein, H. Groen, K. van Gaalen, H. Verhagen, J. Wentzel, A. van der Lugt, and M. de Bruijne. Automated segmentation of atherosclerotic histology based on pattern classification. *Journal of Pathology Informatics*, 4(2):1–7, 2013. ISSN 2229-5089. doi: 10.4103/2153-3539.109844.